N and p-type doping of GaN nanowires : from growth to electrical properties

Zhihua Fang

To cite this version:

Zhihua Fang. N and p-type doping of GaN nanowires : from growth to electrical properties. Condensed Matter [cond-mat]. Université Grenoble Alpes, 2017. English. NNT : 2017GREAY007 . tel-01628203

HAL Id: tel-01628203
https://theses.hal.science/tel-01628203

Submitted on 3 Nov 2017

Communauté
UNIVERSITÉ Grenoble Alpes

THÈSE

Pour obtenir le grade de

DOCTEUR DE LA COMMUNAUTE UNIVERSITE GRENOBLE ALPES

Spécialité : **Nanophysique**

Arrêté ministériel : 7 août 2006

Présentée par

Zhihua FANG

Thèse dirigée par **Bruno DAUDIN** et
codirigée par **Julien PERNOT**

préparée au sein du **CEA Grenoble et de l'Institut Néel-CNRS**
dans **l'École Doctorale de Physique**

n and p-type doping of GaN nanowires : from growth to electrical properties

Thèse soutenue publiquement le **15 mars 2017**,
devant le jury composé de :

M. Martin EICKHOFF
Professeur, Université de Bremen, Allemagne, Rapporteur
M. Jean-Christophe HARMAND
Directeur de recherche, CNRS/LPN de Marcoussis, France, Rapporteur
Mme Ana CROS
Professeur, Université de Valencia, Espagne, Examinateur et Présidente
Mme Maria TCHERNYCHEVA
Chargé de Recherche, Paris, France, Examinateur
M. Christophe DURAND
Maître de conférences, Université Grenoble Alpes, France, Examinateur
M. Bruno DAUDIN
Chercheur CEA, Grenoble, France, Directeur de thèse
M. Julien PERNOT
Professeur, Université Grenoble Alpes, France, Co-directeur de thèse

海纳百川，有容乃大

—永远的母校

天行健，君子以自强不息；地势坤，君子以厚德载物。

—献给曾经追梦的少年

ACKNOWLEDGEMENTS

A PhD (a doctor of philosophy, thèse in French) is the terminal degree in many fields, with “philosophy” indicating its original Greek meaning of “love of wisdom”. As for me, it is not only an academic degree, but also a valuable three-year professional experience. Here, I would thank all the colleagues and friends whom I have encountered during my PhD, as well as my families for accompanying me through this special period.

First of all, I would like to give my sincere thanks to my PhD advisors Dr. Bruno Daudin and Dr. Prof. Julien Pernot. They have not only provided excellent guidance and fresh perspectives for this work, but also inspired my working philosophy through numerous detailed discussions. Moreover, I really appreciate their patience, positive attitudes, and generosity, which are indispensable to the success of this work.

Secondly, I would like to thank Dr. Fabrice Donatini for his useful discussions, valuable advice, and abundant technical help. This work would not be possible without his precious contribution.

Next, my thanks go to Dr. Prof. Régis Andre (leader of the “Nanophysics and semiconductors” group), Dr. Prof. Jean-Michel Gerard (director of the “Photonics, electronics and quantum engineering” service of INAC), Dr. Prof. Etienne Bustarret (leader of the “Wide bandgap semiconductor” group), Dr. Prof. Serge Huant (director of the “Physics, lights and materials” department of Institut Néel), for their dedicated leadership and the creation of a friendly working atmosphere.

I would also like to express my gratitude to all the members of the jury: Dr. Prof. Martin Eickhoff, Dr. Jean-Christophe Harmand, Dr. Prof. Ana Cros, Dr. Maria Tchernycheva, Dr. Christophe Durand for accepting to evaluate my PhD work, despite of their busy schedules.

I am grateful to the worthy interactions with our dear collaborators: Dr. Eric Robin and Dr. Nicolas Mollard for the training on electron microscopy techniques and measurements using the state of art energy-dispersive X-ray spectroscopy, and Dr. Prof. Ana Cros for Raman spectroscopy measurements.

My special appreciations go to Dr. Yoann Cure, Dr. Yann Genuist and Didier Bollot for supporting me with their technical expertise regarding the MBE system, as well as the colleagues from Nanofab clean room (Institut Néel side): Thierry Crozes, Sébastien Dufresnes, Thierry Fournier, Bruno Fernandez, Gwénaëlle Julie, Jean-Francois Motte for their technical support during fabrication process of the devices.

I would like to acknowledge Carmelo Castagna, Cécile Blanc and Sandrine Ferrari, for helping me with the French administrative work.

I want to give my sincere acknowledgements to my close colleagues and friends: Matthias Belloeil, Xin Zhang, Thomas Auzelle, and Pierre Tchoulfian. It was a great

pleasure to meet and work with all of you during my PhD. I have learned a lot from all of you, professionally and personally.

I would like to say thank you to my friends, Agnès, Anna, Caroline, Thibault, Buk, Daria, Siew, Tobias, Mark, Emanuel, Damien, Mathieu, Akhil, Jing, Yu, Xueyin, Quanbo, Peng, Tao, Benedikt, Celine, André, Lya, Gabriel for interesting conversations at lunchtime as well as the good time we spent together after work.

Last not but least, I want to thank all my families, especially my parents. They have inspired and encouraged me to discover science when I was younger; and they have given me numerous support and understanding during this work. I really appreciate them. In addition, I would like to give my thanks to my boyfriend Sébastien. Meeting him was one of the best things happened in my life in the recent years. He has helped and supported me a lot, both professionally and personally, especially during the last year of the PhD.

ABSTRACT

III-nitride nanostructures have been attracting increasing attention due to their peculiar properties and potential device applications as lighting LEDs. The control and evaluation of the doping in the nanostructures is a crucial, yet a challenging issue. This thesis advances the field by exploring the n and p type doping process of GaN nanowires (NWs) grown by molecular beam epitaxy (MBE). In particular, their electrical properties have been revealed through a multi-technique approach at the single NW level.

Firstly, the structural and electrical properties of a series of Si-doped (n-type) GaN NWs have been studied. High resolution energy dispersive X-ray spectroscopy measurements on single NWs have illustrated the achievement of a higher Si incorporation in NWs than in epilayers, and Si segregation at the edge of the NW with the highest doping. Furthermore, direct transport measurements (four probes measurements from 300 K down to 5 K) on single NWs have shown a controlled doping with resistivity from 10^{2} to 10^{-3} Ω.cm, and a carrier concentration from 10^{17} to 10^{20} cm^{-3}. Field effect transistor measurements have evidenced the n-type nature and a high electron mobility of the non-intentionally doped NWs.

Secondly, the growth conditions of Mg-doped (p-type) and axial GaN p-n junction NWs have been determined to achieve significant Mg incorporation. Furthermore, the electrical properties of the axial GaN p-n junction NWs, dispersed on SiO_2 and contacted by ITO, have been studied using electron beam induced current (EBIC) technique. EBIC technique revealed the location of the p-n junction and clearly demonstrated its operation under reverse and forward polarization. Moreover, EBIC showed highly resistive p-GaN in accordance with the difficulties to perform direct transport measurements on p-GaN NWs.

This original study provides a nanoscale description of the electrical and doping properties of the GaN NWs, facilitating the fabrication of the future GaN nanostructures based devices.

Keywords: molecular beam epitaxy, GaN, nanowires, n and p-type doping, axial p-n junction, electron beam induced current

ABSTRACT IN FRENCH

Les nanostructures à base de nitrures d'éléments III suscitent un intérêt croissant, en raison de leurs propriétés singulières et de leurs applications technologiques potentielles, dans les diodes électroluminescentes (LED) notamment. La maîtrise et le contrôle du dopage de ces nanostructures est un enjeu crucial, mais difficile. A ce sujet, cette thèse apporte une contribution nouvelle, en explorant le processus de dopage de type n et p des nanofils (NFs) de GaN crus par épitaxie par jets moléculaires (EJM). En particulier, les propriétés électriques de ces structures ont été caractérisées par une approche multi-technique, à l'échelle du NF unique.

Tout d'abord, les propriétés structurales et électriques d'une série de NFs de GaN dopés au Si (type n) ont été étudiées. Des mesures de spectroscopie de rayons X à haute résolution sur des NFs individuels ont mis en évidence une incorporation de Si plus élevée dans les NFs que dans les couches minces épitaxiées, ainsi qu'une migration du Si à la surface du NF pour le fil ayant le niveau de dopage le plus élevé. Des mesures de transport sur des NFs uniques (quatre contacts avec une température allant de 300 K jusqu'à 5 K) ont démontré un contrôle du dopage, avec une résistivité allant de 10^{-3} à 10^{2} Ω.cm et une concentration de porteurs comprise entre 10^{17} et 10^{20} cm^{-3}. Des mesures réalisées sur des transistors à effet de champ à NFs uniques non intentionnellement dopés ont démontré qu'ils sont de type n avec une mobilité de porteurs élevée.

Parallèlement à cela, les conditions de croissance de NFs de GaN dopés au Mg (p-type) et de jonctions p-n ont été déterminées afin d'obtenir une incorporation significative en Mg. Les propriétés électriques de jonctions p-n axiale à base de NFs de GaN posées sur un substrat de SiO_2 et contactés avec de l'oxyde d'indium-étain (ITO) ont été étudiées en utilisant la technique du courant induit par faisceau électronique (EBIC). L'analyse EBIC a permis de localiser la jonction p-n le long du fil et de clairement montrer son bon fonctionnement en polarisation directe ou inverse. L'analyse EBIC a démontré que le GaN de type p est hautement résistif, confirmant ainsi les difficultés à réaliser des mesures de transport sur ce matériau.

Cette étude originale a permis de décrire les propriétés électriques et de dopage de ces NFs de GaN à une échelle nanoscopique, facilitant ainsi la fabrication des futurs dispositifs incorporant des nanostructures à base de GaN.

Mots clés : épitaxie par jets moléculaires, GaN, nanofils, dopage de type n et type p, jonction p-n axiale, courant induit par faisceau électronique

RÉSUMÉ EN FRANÇAIS

Introduction

L'intérêt récent porté aux nanofils (NWs) de GaN résulte du développement rapide des semi-conducteurs nitrures (III-N). Grâce à leur largeur de bande directe, qui couvre une grande gamme de longueurs d'onde, allant du proche infrarouge (IR) au spectre visible jusqu'à l'ultraviolet (UV) profond, les semi-conducteurs nitrures sont les matériaux idéaux pour la fabrication de dispositifs optoélectroniques tels que les diodes électroluminescentes (LEDs), diodes laser (LDs) et photodétecteurs. Au vu de ces applications technologiques, des décennies d'activités de recherche ont été consacrées à l'amélioration de la qualité des cristaux, des propriétés optiques, structurelles et électriques des matériaux III-N par différentes méthodes de croissance et techniques de caractérisation. Dans l'histoire des nitrures, deux découvertes importantes méritent d'être mentionnées : (1) la proposition de l'utilisation d'une couche tampon d'AlN pour améliorer considérablement la qualité des cristaux de la couche planaire de GaN, par Amano et al. en 1986 [1] ; (2) la révélation de l'activation du dopage accepteur de Mg dans GaN obtenue par recuit dans une atmosphère libre d'hydrogène [2] ou par irradiation par faisceau électronique de faible énergie [3] au début des années 90. Ces deux découvertes ont ouvert la voie à la fabrication des premières LEDs bleues [4], et plus tard aux premières LDs [5], qui sont les composants technologiques de base des disques Blue-ray. Ces avancées ont démocratisé l'utilisation de matériaux à base de nitrures sur des marchés commerciaux variés. Le prix Nobel de physique 2014 a été en outre attribué aux professeurs Isamu Akasaki, Hiroshi Amano et Shuji Nakamura « pour l'invention des diodes électroluminescentes bleues efficaces qui ont permis la fabrication de sources de lumière blanche intenses et économes d'énergie», signant la reconnaissance scientifique des énormes progrès dans le domaine des nitrures.

Cependant, l'un des problèmes majeurs des matériaux nitrures est l'absence de substrat adapté à leur croissance en épitaxie. Les couches planaires III-N hétéro-épitaxie contiennent une forte densité de dislocations, en raison de la contrainte induite par l'incompatibilité thermique et du désaccord de réseau avec un substrat étranger, ce qui pourrait limiter l'amélioration des performances des dispositifs à base de III-N. Les nanofils (NWs) III-N, en revanche, offrent une solution alternative à ce problème. Grâce à leur unidimensionnalité, les NWs peuvent relaxer facilement les contraintes sur leur périphérie et se développer sans dislocation sur des substrats ayant des paramètres de maille très différents.

Les premiers NWs de GaN auto-assemblés ont été annoncés par deux groupes de recherche dirigés par Kishino au Japon [6] et Calleja en Espagne [7] à la fin des années 1990. Depuis lors, les NWs III-N ont trouvé application dans des dispositifs variés, dont les LEDs, les LDs, les photodétecteurs, les sources de photons individuelles, les appareils intrabandes, les cellules solaires et la photosynthèse artificielle [8].

Objectifs et motivations de la thèse

Le dopage est une étape indispensable dans la réalisation d'un dispositif semi-conducteur. Bien que les NWs III-N aient été explorés dans de nombreux dispositifs, le contrôle et l'évaluation des caractéristiques de dopage sont loin d'être atteints.

Dans ce contexte, le but de cette thèse est d'étudier le dopage de type n et p de NWs GaN crûs par épitaxie par jets moléculaires (EJM) assisté plasma, avec des approches différentes. Plus précisément, les objectifs sont :

- l'étude du processus d'incorporation du dopant type n par le Si et du dopant type p par le Mg dans les NWs en utilisant le système d'EJM.
- l'étude des propriétés de transport électrique des zones de type n, de type p, et de la jonction p-n axiale d'un NW de GaN, à l'échelle du fil unique.

Organisation du manuscrit

Ce manuscrit se compose de trois chapitres. Le premier chapitre donne une brève introduction des propriétés de base des semi-conducteurs de la famille III-N et de la technique de croissance l'EJM, tandis que les deux autres chapitres se concentrent sur deux études complètes et originales conduites respectivement sur les NWs GaN dopés au Si et les jonctions p-n axiales.

Au chapitre 2, je vous présente une étude systématique conduite sur une série de NWs de GaN dopés au Si. Dans une première étape, les détails de croissance de cette série de NWs sont décrits, suivis des caractérisations de base utilisant le microscope électronique à balayage (MEB) et la photoluminescence (PL). Dans une deuxième étape, la variation de contrainte et les modes de défauts induits par Si dans ces NWs sont observés par spectroscopie Raman. Par ailleurs, le contenu en Si dans les NWs fortement dopés a été cartographié et quantifié le long du diamètre du NW, à l'échelle du fil unique, en utilisant une spectroscopie à rayons X à énergie dispersive (EDX). Dans la dernière étape, les propriétés de transport électrique de cette série de NWs sont étudiées. Une procédure de contact basée sur la lithographie par faisceau d'électrons a été développée afin d'effectuer des mesures électriques sur un seul NW. Les paramètres physiques importants de ces NWs, tels que la résistivité, le niveau de dopage et la mobilité, ont été évalués à l'aide de mesures de configurations à quatre pointes et à transistor à effet de champ (FET).

Dans le chapitre 3, je passe au dopage par le Mg et aux jonctions p-n des NWs GaN. Dans une première partie, les conditions de croissance appropriées pour les NWs de GaN dopés au Mg sont étudiées, puis les jonctions p-n des NWs GaN sont crûes avec une partie dopée au Mg en haut de la partie dopée au Si. Les signatures des deux dopants sont mises en évidence par des caractérisations optiques. Dans la deuxième partie, les jonctions p-n axiales des NWs GaN sont caractérisées par une technique utilisant un faisceau électronique (EBIC, courant induit par faisceau d'électrons), avec une exploration spéciale des contacts ohmiques de type p.

Collaborations

L'un des attraits de cette thèse est qu'elle a été effectuée dans deux laboratoires de Grenoble (au groupe "Nanophysique et Semiconducteurs", INAC, CEA et au groupe "Semi-conducteurs à large bande interdite", Institut Néel, CNRS), afin de combiner l'expertise respective de ces deux laboratoires dans le domaine de la croissance et de la caractérisation électrique. Par ailleurs, pour approfondir notre compréhension de la physique du dopage dans les NWs GaN, plusieurs collaborations réussies ont été menées avec des partenaires extérieurs.

Je souhaiterais nommer ici ceux qui ont contribué aux résultats présentés dans la suite de ce manuscrit.

La croissance par EJM a été réalisée sous la supervision de mon directeur de thèse Bruno Daudin (groupe Nanophysique et semiconducteurs, INAC, CEA, Grenoble), en collaboration avec des doctorats précédents / actuels du groupe.

La caractérisation électrique a été effectuée sous la supervision de mon co-directeur de thèse Julien Pernot (groupe "Semi-conducteurs à large bande interdite", Institut Néel, CNRS, Grenoble), en collaboration avec Fabrice Donatini.

La fabrication des dispositifs a été effectuée au Nanofab de l'Institut Néel, Grenoble.

Des expériences d'EDX à haute résolution ont été réalisées par Eric Robin et Nicolas Mollard (Minatec Campus, INAC, CEA, Grenoble). La spectroscopie Raman a été réalisée en collaboration avec Ana Cros de l'Université de Valencia, en Espagne.

Conclusions

Le but de ce travail de doctorat était d'étudier le dopage de type n et p dans des NWs de GaN. Pour ce faire, deux études approfondies ont été consacrées aux NWs GaN dopés au Si et à la jonction p-n axiale des NW. Les NWs ont été crûs par EMJ et caractérisés par une combinaison de techniques optiques, structurelles et électriques. Il convient de rappeler ici qu'il n'y avait pratiquement pas de mesures électriques directes sur les NWs de GaN au début de cette thèse. Le travail actuel fait donc avancer la thématique, en apportant la preuve expérimentale d'une jonction p-n axiale dans les NWs de GaN.

A propos des NWs de GaN dopés au Si

En ce qui concerne le dopage de type n, j'ai présenté une enquête systématique menée sur une série de NWs de GaN dopés au Si, crûs dans des conditions identiques, à l’exception des températures des cellules Si.

L'incorporation de Si induit une variation morphologique des NWs à une température de cellule Si supérieure à 938 °C. Un élargissement du NW a été observé et les facettes supérieures du NW sont passées d’une symétrie d’ordre 6 à une symétrie d’ordre 12 lorsque la température de la cellule Si a atteint 950 °C. Un élargissement des largeurs à mi-hauteur (FWHM) du bord de bande et une augmentation de l'émission de paire donneur-accepteur (DAP) dans les spectres de PL ont été reconnus lors du dopage Si. Plusieurs modes de défauts liés au Si ont été observés sur les spectres Raman, et une tension de traction liée à la variation de fréquence du mode E_{2h} augmente avec la température de la cellule Si jusqu'à 950 °C, où la relaxation se produit. La cartographie du contenu en Si à l'échelle nanométrique par spectroscopie d’EDX permet de comprendre ces observations. Les NWs crûs avec une température de cellule Si de 950 °C présentaient un cœur avec une concentration moyenne en Si de $2{,}5 \times 10^{20}$ at / cm^3, et une coquille avec une concentration en Si de $6{,}5 \times 10^{20}$ at / cm^3, alors que les NWs avec la température de la cellule Si de 938 °C contiennent une distribution en Si homogène à 1×10^{20} at / cm^3. Plus de Si peut être incorporé dans un NW de GaN, comparativement aux couches planaires.

Un processus de contact NW basé sur la lithographie par faisceau d'électrons a été développé pour effectuer des mesures électriques sur des NWs uniques. Les mesures de transport direct sur les NWs uniques dopés par le Si ont montré un dopage contrôlé avec une résistivité de 10^2 à 10^{-3} Ω.cm et une densité de porteurs de 10^{17} à 10^{20} cm^{-3}. Les mesures FET combinées à la simulation des éléments finis ont montré une mobilité élevée dans ces NWs, comparable à la valeur de mobilité de couches planaires de GaN dans l’état de l’art.

Jonction p-n axiale NWs de GaN

Dans la deuxième partie du manuscrit, les conditions de croissance par EMJ des NWs de GaN dopés au Mg ont été étudiées, afin d’obtenir une incorporation en Mg importante. Les propriétés électriques de la jonction p-n axiale NWs de GaN ont été étudiées en utilisant la technique EBIC.

En particulier, nous avons constaté que la température des cellules Mg et la température du substrat de croissance jouaient un rôle important dans l'incorporation du Mg dans le système de EMJ. Une recette de croissance en deux étapes a été proposée pour améliorer l'incorporation du Mg, et elle a été utilisée pour la croissance des jonctions p-n axiales.

L’analyse EBIC a permis de visualiser la présence de la jonction p-n dans deux NWs uniques et a clairement démontré son fonctionnement sous polarisation inverse et vers l'avant. Le niveau de dopage accepteur obtenu est d'environ $2\text{-}3 \times 10^{17}$ cm^{-3}, en prenant le niveau de dopage du donneur à $2\text{-}3 \times 10^{18}$ cm^{-3} estimé à partir des résultats des NWs dopés au Si. La longueur de diffusion des trous dans le n-GaN a été mesurée à 75 nm pour le NW # 1 et à 43 nm pour le NW # 2. En polarisation positive, l'EBIC révèle la nature résistive élevée du p-GaN, ce qui est compatible avec l'extension de la largeur de l'appauvrissement de la jonction p-n réduite sous une polarisation négative. Le contraste de tension des électrons secondaires s'est révélé limitée dans notre cas en raison des contaminations par faisceau électronique. Enfin, et non des moindres, nous avons montré que le contact ITO forme un contact ohmique ou quasi-ohmique sur les NWs de GaN dopés type n et p.

CONTENTS

LIST OF ABBREVIATIONS AND ACRONYMS

APT	Atom Probe Tomography
1D	1-Dimensional
2D	2-Dimensional
2DEG	2-Dimensional Electron Gas
III-N	III-Nitride
AFM	Atomic Force Microscopy
BG	Back Gate
BGR	Band Gap Renormalization
CB	Conduction Band
CCD	Charge-coupled Device
CL	Cathodoluminescence
CVD	Chemical Vapor Deposition
D_0X	Donor-bound eXciton
DAP	Donor-Acceptor Pair
EBIC	Electron Beam Induced Current
EBL	Electron Beam Lithography
EDX	Energy-dispersive X-ray Spectroscopy
EELS	Electron Energy Loss Spectroscopy
EL	Electroluminescence
FESEM	Field Emission Scanning Electron Microscopy
FET	Field Effect Transistor
FWHM	Full Width at Half Maximum
FX_A	Free eXciton A
FX_B	Free eXciton B
HAADF	High-Angle Annular Dark-Field
HEMT	High Electron Mobility Transistor
HF	hydrofluoric acid

HRTEM	High Resolution Transmission Electron Microscopy
HVPE	Hybride Vapor-Phase Epitaxy
IPA	Isopropanol
ITO	Indium tin oxide
KPFM	Kelvin Probe Force Microscopy
LD	Laser Diode
LED	Light-Emitting Diode
LG	Lateral Gate
MAD	Multi-wavelength Anomalous Diffraction
MBE	Molecular Beam Epitaxy
MD	Misfit Dislocation
MIT	Metal-insulator transition
ML	Monolayer
MOVPE	Metal Organic Vapor Phase Epitaxy
NID	Non Intentionally Doped
NW	Nanowire
PAMBE	Plasma-Assisted Molecular Beam Epitaxy
PL	Photoluminescence
PMMA	Poly methyl methacrylate
QCSE	Quantum-Confined Stark Effect
RF	Radio Frequency
RHEED	Reflection High Energy Electron Diffraction
RIE	Reactive Ion Etching
RTA	Rapid Thermal Annealing
SAG	Selective Area Growth
sccm	standard cubic centimeters per minute
SCLC	Space-charge-limited Current
SEM	Scanning Electron Microscopy
SF	Stacking Faults

SIMS	Secondary Ion Mass Spectrometry
STEM	Scanning Transmission Electron Microscopy
TD	Threading Dislocation
TEC	Thermal expansion coefficient
TEM	Transmission Electron Microscopy
UHV	Ultra High Vacuum
VC	Voltage Contrast
WZ	Wurtzite
XRD	X-Ray Diffraction
YB	Yellow Band
ZB	Zinc Blend

INTRODUCTION

General context

The emerging interests in GaN nanowires (NWs) derive from the rapid development in III-nitride semiconductors. Thanks to their direct band gap and the wide wavelength range, spanning from the near infrared through the visible spectrum into the deep ultra violet, III-nitride semiconductors are the ideal materials for fabricating optoelectronic devices, such as light-emitting diodes (LEDs), laser diodes (LDs) and light detectors. In the view of these device applications, decades of research activities have been devoted to improve the crystal quality, optical, structural, and electrical properties of III-nitride materials through different growth methods and characterization techniques. In the history of nitrides, two important discoveries are worth mentioning: (1) the proposal of the use of an AlN buffer layer to greatly improve the crystal quality of GaN epitaxial layer by Amano et al. in 1986 [1]; (2) the revelation of Mg acceptor doping activation in GaN achieved by either annealing in a hydrogen free ambient [2] or low-energy electron-beam irradiation [3] at the beginning of the 90s. These two discoveries have paved the way for the fabrication of the first blue LEDs [4] and later on the first LDs [5], which are the core technology components in Blue-ray Disc. These advances have facilitated the wide applications of nitride materials in various commercial markets. Moreover, the Nobel Prize in Physics In 2014 was awarded to Professors Isamu Akasaki, Hiroshi Amano, and Shuji Nakamura “for the invention of the efficient blue light-emitting diodes which has enabled bright and energy-saving white light sources”[*], which signifies the scientific recognition of the huge progress in the nitride field.

---

[*] https://www.nobelprize.org/nobel_prizes/physics/laureates/2014/

However, one of the main issues of the epitaxial growth of III-nitride layers is the lack of suitable substrate. The heteroepitaxial III-nitride layers contain a high density of dislocations due to the strain induced by the thermal and lattice mismatch with foreign substrate, and this could limit the performance improvement of III-nitride based devices. III-nitride NWs, on the other hand, offer an alternative solution for this issue. Thanks to its unique one-dimensionality, NWs can relax the lattice strain at the free sidewalls, and grow in a dislocation-free fashion on lattice-mismatched substrates.

The first self-assembled GaN NWs were reported by two research groups led by Kishino in Japan [6] and Calleja in Spain [7] at the end of the 1990s. Since then, many progress have been made in applying III-nitride NWs in various devices, including LEDs, LDs, photodetectors, single photosources, intraband devices, solar cells, and artificial photosynthesis [8].

The position of this thesis

Doping is indispensable to achieve any kind of semiconductor devices. Although III-nitride NWs have been explored in different devices, the control and assessment of doping characteristics are far from being achieved.

In this context, the aim of this PhD is to investigate the n and p-type doping of GaN NWs grown by plasma-assisted molecular beam epitaxy (PAMBE) through different perspectives. More specifically, the objectives are

- to study the n-type dopant (Si) and p-type dopant (Mg) incroporation process in the PAMBE system.
- to examine the electrical transport properties of n-type, p-type and axial p-n junction GaN NWs at single NW level.

The structure of this manuscript

This thesis consists of three chapters. The first chapter gives a brief introduction of the basic properties of III-nitride materials and the PAMBE growth method, while the other two chapters focus on two complete and original studies on Si-doped GaN NWs and GaN p-n junction NWs, respectively.

In Chapter 2, I will present a systematic study on a series of Si-doped GaN NWs. In a first stage, the growth details of this series of Si-doped GaN NWs are described, followed by the basic characterizations using scanning electron microscope and photoluminescence. In a second stage, the strain variation and defect modes induced by Si in these NWs are witnessed by Raman spectroscopy; moreover, the Si content in heavily doped NWs has been mapped and quantified along the NW diameter on single NW level using energy-dispersive X-ray spectroscopy. In the last stage, the electrical transport properties of this series of Si-doped GaN NWs are investigated. A contacting procedure based on electron beam lithography was developed In order to perform electrical measurements on single NW. Important physical parameters of these NWs, such as resistivity, doping level, and mobility have been further evaluated using measurements of four-probe and field effect transistor configurations.

In Chapter 3, I will switch to Mg-doped and GaN p-n junction NWs. In a first session, the suitable growth conditions for the Mg-doped GaN NWs are investigated, and then axial GaN p-n junction NWs are grown with Mg-doped part on top of the Si-doped part. Photoluminescence characterization will demonstrate the signatures of the both dopants. In the second session, the axial GaN p-n junction NWs are characterized by electron beam induced current technique, with a special exploration on p-type ohmic contacts.

Collaborations

One of the attracting feathers of this PhD work is that it has been carried out in two laboratories ("Nanophysics and Semiconductors" group, INAC, CEA and "Wide bandgap semiconductor" group, Institut Néel) in Grenoble, with the aim of combining their expertise in the field of growth and electrical characterization, respectively. In addition, in order to deepen our understanding of the physics of doping in GaN NWs, several successful collaborations have been realized with external collaborators. To "conclude this introduction", I would like to name those who have contributed to the results hereafter presented in this manuscript.

Growth by PAMBE was carried out under the guidance of my PhD supervisor Dr. Bruno Daudin ("Nanophysics and Semiconductors" group, INAC, CEA, Grenoble) and in collaboration with previous / current PhD students from the group.

Electrical characterization was carried out under the guidance of my PhD co-supervisor Prof. Julien Pernot ("Wide bandgap semiconductor" group, Institut Néel, Grenoble) and in collaboration with Fabrice Donatini (Institut Néel, Grenoble).

All the devices process have been realised in Nanofab Institut Néel, Grenoble.

High resolution energy-dispersive X-ray spectroscopy (EDX) was performed by Dr. Eric Robin (Minatec Campus, INAC, CEA, Grenoble).

Raman spectroscopy was performed in collaboration with Dr. Ana Cros from University of Valencia, Spain.

1 THE BASICS

The objective of this chapter is to give a brief description of some basic properties of the main subject of this work: nitride materials, including nitride nanowires (NWs), as well as the main growth method (molecular beam epitaxy).

1.1 Nitride properties

1.1.1 Structural properties

The III-N semiconductor family (InN, GaN, AlN as well as their ternary and quaternary alloys) mainly exists in the form of two different crystalline structures: wurtzite (WZ) and zinc-blende (ZB). The former contains a hexagonal unit cell with two lattice constants a and c whereas the latter is made of cubic unit cells. The WZ structure is composed of two interpenetrating hexagonal close-packed sublattices formed by metallic and nitrogen atoms respectively, ideally shifted by (3/8)c along the [0001] direction. The ZB structure contains two interpenetrating face-centered cubic sublattices, shifted by one quarter of the distance along the cube diagonal. Thermodynamically, the WZ structure is more stable than the ZB phase under ambient conditions. Thus, the WZ structure is generally the main interest of epitaxial growth; however, ZB could be present in the form of stacking faults [9]. As illustrated in Figure 1.1, the WZ crystal structure of GaN is presented with a ball-stick schematic, in which the Ga and N atoms are portrayed by the blue and pink balls, respectively. The basic parameter is lattice constant a, and c is the length of the hexagonal primitive cell. The atoms are stacked in form of the ABABA along the [0001] axis in the WZ hexagonal unit cell. Figure 1.1 also shows the most common planes in the WZ structure, including polar c-plane, non-polar a- and m- planes as well as semi-polar (11-22) plane. Recommended values of lattice parameters a and c of wurtzite InN, GaN, AlN at 300K are given in Table 1.1 [10].

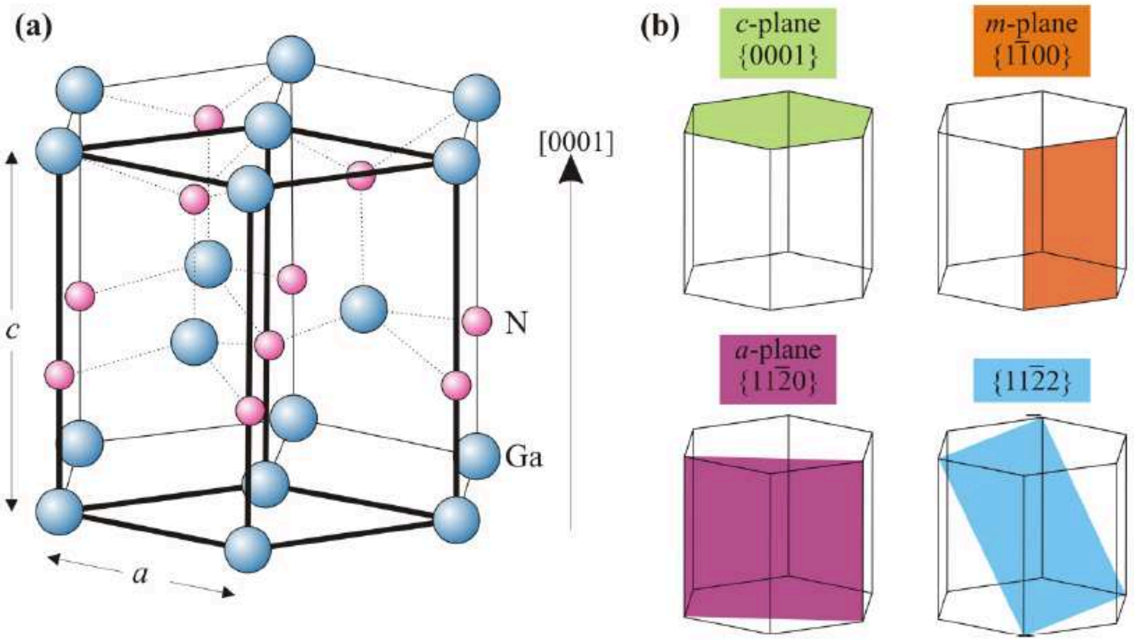

Figure 1.1 Wurtzite (WZ) crystal structure of GaN [11]. (a) The blue and pink balls represent the Ga and N atoms, respectively. The hexagonal unit cell is highlighted with bold lines. (b) The most common plane in this hexagonal structure, including the polar c-plane, the non polar a- and m- planes as well as semi-polar (11-22) plane.

Table 1.1 Lattice parameters a and c for wurtzite InN, GaN, AlN at 300K [10]

Lattice parameter	**InN**	**GaN**	**AlN**
a (Å) at 300 K	3.533	3.189	3.112
c (Å) at 300 K	5.693	5.185	4.982

Polarity In the WZ structure, the [0001] and the [000-1] directions are not equivalent, because of a lack of center of symmetry. The vector going from the metallic atom (In, Ga, Al) and pointing towards N is conventionally defined as the positive direction of the c-axis, i.e. [0001]. Therefore, two polarities can be distinguished, metal-polar (Ga-polar in the case of GaN) when its growth direction is along [0001]; N-polar when its growth direction is along [000-1] (see Figure 1.2).

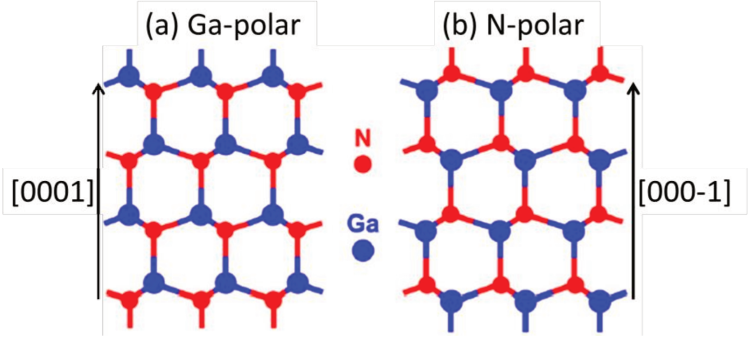

Figure 1.2 Illustration of Ga-polar (a) and N-polar GaN crystal structure from [12].

1.1.2 Electronic properties

Band gap The III-nitrides semiconductors have been promising candidates in optoelectronic devices due to their adjustable direct band gap (0.64 eV to 6.25 eV), which covers a wavelength range from the near infrared to the deep ultra violet on the electromagnetic spectrum (see Figure 1.3 (a)).

In a semiconductor, the band gap E_g is the smallest energy separation between the valence and conduction band edges. When the minimum of the conduction band energy and the maximum of the valence band energy occur at the same momentum value, this semiconductor is called a direct band gap semiconductor. As shown in Figure 1.3 (b), the minimum of the conduction band of wurtzite GaN lies just above the maximum of the valence band, which consists of three subbands: the heavy holes band, the light holes band, and the split-off band. In this sketch, the E_g for GaN at 300 K is shown to be 3.39 eV. The E_g of wurtzite InN, GaN, AlN at 300 K is listed in Table 1.2 [10]. The temperature dependence of E_g can be described by Varshni's law, as shown in equation (1.1). The Varishni parameters α and β for InN, GaN, AlN, respectively, are listed in Table 1.2 [10].

$$\boldsymbol{E_g(T) = E_g(0) - \frac{\alpha T^2}{\beta + T}} \tag{1.1}$$

Table 1.2 The bandgap E_g of wurtzite InN, GaN, AlN at 300 K and 0 K [10]

	InN	**GaN**	**AlN**
E_g (eV) at 300 K	0.64	3.39	6.14
E_g (eV) at 0 K	0.69	3.51	6.25
Vashni parameter α (meV / K)	0.414	0.909	1.799
Vashni parameter β (K)	454	830	1462

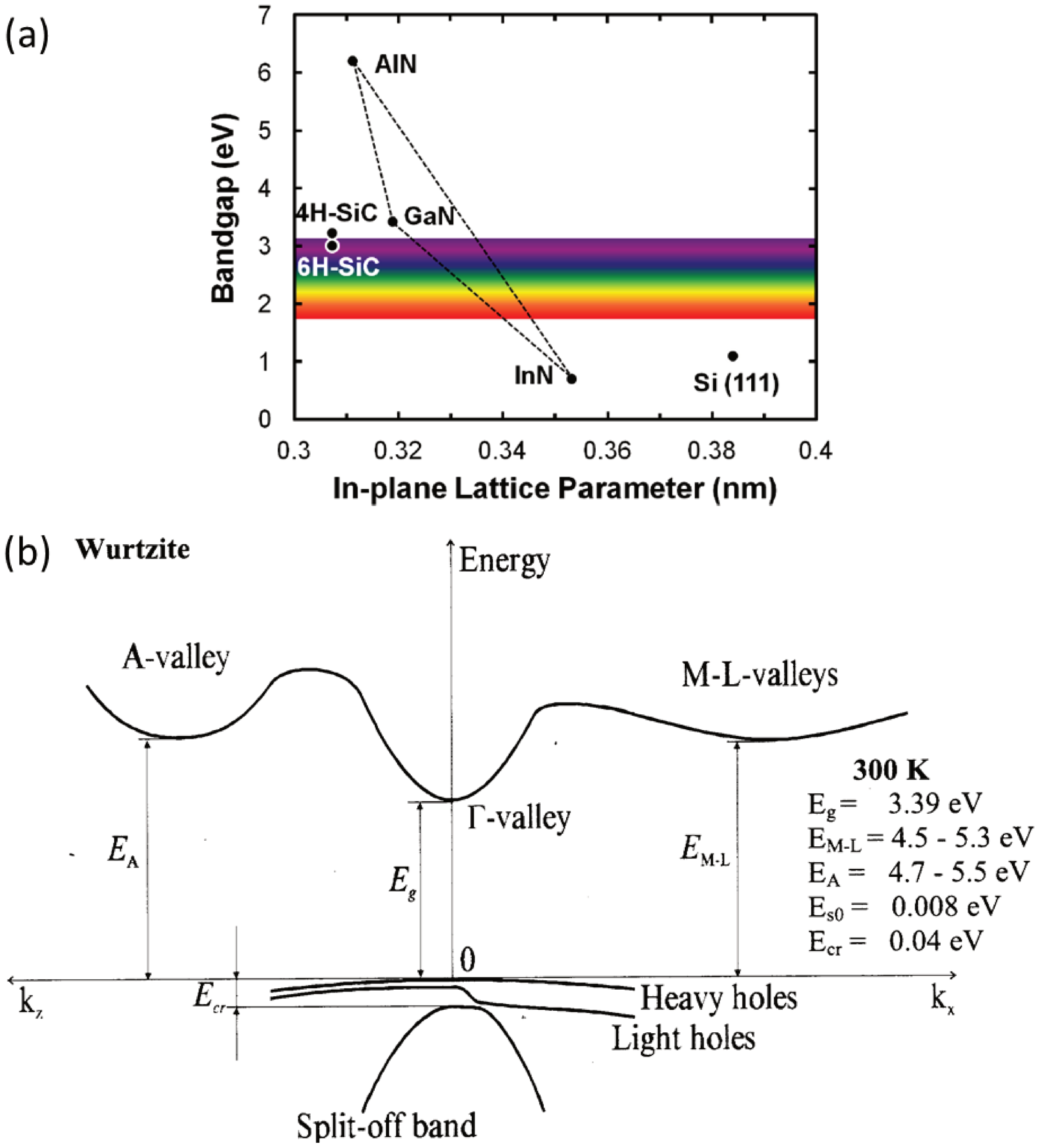

Figure 1.3 (a) In-plane lattice parameters and bandgap energies at 300K of III-V compound semiconductors and common growth substrates (SiC and Si), and the bowing parameters for their ternary alloys are neglected, taken from [13]. (b) Sketch of the band structure in GaN WZ crystals, taken from [14].

For III-nitride semiconductors, different band gaps can be obtained by varying the composition of their ternary alloys. For an alloy $A_xB_{1-x}N$ (for example, $In_xGa_{1-x}N$ or $Al_xGa_{1-x}N$), E_g can be calculated using the following equation:

$$\boldsymbol{E_g(A_xB_{1-x}N) = xE_g(AN) + (1-x)E_g(BN) - x(1-x)b} \qquad \textbf{(1.2)}$$

where x is the composition percentage of A specie, and b is the bowing parameter serving as the correction factor for the linear relation between A and B species.

Polarization For III-nitrides, the electronegativity of the N atom is bigger than that of the metallic atom (In, Ga, Al), forming an electrostatic dipole along the III-N bond. Due to lack of center of symmetry along the [0001] direction in the WZ structure, these local spontaneous polarizations do not compensate and there is a macroscopic spontaneous polarization P_{sp} present along the c-axis in III-nitrides materials. The values of P_{sp} for InN, GaN, and AlN have already been theoretically calculated by Bernardini et al.[15].

Meanwhile, piezoelectric polarization is also present in the III-nitride materials due to strain. Therefore, the total polarization is the sum of spontaneous polarization and piezoelectric polarization. The presence of this polarization can have significant effects on device structures and has inspired new applications for III-nitride materials.

1.2 Epitaxial layers and nanowires (NWs)

1.2.1 2D layer growth — substrate issues

The choice of substrate is one of the first things to do when it comes to the epitaxy of a given material. Unfortunately, for III-nitrides, this choice is not easy. In fact, the main issue for the epitaxy of 2D III-nitride layers is the lack of suitable substrate.

Homoepitaxy Homoepitaxy could be ideal for the epitaxy growers since there would be no worries with mismatch and influence from the foreign substrates. However, for a long time, commercial bulk GaN or AlN wafers were not available. Many efforts have been devoted to optimize the growth conditions for producing large bulk nitride substrates with low dislocation density. Additional to traditional vapor phase methods, such as Hydride Vapor Phase Epitaxy (HVPE) and Metal Organic Chemical Vapor Deposition (MOCVD), novel solution-based methods such as ammonothermal [16], Na-flux [17], high pressure [18] etc. have been developed to improve the crystal growth. Even though the defect density can be reduced to 10^2-10^3 cm^{-2}, these methods are still limited in terms of the crystal size (around 10 mm×10 mm) and cost. Nowadays only a few companies, such as Unipress (Poland), and Sumitomo Electric (Japan), sell GaN bulk substrate with 2 inch size.[†] Although these substrates have already been use to fabricate for example, laser diodes [19], and power electronic devices, bigger and cheaper good quality bulk nitride substrates could really boost the applications of these materials.

Heteroepitaxy Based on this situation, most researchers have relied on heteroepitaxy, which means to epitaxially grow a single crystal structure on a foreign substrate. Many criteria need to be considered, when it comes to choose this foreign substrate, including

---

[†] http://topganlasers.com/nitride-epi-wafers/
http://global-sei.com/sc/products_e/gan/index.html

lattice mismatch, thermal expansion coefficient (TEC) difference, surface chemistry, temperature stability, thermal conductivity, electrical conductivity, substrate size availability, and last but not the least cost. All these parameters could influence the crystal orientation, polarity, strain, defect concentrations of the epilayer structure, and eventually the device performance.

In Table 1.3, I have listed some of the crucial properties of three common substrates in the case of GaN epilayer growth. Concerning the cost, only the price of a 2 inch wafer is listed as an example. Other factors, such as wafer processing and packaging, should also be considered in device fabrication. Moreover, Si holds the unique advantage of being compatible with the standard COMS technology in microelectronics.

Table 1.3 Crucial properties of three most common substrates (sapphire, SiC, Si) for GaN heteroepitaxy growth [20]

	Sapphire Al2O3 (0001)	**6H-SiC (0001)**	**Si (111)**
Lateral lattice (a) mismatch (%)	−14%	−3.5%	−17%
TEC mismatch (1/K)	$+1.7\times10^{-6}$	-1.1×10^{-6}	-2×10^{-6}
Thermal conductivity (W/cm K)	0.3	4	1.56
Electrical conductivity	Insulating	From semi-insulating to metallic	From semi-insulating to metallic
Available size	Up to 6 inch	Up to 6 inch	Up to 8 inch
Cost / 2 inch wafer	50 €	120-200 €	10 €

1.2.2 NWs

On the other hand, NWs could provide an interesting solution to this substrate dilemma. In the particular geometry of NWs, the strain can be relieved at the free sidewalls, the substrate lattice mismatch and thermal expansion compatibility are much less important; therefore fabrication on a wide variety of substrates, including Si, is possible. Moreover, better crystal quality can be obtained compared to 2D epilayers counterparts because of the absence of dislocations.

1.3 Growth methods

1.3.1 Molecular beam epitaxy

Based on the knowledge from solid-state physics, surface physics, and materials science, molecular beam epitaxy (MBE) was firstly developed as a new crystal growth technology for epitaxial GaAs layers by the scientists and engineers from IBM and Bell in the 1960s [21], [22]. With the growing interest in III-nitrides materials in the 1990s, MBE has become an essential tool for fundamental studies in this field. The definition of MBE could be “the deposition of epitaxial films onto single crystal substrates using atomic and molecular beams produced from Knudsen cells under ultra-high vacuum (UHV) conditions”, as described in a review paper in 2004 [23].

In the specific case of III-nitride systems, MBE can be distinguished depending on how the nitrogen is introduced. For instance, nitrogen can be provided either by dissociating ammonia molecules (ammonia-MBE, often referred as NH_3-MBE), or by creating a plasma with the help of a radio-frequency (RF) discharge (plasma-assisted MBE, or PA-MBE) [23].

In this thesis, all the samples have been grown in a plasma-assisted MBE.

1.3.2 The traits of MBE

The choice of growth techniques largely depends on the desired structure and needs. Some of the characteristics of MBE are listed in the following:

- An UHV - based technique: the control on the vacuum environment and on the quality of the source materials allows a high material purity and crystal quality. Inside the growth chamber, ballistic transport is fullfilled instead of diffusive.
- Insitu monitoring techniques such as reflection high-energy electron diffraction (RHEED) are available to investigate the growth mechanisms.
- In MBE, it is possible to grow atomically sharp interface thanks to lower growth temperature and growth rate.
- However, MBE suffers from a lower yield, due to a lower growth rate and wafer capability, in terms of mass production [24].

2 SILICON DOPED GAN NWS

Ever since the very first epitaxial growth of GaN layer by hydride vapour phase epitaxy [25], efforts have been spent to study doping in these layers. However, this study of impurity incorporation was very ambiguous, since the as-grown GaN epitaxial layers at that time had a poor crystal quality and very high non-intentional doping with electron concentrations in the range of 10^{19} cm^{-3} [26]. In 1986, Amano et al. discovered that the use of an AlN buffer layer could greatly improve the crystal quality of GaN epitaxial layer [1], which paved the way to systematically examine the effect of doping.

In the late 90s, with the development of growth techniques, impurity incorporation in epitaxial GaN layers grown under different conditions has been investigated both theoretically [27], [28] and experimentally [29], [30].

Silicon, oxygen, germanium are common donor impurities typically used for GaN n-type doping. In fact, impurity incorporation is more complicated in GaN than in other semiconductors, such as Si, or GaAs, due to the large mismatch in the atomic radii of Ga and N. The property of the substitutional impurity depends on its location: for silicon or germanium, when substituting for Ga, it is a donor in GaN; while replacing N, it is an acceptor; whereas, for oxygen, the situation is the opposite. Both Si and Ge prefer to substitute Ga atoms energetically, which make them donors in GaN. This can be intuitively explained by the fact that Si and Ge have atomic radii very close to gallium. For the very same reason, O prefers to replace N atom, thus serves as a donor in GaN [27], [28].

GaN epitaxial layers grown by various techniques doped with either silicon, or oxygen, or germanium, have already been investigated experimentally, showing that these three dopant impurities are effective shallow donors [29]–[32]. In an MBE growth system, Si and Ge are often employed since they can be provided by an effusion cell like for Ga.

Comparing to Ge, Si is a more widely used, more abundant, and cheaper material, thus it becomes the first choice for doping in GaN.

However, it has been evidenced by several groups that Si doping is associated with defects formation and increasing strains in GaN epilayers [33]–[35].

As discussed in the previous chapters, GaN NWs provide an interesting alternative for new nanoelectronic devices due to remarkable crystal quality and quasi-1D structure [36]–[40]. For realizing these various devices, a precise control and quantitative assessment of the doping is essential.

Concerning Si doped GaN NWs grown by MBE, both Calarco et al. and Furtmayr et al. have addressed this issue in a few publications. They have found visible morphology and density changes of GaN NWs upon Si doping. More nucleation sites at the NW side walls and the existence of an additional SiN layer at the NW/Si substrate interface have been proposed for explaining these changes [41], [42]. However, many important questions remain open: What is the growth mechanism behind these morphology variations? How much Si can be incorporated? What are the spatial distributions of Si dopants along the growth direction and the wire radius and their impact on the growth kinetics? Is it possible to incorporate more Si in GaN NWs compared to epitaxial layer?

Furthermore, the electrical transport properties of MBE grown Si doped GaN NWs are rarely explored. It is extremely technologically challenging to make conventional transport measurements, such as Hall-effect measurement and capacitance-voltage measurement on NWs, because of the nanoscale dimension and quasi-1D geometry. Some other indirect measurements have been reported. Both Calarco et al. [42]–[44] and Sanford et al. [45]–[47] have carried out extended studies to extract the carrier concentration and mobility of GaN NWs via various photoconductivity measurements. Interesting phenomena such as the effect of surface Fermi-level pinning and surface recombination have been witnessed. Notwithstanding, direct transport measurements on single MBE-grown GaN NW are in great need for the further understanding of the electrical properties of these NWs.

This chapter intends to present our study of the structural and electrical properties of Si-doped GaN NWs. In the first section, we will briefly introduce PAMBE and the growth method employed in this thesis. In the second section, we will discuss the structural properties of Si-doped GaN NWs with the help of Raman spectroscopy and high resolution energy disperse X-ray spectroscopy. Lastly, we will address the electrical properties of single NWs via direct transport measurements (four-probe resistivity and its temperature dependence, field effect transistor measurements, etc.).

2.1 Growth by PAMBE

2.1.1 Plasma-Assisted Molecular Beam Epitaxy

As mentioned in chapter 2, the MBE machine used in this thesis is a RF - PAMBE from the French company Meca2000. A sketch of the Meca2000 system and the principle of growth in such PAMBE are depicted in Figure 2.1.

The main growth chamber is maintained in UHV (10^{-11}-10^{-10} mbar), thanks to intensive pumping by several pumps, including one primary pump, two turbomolecular pumps, and one ionic pump. The transfer system consists of two airlocks, which can help to ensure the high vacuum while introducing and taking out the sample. The chamber wall is equipped with liquid nitrogen circulation, in order to trap impurities and keep low pressure inside the chamber.

Both the metallic elements such as Ga, Al, In, as well as the doping elements such as Mg, Si are provided by Knudsen cells. The metal flux can be varied by heating the corresponding metal up to a certain temperature. N in our machine is supplied by the dissociation of N_2 molecules using a radio frequency (RF) discharge. During the growth, the pressure inside the chamber is increased to around 1.5×10^{-5} mbar, due to the existence of nitrogen flux. The atomic flux transport is still ballistic at this pressure, since the average mean free path of the atoms is around 10 meters, much larger than the dimensions of the MBE machine. Therefore, the atomic fluxes can arrive ballistically with incident angles and react on the substrate, which is heated by heater filaments at the backside and can be rotated for homogenous nucleation.

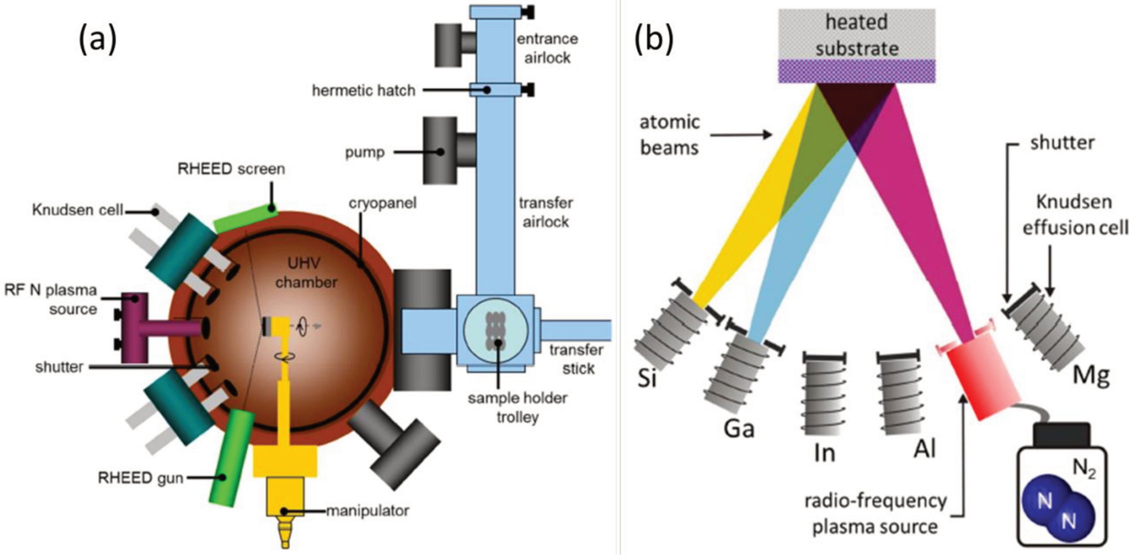

Figure 2.1 (a) Sketch of the Meca2000 PAMBE machine used in this PhD [48]. (b) Scheme of the different metal cells as well as the N2 plasma source inside a PAMBE growth chamber [48].

One of the merits of MBE system is the possibilities of in situ characterizations. In our MBE, RHEED is the only tool available for in situ and real time characterization. It presents a live picture of the reciprocal space lattice of the sample surface; therefore, it can be employed to monitor the surface morphology during the growth. As illustrated in Figure 2.2, an electron beam of 32 keV is sent towards the substrate with a grazing angle (<3°). The diffracted beam patterns are projected on a phosphorescent screen. These patterns are processed by image treatment software called "AnaRheed", which is developed by Y. Cure from INAC, CEA. In addition, RHEED is very useful for the calibration of MBE atomic fluxes through RHEED oscillations, which will be addressed in 2.1.2.3.

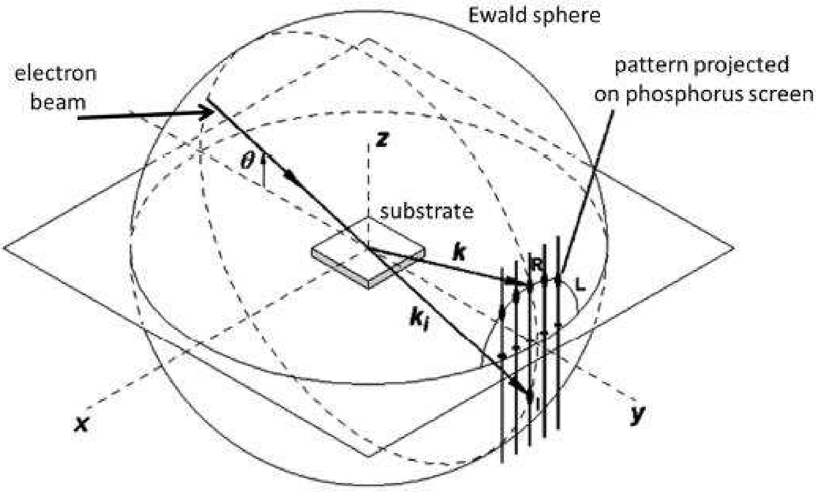

Figure 2.2 The principle of RHEED [48].

2.1.2 Sample preparation procedures and calibrations

2.1.2.1 Substrate preparation before growth

As discussed previously, one of the crucial advantages of NW growth is that it can be grown on a large range of substrates, including widely available substrate such as Si. In this thesis, Si wafers from Sil'tronix have been used as growth substrates. The specifications of these wafers are listed in the following:

- Orientation (111)
- Diameter 2 inch (50.8 mm)
- Thickness 275 μm
- Highly n-doped (with P atoms), with a low-resistivity (less than 5 mΩ.cm).

Different steps have been applied to clean the Si wafer. Before loading into the MBE chamber, the Si substrate is dipped in a diluted (around 20%) hydrofluoric acid (HF) solution for 45 seconds, in order to etch away the native SiO_2 on its surface. Then, this substrate is placed onto a substrate holder made of molybdenum (also called "molybloc"), then transferred into the first airlock, and kept under the vacuum. Once transferred onto the oven inside the chamber, the substrate is heated by radiation from the oven filament up to an elevated temperature (around 870 °C) for 10 minutes. This annealing helps to eliminate the last whiffs of SiO_2 on the substrate, until the observation of a clear 7×7 reconstruction in RHEED pattern, which is a signature of clean Si top surface [49][50].

2.1.2.2 Substrate temperature calibration

The substrate temperature is a very important parameter for the growth of nanostructures in MBE. However, the precise measurement of the substrate temperature in vacuum is not easy. In our case, three methods have been applied in order to estimate this temperature reasonably:

- The electrical power applied on the heater filament is recorded for each sample, (unit is watts). However, it depends on the thermal inertia of the molybloc, and the gradual diminution of the filament diameter along with its use.
- The temperature measured by a thermocouple at the backside of the substrate, (unit is Celsius degree). Yet, this measurement depends on the exact environment geometry and the exact contact position of the thermocouple.
- A characteristic time of Ga adatoms desorption on clean Si(111) surface in situ followed by RHEED, (unit is second). A typical example for such desorption data is shown in Figure 2.3. This Ga desorption method [51][52] can keep a good reproducibility from sample to sample.

Additionally, the temperature is not homogenous on the wafer substrate, due to heating inhomogeneity and the mechanical design of the substrate holder. The temperature difference from the center to the edge of the wafer, estimated to be around 40 °C, is important for the NW morphology, as we will see later, therefore, the Ga desorption calibration has been done systematically at the center of the wafer for each growth in order to be reproducible.

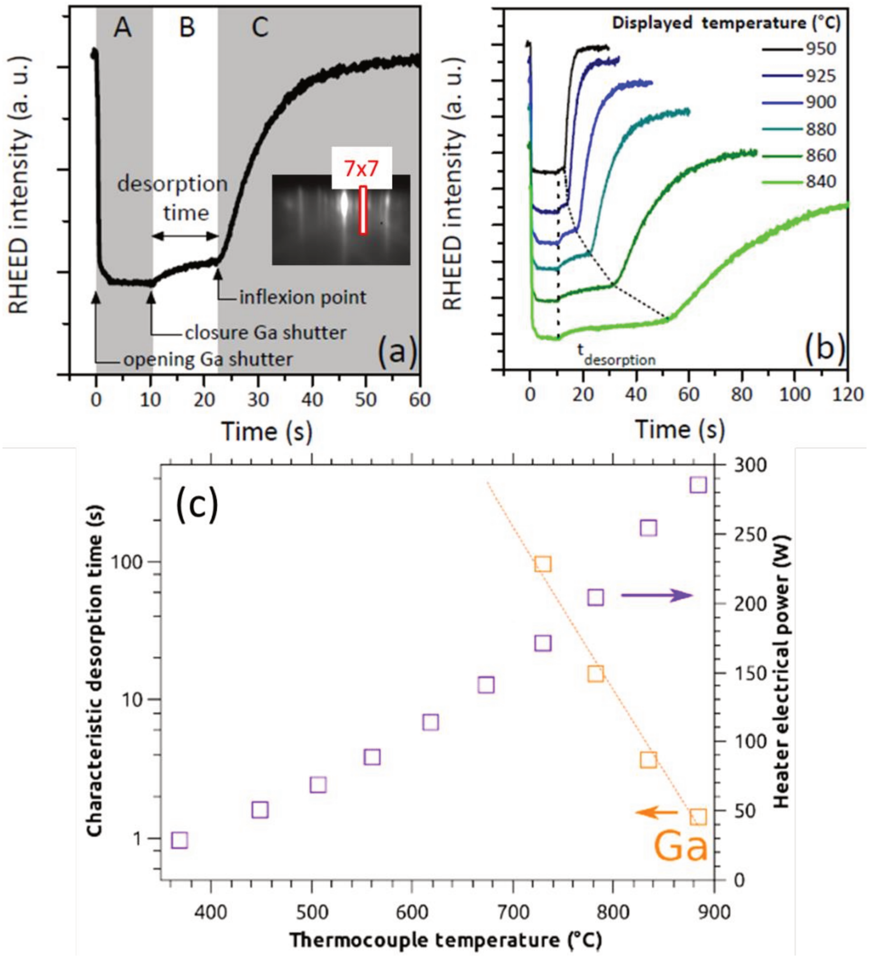

Figure 2.3 Ga desorption for substrate temperature calibration. (a) Si 7×7 RHEED intensity evolution as a function of time during Ga deposition for 10 s and the subsequent desorption; inset: RHEED picture of the Si 7×7 surface reconstruction, the rectangle represents the area where the 7×7 intensity is measured [48]. (b) The same transients at different substrate temperatures [48]. (c) Summary of Ga desorption times and heater electrical power as a function of the thermocouple temperature [53].

2.1.2.3 Atomic flux calibrations

The basic experimental parameters to control the atomic fluxes are effusion cell temperatures for metals, RF input power and N_2 flow for nitrogen atoms. In our case, the metal flux is calibrated to the corresponding 2D layer growth rate using RHEED intensity oscillations at low substrate temperature under N-rich conditions.

The RHEED oscillations rely on the observation of the specular RHEED intensity during the growth of a 2D layer in a monolayer (ML) by ML mode. As show in Figure 2.4 (A), when one ML is fully deposited, the roughness of the sample surface is at its minimum, resulting in a larger reflectance, therefore, the specular RHEED spot intensity is at its local maximum (a). On the other hand, when one ML is partially completed, the surface roughness is increased, leading to more scattering of the impinging electrons, which reduces the intensity of the RHEED specular spots. Similarly, when the ML is fully completed, the intensity of the RHEED spots is at its local maximum again (c). Hence, one ML has been grown during the time interval between two local maximums of the specular RHEED spot intensity. When plotting the RHEED specular spot intensity as a function of time, we can determine a growth rate of the 2D layer in the unit of ML per seconds. Under nitrogen rich condition, this growth rate can represent the metal flux. For example, the growth rate of GaN 2D layer is shown in Figure 2.4 (B). We can calibrate the Ga flux before the stoichiometry [54].

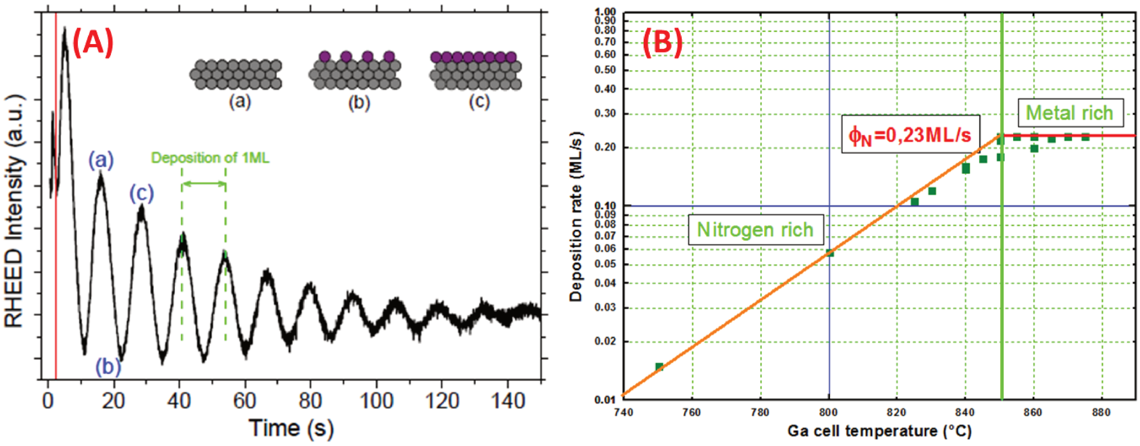

Figure 2.4 RHEED oscillations and atomic flux calibrations. (A) Oscillations of the specular RHEED spot intensity as a function of time during GaN 2D layer growth, (a-c) illustrate the corresponding sample surface during the growth. (B) GaN 2D layer growth rate as a function of Ga cell temperature, two growth regimes can be notified: below 850 °C, the growth rate raises along Ga cell temperature, indicating nitrogen rich condition, therefore Ga flux can be represented by the growth rate; above 850 °C, the growth rate saturates, giving a nearly constant value of 0.23 ML/s, which corresponds to the nitrogen flux.

This calibration can give intuitive information on the metallic flux compared to the nitrogen flux. However, the case of NW growth is a bit different. The NWs are generally growing at a higher substrate temperature than the 2D layer, implying more Ga atom desorption. Moreover, the Ga adatom surface diffusion from the NW sidewall to the top plays a crucial role in the NW elongation stage. Therefore, the real Ga flux during NW growth is always higher than this 2D layer calibration. As shown in Figure 2.5, long GaN NWs with intermittent AlN markers can be employed to estimate the Ga flux during the NW growth. And the NW growth rate is indeed higher than that of 2D layer.

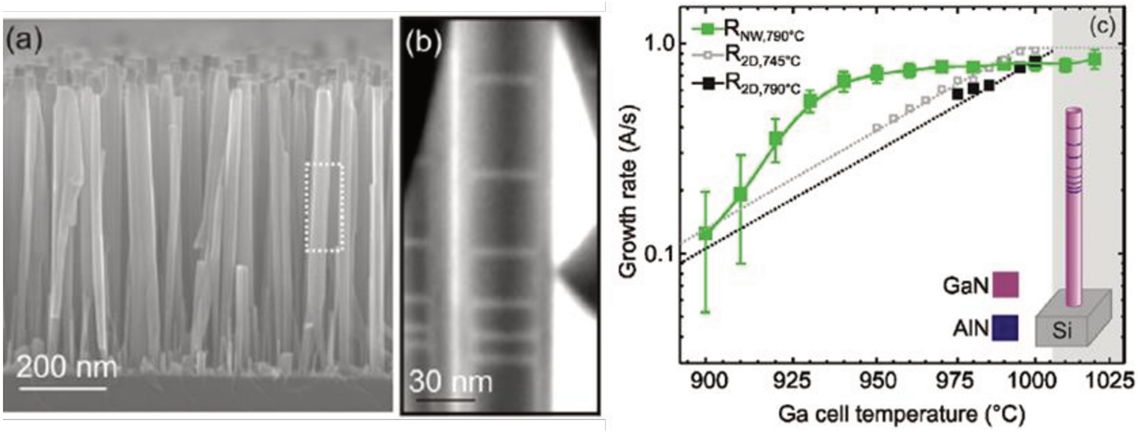

Figure 2.5 Ga flux calibration using AlN markers [55]. (a) Side-view SEM image of GaN NWs. (b) Scanning transmission electron microscopy (STEM) image of a single GaN (darker) NW with the AlN (brighter) markers. (c) Compared evolution of the growth rate of GaN NWs and a compact 2D layer grown at the substrate temperature of 745 °C and 790 °C as a function of the Ga effusion cell temperature.

2.1.3 The growth of GaN NWs

After having introduced substrate surface preparation procedure and temperature calibrations, let us now concentrate on the growth of GaN NWs. As mentioned in Chapter 1, the earliest reports on the growth of GaN nanostructures by PAMBE were on sapphire substrate in 1997 [6] and on silicon substrate in 1998 [7]. Since then, many efforts have been made to optimize the growth conditions, and further investigate the growth mechanism of these nanostructures.

2.1.3.1 The influence of substrate temperature and Ga/N flux

In 2009, Fernandez-Garrido et al. [56] has summarized a growth diagram for GaN NWs grown on bare Si (111) substrate (Figure 2.6 (a)). The different growth regimes have been illustrated as a function of impinging Ga/N flux ratio and growth temperature, while keeping the active N flux constant. We can conclude that the growth window for GaN NWs (termed as nanocolumns in [56]) consists of an excess of nitrogen (Ga/N flux ratio<1) and a temperature around 800 °C. At a higher temperature, it is challenging to grow GaN NWs due to strong Ga desorption and GaN decomposition. At a lower temperature, or Ga rich condition, the GaN NWs coalesce until forming a compact layer.

Within the growth window of GaN NWs, different conditions can have a crucial influence on the morphologies of the NWs. K. Hestroffer has quantitatively studied the GaN morphology variations depending on the substrate temperature (Figure 2.6(b)) [48], [51]. We can see that the NW density decrease gradually from 780 °C to 795 °C; and it reduces to 0 dramatically starting from 805 °C resulting from high rate of GaN decomposition. Note that there is a temperature gradient along the wafer radius, as a result, a variation of density can be generally observed on one single wafer, which is beneficial for carrying out density-dependence study on one single wafer. Meanwhile, several groups have reported the effect of Ga/N flux ratio on NW morphology [57], [58] [55]. As shown in Figure 2.7, under N-rich condition, the average growth rate rises almost linearly with increasing Ga/N flux ratio, since more Ga adatoms are involved in the absorption and diffusion process. This is advantageous when high growth rate is desired for growing NWs with a length of a few micrometers. Meanwhile, the NWs become wider under higher Ga/N flux ratio, which can lead to undesired NW coalescence. Therefore, one of the strategies to grow long GaN NWs is to nucleate the NWs under low Ga flux, and then increase Ga flux for growing at a higher speed during the axial elongation phase.

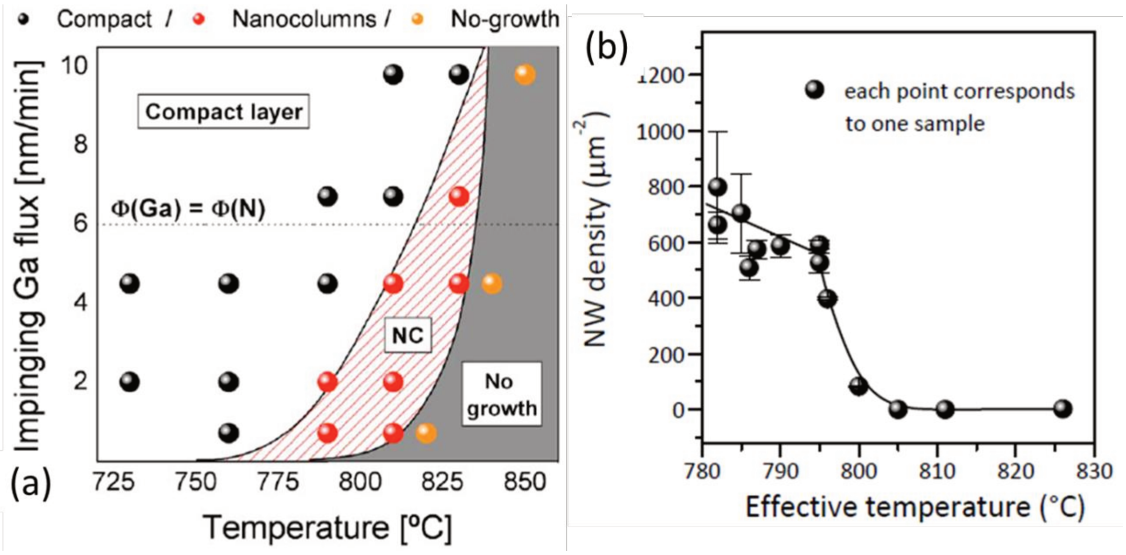

Figure 2.6 GaN NW growth condition diagram. (a) The growth diagram as a function of Ga flux and growth temperature under a fixed value of N flux [56]. (b) NW density dependence on substrate temperature with Ga/N flux ratio of 0.3 [48].

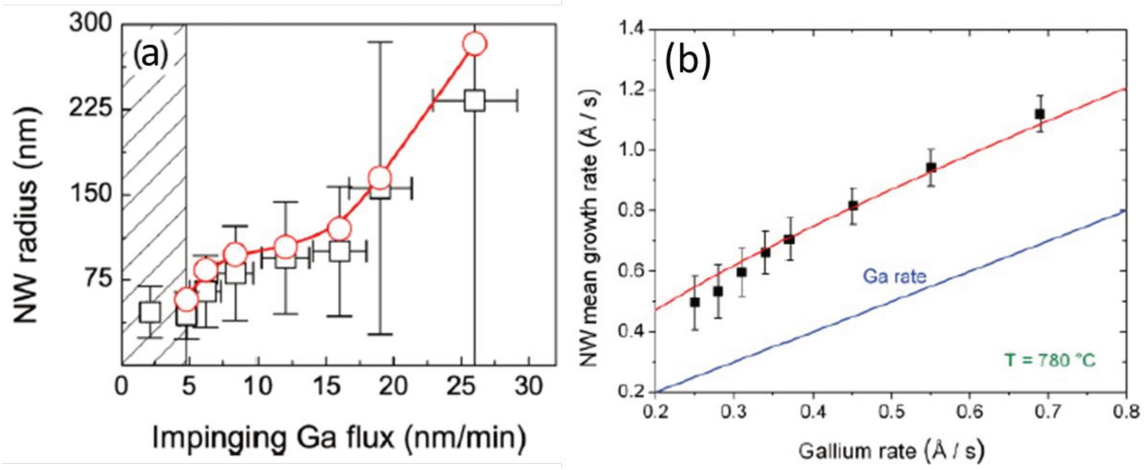

Figure 2.7 The influence of Ga/N flux ratio on NW morphology. (a) The NW radius dependence on impinging Ga flux. N flux is 10.8 nm/min in this case; the dramatic increased NW radius in Ga-rich condition is a result of NW coalescence [57]. (b) Within N-rich condition (N rate is 2.8 Å/s in this situation), the NW mean growth rate augments when the Ga rate is increased [58].

2.1.3.2 Nucleation on bare Si (111) or with an AlN buffer

The GaN NWs exhibit distinct morphologies under different nucleation conditions, either directly on Si (111) or with an AlN buffer layer on Si (111). When growing on bare Si, the nucleation of the NW takes about 45 min at a substrate temperature around 830 °C, evidenced by the apparition of the broken-ring RHEED pattern shown in Figure 2.8 (b). A spread in the in-plane NW orientations (also called “in-plane mosaicity”) can be observed from the SEM image Figure 2.8 (a), which agrees with the RHEED pattern.

On the other hand, by employing an AlN buffer layer with a thickness of 2-3 nm, a more homogeneous nucleation, more straightness, and decreased mosaicity of the NWs can be obtained (Figure 2.8 (c, d)) [41]. A more detailed exploration of the NW nucleation mechanism in these two cases, can be found in the thesis of K. Hestroffer [29] and T. Auzelle [42].

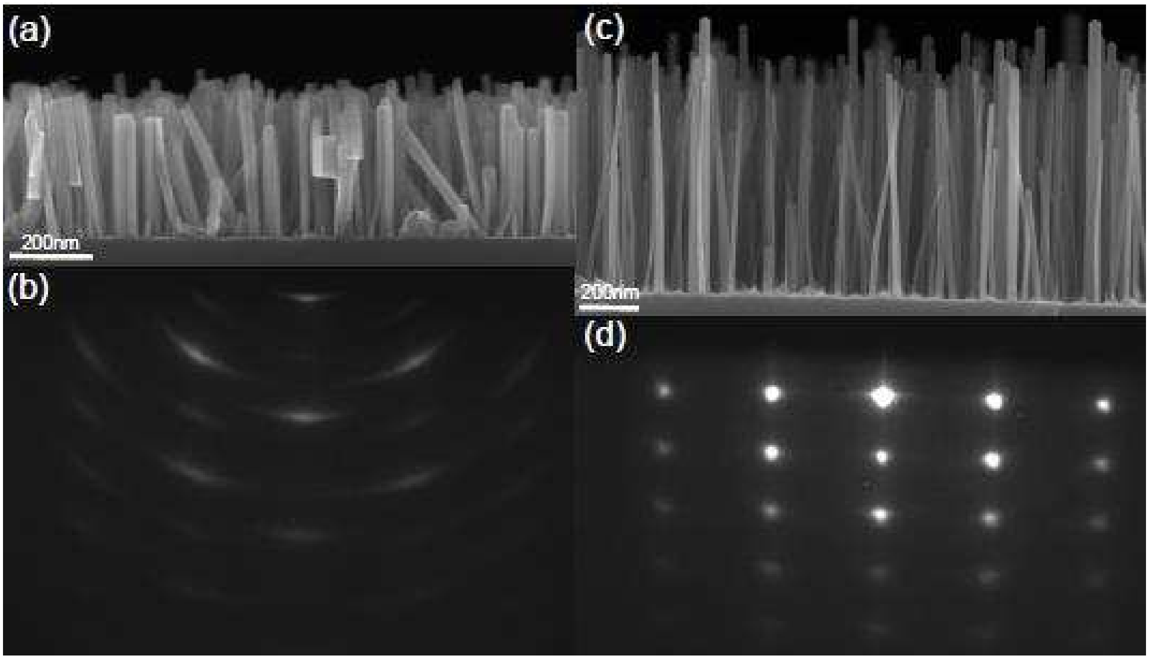

Figure 2.8 NW grown on bare Si and with a AlN buffer on Si [59]. SEM images and corresponding RHEED patterns of GaN NWs grown directly on Si (111) (a, b) and with an AlN buffer layer on Si. (c, d).

2.1.3.3 The impact of the nitrogen plasma cell

One of the limitations of PAMBE for mass production is the low growth rate (typically 200-400 nm/h). The production of active nitrogen species is very crucial for improving the growth rate. However, the high N_2 molecule bond energy of 9.5 eV [60] makes it difficult to break the molecules into atoms, and further to be incorporated in III-V nitrides. Efforts in developing high-density nitrogen radical plasma source have been reported to reach more than 2 μm/h growth rate in the case of GaN 2D layer [61]–[64].

In our MBE, a standard Riber nitrogen plasma cell is used. The N_2 molecules are resonantly excited by a RF electromagnetic wave at 13.56 MHz, and N_2 flow is adjusted by a mass-flow regulation. In principle, the N_2 can be varied between 0.2 and 10 standard cubic centimeters per minute (sccm); the input power can be varied up to 600W. In fact, a RF power of 300W and a N_2 flow of 0.6 sccm are routinely employed as growth conditions, in order to obtain a stable plasma in the MBE machine. And these conditions lead to a typical N-limited growth rate of 0.23 ML/s (see Figure 2.9 (a)).

As part of this thesis, a new plasma cell Riber RFN-50/63 has been installed for producing higher N flux. Through working at a higher RF power (400-500 W) and a higher N_2 flow (1.1-1.4 sccm), more active nitrogen species are indeed produced (see Figure 2.9 (b)).

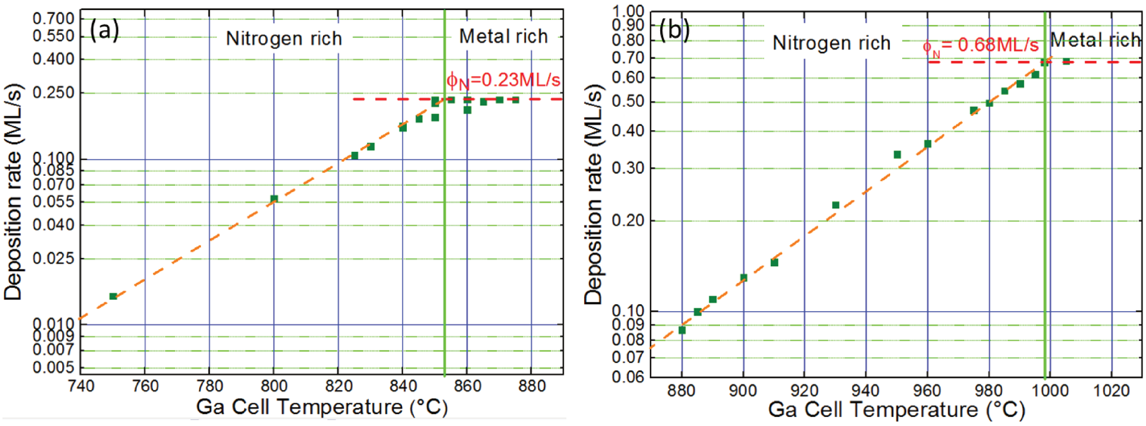

Figure 2.9 Ga cell flux calibrations through RHEED oscillations while growing 2D GaN layer with two plasma cells. (a) With the old plasma cell, it gives a nitrogen flux of 0.23 ML/s at stoichiometry. (b) With the new plasma cell (Riber RFN-50/63), it gives a nitrogen flux of 0.68 ML/s at stoichiometry.

In the framework of this thesis, several samples have been grown employing the new plasma cell, an elevated growth rate is indeed observed. However, we have encountered some difficulties.

- There were some stability issues with this new plasma cell. This cell sometimes turns off automatically after a few hours for unknown reasons.
- The vacuum inside the MBE chamber is increased to around 3.5×10^{-5} mbar with the new plasma cell, comparing to around 1.5×10^{-5} mbar with the previous cell. In principle, ballistic tranport should still be fulfilled at a vacuum of 3.5×10^{-5} mbar, however, metallic contamination has been observed around the plasma cell after two months of operation. The cell was returned back to Riber for repair, due to an unexpected Fe contamination.
- In terms of NW growth, it is difficult to control its density. More Ga flux is needed and supplied accompanying with higher N flux, resulting in more NW nucleation, therefore higher density at a typical NW growth substrate temperature. Since I am growing long NWs, this increase of density can lead to coalescence, which is detrimental for implementing electrical measurements.

Therefore the samples in this thesis were grown with the previous plasma cell unless otherwise mentioned, though the attempts of using the new plasma cell were interesting.

2.1.4 The growth of Si doped GaN NWs

Since Si has an atomic radius close to Ga, it can be easily incorporated into GaN. A typical growth routine has been followed for the Si doped GaN NWs series. The substrate temperature has been calibrated as 5.6 s for Ga desorption (effective temperature around 830 °C) and kept the same during the growth. AlN buffer layer (around 3 nm thick) is deposited to ensure a more homogeneous nucleation and decrease the mosaicity of the NWs [65]. The nominal Ga/N flux is 1/3 and the same for all the samples in this series. The growth time was 20 hours unless otherwise mentioned. Sample N2059 is non-intentionally doped (NID) GaN NWs and serves as a reference. In addition, sample N2129 has been grown at the exact same growth conditions as N2059, as the second reference. For the other samples, n-type doping is achieved by exposing GaN NWs to the Si flux, starting 20 minutes after completion of their nucleation till the end of the growth. In a nutshell, this series of samples have been grown in the same conditions except the doping level via varying the Si cell temperature from 850 °C to 950 °C.

Table 2.1 The lists of samples studied with different Si cell temperatures

Sample Name	**N2059 & N2129**	**N2061**	**N2076**	**N2067**	**N2074**	**N2088**	**N2060**
Si cell temperature (°C)	400	850	875	900	925	938	950
NW radius (nm)	20-30	20-30	25-30	40-55	33-45	40-70	-(Conical shape)
Average NW length (μm)	3.04	2.98	3.21	2.26	2.91	2.08	1.64
Average NW density (μm^{-2})	57	50	41.6	49	35.6	38.6	6.3

2.2 Basic Characterizations

2.2.1 Morphology evolution followed by FESEM

Field-emission scanning electron microscope (FESEM) serves as the first tool to follow NWs morphologies. A ZEISS Ultra 55 microscope situated at Minatec, has been used in this thesis.

Top and side view SEM images taken from as-grown samples at the center of the wafer are illustrated in Figure 2.10. The NID GaN NWs have a typical length of 3 μm and a radius of 20~30 nm. The influence of Si on the morphology of the NWs is not very obvious at low Si doping. In contrast, a widening of the NW can be observed at higher Si doping, which is more pronounced with the highest Si content. Intriguingly, the top facets of the NW switched from 6-fold symmetry to 12-fold symmetry with the highest doping as shown in Figure 2.10 (h), indicating a different growth regime.

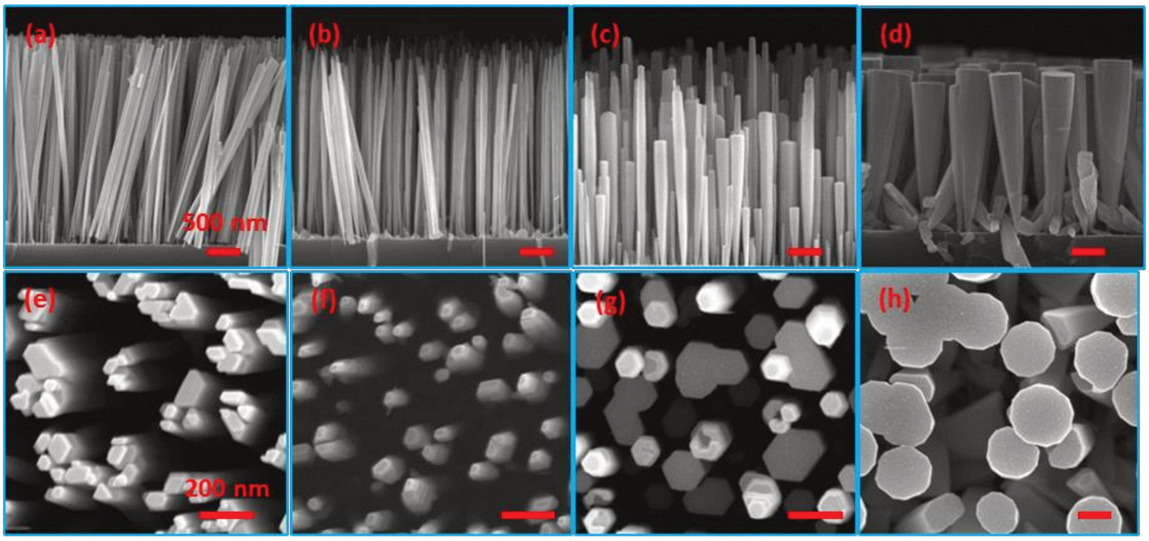

Figure 2.10 Morphology variations of Si doped GaN NWs. Side view (a) and top view (e) SEM images of NID GaN NWs from sample N2059. Side view (b, c, d) and top view (f, g, h) SEM images of Si doped GaN NWs from sample N2061, N2088, and N2060, respectively. The scale bar is 500 nm in the first row, and 200 nm in the second row.

A quantitative summary of the morphology variations is displayed in Figure 2.11. The length and the radius of the NWs are found to be almost constant up to a Si cell temperature of about 925 °C. Upon higher Si doping (two samples with Si cell temperature of 938 °C and 950 °C), the radius of the NWs is gradually increased while their length is decreased. Meanwhile, the density of the NWs declines along with higher Si doping, which has been attributed to reduced NW nucleation upon Si incorporation [41]. A closer observation of the most doped NWs (Figure 2.11(c), (d)) reveals a continuous increase of the NW radius from the base, until reaching a certain equilibrium value. The diameter of GaN NWs grown by MBE has been demonstrated to be self-regulated so that the effective Ga/N flux ratio is close to the stoichiometric value in steady-state growth conditions [57]. Consistently, the present results suggest that heavy Si doping is associated with an increased diffusion length of Ga adatoms along the NW side walls, which leads to an increased Ga effective flux on top and to the concomitant, self-controlled diameter widening until reaching the equilibrium.

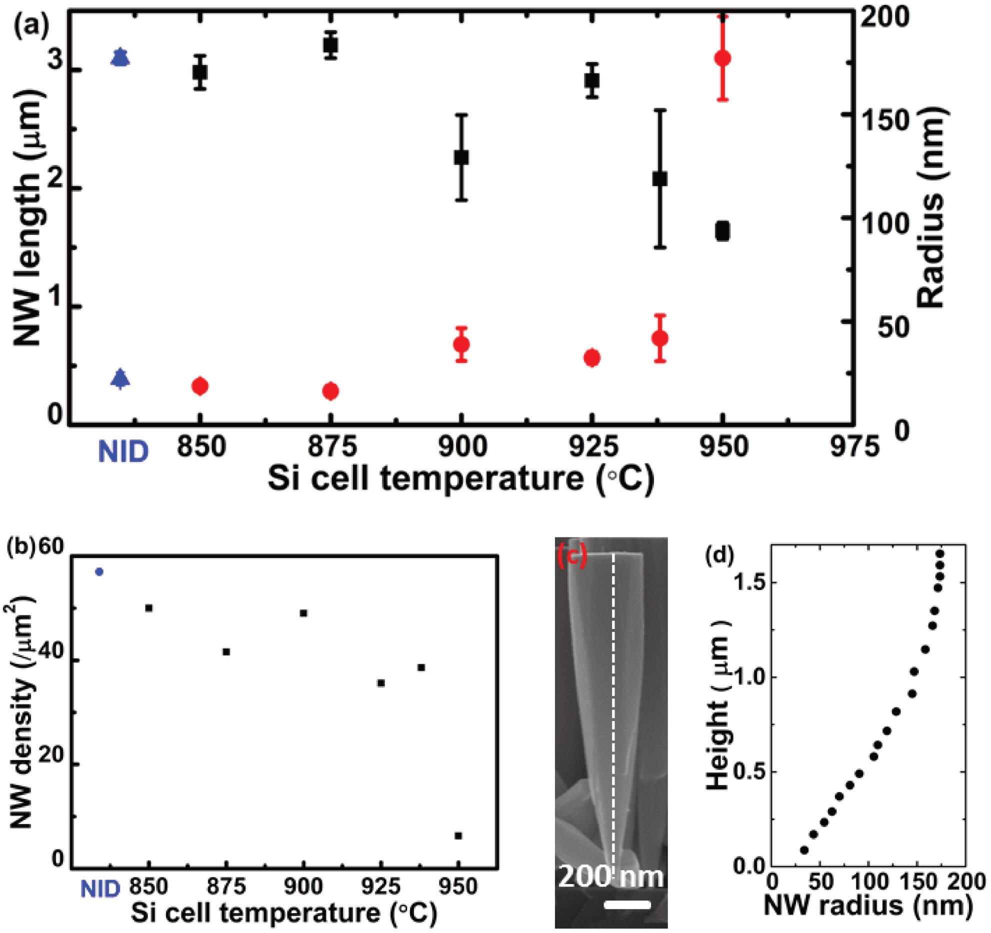

Figure 2.11 NW length, radius, and density evolvements summarized based on SEM images. (a) NW length, and radius as a function of Si cell temperature. (b) NW density variation as a function of Si cell temperature. The data were calculated from SEM images showing an area of a few μm^2. (c) Side view of one NW grown with Si cell temperature of 950°C. (d) NW radius alteration with the height of the NW, measured along the dashed line in (c).

2.2.2 Optical characterizations by photoluminescence

2.2.2.1 Photoluminescence (PL) spectroscopy

PL spectroscopy is a very useful characterization tool to study the optical properties of semiconductors. It involves exciting the sample above its band gap with a laser, and collecting the photon emission from the electron-hole pair radiative recombination. The analysis of the obtained spectra allows to access valuable information on the sample, such as crystal quality, defects, impurities, and chemical composition in the case of alloys.

In our setup, macro-PL spectra were obtained after excitation of the samples with a continuous-wave frequency-doubled Ar laser emitting at 488 nm (the excitation wavelength was therefore 244 nm). The laser spot diameter is on the order of 100 μm and the luminescence signal is collected through a Jobin-Yvon HR460 monochromator equipped with an ultraviolet-enhanced charge-coupled device (CCD) camera. The measurement temperature can be set between 5.7 K and 300 K through a liquid He immersion cryostat. In this thesis, only low temperature around 5.7 K PL has been performed.

Figure 2.12 (a) shows typical PL spectrum of as-grown NID GaN NWs. The intense emission peaks between 3.47 and 3.50 eV are of excitonic origin, whereas the broad band around 3.26 eV is commonly related with emissions from donor-acceptor pairs (DAP) followed by several phonon replicas [66]. In addition, the large Gaussian-shaped yellow luminescence (YL), which is sometimes observed around 2.2 eV in GaN epilayers, is generally absent in NWs. As illustrated in Figure 2.12 (b), the near band edge emission is generally composed of several peaks, indicating different radiative recombination processes. The donor bound excitons (D_0X) at 3.472 eV is the strongest peak, which mainly relates to shallow donors such as oxygen or silicon atoms. Different free excitons can be observed at a higher energy, such as free A excitons (FX_A) at 3.479 eV, free B excitons (FX_B) at 3.483 eV, and free C excitons at (FX_C) at 3.503 eV. FX_A excitons correspond to recombination of bound electron-heavy-hole pairs, whereas FX_B and FX_C involve the light holes and holes in the split off band, respectively (Figure 1.3 (b)). Another peak at 3.45 eV is sometimes present in the spectra, and its origin has recently been related with the presence of inversion domain boundaries [67]. At a lower energy from the band edge, a peak located around 3.42 eV has been assigned to excitons bounds to the stacking faults (SF) in the NWs [68]. For detailed studies on the PL spectra of GaN, please refer to a review paper by Reshchikov and Morkoc [69].

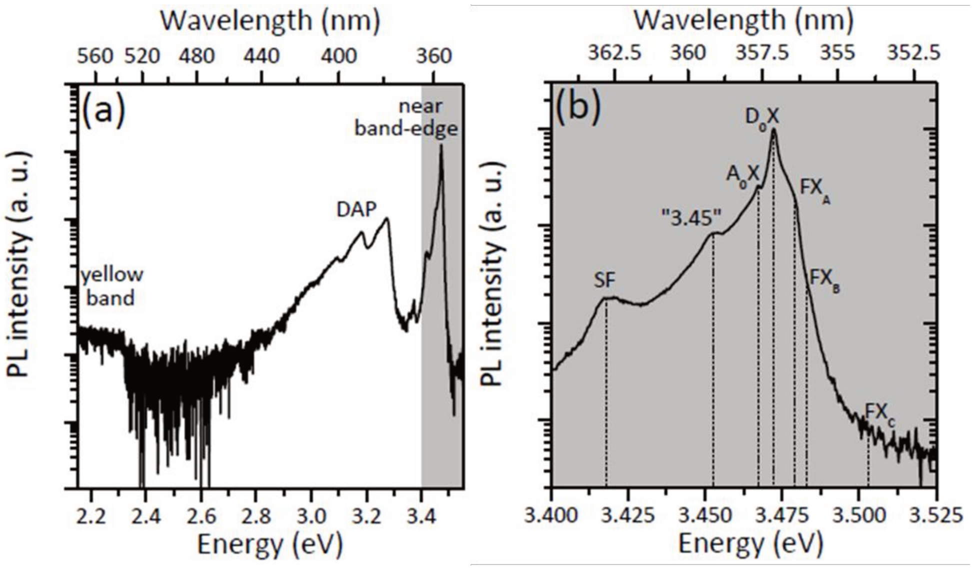

Figure 2.12 Typical PL spectrum of as-grown NID GaN NWs [48]. (a) PL spectrum of as-grown NID GaN NWs, showing near band-edge emission and the DAP. (b) A close up of the gray area in (a), displaying different peaks within the near band-edge emission.

2.2.2.2 PL spectra of Si doped GaN NWs

Doping produces energy levels within the band gap of the semiconductor, and these levels can serve as recombination centers, manifesting in the PL spectra. Therefore, we can employ PL characterization to learn more about the doping of the material.

In the particular case of GaN, doping has a significant impact on emissions from the near band edge, DAP, as well as YL. The strongest peak of the near band edge emission (D_0X line) is situated as 3.472 eV (357 nm) at low temperature (5-10 K) for relaxed NID GaN material. [70] The doping in GaN 2D layer can vary both the position and the full width at half maximum (FWHM) of the near band edge peak through different physics effects, such as strain, band gap renormalization (BGR) and band filling effects.

Si doping can induce strain in GaN, it has been reported in [30] that there is a linear relationship between the biaxial strain and the free exciton energies. When increasing the doping, band gap renormalization (BGR) is becoming more evident due to electron-electron and electron-ion interaction. This effect can lead to the energy downshift of the low-energy edge of the PL line, and dominates until a carrier concentration of around 9×10^{18} cm^{-3} [71], [72]. Under heavy doping, especially above the metal-insulator transition (MIT) (critical doping level $N_d = 1.6\times10^{18}$ cm^{-3} [73]), band filling effects occur, shifting the PL peak to higher energy. Additional broadening of the PL linewidth can come from potential fluctuations induced by the random distribution of the dopant atoms [74], [75].

Moreover, both the DAP and the YL emission intensities can reflect the amount of impurities and defects in the crystal, acting as an intuitive optical signature of the doping level.

Figure 2.13 displays the low temperature PL spectra of this Si doped GaN NWs series. For NID samples (N2059 & N2129), the PL spectra are dominated by a thin intense near-band edge emission at 3.47 eV with a FWHM of a few meV, suggesting a good crystal quality. DAP emissions at 3.28 eV are present in both samples, and about 10 times less intense than the corresponding near-band edge emissions. As usual, two phonon replicas with around 90 meV separations accompany them.

When adding Si (N2061, N2076 & N2067), the near-band edge emission peak becomes broader, and more asymmetric towards lower energies due to Si incorporation as shallow donors, meanwhile, the intensity of the DAP emission arises, even higher than that of the near-band edge emission in sample N2061, indicating a significant increase of impurities in the doped samples. Similar features have been observed in the literature as well [76]. At higher Si cell temperature (N2074, N2088 & N2060), we can see a more obvious broadening of the PL peak as well as a shift to higher energy due to band filling effects.

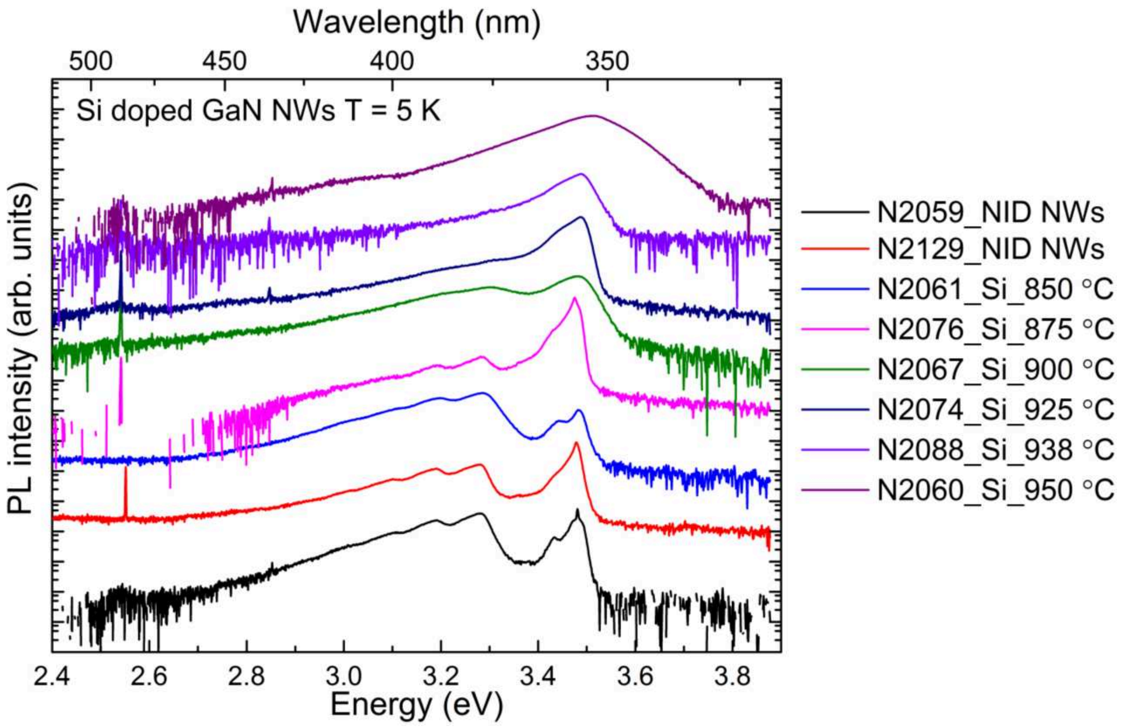

Figure 2.13 PL spectra of as-grown Si doped GaN NWs series. The spectra of NID samples (N2059 & N2129) are shown at the bottom as references, whereas the Si cell temperature is increasing gradually from the bottom to the top. All the spectra have been collected at 5 K. The PL intensity is in logarithmic scale and shifted vertically for clarity.

Various efforts have been made to determine the carrier concentration n quantitatively through PL spectra. However, the combining effect of BGR and band filling effect makes it very challenging to resolve this issue. [72]

Near-band edge peak position shift As stated before, the combining effect of BGR and band filling effect makes the position of the near-band edge peak almost constant at moderate doping; it is only when the band filling effect is much more prominent at higher doping, that we can observe a blue shift of the peak position [29].

As we can see in Figure 2.14 (a), compared to the NID sample, the band edge peaks of highly doped samples (N2088 & N2060) exhibit a noticeable blue shift and significant broadening. Indeed, for N2088, the PL peak position is located at 3.49 eV with a linewidth of 71 meV, whereas, for N2060, the maximum of band-edge emission is situated at 3.52 eV with a FWHM of 129 meV. In the light of PL measurements on homoepitaxial GaN layers, we can estimate a carrier concentration of 4×10^{19} cm^{-3} and 7×10^{19} cm^{-3} for sample N2088 and N2060, respectively. These values are relatively consistent with the EDX data, which will be discussed later in this chapter.

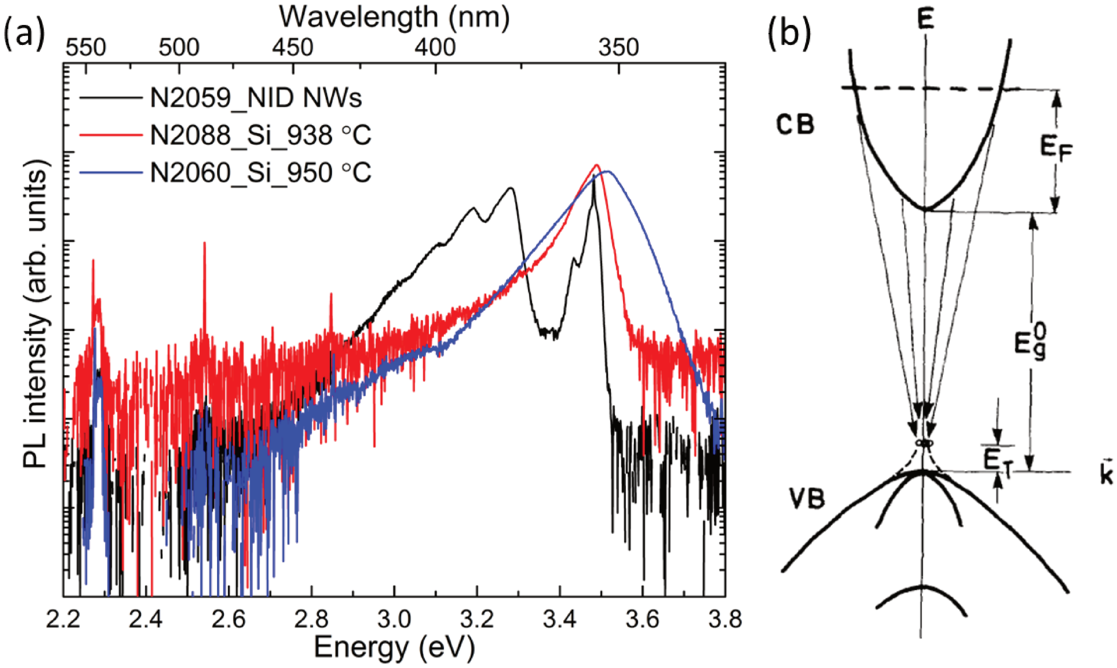

Figure 2.14 The PL spectra of highly doped GaN NWs compared to that of NID ones. (a) The PL spectra of three samples (one NID, two others with high doping) in logarithmic scale. (b) The band diagram illustrating band filling in heavily doped GaAs taken from [77].

FWHM of the near band edge peak In order to achieve a more quantitative understanding, I have summarized in Figure 2.15 the FWHM of the near-band edge PL peak as a function of carrier concentration n at 300K in Si doped GaN epilayers as well as my data from EDX measurements. The experimental points are from various publications [30], [71], [78]. Note that for samples with doping level above the MIT critical concentration ($N_{MIT} = 1.6\times10^{18}$ cm^{-3} [73]), the carrier concentration n = $N_d - N_a \approx N_d$, assuming negligible compensating acceptors. Therefore, Si concentration value N_d measured by EDX can be used to represent the carrier concentration for heavily doped samples.

We can see that the FWHM of the GaN PL band edge peak enlarges with increasing carrier concentration, either for epilayer or for NWs. As mentioned before, two phenomena are responsible: band filling effect (also called Moss-Burstein effect) and potential fluctuations. As schematically shown in Figure 2.14 (b) [77], the band filling in heavily doped GaAs is explained as the luminescence coming from indirect transition (in k space) between free electrons in the conduction band and localized holes in the valence band. However, the experimental points of GaN show that the FWHM follows a $n^{2/3}$ power law (dash-dot line in Figure 2.15), which is expected in [77], [30]. We noticed that there is a little detachment between my data and the ones of the literatures. The carrier concentrations seem to be higher in the case of NWs at the same PL peak FWHM. Possible doping inhomogeneity between neighboring NWs or inside a single

NW could be responsible, furthermore, it has been reported that there is a significant discrepancy between the PL spectra from as-grown sample to single NW, as well as from NW to NW [79]. Therefore, we need to be more careful when using the optical signals to estimate the carrier concentrations in NWs. It was one of the main goals of this thesis to perform direct transport measurements in order to have a more reliable estimation of the carrier concentrations.

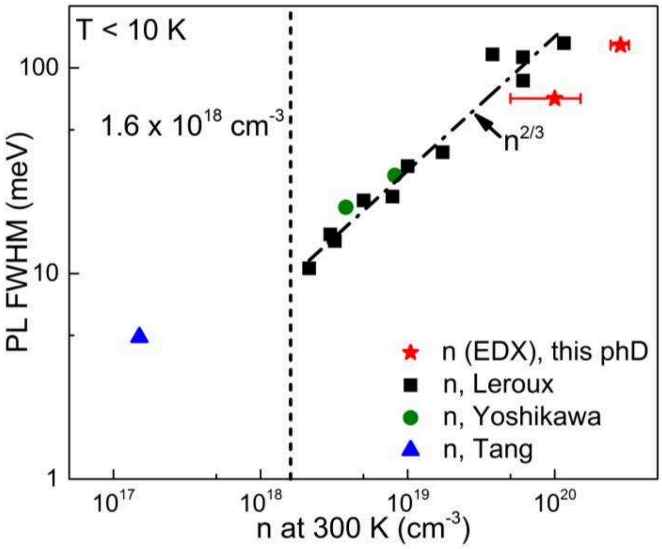

Figure 2.15 FWHM of low temperature PL peak as a function of electron concentration n at room temperature for Si doped GaN epilayer [30], [71], [78], as well as NWs in this PhD. Both the x and y axes are in logarithmic scale. The short dashed line shows the critical electron concentration for the MIT at1.6×10^{18} cm^{-3} [73], the dash-dot line is a fitting of the data from [30], exposing that the FWHM follows a $n^{2/3}$ power law.

2.3 Structural properties

2.3.1 Defect modes evidenced by Raman spectroscopy

Ever since the discovery by C. V. Raman in 1928 [80], Raman spectroscopy has become a versatile and interesting material investigation tool. By probing the inelastic light scattering, Raman spectroscopy can reveal detailed information on crystal structure, electronic states, chemical composition, and strain and so on. Moreover, it does not require sophisticated sample preparations, and is often referred as a fast and non-destructive technique.

Concerning the Raman spectra of GaN, two modes have been intensively studied in the literatures. The E_{2h} mode is sensitive to the strain and the phonon shift can be directly related with the stress. The coupled LO-phonon plasmon modes (LPP modes) result from the interaction between the macroscopic electric field of the longitudinal-optical phonons and the field of the collective excitation of the free carriers, therefore, its frequency strongly depends on the free carrier concentration. Both the low (LPP^-) and high (LPP^+) energy branches have been employed to estimate the concentration and mobility of the carriers (electrons) in GaN epilayers, through the modelingof the peak position and the width of these modes. [81]–[83]

Regarding GaN wires, surface optical phonon modes (SO) due to the high surface / volume ratio has been reported previously. [84] The attempts to approximate the carrier concentrations of NID and Si doped wires have been addressed in a few publications [42], [85]–[87]. Therefore, it was very interesting to perform Raman measurements on this series of Si doped GaN NWs.

As stated in Chapter 1, micro-Raman measurements are conducted in collaboration with Prof. Ana Cros from University of Valencia, Spain. A 532 nm doubled YAG laser has been employed to excite the samples while a HORIBA Jobin Yvon iHR320 spectrometer was used to detect the spectra. The spectrometer is equipped with a Peltier-cooled CCD detector. Spectra were obtained in backscattering geometry at room temperature from as-grown NWs. A ×50 microscope objective was used to focus the excitation laser on the sample and collect the scattered light to the spectrometer.

Figure 2.16 shows the spectra obtained from this series of Si doped samples. The spectrum of the Si substrate has been included at the bottom as a reference. The peak corresponding to the E_{2h} mode is observed in all samples. For NID sample, its center is at 565.6 cm^{-1}, somewhat lower than the value expected for relaxed bulk GaN (567 cm^{-1}) [88]. A small but progressive decrease of the phonon frequency is observed as the silicon content of the samples increases (Figure 2.16(b)). This trend is broken in the last sample, where the mode shifts back to higher frequencies. This behavior points to an increase of the tensile strain with silicon content up to a value of 0.15%, beyond which the relaxation of the lattice takes place. A similar behavior has been previously reported by Sánchez-Páramo et al. for silicon doped GaN layers [34], where the lattice relaxation was observed for silicon concentrations above 5×10^{18} cm^{-3}. As the amount of silicon in the lattice increases, the E_{2h} peak becomes somewhat wider, changing from 7 cm^{-1} to 10 cm^{-1}. This is a consequence of the lattice disorder induced by the impurities.

The LPP^+ peak is observed in NID GaN NWs at 739.0 cm^{-1}, right above the SO peak, which is often observed in thin NWs [84]. The frequency of this mode corresponds to a free carrier density around 2×10^{17} cm^{-3}. This estimation is consistent with the red-shift of the E_{2h} mode. Unfortunately, for higher Si concentrations the plasmon is overdamped and the LPP^+ peak cannot be observed. For the sample with moderate Si cell temperature (900 °C), a broad band centered at 658 cm^{-1} starts to arise. The intensity of this band increases strongly with higher silicon content. This peak is ascribed to a disorder activated mode and has been reported for Mg, Ge and Si doped samples [89], [90]. At the same time, four new modes arise at 319, 390, 414 and 763 cm^{-1}. They are clearly visible in the sample with the highest Si cell temperature, but the mode at 414 cm^{-1} can also be observed in the samples of Si cell temperatures of 900 °C and 938°C. Most of these modes have not been reported before, although the mode at 414 cm^{-1} is close to a zone boundary phonon which could be activated due to the disorder induced by the incorporation of silicon to the GaN lattice.

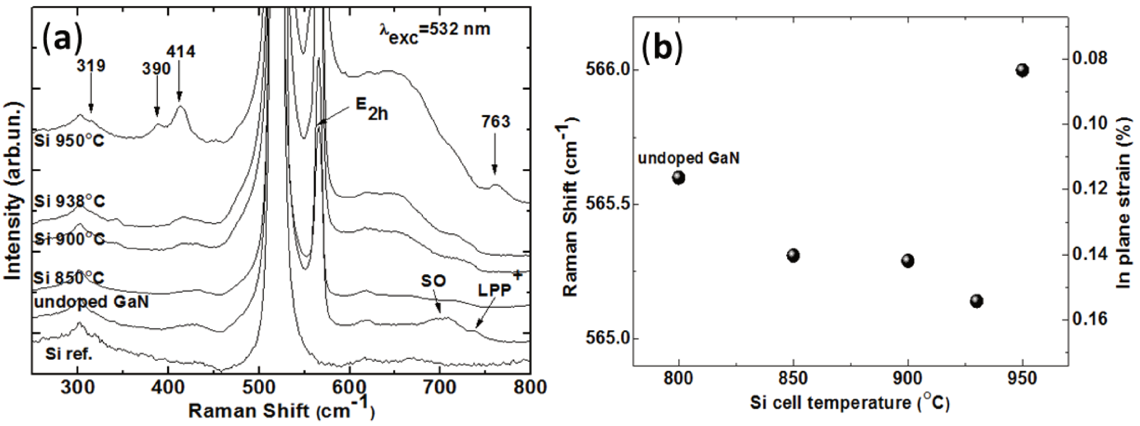

Figure 2.16 Raman spectra of as-grown Si doped GaN NWs. (a) Raman spectra of as-grown samples with different Si cell temperatures, together with a Si substrate reference; (b) Evolution of the peak frequency of the E2h mode as a function of Si cell temperature. The right scale gives the corresponding in-plane strain calculated within the biaxial and deformation potential approximations [91].

2.3.2 Si content mapped by high-resolution Energy-dispersive X-ray spectroscopy (HR-EDX)

2.3.2.1 The principle of EDX and our setup

To untangle the mysterious structure properties, it is of great importance to have knowledge of Si content as well as its distribution. However, secondary ion mass spectrometry (SIMS) is challenging to perform on nanostructures, due to the huge noise signal from the substrate. In this thesis, HR-EDX has provided an interesting alternative to resolve this issue.

EDX is an elemental analysis technique which detects the X-ray spectrum emitted by a solid sample when bombarded by a focused electron beam. Two types of X-rays can be generated upon the inelastic interaction of the electron beam with the specimen atoms: Continuum (also called Bremsstrahlung) X-rays and characteristic X-rays. The former comes from the deceleration of incident electrons by the strong electromagnetic fields of atomic nuclei. Whereas the latter is the result of electron transitions between inner orbits, which are empty due to electron beam bombardment (illustrated in Figure 2.17 (a&b)). The latter is characteristic for each constituent element and reveals themselves as peaks superimposed on the former on the spectra. The wavelengths of these characteristic X-ray peaks can directly relate to the atomic numbers of the elements by Moseley's law. And the intensity can be employed to deduce element concentrations, if making use of reference specimens with known concentrations. The X-ray signal originates from the inside of the electron-sample interaction volume (Figure 2.17 (c)), therefore the spatial resolution of EDX is highly correlated with the electron sample interaction range. And this distribution is determined by various factors, such as the incident beam energy, the atomic number of the constituent elements, the mean sample density, and sample thickness. The trajectories of incident electrons can be estimated by Monte Carlo simulations using software called CASINO[‡], which provides guidelines for determination of the spatial resolution of EDX. This software is also very useful in understanding another electron beam based experiment — electron beam induced current (EBIC), which will be discussed in details in Chapter 4.

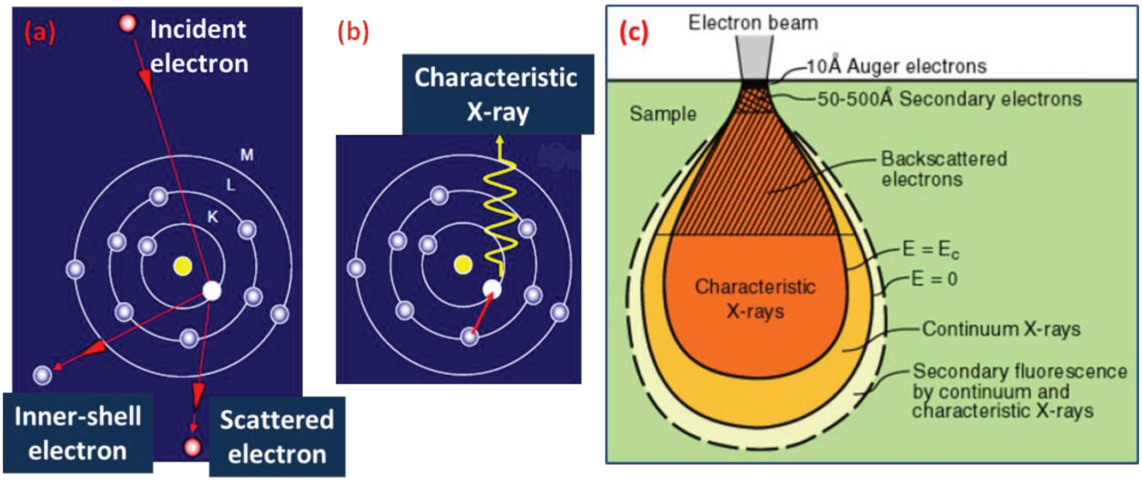

Figure 2.17 Schematics of EDX principle and electron sample interaction volume. (a) Incident electron inelastically interacts with an inner-shell electron of the sample, creating a vacancy on inner orbits, such as K; (b) An electron from another orbit (such as L) drops to fill this vacancy, a characteristic x-ray (Ka) is emitted; (c) Electron beam sample interaction volume showing the range where different signals in SEM originate from§.

As stated in Chapter 1, the HR-EDX experiments have been conducted in collaboration with Dr. Eric Robin from Minatec Campus at CEA Grenoble. High detection sensitivity is achieved thanks to the Flat Quad 5060F annular detector from Bruker, which is implemented onto an Ultra55 Zeiss SEM. This detector consists of four bean-shaped silicon diodes arranged around a central hole, through which the electron beam can pass (see Figure 2.18 (a)). During the observation, it is positioned a few millimeters above

---

[‡] Please refer to http://www.gel.usherbrooke.ca/casino/index.html

§ The Figure 2.17 is extracted from L. Kwakman, Master course November-December 2012, UJF, Grenoble, France.

the sample, allowing a very high counting rate even at low incident electron beam voltage (< 8 kV) (see Figure 2.18 (b)). As a result, a detection limit around 10^{19} at cm^{-3} can be achieved.

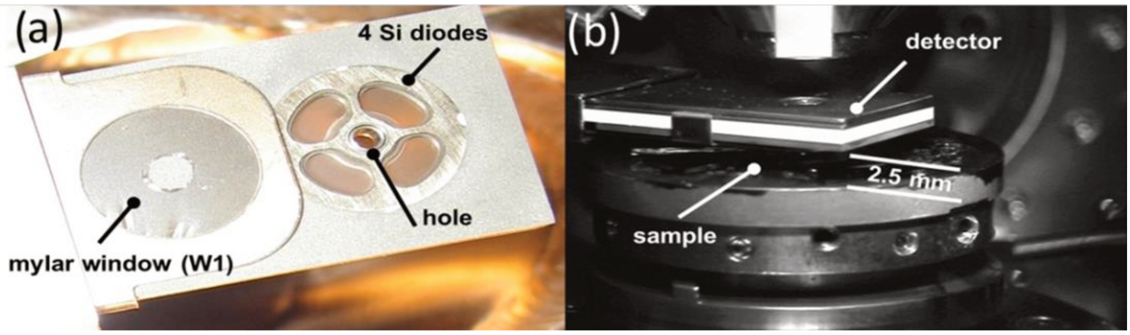

Figure 2.18 The Flat Quad 5060F annular detector used for HR-EDX experiments. (a) Bottom view of the detector: the four bean-shaped Si diodes, the central hole and the first retractable mylar window is indicated. (b) Side view of the detector inside the SEM; the samples are around 2.5 mm below the detector.

In order to detect dopants and quantify their concentrations in nanostructure, high spatial resolution is extremely demanding. It is possible to have high resolution given the condition of low incident electron beam voltage, however, the peak / background ratio declines at the same time. In order to extract low intensity signal from a relatively high background signal, we have used specific windows in the detection which serves as X-ray filters, and can enhance the signal to noise ratio in the energy range around the X-ray line of the analyzed dopants. Furthermore, a new analysis procedure** has been employed to eliminate the background signal. In addition, X-ray maps were collected using a FEI Osiris TEM equipped with super X detectors at 200 kV on the same sample, and these TEM-EDX data are compared with SEM-EDX results.

2.3.2.2 Sample preparation and results

Despite the low signal / noise ratio because of low incident beam voltage (3-5 kV), another significant source of noise in our case is the Si substrate, which could completely cover the Si signal from GaN NWs. Thus, different sample preparation methods have been applied to mitigate the noise.

One straightforward solution is to transfer the NWs onto a non-Si-containing substrate. We have chosen graphite substrate due to its facile reuse capability and conductive nature. Si Ka1 line at 1.74 keV has been detected successfully, not so far from the Ga

---

** For more details concerning this new data treatment procedure, please check Eric Robin CEA-INAC patent N° 14 62333 (2014)

La1 line at 1.10 keV. However, the spatial resolution is not only limited by the electron NW interaction distribution, but also electron scattering along the NW, moreover, no Si distribution information can be extracted in this case since the NW is laying on the substrate.

Another sample preparation procedure is more complicated, and it is similar to traditional transmission electron microscope (TEM) sample preparation. Firstly, a few drops of epoxy resin were dipped onto the as-grown sample, then the sample was stored in an oven for 24 hours. Once the resin was solidified, subsequent polishing steps were followed by using different polisher machines and solutions without colloidal Si. The purpose of the polishing is to remove the excess resin on top of the NW and to create a flat top surface for EDX observations. With this procedure, the resin that fills the space screens the electron scattering in between the NWs, and the influence of the Si substrate can be neglected due to the micrometer length of the NWs. In the end, carbon coating is deposited on the sample to avoid charging effect during the EDX observation.

All the samples in this Si-doped NWs series have been prepared using the procedure above, unfortunately, quantitative results are only obtained for two samples with higher Si cell temperatures (938 °C and 950 °C), for the rest of the samples in the series, the Si level is below the detection limit (around 10^{19} at cm^{-3} as mentioned before).

Two NWs grown with the highest Si cell temperature (950 °C) have been analyzed by EDX in a TEM and SEM, respectively. (Figure 2.19 (c, d, e)) As discussed previously, the top facet of these NWs possesses 12-fold symmetry. The hexagonal top facet owes to polishing steps, which has cut the NWs at a certain height at radius of 100-130 nm, below the symmetry change of top facet. The measured Si concentrations from the two NWs with two techniques are similar, which confirms the accuracy of SEM-EDX, as well as excludes a potential contamination of the samples. From the TEM-EDX data profile, the NW has a core with an average Si concentration of 2.5×10^{20} at/cm^3 and an outer part of around 17 nm with a much higher Si concentration of around 6.5×10^{20} at/cm^3. The SEM-EDX data (white points in (d)) from the other NW fall in the same range. More observations show that all NWs grown with the highest Si cell temperature have very similar Si concentrations ranging from 2-4 x 10^{20} at/cm^3 in the core with a mean value around $(2.8\pm0.4)\times10^{20}$ at/cm^3 (calculated from 10 NWs, see Figure 2.20). The outer part of the NWs is strongly enriched in Si compared to the core and contains Si from 6×10^{20} up to 10^{21} at/cm^3. The overall thickness of this Si-rich shell ranges between 10 nm up to 40 nm.

On the other hand, similar measurements on the sample grown with Si cell temperature of 938 °C have shown significantly different outcome (Figure 2.19 (a&b)). TEM-EDX presents a relatively constant Si concentration throughout the NW with an average value of 10^{20} at/cm^3, and it is consistent with concentrations measured by SEM-EDX ((0.5-

1.5)×10^{20} at/cm^3).

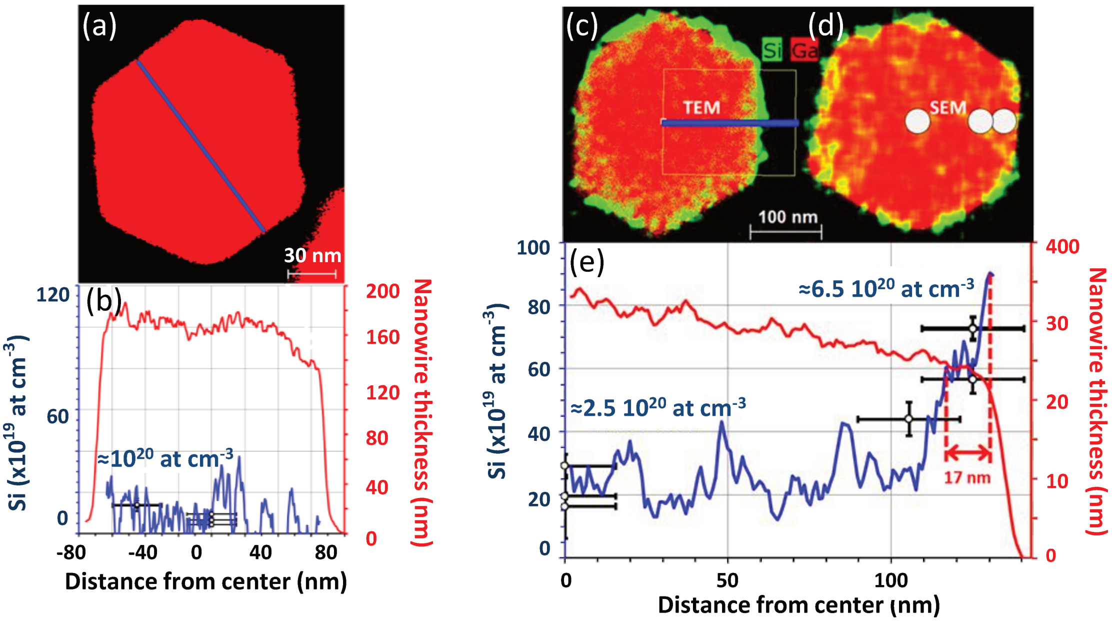

Figure 2.19 EDX measurements of NWs grown with Si cell temperature of 938 °C (a, b) and 950 °C (c, d, e). TEM-EDX and SEM-EDX (at 4 kV) maps for NWs grown with Si cell temperature of 938 °C and 950 °C. Two elements are highlighted, with green and red corresponding Si and Ga, respectively. Si concentrations were computed using the zeta-factor method [92] for STEM EDX data (blue line profile in (b&e)) and ϕρz standard method [93] for the SEM EDX data (white circles in (b&e)). The NW thickness of the STEM observation is shown on the red curve in (b&e).

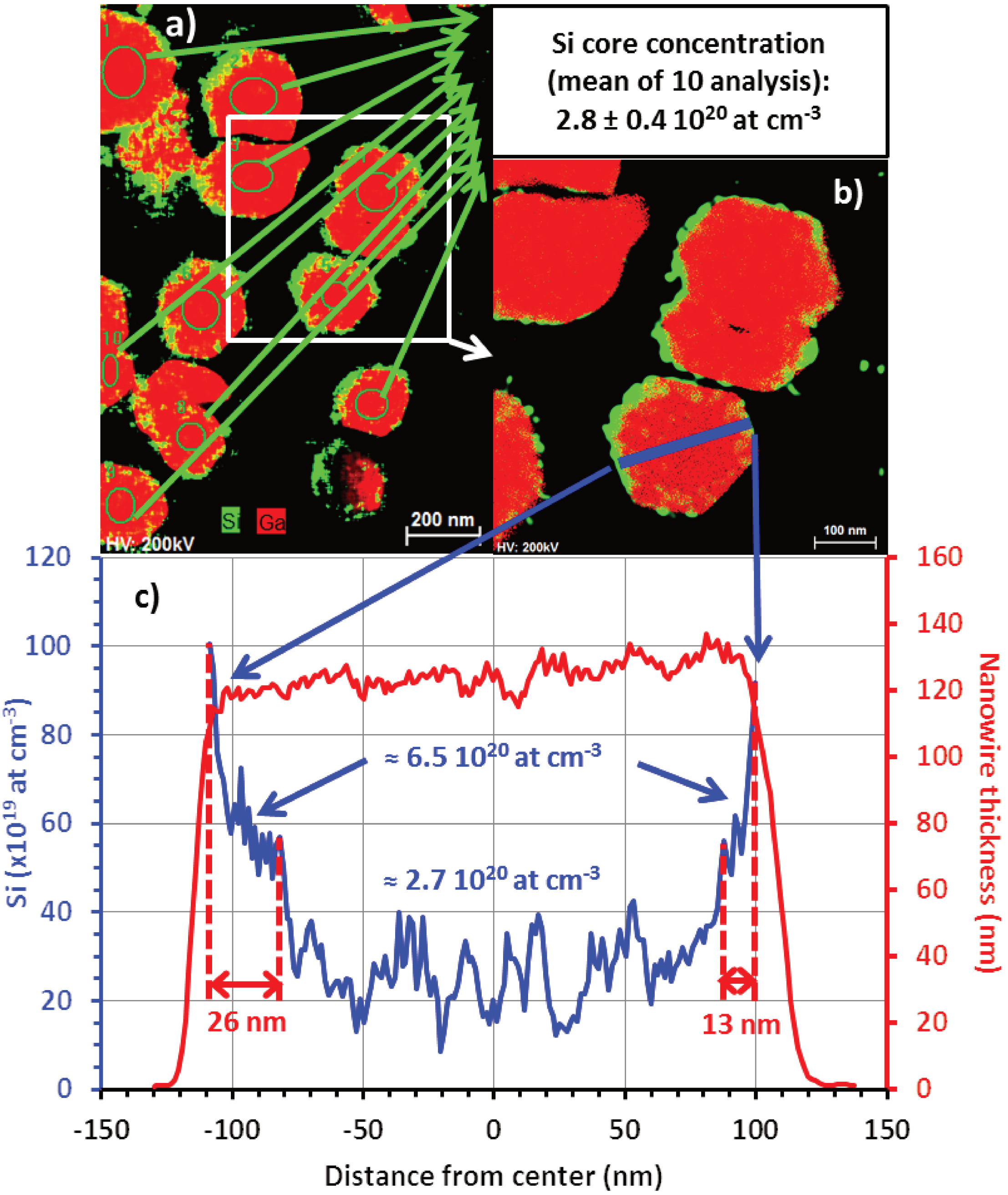

Figure 2.20 EDX measurements of 10 NWs grown with Si cell temperature of 950 °C. TEM-EDX and SEM-EDX (at 4 kV) maps for 10 NWs grown with Si cell temperature of 950 °C. Two elements are highlighted, with green and red corresponding Si and Ga, respectively. Si concentrations were computed using the same methods as in Figure 2.19 [88] [89] for both STEM EDX and SEM EDX data. The NW thickness of the STEM observation is shown on the red curve in (c).

The Si concentration plateau of $(2.8\pm0.4)\times10^{20}$ at/cm^3 measured by EDX in the most heavily doped sample is assigned to a Si solubility limit, which is significantly higher than the theoretically predicted value (around 5×10^{19} at/cm^3) in GaN bulk material [94]. Interestingly, in the case of 2D layers, Sánchez-Páramo et al. have reported a lattice relaxation of Si-doped 2D GaN layers above a concentration of 5×10^{18} cm^{-3} associated with crack formation in the 2D layer [34]. The present results suggest that the large amount of free surfaces, which are specific to NWs, are favorable for the relaxation of tensile strain induced by the presence of Si, making its incorporation easier, while leading to an elastic strain relaxation without the formation of cracks. Surface segregation of Si in the periphery of the GaN NWs when above the solubility limit is consistent with the increasing intensity of the broad Raman band around 658 cm^{-1} for increasing Si content and is assigned to an increase of Si-related defects in the periphery of the NWs for the Si cell temperature above 900 °C. This feature is consistent with the theoretical prediction of Si segregation to the surface under N-rich and Si-rich growth conditions [49], [94]. In fact, a similar phenomenon has been recently reported on highly doped GaN NWs grown on diamond where the presence of a shell with Si content above the solubility limit has been observed [95].

In the case of the highest Si content related with the formation of Si-enriched GaN outer shell, the symmetry of the top facets of the NWs is changed from 6 to 12. It has been demonstrated for long that MBE-grown NID GaN NWs exhibit a 6-fold symmetry top facet, with vertical walls made of m-planes [51], [96]. Such a morphology is consistent with theoretical calculations which have shown that m-plane surface energy (118 meV/Å^2) is indeed smaller than a-plane surface energy (123 meV/Å^2) [97]. The symmetry change of the most heavily doped sample is a clue that a Si enriched shell exists and the associated defects have a tendency to equalize the surface energy of m-planes and a-planes in this case. Moreover, the trend of symmetry change is already observable for some NWs for the sample with Si cell temperature of 938 °C and the appearance of a broad Raman band around 658 cm^{-1} further confirms the association of the symmetry change and the progressively increased defect concentration in the shell of the NWs. Furthermore, this lattice deformation and change in surface energy is expected to discourage nucleation on the NW sidewalls and promote either Ga adatom desorption or diffusion along them, consistent with the previous hypothesis that the increase of Ga adatom diffusion length along the sidewalls might be responsible for the progressive NW widening.

2.4 Electrical transport properties

Understanding the growth mechanism of Si doped GaN NWs through PL, Raman as well as EDX can provide insightful guidelines for the fabrication of the NWs, whereas, the study of electrical transport properties is very crucial for device applications.

Direct electrical transport measurements on single NW devices can provide significant information on doping level, resistivity, and mobility, which paves the way to eventually investigate the NW devices on an ensemble or device level [98]. In 2D layer structures, the transport properties are often assessed by mainly two methods, Hall-effect measurement (carrier concentration) and capacitance-voltage measurement (doping level). There are a few pioneering papers showing similar measurements on NWs [99]–[103], however, it demands very high precision on the lithography process, and is still challenging concerning the dimensions of GaN NWs.

In this thesis, four-probe resistivity and its temperature dependence measurement have been performed on single GaN NW devices. With this, we are able to systematically study the impact of Si doping on the NW resistivity and investigate different conduction regimes. Moreover, by combining field effect transistor (FET) measurements and finite element simulation, we are able to determine the carrier concentration and furthermore the mobility of NID NWs. Controlled doping in a wide range of concentrations can advance the process of device development. It is noteworthy that the specific geometry (the conical shape and the length of around 1.5 μm) and inhomogeneous dopant distribution (Si enriched shell witnessed by EDX measurements) of the most doped sample make it difficult to perform reliable electrical characterization on these NWs, therefore the following explorations concern only the other Si-doped samples from this series.

All the measurements have been performed in the FEI Inspect F50 FESEM-setup equipped with a nano-probing SmarAct system. A Gatan liquid helium stage has been used in the case of temperature dependence measurements.

2.4.1 Single NW contacting

One of the obligatory and challenging tasks to achieve direct electrical measurements in this thesis was to develop a high yield, reproducible, facile NW contacting procedure.

In the literature, several interesting techniques have been proposed [104]. Scanning tunneling microscopy (STM) tips have been reported to directly contact ZnO NWs and perform four-probe resistivity measurements [105]. Metal electrodes on NWs can be deposited via ion or electron beam induced deposition technique [106], or more frequently, by electron beam lithography (EBL) [107]. More particularly, an innovative EBL technique based on cathodoluminescence (CL) imaging has been developed in Institut Néel [108], and this technique has been successfully implemented to study GaN microwires [109] as well as ZnO NWs [110][111].

Table 2.2 lists some practical characteristics of a few techniques used in my thesis. And Figure 2.21 shows an example of the SEM images of GaN NWs contacted by these techniques.

Table 2.2 The characteristics of NW contacting techniques

Characteristics	**CL-assisted EBL**	**Conventional EBL**	**Tungsten (W) tip**	**Laser lithography**
NW geometry	Dispersed	Dispersed	Dispersed or as-grown NW	Dispersed
Substrate	Si + SiO_2	Si + SiO_2 + markers	Si + SiO_2 or growth substrate: Si in my case	Si + SiO_2
Practically achieved resolutions	Around 100 nm	Confined by the process, around 100 nm	Depend on the radius of the tip, 100 nm possible	Limited by the laser wavelength, around 1-2 μm
Features	One-step EBL, optical selection of the NWs,	Two step EBL, pre-imaging of the selected NWs	Tip preparation needed	No need to select the NWs, many NWs randomly connected
Time consumption per sample	1 week	1 week	A few minutes for each NW	2-3 days
Difficulties	Difficult to distinguish single NW from a bunch of NWs	Slow process	Technically difficult, almost impossible on dispersed NWs; unsure to connect only one NW	Only two contacts possible, due to the 2-3 μm NW length
Applications	Less dense NWs, four-probe contacts	Four-probe measurements; complicated contact structure	Quick check for as-grown NWs	Quick check for contact process optimizations; two-probe measurements

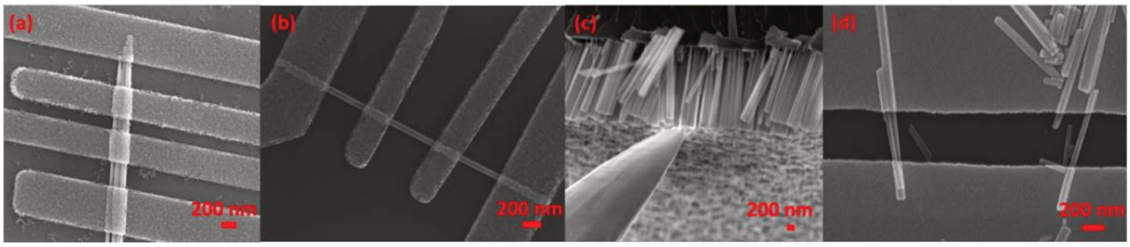

Figure 2.21 GaN NWs contacted by different methods. (a) a bundle of NWs contacted by CL-assisted EBL; (b) one single NW contacted in four-probe geometry by conventional EBL; (c) a W tip connecting as-grown NW; (d) NWs in two-probe geometry fabricated by laser lithography.

2.4.1.1 Conventional EBL

In this thesis, the dimension of the NWs is around 2-3 μm in length, and a few tenth of nanometers in radius. In order to study systematically the intrinsic electrical properties of GaN NWs, conventional EBL is chosen to be the main technique to fabricate the contacts.

I have employed a FESEM FEI Inspect F50 fitted with Raith Elphy Quantum lithography system. Figure 2.22 illustrates the different steps in the lithography process.

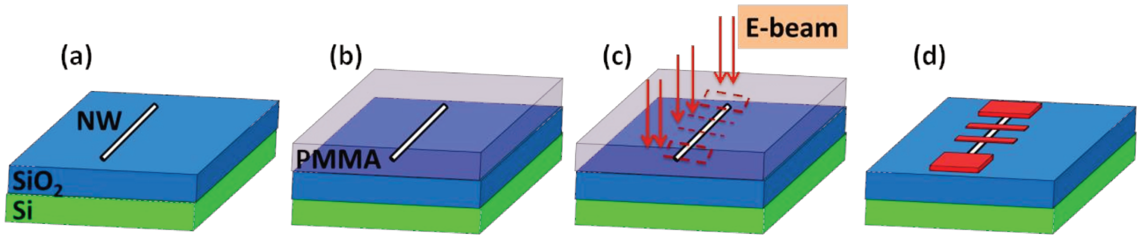

Figure 2.22 Sketch of different steps for single NW contacting in EBL. (a) NW dispersed on Si + SiO_2 substrate; (b) The spin coating of PMMA; (c) Electron beam writing and subsequent development; (d) Metal deposition and lift-off.

Substrate preparations Si wafer covered with 500 nm thick insulating thermal oxide is patterned by laser lithography in order to realize a set of alignment markers. Figure 2.23 (a, b) has shown the Elphy software design of the alignment markers, and the “cross” markers consist of Ti (5 nm thick) and Au (50 nm thick). These markers are used to precisely locate the positions of the NWs in the following steps (Figure 2.23 (c)). Before dispersing NWs onto this substrate, it is firstly cleaned in acetone, then thoroughly rinsed in isopropanol (IPA).

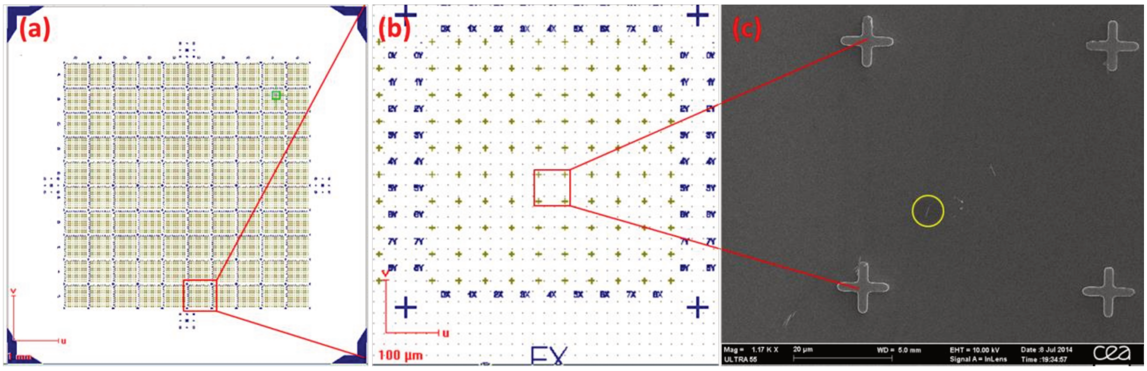

Figure 2.23 The design of the alignment markers and one single NW identified on the substrate with markers. (a) The software drawing of the alignment markers in the field of 8×8 mm, which is also the real size of the substrate. (b) A magnified view of the alignment markers in the field of 550×550 µm. (c) SEM image of dispersed NWs on substrate with “cross” markers, the distance between neighboring “crosses” is 50 µm, one single NW (inside the yellow circle) was identified for further lithography process

NWs dispersions After the growth, the NWs are standing vertically on the growth substrate. As discussed before, there is a temperature gradient along the substrate radius, which leads to density inhomogeneity of the as-grown NWs. In order to provide mostly single NWs, an area with the smallest density (mostly the center of the Si substrate) is chosen for dispersion.

With the aim of transferring NWs onto foreign substrates, two methods are generally used nowadays, through either solution or mechanical scratch.

In the first method, a small piece of as-grown sample (around a few mm^2) was cleaved, then put into a small plastic container with volatile solvents such as IPA, or ethanol. Afterwards an ultrasonic bath was employed to harvest the NWs from the as-grown substrate. The NWs were transfer onto foreign substrates by casting a few drops of the NWs suspension, and evaporation of the solvents. This method has the advantage of being reproducible; meaning the density of the NW dispersion can be controlled by the concentration of the solution, and the number of the drops casted.

In practice, the evaporation of the solvents is not always complete, leaving some residues, which could be a potential source of contamination for the NWs. Therefore, I have chosen to use a simple mechanical scratch method. In this case, a cleanroom paper has been used to transfer the as-grown sample onto foreign substrates, by scratching it gently on the growth substrate. The density of the dispersion was first monitored under optical microscopy, and afterwards observed by SEM.

Meanwhile, the single NWs with good dimensions were identified under SEM and their positions were noted using the corresponding coordinates with respect to the markers, such as in Figure 2.23 (c).

Then this sample was transferred inside the FEI Inspect F50 FESEM, and field calibration alignments have been done in two fields: 700×700 μm for making big contacts to be connected with metal tips, 70×70 μm for the delicate contacts on single NW, respectively. The e-beam working distance is 10 mm, with an energy of 30 keV. The e-beam current is 1 nA for the bigger field, and 20 pA for the smaller one. Then a high-resolution image is taken in the field of 70×70 μm for each intended single NW with respect to the "crosses" (Figure 2.25 (a)), in order to locate and draw lithography mask later on.

Spin coating of the resist EBL is a technique based on the chemical modification of polymer resist films induced by electron irradiation. Poly-methyl methacrylate (PMMA), one of the first positive[††] electron beam resists developed in 1968, is still widely used today, due to its simplicity, high resolution, and excellent adhesion to most

---

[††] The positive resist means that after development, the exposed structure is deeper than the surrounding due to chopping of polymer chains.

surfaces. The exposure of the electron beams can break the long polymer chain of PMMA into smaller, more soluble fragments (Figure 2.24). Similarly, copolymer (PMMA/MMA), is also a high sensitive resist. In addition, it is often used in bi-layer resists with PMMA, with the aim of producing undercut profiles beneficial in the lift-off process later on.

In the case of NWs, the thickness of the resist needs to be at least two times the diameter of the NWs, in order to facilitate the lift-off process. Therefore, the choice of the resist depends on the diameter of the NW. In terms of Si-doped GaN NWs series, one PMMA layer of thickness around 310 nm is used to contact NWs with diameter less than 80 nm, whereas, for NWs with a diameter up to 150 nm, a bi-layer consisting of PMMA/MMA and PMMA is employed. Table 2.3 lists the spin coating conditions of these resists.

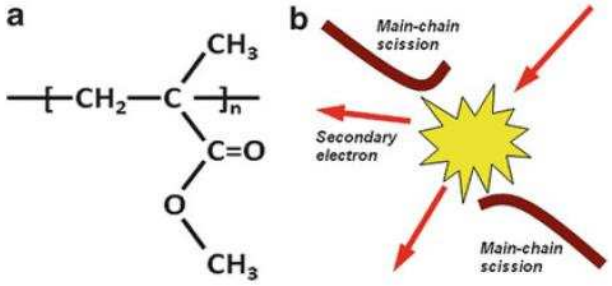

Figure 2.24 (a) Chemical structure of PMMA. (b) The scission of the polymer chain after electron beam exposure [112].

Table 2.3 Spin coating conditions of the resists used in this thesis

Applications	Name	Speed (turns/nm)	Time (s)	Baking conditions	Thickness (nm)
Monolayer resist	AR-P679.04 (PMMA 4%)	4000	30	180°C, 5min	310
Bi-layer resist	AR-P619.06 (PMMA/MMA 33%, 6%)	5000	30	200°C, 5min	300
	AR-P679.04 (PMMA 4%)	5000	30	180°C, 5min	200

Electron beam exposure and development After coating the sample with the resist, it is replaced inside the SEM, at the same position as before. The lithography software allows to draw a mask of the patterns which will be realized on the NWs. Figure 2.25 (b) has shown a mask of four-probe contact patterns in the field of 70×70 μm, and bigger patterns have been drawn in the field of 700×700 μm.

The exact same calibration alignments were done, so that the overlap between the real NWs and the mask is optimized. The SEM setting is the same as before, and the e-beam exposure was performed with proper dose[‡‡] for each single NW.

After exposure, the sample was taken out of the SEM, and ready for the development. For this purpose, the sample was immersed in a solution MIBK/IPA (1/3) in 30 seconds, then it was rinsed in IPA for 1 min, and dried with nitrogen flow.

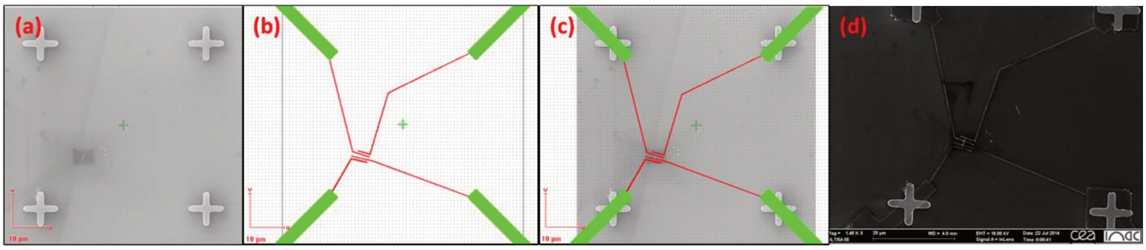

Figure 2.25 Images during EBL process. (a) A high resolution SEM image of single NW before putting the resist. (b) The lithography mask drawn based on the image in (a), green and red represent a dose factor of 1.5 and 2.5, respectively. (c) The overlapping of the mask and the image. (d) A SEM image of the final device.

Metal evaporation and lift-off After development, some surface treatments are needed to improve or facilitate ohmic contacts. Obviously, the nature of the treatment depends on the doping level and type of the NW.

In terms of Si doped GaN NWs, two reactive ion etching (RIE) processes were adopted based on previous experience with GaN microwires [113]. RIE O_2 plasma was applied for 5 seconds at 15 °C, in order to further remove the possible resist residuals after the development. Another RIE process of SF_6 plasma was employed for 5 seconds at 15 °C, with the aim of etching away the possible oxides on the NW surface.

The metal deposition is done using an evaporator called Plassys. A metal combination of Ti/Al (30/50 or 90 nm[§§]) has been utilized to contact Si doped GaN NWs.

For subsequent lift-off, the sample was immersed in acetone for a few hours, in order to remove all the remaining resist. SEM images of realized devices are shown in Figure 2.21 (b) & Figure 2.25 (d).

[‡‡] Dose is defined as charge per unite area, and it indicates the amount of energy deposited per area. The right electron dose needed for each exposure highly depends on the resist, the dimension and the density of the patterns. Therefore, a dose test is normally performed.

[§§] The thickness of the metal contacts is similar to the diameter of the NWs. Depending on the NW size, the thickness of Al layer is varied.

2.4.2 Electrical transport theoretical background

The resistivity of a semiconductor ρ is related with both the density of available free carriers n and their mobility μ through the following equation:

$$\rho = \frac{1}{qn\mu} \qquad (2.1)$$

Where q is the electric charge. It is crucial to obtain information of these three basic parameters for the understanding of the electrical properties of the semiconductor.

Carrier concentration n Carrier concentration n and doping level (N_d or N_a) are inextricably connected in semiconductors. When dopants (donors or acceptors) are incorporated into a semiconductor, they create energy levels within the band gap. Taking donors as an example, the doping atoms produce an impurity level E_d within the band gap, close to the conduction band. As shown in Figure 2.26 (a), the extra electrons of these donor atoms need a small thermal energy to jump to the conduction band, and this energy is called the ionization energy. From the energy diagram, we can see that the ionization energy equals the energy distance between E_d and the bottom of the conduction band E_c, in the case of low Si doping ($N_d < 10^{17}$ cm^{-3}) in GaN, this energy is about 30 meV [73].

With increasing doping level, E_d will split into a band of energies, widening and approaching to the conduction band; eventually overlap with the bottom of the conduction band E_c. Above this point, the Fermi level lies inside the conduction band, the ionization energy becomes 0 meV, and all the donors are ionized ($n = N_d$). In this case, the semiconductor has a metallic behavior, with the carrier concentration constant with varying temperature. This semiconductor is degenerate, and the critical Si doping concentration in GaN to reach metal-insulator transition (MIT) is experimentally determined to be around 1.6×10^{18} cm^{-3} [73].

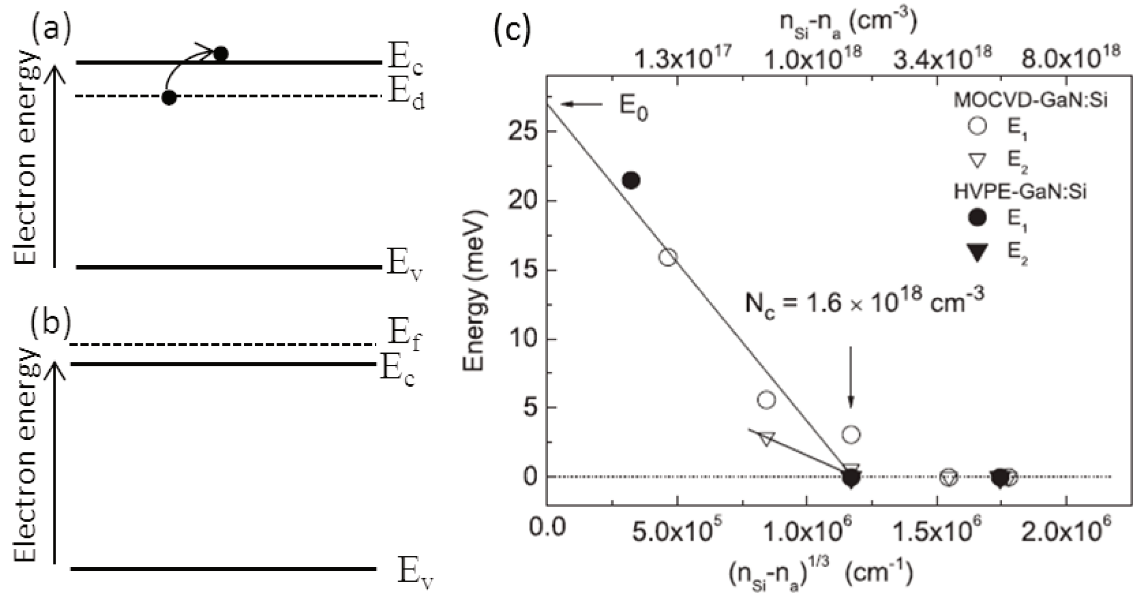

Figure 2.26 Donor ionization and MIT. (a) Schematic of energy band showing the donor ionization process, with one electron jumping from donor level to the edge of the conduction band. (b) Energy band diagram of a n-type degenerate semiconductor, displaying that the Fermi level lies inside the conduction band. (c) Ionization energy of Si in GaN 2D layer as a function of uncompensated Si donors, $n_{Si} - n_a$, taken from [73], a critical doping concentration N_c is determined to be 1.6×10^{18} cm^{-3}, when the ionization energy starts to drop to 0.

In a n-type semiconductor, the total number of free electrons per unit volume n in the conduction band can be calculated as the number of available states N(E) multiplying the state occupation probability f(E), and integrating the product from the bottom of the conduction band E_c to the top E_{cmax}:

$$\boldsymbol{n} = \int_{E_c}^{E_{cmax}} \boldsymbol{f(E)\ N(E)\ dE} \qquad \textbf{(2.2)}$$

The occupation probability f(E) is generally given by Fermi-Dirac distribution function:

$$\boldsymbol{f(E)} = \frac{\mathbf{1}}{\mathbf{1} + e^{\left[{(E-E_f)}/{kT}\right]}} \qquad \textbf{(2.3)}$$

In which E_f is the Fermi level, k is the Boltzmann constant, and T is the absolute temperature. Figure 2.27 shows the Fermi-Dirac distribution function, as well as the energy distribution of the carriers for an n-type, intrinsic and p-type semiconductor [9]**.**

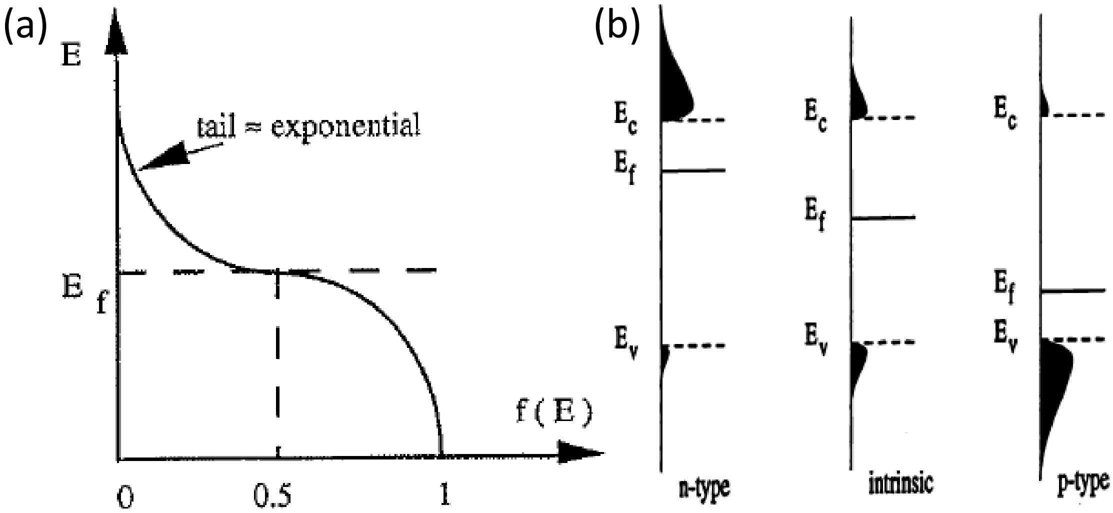

Figure 2.27 (a) Fermi-Dirac distribution function at T > 0. (b) The energy distribution of the electrons and holes for an n-type, intrinsic and p-type semiconductor [9].

Mobility The carrier mobility in a semiconductor is determined by scattering processes, such as phonon scattering, impurity scattering, or defects scattering. If more than one scattering process occurs, the mobility μ can be approximated by a so-called Matthiessens' rule:

$$\frac{1}{\mu} = \sum_k \frac{1}{\mu_k} \qquad (2.4)$$

The scattering processes present in n type GaN are generally polar optical phonon scattering, piezoelectric phonon scattering, acoustic phonon scattering and ionized impurity scatterings. [9]

2.4.3 Resistivity measurements

2.4.3.1 The necessity of four-probe resistivity measurements

Two probe measurements are often used to estimate the resistivity of a wire assuming insignificant contact resistances. In this configuration (shown in the inset of Figure 2.28 (a)), a current is introduced into the wire, while the voltage between the two same contacts is measured. The deduced resistance consists of one part from the wire and another part from the contact, as written in equation (2.5):

$$R_{2P} = 2 \times R_C + R_{GaN} \qquad (2.5)$$

where R_C is the contact resistance, considering that the two electrodes are identical; and R_{GaN} is the resistance of the wire between the two electrodes. This estimation is only valid when the contact resistance is much smaller than the wire resistance.

However, in the real world of GaN NWs, this requisite of low-resistance ohmic contacts is difficult to meet. The contact resistance generally depends on the relative semiconductor / metal work functions, interface states, which induce Fermi level pinning, as well as the active contact area. It is challenging to find the ideal metal to match with the work function (Fermi level) of GaN, which is a function of doping. In addition, the non-negligible interface states and small contact area in the case of NWs can hinder the formation of low-resistance ohmic contacts. Consequently, the contact resistance (even if it is ohmic) is non-negligible or even significant compared to the resistance of the wire itself, as shown in Figure 2.28.

Therefore, four-probe configuration is adopted to measure the resistivity of GaN NWs. As shown in the inset of Figure 2.28 (b), a current I is injected through the two outer contacts on the NW while the voltage drop V between the two inner contacts is measured. Using this method, the resistivity of the NW can be inferred independently to the contact resistance. Assuming a homogeneous conduction through the whole section of the NW, the resistivity of the NW between the two inner contacts can be calculated using equation (2.9).

$$\boldsymbol{\rho = \frac{V}{I} \times \frac{3\sqrt{3}}{2} r^2 / L} \tag{2.6}$$

where L is the length of the NW between the two inner contacts, r is the radius of the circumscribed circle of the hexagonal cross section of the NW, and $\frac{3\sqrt{3}}{2} r^2$ represents the surface area of the hexagonal cross section of the NW.

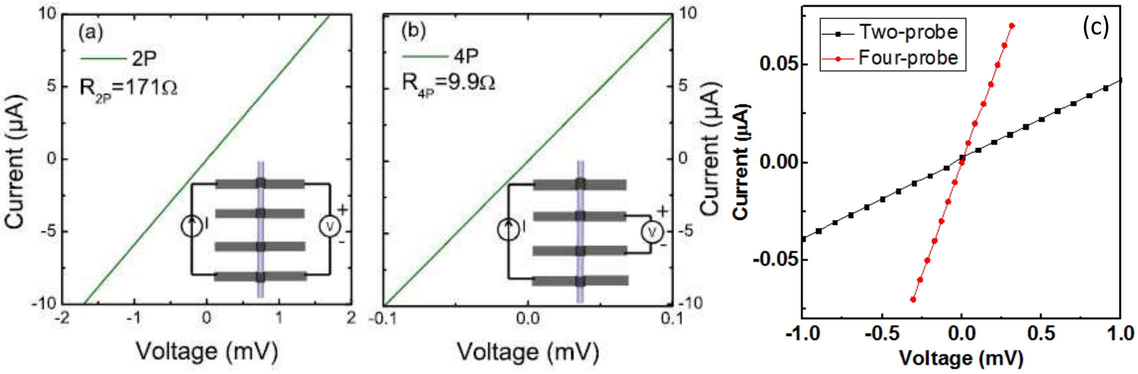

Figure 2.28 The comparison of two-probe and four-probe measurements. Two-probe (a) and four-probe (b) I-V characteristics of a highly Si-doped GaN microwire [109]. (c) two-probe and four-probe I-V curves for a highly Si-doped GaN NWs (sample N2074).

2.4.3.2 Room temperature resistivity measurements

Numerous NWs were connected in four-probe configuration by traditional EBL, and room temperature resistivity measurements have been performed on 20 single NWs from various samples of Si doped GaN NWs as well as the NID ones, (see Table 2.1 for the detailed growth conditions), except for the most heavily doped sample N2060.

Current density is limited to 900 A.cm^{-2} to avoid heating issues during the measurement, and reverse polarity measurements have been done to exclude the effect of the potential offset.

Figure 2.29 presents the four-probe resistivity value as a function of NW radius for five samples with different doping levels. The resistivity value spreads from 10^2 Ω.cm to 10^{-3} Ω.cm, corresponding to the range from NID NWs to the one with Si cell temperature of 938 °C.

For NID NWs, the resistivity spreads from 10^2 to 3×10^{-2} Ω.cm for 6 NWs, suggesting a different residual doping among these NWs or the influence of different surface states in NWs. The possible origins of this residual doping will be discussed in the section 2.4.4.

For the doped NWs, the resistivity of NWs having different radii and coming from the same sample is quite constant. This is a signature of negligible surface conduction or reduced conduction due to near-surface depletion at room temperature, and hence validating the assumption of a homogeneous conduction through the whole section of the NW. However, caution must be taken for the sample grown with Si cell temperature of 875 °C since the two wires radii are close (27 nm and 31 nm). The resistivity of NWs from the different samples gradually decreases from 2×10^{-2} Ω.cm to 10^{-3} Ω.cm, while increasing the doping level. These two features have revealed the ability to achieve homogeneous doping level from one wire to another and furthermore to control the doping level through variation of the Si cell temperature in the MBE system.

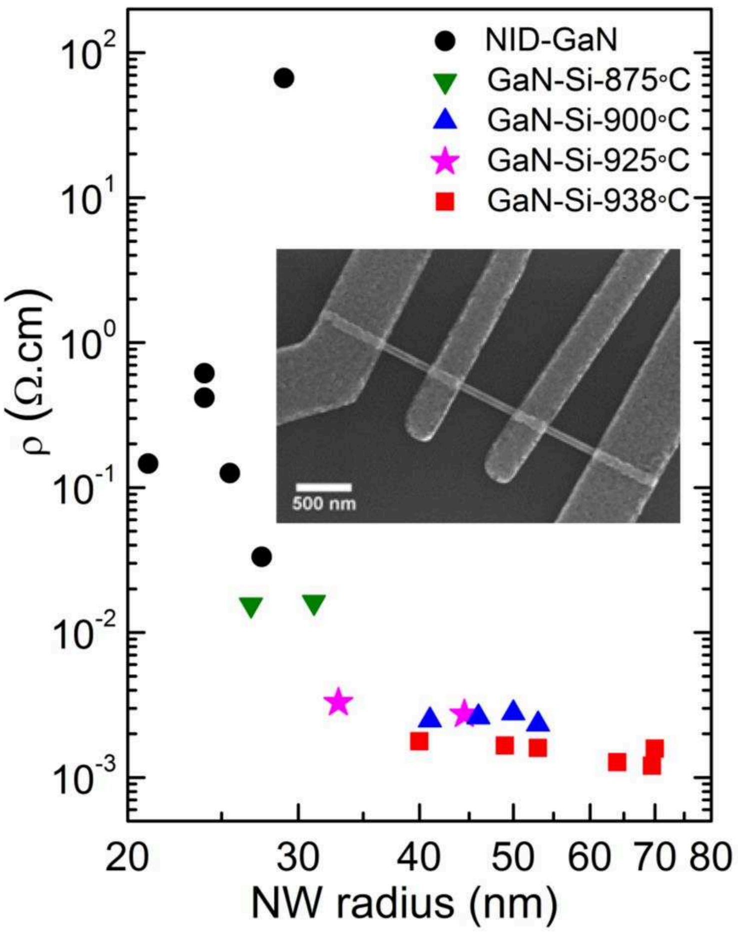

Figure 2.29 Four-probe resistivity as a function of NW radius for samples with different Si doping levels at room temperature, and a SEM image of one contacted NW is shown in the inset.

Specific contact resistance We can easily deduce the contact resistance R_c (Ω) by combining two-probe and four-probe measurements. However, R_c is area-dependent, thus, another important parameter — specific contact resistance (also referred as contact resistivity) ρ_c is generally used to study the metal / semiconductor contacts. We have $\rho_c = R_cA$ ($\Omega.cm^2$), where A is the active area of the contact. A is difficult to determine since the current transport can occur in only part of the physical contact depending on the geometry of the contact. A model has been described by Mohney et al. on the adaptation of the traditional transmission line model (TLM) to the specific case of semiconductor NWs. [114] In this model, l is the length of the physical contact, L_T is called the transfer length, which represents the part of the contact participating in the current transport. In the case of hexagonal NWs, we have:

$$\boldsymbol{R_c = \frac{\rho L_T}{S}\coth\left(\frac{l}{L_T}\right), L_T = \sqrt{\frac{3\sqrt{3}}{10}\frac{\rho_c r}{\rho}}} \qquad \textbf{(2.7)}$$

where ρ stands for NW resistivity, and $S = \frac{3\sqrt{3}}{2}r^2$ represents the surface area of the hexagonal cross section of the NW (see the schematics in Figure 2.30). When the physical contact length $l \gg L_T$, we have the active area $A = 5 \times r \times L_T$; whereas if $l \ll L_T$, we have $A = 5 \times r \times l$.

Assuming $l \ll L_T$, we can calculate the specific contact resistance ρ_c for NWs grown with different Si cell temperatures. As summarized in Figure 2.30 (c), two things can be observed: a dispersion of ρ_c for different NWs from the same sample due to individual contact geometry; a global decrease tendency of ρ_c with increasing Si cell temperature. For NID NWs, ρ_c is above 10^{-4} Ω.cm^{-2}, whereas for Si doped NWs, the majority of ρ_c is on the order of 10^{-5} to 10^{-6} Ω.cm^{-2}, which agrees with literature for Ti/Al contact [115].

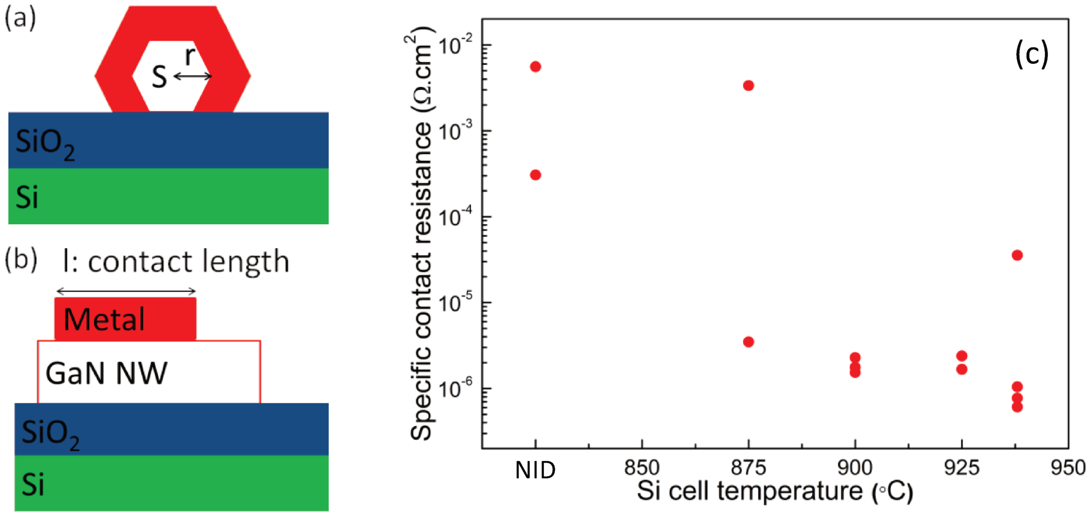

Figure 2.30 (a) and (b) Schematics of the Mohney model [114]. (c) Calculated ρ_c for samples with different Si cell temperatures, note that ρ_c is presented in logarithmic scale.

The influence of the surface states in NWs Due to the large surface-to-volume ratio, wires are more sensitive to some effects, such as surface Fermi-level pinning, than their bulk or 2D layer counterparts. Different surface Fermi-level pinning could induce either a conducting (surface accumulation) or insulating (surface depletion) layer at the surface of the wire, which complicate the comprehension of the electrical transport measurements. Figure 2.31 illustrates the influence of surface Fermi-level pinning on band diagram and electron distribution along the wire radius in an n-type wire.

As shown in middle column of Figure 2.31, when there is no influence of surface Fermi-level pinning, which is generally the case in bulk or 2D layer, no band bending at the surface is present and the electrons are homogenously distributed along the wire radius.

In some cases, the surface Fermi-level pinning could lead to a downwards band bending and accumulation of electrons below the wire surface (two left columns in Figure 2.31). This effect creates an extra conduction channel, which could modify the overall resistivity of the wire.

In other cases, an upwards band bending as well as a depletion of electrons are present at the wire surface. Therefore, an effective conduction radius r_0, instead of real wire radius r ($r_0 < r$) should be used for resistivity measurement analysis. Furthermore, when $r_0 = 0$, the wire is fully depleted, and it behaves like an insulator, as shown in last column in Figure 2.31 [116].

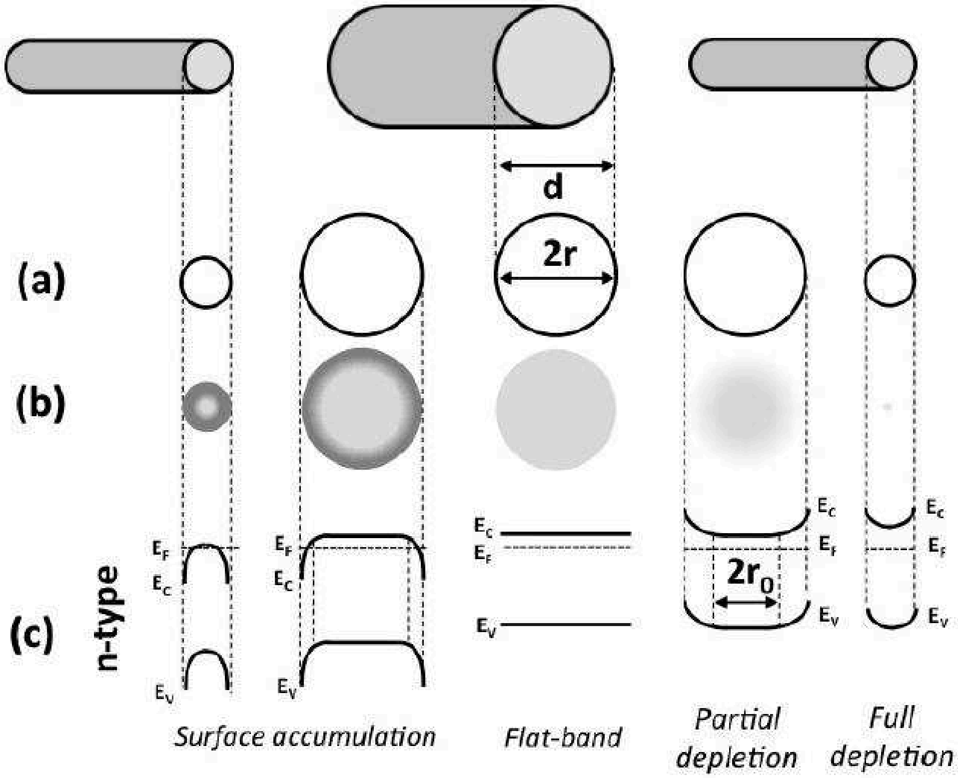

Figure 2.31 Band bending along the wire radius and its effect on the spatial distribution of electrons in n-type wire under different surface Fermi-level pinning [116]. (a) The wire section considered. (b) Radial distribution of electrons in the wire. (c) Band diagrams of the wire in the case of n-type semiconductor.

The origins of this Fermi-level pinning is normally the surface states induced by the interaction between the wire and species in atmosphere [117]. Regarding GaN wires, the pinning of the Fermi level at the surface has been observed to create a depletion layer (no accumulation layer reported so far) [46], [107], [117]. The thickness of this depleted region highly depends on the characteristics (such as density, energy) of the surface states and on the doping level of the sample. A model has been proposed to describe the surface depletion in GaN NWs [44], [107], and the critical diameter d_{crit} below which the wire is completed depleted is presented by:

$$d_{crit} = \sqrt{\frac{16\varepsilon\left(\Phi_B - kT \cdot ln\, {}^{N_c}/_{N_D}\right)}{q^2 N_D}} \tag{2.8}$$

In this equation, N_c stands for the effective density of states in the conduction band, which equals 1.2×10^{18} cm^{-3} for GaN at 300K[***]. kT is 26 meV at room temperature. ε is the dielectric constant of GaN, and q is the elementary charge. Φ_B signifies the distance between the level where the Fermi-level is pinned and the condition band, which is between 0.1 and 1 eV depending on different samples [118], and expected to be 0.55 eV below the conduction band according to previous photoemission spectroscopy studies on GaN surfaces [119]. From this equation, we can see that d_{crit} is inversely proportional to the doping level N_D, meaning that for low doping wires, the surface depletion is more significant than for highly doped samples. Regarding for wires with different radii, we can conclude that the surface depleted layer has more influence for wires with smaller radius.

In Figure 2.32, we have plotted the ratio between the four-probe resistance of the wire R and the length of the wire between the two inner contacts L as a function of the wire radius r. The dotted lines present simulations of bulk-like conduction, in which the ratio $R/L = \rho/(\pi r^2)$ follows a $1/r^2$ relationship. Note that in Figure 2.32, both the x axis and the y axis are in logarithmic scale, therefore, the bulk-like conduction manifests itself as a straight line. We can find that indeed, for highly Si doped GaN samples, either microwires [92], or NWs N2088 (GaN-Si-938°C), the surface effects are negligible, evidenced by the fit with the simulated lines. For smaller and less doped NWs, the d_{crit} is on the same order of magnitude compared to the wire radius, the surface depletion (even full depletion) is witnessed by the deviations of the R/L values from the dotted line with ρ = 8.9 mΩ.cm in [117].

For my samples, it is clear that for N2088 (GaN-Si-938°C), the wire follows a bulk-like conduction regime, in fact, the critical diameter d_{crit} calculated using equation (2.8) for this sample is 7.5 nm, which is negligible compared to the average diameter of the wires from this sample (117 nm). For the other less doped GaN NWs, the current data seems to show that the surface depletion plays a rather minor role in the resistivity measurements; further investigation is limited due to the number of the measured NWs and the NW radius dispersions from each sample. In terms of NID NWs, it is difficult to draw a reliable conclusion, since either an inhomogeneous residual doping (evidenced by FET measurements later) or surface depletion could be responsible for the high resistivity of some NWs.

[***] Data from website: http://www.ioffe.ru/SVA/NSM/Semicond/GaN/bandstr.html

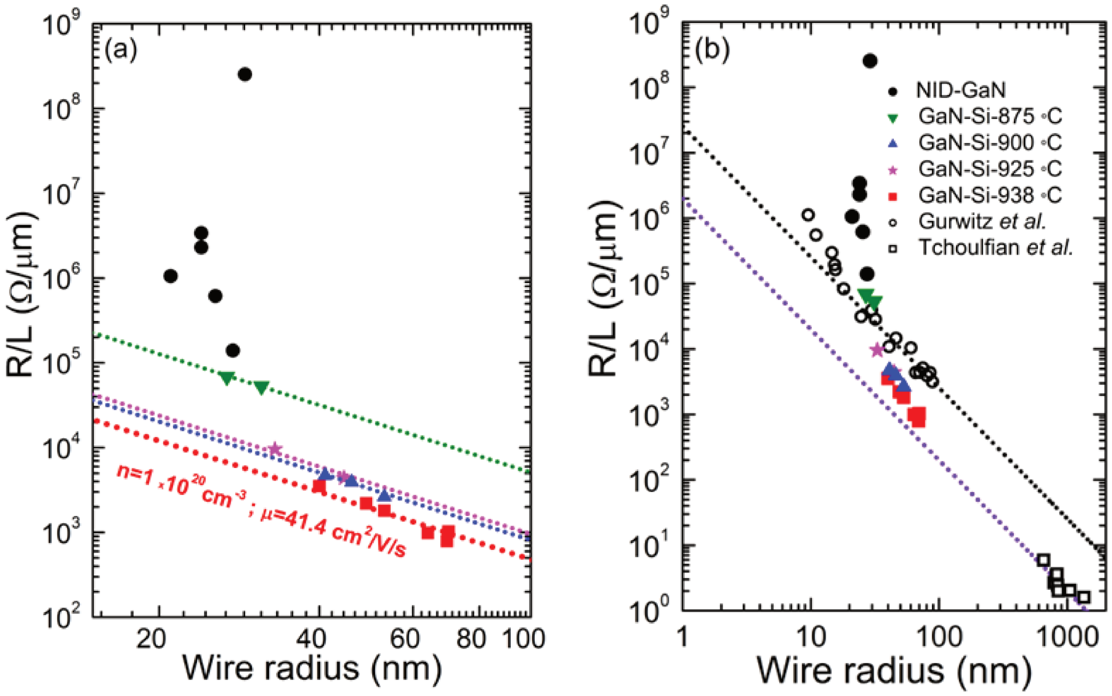

Figure 2.32 Ratio between the four-probe resistance of the wire R and the length of the wire between the two inner contacts L as a function of the wire radius r. The dotted lines present simulations of bulk-like conduction in the whole section of the wire supposing the resistivity value is constant. (a) The same experimental data as in Figure 2.29, displayed in the fashion of R/L versus r. (b) The comparison between my data and data from literature. Two sets of data have been shown as examples of the literature: GaN NWs (open circle) from [117] and Si doped GaN microwires (open square) from [109]. The dotted lines in (b) correspond to resistivity values of $\rho = 8.9$ mΩ.cm for the black one and $\rho = 0.625$ mΩ.cm for the violet one [116].

2.4.3.3 Temperature dependent measurements

Room temperature four-probe measurement allows us to investigate the resistivity of the NWs, however, it does not provide much information about the conduction regime in the NWs. Therefore, temperature dependent four-probe resistivity measurements down to 5 K have been performed on four representative NWs with different doping levels.

Figure 2.33 (a) presents the results of four-probe resistivity as a function 1/T for these four NWs. It reveals a temperature dependent conduction for the NID and lightly doped GaN NWs, and a metallic behavior for more doped NWs. For the former, free electron in the conduction band dominates with a typical donor ionization regime for T > 50 K, while a temperature independent conduction controls the resistivity for T < 50 K. This behavior signifies a doping level below the MIT dominating the conduction at high temperature. As mentioned previously, the critical electron concentration for the MIT has been established to be 1.6×10^{18} cm^{-3} based on the experimental work on Si doped GaN epilayers [73]. The resistivity temperature dependence of the NID and lightly doped NWs for T > 50 K exhibits the same behavior as observed for Si-doped GaN epilayers containing a carrier concentration of 0.1 to 0.6×10^{18} cm^{-3}. However, the resistivity temperature dependence of these two NWs differs from that of epilayers at low temperature ($T < 50$ K). Whereas nearest neighbor hopping happened in epilayers [55], a metallic conduction is found to control the resistivity in NWs. This degenerated conduction could be assigned to two different mechanisms in the specific case of NWs: i) near surface carrier depletion due to upward band bending induced by surface states or adsorbed species [117], leading to metallic conduction in a core at low temperature, surrounded by a semiconducting shell, which dominates the conduction at high temperature; ii) inhomogeneous radial doping with a NW shell doping above the n_{MIT}.

For more doped NWs, the resistivity does not vary with respect to temperature, until down to 5 K, showing a metallic behavior. This finding is consistent with EDX observation (an average Si concentration of 10^{20} at / cm^3) for sample grown with Si cell temperature of 938°C. In addition, this outcome is also compatible with the high doping level achieved on microwires previously reported (the gray dashed line) [109].

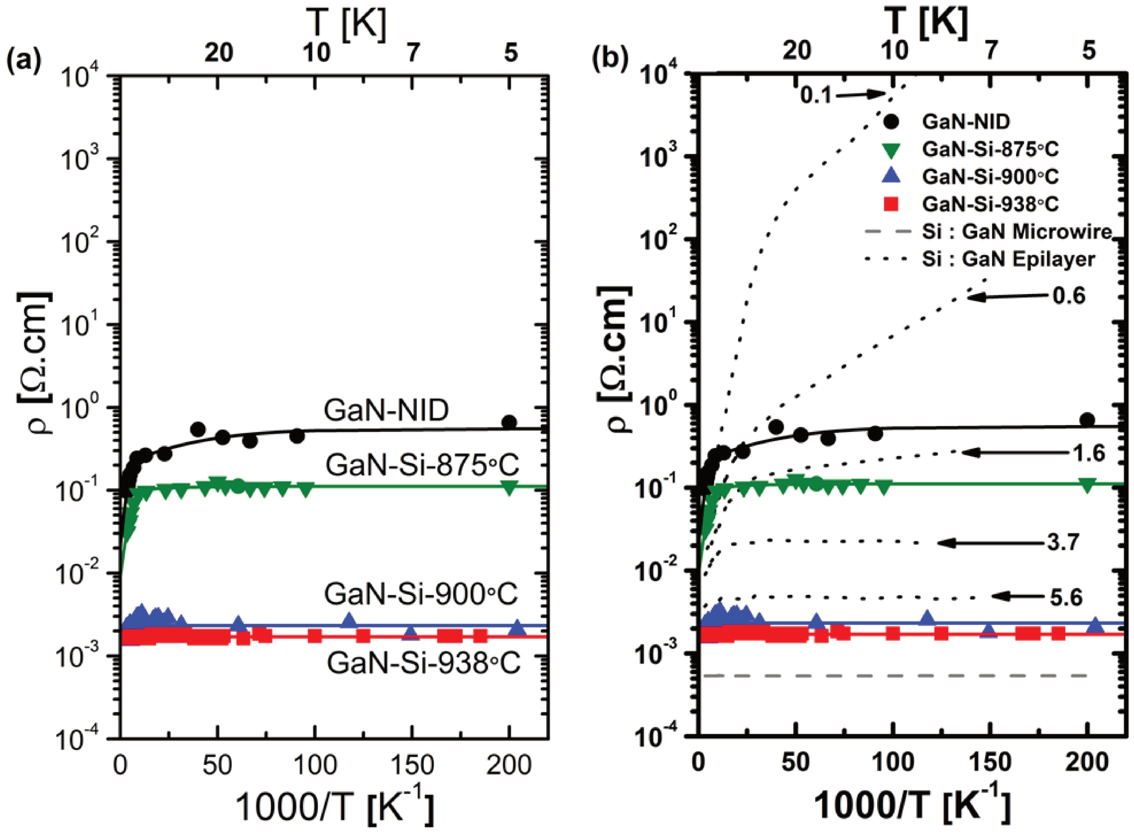

Figure 2.33 Four-probe resistivity temperature dependence data. (a) Four-probe resistivity of samples with various doping levels (different colors) versus the inverse of the temperature (1000/T), symbols denote the experimental points, solid lines represent fits according to the exponential law $\frac{1}{\rho} = \sigma_0 + \sigma_1 e^{-E_a/kT}$, where the first term represents the metallic conduction, the second term stands for the ionization of the electrons from the Si donor level to the conduction band. (b) The dotted line represents resistivity data determined by Hall measurements for GaN epilayers with different Si doping levels (carrier concentration is designated close to the corresponding line, with a unit of 10^{18} cm^{-3}) [73], and the gray dashed line stands for high conducting Si-doped GaN microwire previously reported [109].

2.4.4 Doping level of NID NWs determined by FET

2.4.4.1 FET measurements

The back gate (BG) FET is commonly used to estimate doping level and mobility in the NW devices, one of the pioneering works on GaN NW FETs has been conducted by Lieber's group [37]. As shown in Figure 2.34, the NW has been dispersed on a Si substrate with thermal oxide on top, and the source, drain contacts were realized by EBL. The source and drain I_{sd}-V_{sd} relationship is linear indicating ohmic source and drain contacts, and the Si back gate can be employed to control the amount of charges in the NW channel. In their case, the conductance of the NW decreases with increasing negative BG bias V_g, manifesting the n-type behavior of the NW. Gradually increasing the negative BG bias V_g, the threshold voltage V_{th} to completely deplete the NW was experimentally found to be −8 V. We have the total charge in the NW $Q = CV_{th}$, where C is the gate-NW capacitance. C can be represented by equation (2.9):

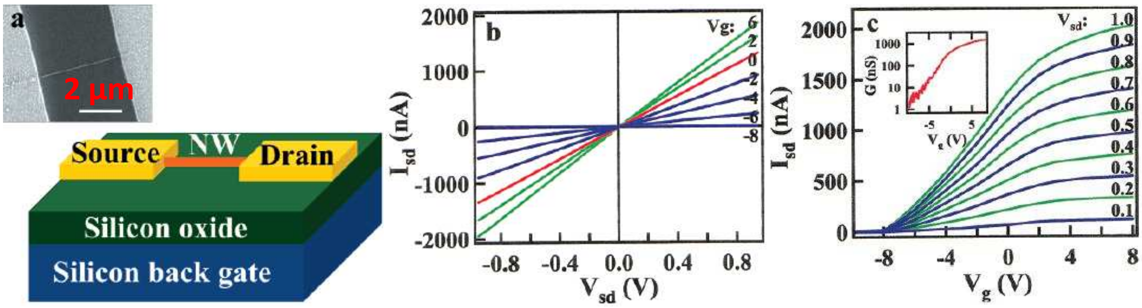

Figure 2.34 BG-FET measurement from Lieber's group [37] (a) Schematic of a BG FET NW device, and (inset) a SEM image of GaN NW FET device. (b) Source and drain I_{sd}-V_{sd} characteristics under different gates measured on a GaN NW of 17.6 nm diameter. The gate voltages for each I_{sd}-V_{sd} curve are indicated. (c) I_{sd}–V_g characteristics while varying V_{sd} from 0.1 V to 1 V. The conductance G as a function of gate voltage V_g is shown in the inset.

$$\frac{C}{L} \cong \frac{2\pi\epsilon\epsilon_0}{\ln\left(\frac{2h}{r}\right)}, \text{when } h \gg r \tag{2.9}$$

where ϵ is the relative dielectric constant of the oxide, h is the thickness of the gate oxide, and L, r are the length and the radius of the NW channel between source and drain, respectively. Therefore, the doping density (donor density in this case) N_d can be calculated with the following equation:

$$N_d = \frac{Q}{e\pi r^2 L} \tag{2.10}$$

Meanwhile, the mobility of the carriers can be estimated through the transconductance of the device in the linear regime. We have equation (2.11):

$$dI/dV_g = \mu\left(C/L^2\right) V_{sd} \tag{2.11}$$

However, this model lacks of accuracy due to difficulties to estimate the gate-NW capacitance C and the interface charges between NW and the oxides. Indeed, this model assumes that an electrostatically metallic cylinder wire is surrounded entirely by the dielectric oxide, and there is no movable charges at the interface, which are not true in reality. In fact, it has been already reported that this model overestimates the capacitance with a factor of 2 to 3 compared with the value obtained by numerical simulation [120], [121].

Thus, we have performed 2D finite element simulations by NextNano^{3}[†††] to model the

---

[†††] www.nextnano.de/ (accessed Jan 1, 2015)

gate-NW capacitance and further extract the doping level of the NW channel (detailed information in the following section). Moreover, since it is difficult to control the interface charges in the BG geometry, we have conducted lateral gate (LG) FET measurements, serving as a complementary way of characterization.

In our NWFETs, the source, the drain and the LG are fabricated by EBL mentioned before, and either the BG, which is the metalized backside of Si substrate, or the LG can be biased to modify the current in the NW channel. Figure 2.35 has shown a SEM image of one real device, and the schematics of BG and LG FET measurements. Just a reminder that all the measurements have been performed in the FEI Inspect F50 FESEM-setup, which means that vacuum is the dielectric material in the case of LG FET.

Two sets of typical NW channel current (I_{sd}) as a function of source-drain voltage (V_{sd}) data measured from a single NID GaN NW-FET at different BG and LG voltages are demonstrated in Figure 2.35 (d)&(e). The linear I_{sd}-V_{sd} relationship at zero gate voltage displays the ohmic characteristics of the source and drain contacts; and the conductance decreases when the negative BG or LG voltage increases, indicating that the intrinsic doping for NID NW is n-type, which is consistent with literature results. For doped NWs, however, the conductance does not vary while changing the gate voltage, meaning that the doping level in these NWs is much higher than that in NID ones.

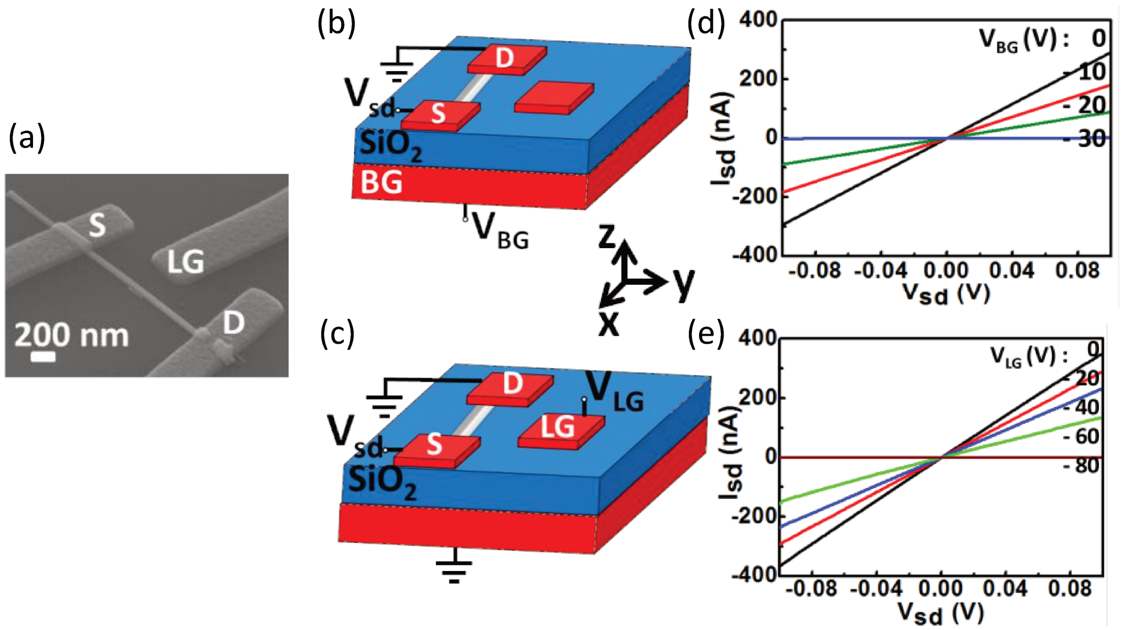

Figure 2.35 BG and LG FET measurements on a NID NW. (a) Tilted view SEM image of one FET device with both BG (not shown) and LG. Schematic of BG and LG FET measurements, (b) and (c) respectively. BG (d) and LG (e) dependent I_{sd}-V_{sd} data measured on one NID NW with the radius of 30 nm. The BG and LG voltages for each I_{sd}-V_{sd} curve are indicated.

2.4.4.2 Finite element simulations

In our simulation, the device is modelled as a cross section cut in the (y, z) plane direction, and GaN NW was represented by a hexagon. The oxide, BG and LG were modeled as rectangles with the corresponding physical dimensions (see in Figure 2.36). The device is simulated at $V_{sd} = 0$ V to electrostatically model the charge depletion at a certain gate voltage. Firstly we presume a doping level of the NW as an input parameter, and then by applying a small voltage sweep of either BG or LG, the NW is gradually depleted as shown in Figure 6 (h, j, l) and (i, k, m), respectively. Thanks to NextNano^3, the 2D electron density in the NW at each voltage sweep step can be visualized by considering all the device geometry and different materials properties, as well as solving the Poisson equation. As shown in Figure 2.36, the electron density in the NW cross section at zero gate voltage is 1×10^{18} at / cm^3, which is the input doping level. The NW is gradually depleted of carriers when applying a negative gate bias with the BG or the LG. Noticeably, the depleted region starts from the bottom of the NW, and gradually increases when applying a BG; whereas, the NW is depleted starting from the right side when using a LG. When applying a small gate voltage, we have the gate-NW capacitance:

$$\boldsymbol{C\,(N_d) = \frac{dQ(N_d)}{dV}} \qquad \textbf{(2.12)}$$

where dQ/dV can be extracted as the slope of 2D electron density in the NW versus the gate voltage curve, from Nextnano^3 simulation result at an assumed doping level N_d. Assuming that C does not vary while changing the gate voltage, we have

$$\boldsymbol{C(N_d)V_{th} = \mathbf{Q} = N_d\,(\frac{3\sqrt{3}}{2}r^2)\mathbf{L}} \qquad \textbf{(2.13)}$$

where V_{th} is the threshold voltage determined experimentally when the I_{sd} is below the measure limit, Q is the total charge in the NW. Numerically solving these two equations, we can determine $N_{d.}$

Numerous NID NW FET devices have been evaluated using this method. The doping level of these NWs ranges from 4×10^{17} at/cm^{-3} to 6×10^{18} at/cm^{-3}, showing an inhomogeneous residual doping among these NWs, which is consistent with resistivity measurements. The gate-NW capacitance value is around a factor of 2 or 3 lower than that calculated by the analytical equation (2.9), which agrees with the literature and confirms the necessity of numerical simulation in the NW FET system [120], [121].

In addition, we have found that the doping level determined by BG is twice larger than that evaluated by LG for the same NW measured in both geometries. One reason for this discrepancy could be that in the case of LG, only the part of the NW facing the LG was depleted, whereas the whole NW channel was involved in depletion in the case of BG. Moreover, the method of BG is less accurate due to the difficulties to estimate the interface charges between the NW and the oxide.

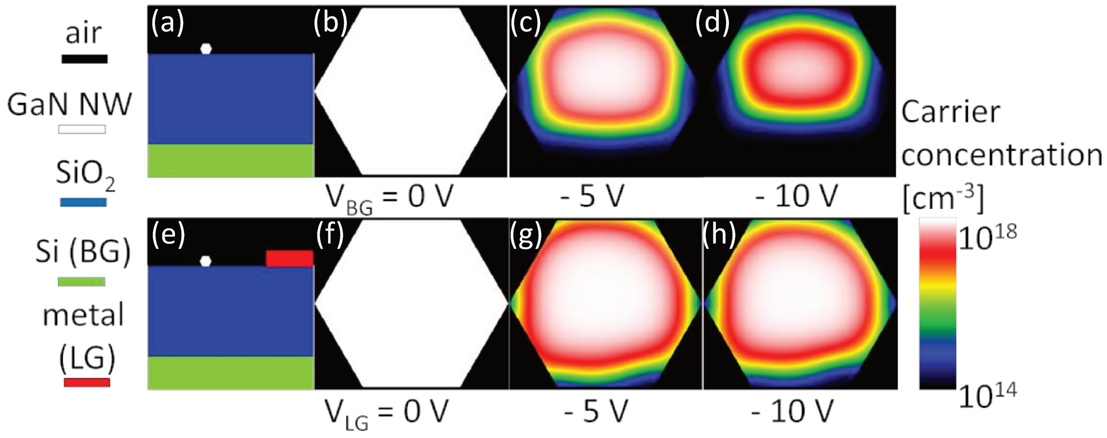

Figure 2.36 Cross-sectional (y-z plane) schematics of the BG (a) and LG (e) models considered in NextNano^3 simulations. Calculated 2D electron density maps in one GaN NW, with BG (b, c, d) and LG (f, g, h) of 0, −5, −10 V, respectively.

In this 2D simulation, the length of the NW is excluded from the parameters; however, since the L/r ratio of the MBE-grown NWs varies from 25 to 55, 3D simulation is not really necessary considering that there is not so much difference between 2D and 3D simulation results according to [121]. The error bar in this model comes from the uncertainty of the determination of the device dimensions from the SEM images, such as the NW length, radius and the distance between the LG and the NW.

2.4.4.3 The possible origins of the non-intentional doping

From the FET measurements and finite element simulations, we have revealed a high inhomogenous intrinsic doping for NID NWs.

The intrinsic n-type doping in GaN has been commonly associated with nitrogen vacancies, unintentional impurities such as oxygen, and silicon [28]. Under the particular growth conditions of MBE NWs, nitrogen vacancies have high formation energy [122], whereas oxygen is barely present in the high vacuum system of MBE. Therefore, silicon diffusion from the substrate into the NWs has been suspected to be the main source of residual doping.

In 2008, Furtmayr et al. have observed a high concentration of Si at the interface between NW base and Si growth substrate by electron energy loss spectroscopy (EELS), confirming Si diffusion into the NW [41]. A few years later, Schafer et al. have performed four-probe resistivity measurements on three different segments on NID GaN NWs [123]. Figure 2.37 (b) has shown that the conductivity of the NW drops gradually when the distance to the NW base is increased, which is a signature of Si diffusion from the substrate into the NW. In our case also, the measured high residual n-type doping is probably due to the Si diffusion from the substrate.

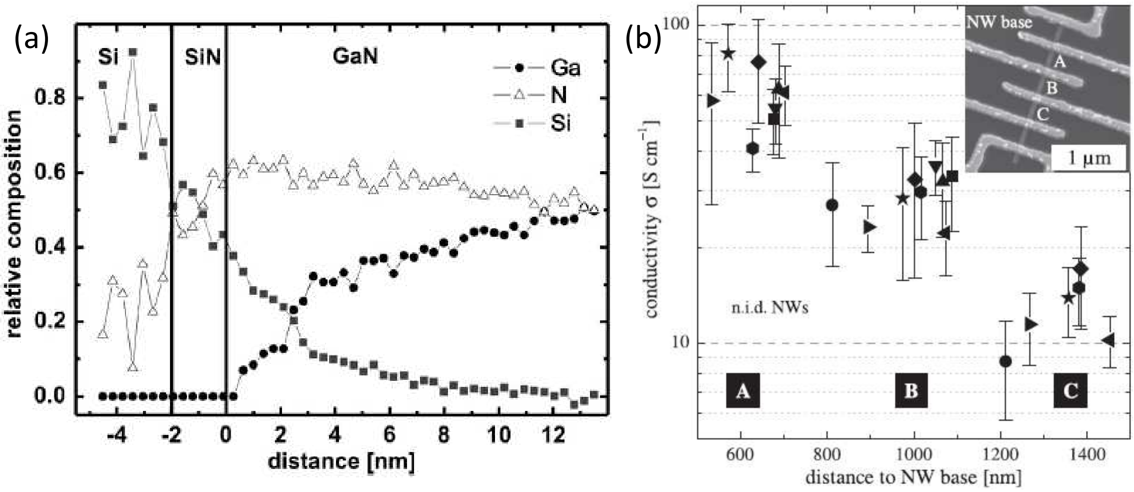

Figure 2.37 Evidences of Si diffusions into the NWs. (a) Relative atomic compositions at the GaN NW / Si substrate interface measured by EELS [41]. (b) Conductivity values for nine different single NID NWs at three different segments, each NW is represented by one of type of symbol. The three individual segments marked by A, B, C, are in accordance with the sample structure shown in the inset [123].

2.4.5 Mobility

Since the doping level obtained for NID NW is around the metal-insulator transition, we consider that full ionization is achieved in the NWs. Combining the four-probe resistivity and the doping level, we can deduce the mobility by using equation (2.1). For N2088, we can assume $n = N_d$, with N_d determined by FET and EDX, respectively. Mobility dependence on the carrier concentration of these NID NWs is shown in Figure 2.38. Most of the NID GaN NWs have a state-of-art mobility and a similar behavior compared to GaN films [73], [124]–[128] limited by impurity scattering. The two NWs with low mobility values are affected by surface scattering due to their extreme small radius around 20 nm [129]. Even with doped NWs, such as N2088, the mobility value is quite similar compared to the state-of-art value on the Si doped MOVPE GaN microwires, it implies that we can achieve high doping level in GaN NWs without reducing the mobility.

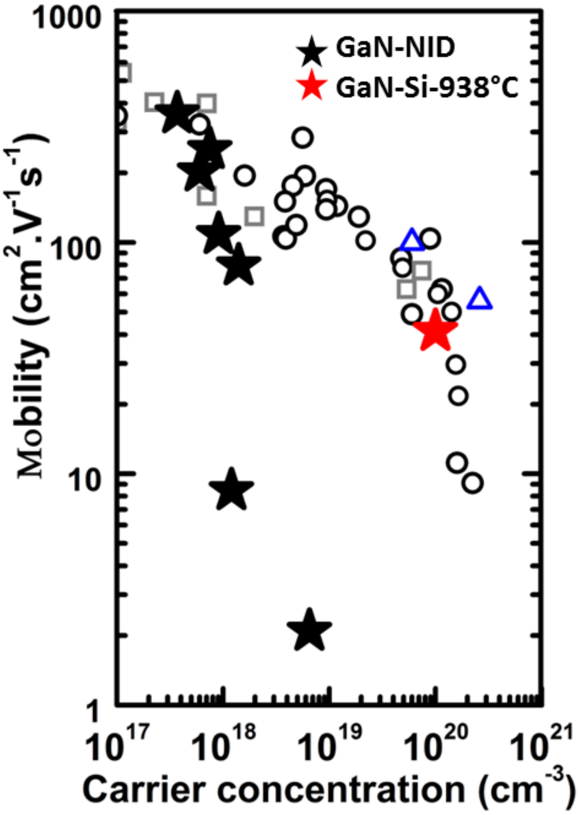

Figure 2.38 Mobility value versus carrier concentration for GaN. For NID GaN NWs and GaN wires grown with Si cell temperature of 938 °C, we assumed $n = N_d$, determined by FET and EDX, respectively. Experimental mobilities have been reported for NID GaN films (gray open squares) [124], [125] and Si doped GaN films (black open circles) [73], [90], [125]–[128], and two Si-doped GaN microwires (blue open triangles) [87], [109]. The mobility values of our NWs are shown as solid stars; black and red correspond to NID GaN NWs and GaN wires grown with Si cell temperature of 938 °C, respectively. For NID NWs, the radii of the two NWs with lower mobility (less than 10 cm^2.V^{-1}.s^{-1}) are 24 nm and 20 nm, and those of the other ones are in the range of 30-40 nm.

2.5 Conclusions of the chapter

To summarize, we fabricated GaN NWs with different Si doping levels by PAMBE, and systematically investigated their optical, structural, and electrical properties.

In particular, we found that the Si content in GaN NWs is higher than in the 2D layer counterparts, up to 2-4×10^{20} at/cm^3 accompanied by a Si-enriched shell for the most doped sample. Direct transport measurements on single NWs have shown a controlled doping with resistivity from 10^2 to 10^{-3} Ω.cm, and a carrier concentration from 10^{17} to 10^{20} cm^{-3}. FET measurements combined with 2D finite element simulation have shown a high mobility in these NWs, comparable to the state of the art mobility value of GaN epilayer.

3 GAN P-N JUNCTIONS

In the previous chapter, I have demonstrated a detailed investigation on n-type GaN NWs from different perspectives. I have studied the influence of the doping growth condition (namely Si cell temperature) on optical, structural, and electrical properties of the NWs, and further facilitated the understanding of the growth mechanism, the doping process and the peculiar properties of the doped NWs. In this chapter, I would like to extend the study to one of the most important basic building blocks of semiconductors devices — p-n junctions. In particular, I will focus on the growth optimization of the GaN p-n junction NWs in PA-MBE system, with a special attention on p-type GaN NWs, and furthermore, the electrical properties of the axial GaN p-n junction NWs through electron beam based techniques, including some investigations on p-type contact.

Compared to GaN epilayer p-n junctions, GaN wires p-n junctions manifest many advantages.

- First of all, as mentioned in Chapter 1 & 2, GaN wire structures can be readily grown on lattice mismatched substrates, such as Si, without creating a high density of dislocations. It permits a reasonable flexibility for device fabrications, and facilitates integration with other technologies, such as Si based technology in microelectronic industry.
- Secondly, it is possible to incorporate more dopants, and likely to achieve high carrier concentrations in the wires. As concluded in Chapter 2, Si dopants up to 10^{20} at/cm^3 can be incorporated in GaN NWs without element segregation and defect formation, which is above the theoretical solubility prediction (around 5×10^{19} at/cm^3) [94]. In terms of Mg dopants, a significant Mg content in both AlN and InN NWs have been reported by Mi's group associated with a reduced

Mg formation energy at the NW surface [36], [130], [131]. Therefore, GaN wires could be a promising solution to obtain high Mg (p-type) doping, which will greatly ameliorate the performance of most GaN based devices.

- Moreover, the wires could provide more degrees of freedom in heterojunction growth, such as facet-selective growth aiming at achieving multicomponent and multifunction nanodevices [132]. Device design on different facets (polar, non-polar) can be used to integrate radial, axial, or core-shell heterojunctions, which offers new possibilities compared to epilayers [133]. For example, GaN core-shell p-n junction wires can benefit from the increased active surfaces due to their particular geometries, candidating for more efficient LEDs [134], [135].

However, new opportunities always come with new challenges. There are only a few publications on the growth of p-type or p-n junction GaN NWs [76], [136], [137]. Mg doping in GaN is influenced by many parameters at the same time, such as Mg cell temperature, surface stoichiometry and substrate temperature. It is necessary to study systematically the Mg doping behavior in the MBE system.

Moreover, in the case of NW hetrostructures, one of the biggest challenges is the lack of metrology. New measurements and models are crucial to understand the underlying physics of these structures and further facilitate their use in various devices. Last but not the least, achieving ohmic contact on p-type GaN epilayer is difficult despite the tremendous efforts devoted to it. Many parameters, such as surface treatments and annealing conditions, play important roles in determining the specific contact resistance. Furthermore, ohmic contacts on NW structures are even more challenging due to the reduced contact areas, which make the contact resistance very sensitive to the technological processes and the annealing conditions. This absence of knowledge to fabricate ohmic contact especially on p-type GaN NWs, not only limits the understanding of the characteristics of the NW structures, but also restricts the further device developments based on these structures.

In terms of axial GaN p-n junction NWs, only a few novel characterization techniques have been reported (Figure 3.1). Non-contact, atomic-force-microscope-based (AFM-based) techniques such as scanning microwave microscope and kelvin probe force microscopy (KPFM) have shown to be able to distinguish n-type region from p-type part, and further map the space charge region in the p-n junction [138], [139]. However, quantitative understanding of doping levels at each side of the junction needs extensive modeling and more complete input parameters. Techniques, which require the fabrication of electrical contacts, such as electroluminescence (EL) and secondary electron voltage contrast (VC) have also been applied to characterize axial GaN p-n junction NWs [140], [141]. EL signal has indicated the presence of the p-n junction, however, non-ideal p-doping and asymetric Schottky-like p-contact are shown to significantly suppress the EL signal, suggesting that this work is far from complete [140]. SEM VC imaging has been reported for mapping electrostatic potential along the axial GaN p-n junction NW. The electric field profiles and depletion widths at different biases can provide valuable information about the NW p-n junction, indicating the great potential of electron beam based techniques in the field of NW junction characterization.

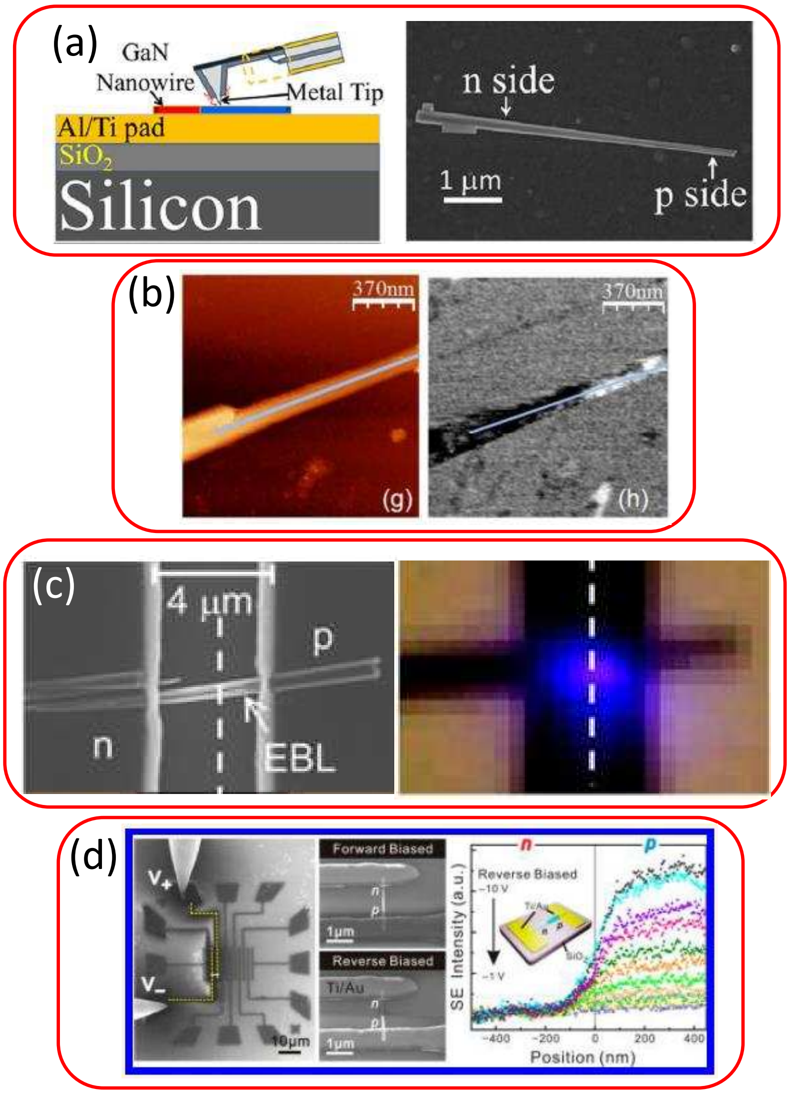

Figure 3.1 Different novel characterization techniques applied on axial GaN p-n junction NWs in recent literatures. (a) Schematics of scanning microwave microscopy measurement on dispersed GaN p-n junction NW, taken from [138]. (b) AFM (left) and KPFM (right) images of one p-n junction NW, clear contrast between n-type and p-type part can be noticed from KPFM image, taken from [139]. (c) SEM and EL images of one n-p NW device, the EL signal is located between the two contacts, signifying the location of the junction, taken from [140]. (d) SEM image and schematics of the secondary electron VC measurements (left), clear potential contrast variation with respect to the applying bias (right), taken from [141].

Indeed, electron beam based techniques are very versatile in the semiconductor characterization field. The interaction of a focused electron beam with a sample / device can be utilized to obtain morphological, chemical, optical, as well as electrical information. In particular, electron beam induced current (EBIC) and secondary electron VC have been demonstrated to characterize core-shell GaN p-n junction microwires grown by MOVPE [134]. Bulk-like behavior has been observed in these microwires junctions, where donor level and acceptor level were determined to be 3.5×10^{18} cm^{-3} and 3×10^{18} cm^{-3} respectively, and the local minority carrier / exciton diffusion lengths on both p and n sides are comparable with those determined in epilayers (Figure 3.2). So the questions are: Can we apply these two techniques on axial GaN p-n junction NWs? If yes, what peculiar behavior could we observe in the special case of NWs?

Actually, the EBIC technique has already been applied on axial NW p-n junction GaAs NWs, where the minority carrier diffusion lengths were found to be 10-fold lower compared to those in bulk or thin layers due to a large number of surface states, and a passivation process was shown to significantly improve the diffusion lengths [142]. Moreover, as mentioned before, secondary electron VC has been reported to apply on axial GaN p-n junction NWs [141] (Figure 3.2). However, many issues such as electron beam scanning contamination or optimization of p-type contact remain unclear.

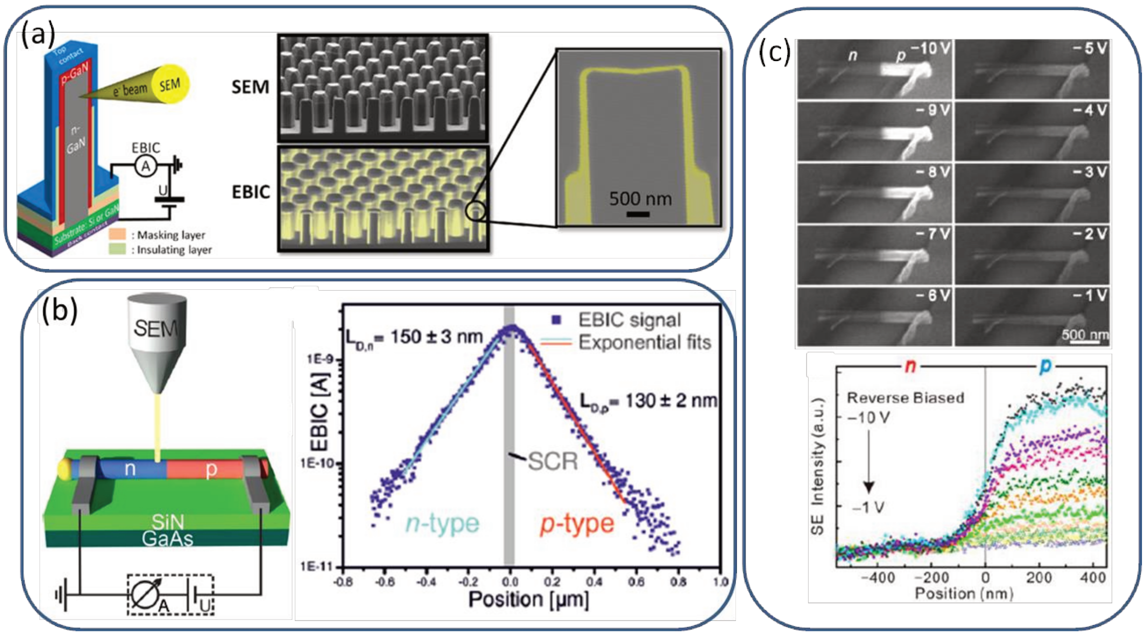

Figure 3.2 Electron beam based techniques (EBIC and secondary electron VC) on wire devices in recent literatures. (a) Schematics of core-shell GaN p-n junction microwire characterized by EBIC (left), SEM and EBIC images of the measured devices (right), taken from [134]. (b) Schematics of axial GaAs p-n junction NW characterized by EBIC (left) and minority carrier concentration determinations using the EBIC signal profile (right), taken from [133]. (c) Secondary electron VC variation on axial GaN p-n junction NW under different biases, taken from [141].

Therefore, in this chapter, I would like to focus on the growth condition optimization of axial GaN p-n junction NWs (in particular, the p-type part) in MBE system and furthermore the electrical measurements with the help of electron beam based techniques such as EBIC and secondary electron VC, including an exploration on p-type contact. So here are the questions I would like to address:

- What are the main parameters influencing Mg incorporation in GaN NWs grown by MBE? How can we improve Mg content by playing with these parameters?
- Could we achieve p-n junction NWs? Where is the junction? Is it abrupt? Does its position correspond the growth conditions?
- What are the donors and acceptors concentrations near the p-n junction? Does the NW structure really show a better dopant incorporation compared to epilayers in the case of Mg doping?
- What are the diffusion lengths of minority carriers or exciton concentrations near the junction? What is the influence of the surface states?

3.1 Growth optimizations

Before investigating the properties of p-n junction NWs, it is necessary to master their growth. As shown in chapter 2, well-controlled n-type GaN NWs can be achieved by varying the Si cell temperature in the MBE system. Now we will focus on the more complicated part: p-type.

p-type doping has always been a big challenge and a subject of study in the nitride field. Neugebauer and Van de Walle have made a comparison of possible acceptor impurity candidates (Li, Na, K, Be, Zn, Mg, Ca) in GaN using first-principles total-energy calculations. They have found that Mg substitute on the Ga site is superior compared to the other candidates considering solubility and stability against compensation by interstitials [143].

In this section, I will first briefly review the state of art literature in the growth of Mg doped GaN epilayers as well as NWs. Then I will present our investigations on the PA-MBE growth of Mg doped GaN NWs through adjusting different parameters (Mg cell temperature, substrate temperature, surface stoichiometry). At last, I will extend the study to the growth of axial GaN p-n junction NWs.

3.1.1 State of art literature

Mg doped GaN 2D layer One of the most important breakthroughs in the field is the discovery of Mg acceptor doping activation by post-growth process in the case of hydrogen involved growth techniques at the beginning of the 90s. This post-growth process can be either low-energy electron-beam irradiation [3] or annealing in a hydrogen free ambient [2]. This discovery has enabled p-type conductivity for the development of the first blue LEDs [4] and later on the first LDs [5]. Since then, tremendous efforts have been made to improve hole concentrations in order to reduce series resistance and achieve better ohmic contacts on p-type.

The state of art MOVPE grown Mg-doped GaN epilayers exhibit a hole concentration of 3×10^{18} cm^{-3}, a hole mobility of 9 cm^{2}.V^{-1}.s^{-1}, and a resistivity of 0.2 Ω.cm, after post-growth dopant activation [144]. Compared to MOVPE, MBE is an interesting alternative growth technique. Due to the UHV (free of hydrogen) growth environment, the Mg dopants are electrically active in as-grown MBE samples, meaning that no post-grown activation is required. Moreover, the MBE samples are grown at a lower substrate temperature, the "Mg memory" effect is less severe in MBE growth, leading to sharp doping profiles [145]. It was reported that the compensation effects are lower in MBE material, since the presence of hydrogen could mediate the formation energy of nitrogen vacancy (V_N) in MOVPE material [146] and there is less Si diffusion from the substrate in the MBE system.

Table 3.1 shows the electrical characteristics for the current state of art Mg-doped GaN epilayers grown by different techniques. One of the best Mg doped GaN epilayers grown by PA-MBE presents a Mg incorporation up to 7.5×10^{19} cm^{-3}, a hole concentration of 1.4×10^{18} cm^{-3}, and a mobility of 7.5 cm^{2}.V^{-1}.s^{-1} under slightly nitrogen-rich growth condition [145]. Epilayers with similar electrical characteristics have also been reported using NH_3-MBE growth technique [147][148][149]. Novel variants of PA-MBE, such as metal modulated epitaxy (the metal sources are periodically modulated, when the nitrogen flux remains constant), and phase shift epitaxy (desynchronization of host material growth process from dopant incorporation), have been demonstrated to produce GaN epilayers with Mg doping up to 1.45×10^{20} cm^{-3}, and a hole concentration on the order of 10^{18} cm^{-3} [150]–[154].

Table 3.1 Electrical characteristics of the state-of-the-art Mg-doped GaN epilayers grown by different techniques

Growth techniques	**MOVPE**	**NH_3-MBE**	**PA-MBE**	**Metal modulated epitaxy**	**Phase shift epitaxy**
Substrate temperature (°C)	1030	740	650	500	600
Mg content (cm^{-3})	Not mentioned	3×10^{19}	7.5×10^{19}	Not mentioned	1.45×10^{20}
Hole concentration (cm^{-3})	3×10^{18}	1×10^{18}	1.4×10^{18}	4.5×10^{18}	1×10^{18}
Mobility (cm^{2}.V^{-1}.s^{-1})	9	9	7.5	1.1	7.8
Resistivity (Ω.cm)	0.2	0.75	0.6	1.3	0.8
Reference	[144]	[147]	[145]	[150]	[154]

p-type GaN with high hole concentration remains desirable for lower series resistance and ohmic contacts, however, it is challenging due to the complexity of doping GaN with Mg.

The incorporation of Mg is limited by the solubility of Mg in GaN under specific growth conditions. Mg is a volatile species and evaporates at ~250 °C [155]. Incorporating Mg into an epitaxially growing film in the PA-MBE system depends not only on Mg atomic flux, but also on surface stoichiometry (or III-V ratio) and the substrate temperature (see Figure 3.3 (b)). In addition, it has been reported that Mg doping is sensitive to the surface polarity of the epilayer. Higher Mg incorporation has been found in Ga-polar epilayer, and Mg induced surface polarity inversion has been observed under high Mg atomic flux [156], [157]. Moreover, it has been reported that Mg tends to accumulate at the surface [157], [158].

Not all the Mg dopants are electrically active, in fact, the doping efficiency of Mg in GaN is usually <10% at room temperature, and Mg is notorious for its high activation energy (around 245±25 meV [159]) in GaN. When incorporated in GaN, Mg atom can possess different positions, including substituting for N (Mg_N), substituting for Ga (Mg_{Ga}), and interstitial site (Mg_i), and only Mg_{Ga} behaves as an acceptor. First-principles calculations have shown that Mg prefers the substitutional Ga site, since the formation energy of Mg_N, Mg_i is higher (see Figure 3.3 (a)) [122]. Moreover, both hydrogen (H^+) and nitrogen vacancy (V_N^{3+} and V_N^+) have a low formation energy in p-type materials, and they can act as compensating centers.

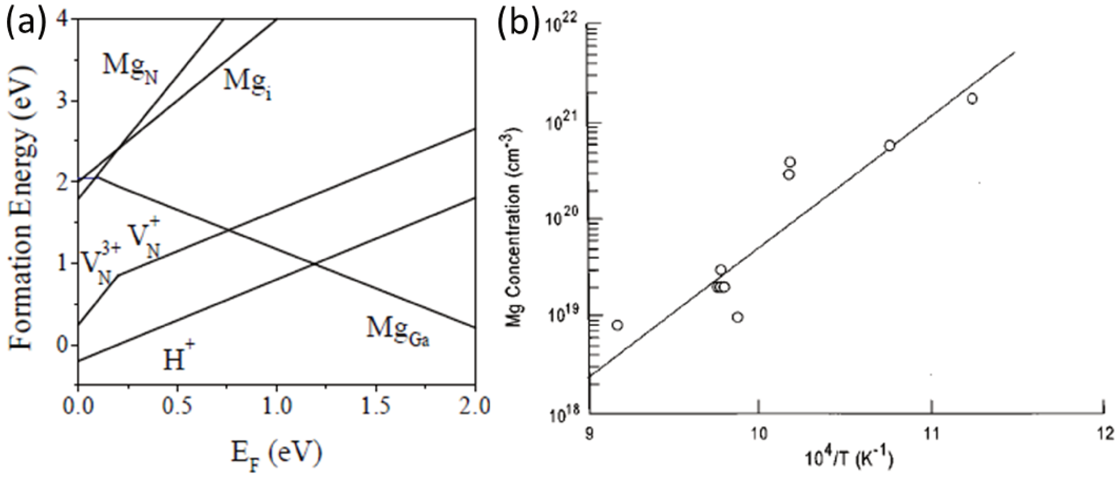

Figure 3.3 (a) Formation energy versus Fermi level (E_F) for different defect or impurity levels in Mg doped GaN (including Ga-substitutional Mg, N-substitutional Mg, interstitial Mg, N vacancy, and interstitial H), assuming Ga-rich conditions [122]. (b) Mg concentrations as a function of the reciprocal growth temperature for GaN epilayers grown in the PA-MBE system [155].

Mg doped GaN NWs In the case of NWs, the Mg-doped GaN NWs were firstly reported by Lieber's group in 2003 [160]. These NWs were fabricated by nickel-catalyzed chemical vapor deposition (CVD), and have shown p-type behavior in back gate FET measurements [160]. Three years later, the Mg-doped GaN NWs grown by PA-MBE were presented [161], however, no growth investigation or electrical properties were mentioned.

Furtmayr et al. have investigated the growth of Mg-doped GaN on Si (111) by PA-MBE at different Mg fluxes, and an increased radial growth rate (see Figure 3.4 (b)) and a decreased nucleation time have been observed upon Mg doping [41]. Further explorations on the samples reveal an Mg incorporation of 4×10^{20} cm^{-3} under the highest Mg cell temperature (see Figure 3.4 (a)), and the presence of stacking faults at Mg cell temperature above 260 °C (corresponding to Mg concentration around 4×10^{19} cm^{-3}), which cause the inclusions of cubic GaN in the WZ lattice [162].

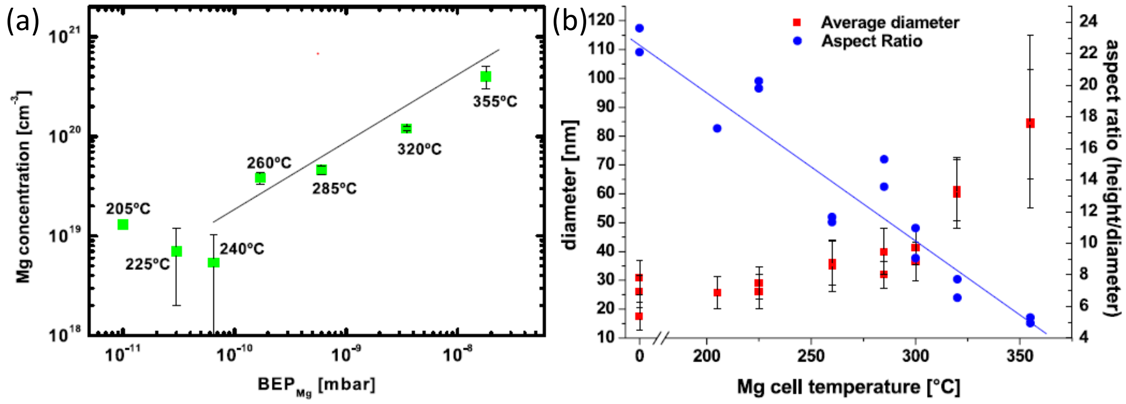

Figure 3.4 Mg concentration in GaN NW and NW morphology evolvement versus Mg cell temperature [162]. (a) Mg concentration in GaN NWs (from SIMS measurements) as a function of Mg beam equivalent pressure. The Mg cell temperature is noted near the corresponding data point, and the substrate temperature is 790 °C for the all the samples. (b) Average NW diameter and aspect ratio (height / diameter) as a function of Mg cell temperature.

Later on, Limbach et al. have studied the influence of substrate temperature (665-785 °C) on the morphological and optical properties of lowly Mg-doped GaN NWs grown by PA-MBE [136]. The range of 725-785 °C has been identified as a suitable temperature window for producing cylindrical NWs. In addition, the NW nucleation occurs faster, and the coalescence tendency increases under the supply of Mg [42], [136], [163].

Recently, Mi’s group has reported Raman scattering measurements on Mg-doped GaN NWs grown at a substrate temperature of 780 °C in the PA-MBE system. Local vibrational modes at 655 cm^{-1} and a few modes around 2200 cm^{-1} have been observed at high Mg doping in the NWs [164]. These NWs have shown interesting potential applications in overall water splitting [165], [166]. Moreover, Mg doped GaN NWs grown on diamond substrate by PA-MBE have been reported, and Mg content up to 1×10^{20} cm^{-3} has been demonstrated by SIMS measurements [95].

However, it is difficult to compare between different publications due to difference in the growth method, uncertainty of temperature determination in PA-MBE, and differences in the way Mg content is specified. We can conclude that Mg doping in GaN is complicated by many factors, including surfactant effect, polarity sensitivity, high vapor pressure of Mg, compensation centers, dependence on surface stoichiometry and substrate temperature, etc. As a result, the growth window for producing electrically active p-type GaN is quite narrow. Here, I will present the exploration of the growth of Mg doped GaN NWs in PA-MBE system through the variation of two main parameters: Mg cell temperature and substrate temperature. Based on the growth knowledge of n-type and p-type GaN NWs, the growth and optical properties of axial GaN p-n junction NWs is also investigated.

3.1.2 Growth of p-type GaN NWs

Mg cell temperature Although the influence of Mg flux on GaN NWs grown by PA-MBE has already been reported [41], [76], it is important and necessary to conduct similar experiments in our system in order to get on the right track for the investigation of Mg doping incorporation in GaN NWs.

A series of samples has been grown at the same growth conditions except the variation of the Mg cell temperature from 190 °C to 270 °C (see Table 3.2). The substrate temperature has been calibrated as 5 s for Ga desorption (thermocouple-displayed temperature at 885 °C, and effective temperature around 835 °C) and kept the same during the growth. The nucleation occurs directly on Si substrate without any buffer layer, in order to obtain low density NWs. The nominal Ga/N flux is 1/3 and the same for all the samples in this series. The growth time was 6 hours for all the samples. Sample N2437 is NID GaN NWs and serves as a reference. For the other samples, Mg doping is achieved by exposing GaN NWs to the Mg flux, starting from the nucleation till the end of the growth.

Table 3.2 The list of samples studied with different Mg cell temperatures

Sample Name	**N2437**	**N2442**	**N2439**	**N2441**	**N2446**	**N2443**	**N2444**
Mg cell temperature (°C)	95	190	210	230	240	250	270
Average NW radius (nm)	26.7	28.9	27.6	26.1	31.6	50.6	66.9
Average NW length (nm)	419	482	521	315	409	239	394

Figure 3.5 shows the top and side view SEM images taken from as-grown samples at the center of the wafer. The NID GaN NWs (sample N2437) have a typical length of 400-550 nm and a radius of 20-30 nm. The NWs are less straight and there is a spread in

the in-plane NW orientations because of the nucleation on bare silicon. We can observe a tendency of NW widening with increasing Mg cell temperature, as reported previously [41]. In addition, a certain degree of NW coalescence has been noticed at high Mg cell temperature, without any change of crystal symmetry as found in the case of Si doping. A quantitative summary of the morphology variations is illustrated in Figure 3.6. At low Mg cell temperature, the influence of Mg doping on the morphology of the NWs is not so evident. Starting from Mg cell temperature of 230 °C, the radius of the NWs is gradually increased and their length is decreased with increasing Mg cell temperature.

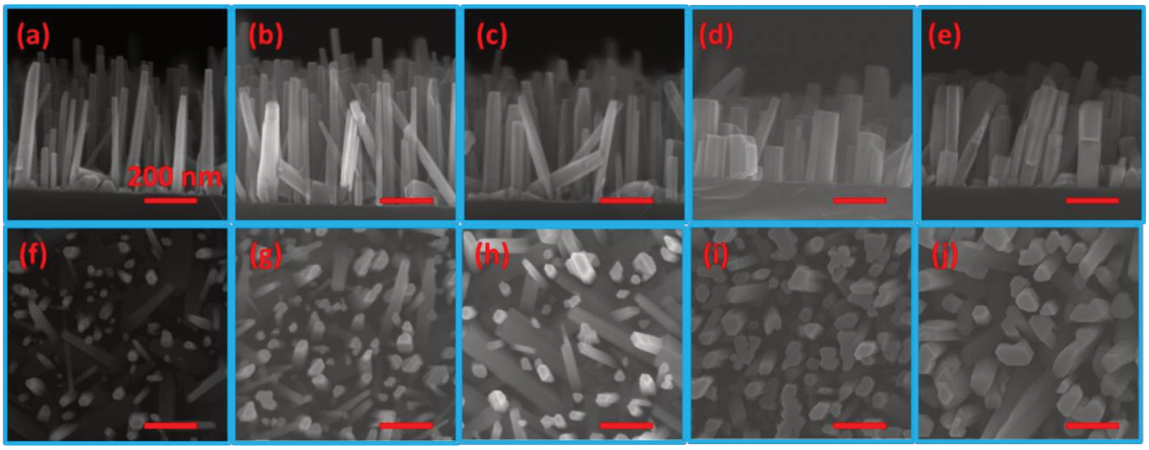

Figure 3.5 Morphology variations of Mg doped GaN NWs. Side view (a) and top view (f) SEM images of NID GaN NWs from sample N2437. Side view (b, c, d, e) and top view (g, h, i, j) SEM images of Mg doped GaN NWs from sample N2442, N2446, N2443 and N2444, respectively. The scale bar is 200 nm and the same for the all images.

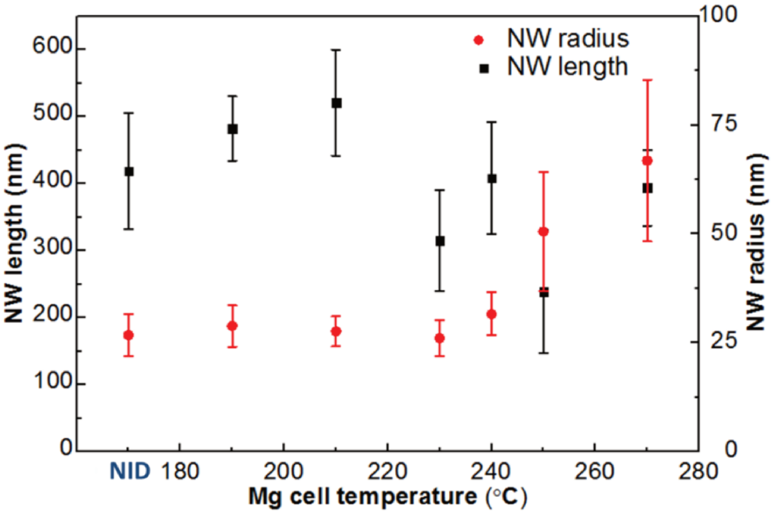

Figure 3.6 NW length (data points in back, left y-axis) and radius (data points in red, right y-axis) as a function of Mg cell temperature.

PL emission can reveal some insights of the material properties and defect formation in Mg-doped GaN. Figure 3.7 exhibits the low temperature (5 K) PL spectra of this series of Mg- doped GaN NWs. The spectrum of NID sample (N2437) is represented at the bottom. It contains a high intensity near band edge emission, and a low intensity DAP emission at 3.26 eV with two LO phonon replicas. The near band edge emission is dominated by donor bound exciton peak at 3.479 eV with a FWHM of 28 meV, which is a result of sample growth one week after the opening maintenance of MBE machine.

When Mg is introduced, the luminescence intensity of the NWs is reduced compared to that of NID NWs. For low Mg cell temperature, the intensity of the DAP emission increases while the near band edge gradually vanishes (sample N2442 & N2439). Moreover, broad emission bands at lower energies (with a maximum intensity at around 2.9 eV) start to be dominant for moderate Mg doping (sample N2441 & N2446). Similar transition has already been observed for Mg doped GaN epilayers (for example: Figure 3.8 (a)) [69], [167]. For the highest Mg cell temperature at 270 °C, broad emissions with two maxima at 3.45 eV and 3.29 eV have been observed. The peak at 3.45 eV is possibly correlated with Mg induced inversion domains [67], [69], whereas the one at 3.29 eV is probably the DAP emission. The ratio of the maximum intensities of DAP emission to the near band edge emission is plotted as a function of the Mg cell temperature in Figure 3.8 (b). This ratio increases with increasing Mg cell temperature up to 210 °C, then decreases when further rising Mg cell temperature. It suggests Mg incorporation is effective in the Mg cell temperature of 190 °C to 240 °C. The assignment of different PL peaks is out of the scope of this thesis and would require more delicate experiments, such as temperature-dependent PL, or time-resolved PL etc.

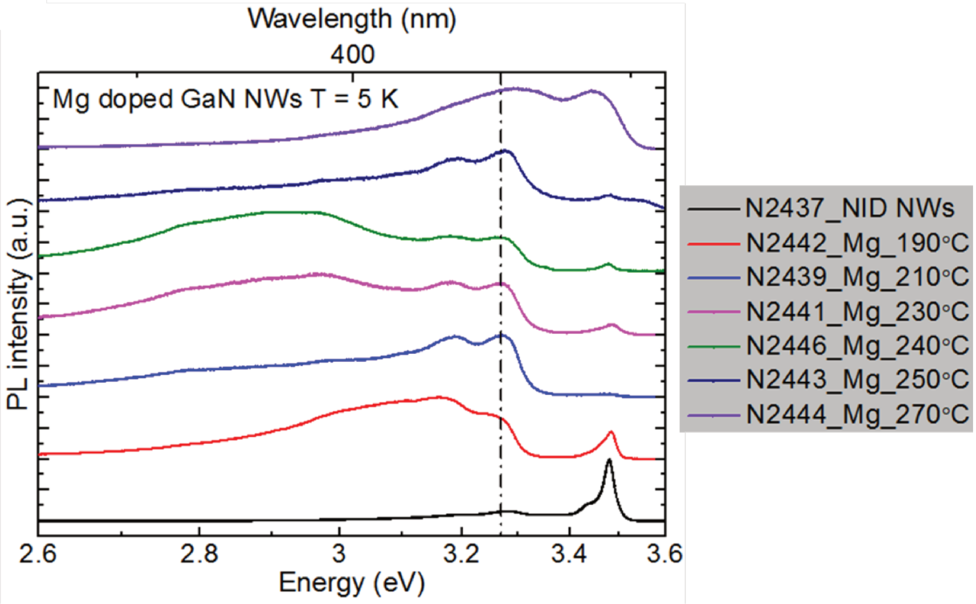

Figure 3.7 PL spectra of as-grown Mg doped GaN NWs series. The spectrum of NID samples (N2437) is shown at the bottom as a reference, whereas the Mg cell temperature is increasing gradually from the bottom to the top for different samples. All the spectra have been collected at 5 K. The PL intensity is in linear scale and shifted vertically for clarity. The black dashed line feathers the DAP peak at 3.26 eV.

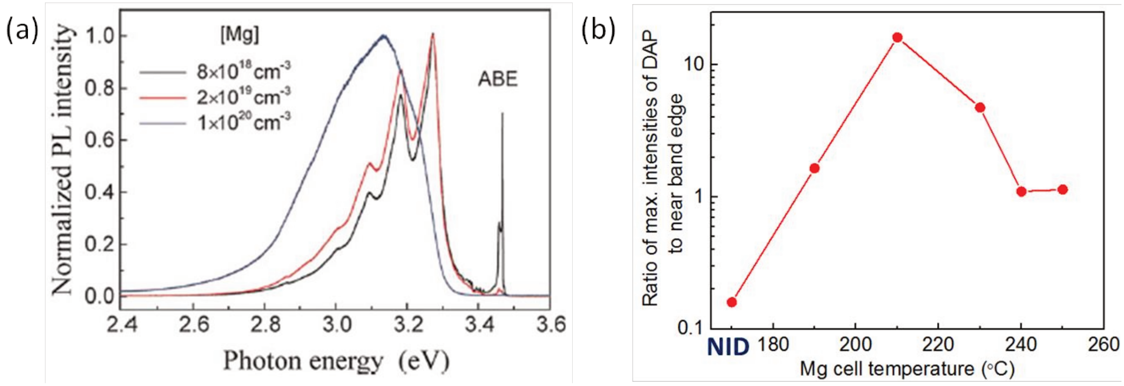

Figure 3.8 (a) Low temperature PL (2K) spectra of GaN epilayers with different Mg doping level, taken from [167]. (b) The ratio of max. intensities of DAP emission to near band edge emission as a function of Mg cell temperature.

Growth temperature As mentioned before, Mg is a volatile species and Mg incorporation in the GaN is strongly related with the growth temperature [155]. From Figure 3.3 (b), we can see that the Mg incorporation in epilayers is increased, as the growth temperature is decreased in the temperature range of 560 °C to 838 °C. However, this is not compatible with the relative high growth temperature of GaN NWs (generally from 730 °C to 875 °C [56], [168]). Therefore, a compromised growth temperature is needed for improving Mg incorporation in GaN NWs.

Nevertheless, the situation is complicated in the case of NWs. The morphology and the crystal quality of the NWs are closely related with the substrate temperature. As shown in Figure 2.6 (b), when reducing the substrate temperature, the density of the NWs increases, until further coalescence [48], [58]. In addition, the optical and structural properties of the NWs degrade when the growth temperature decreases, especially below 800 °C. The presence of stacking faults has been reported for NWs grown at low substrate temperature [169].

Therefore, we propose a two-step growth method for improving Mg incorporation. It means growing Mg doped GaN NWs on the base of NID (or Si-doped) GaN NWs. Suitable NW growth conditions (such as high substrate temperature) are employed for the NID (or Si-doped) GaN NWs base, whereas favorable Mg incorporation growth conditions (such as lower substrate temperature) can be applied during the growth of Mg doped GaN NWs.

In addition, Mg incorporation is closely linked with surface stoichiometry. Under nitrogen-rich condition, Mg can easily incorporate into available Ga substitutional sites, forming Mg_{Ga}, which behaves as an acceptor. In the case of PA-MBE grown GaN NWs, nominal nitrogen-rich condition (Ga/N flux ratio < 1) is commonly applied. It has been recently demonstrated that the diameter of GaN NWs grown by PA-MBE is self-regulated so that the effective Ga/N flux ratio is close to the stoichiometric value in steady-state growth conditions [57]. Therefore, a slight reduced Ga flux is used during the Mg incorporation, so that the growth surface remains nitrogen-rich.

3.1.3 Growth of axial GaN p-n junction NWs

Following the aforementioned two-step growth method, three GaN p-n junction NW samples have been grown. Table 3.3 lists the detailed growth conditions for each sample. Both the thermocouple displayed temperature and the Ga desorption time have been noted for the substrate temperature during the growth of Si-doped GaN base (see substrate temperature calibration in 2.1.2.2 for more details). Sample N1913 was grown by a previous colleague, and the presence of p-n junction in this sample has been observed by KPFM recently [139]. Sample N2490 and N2495 were grown during my thesis in consecutive days. Although the thermocouple displayed temperature of Si-doped GaN base for N1913 is different from those for N2490 and N2495, the real growth temperature should be similar according to the Ga desorption time. All the three samples were grown under nominal nitrogen-rich conditions (Ga/N flux ratio ~ 1/3). The Ga flux was kept the same for N1913, whereas the Ga cell temperature was decreased by 5 °C starting from Mg-doped part for the other two samples.

Table 3.3 Growth conditions of three GaN p-n junction samples

Sample Name		**N1913**	**N2490**	**N2495**
Si-doped GaN base	Substrate temperature (°C) (Ga desorption time(s))	860 (3.9 s)	888(~3.5 s)	890 (~3.5 s)
	Si cell temperature (°C)	875	900	900
	Growth time (h)	11	5.5	7
Mg-doped GaN top	Substrate temperature (°C)	775	873	840
	Mg cell temperature (°C)	220	240	240
	Growth time (h)	6	15.5	12.5

Figure 3.9 shows the top and side view SEM images of these samples. For sample N1913, the NWs have a typical length of around 2 μm, with a relative large length dispersion. The top surface of the NWs is flat with a radius around 95-130 nm. The NW widening on the upper part is probably a result of Mg incorporation. For N2490, two types of NWs seem to be present. One type of NWs exhibit a NW widening on the upper part with a length of around 1.6-1.8 μm, while the other type is thin along the NW with a length above 2 μm. For N2495, the NWs have a length of around 2.1 μm with obvious enlargement at the top (NW top radius above 150 nm). A certain degree of NW coalescence is observed from this sample.

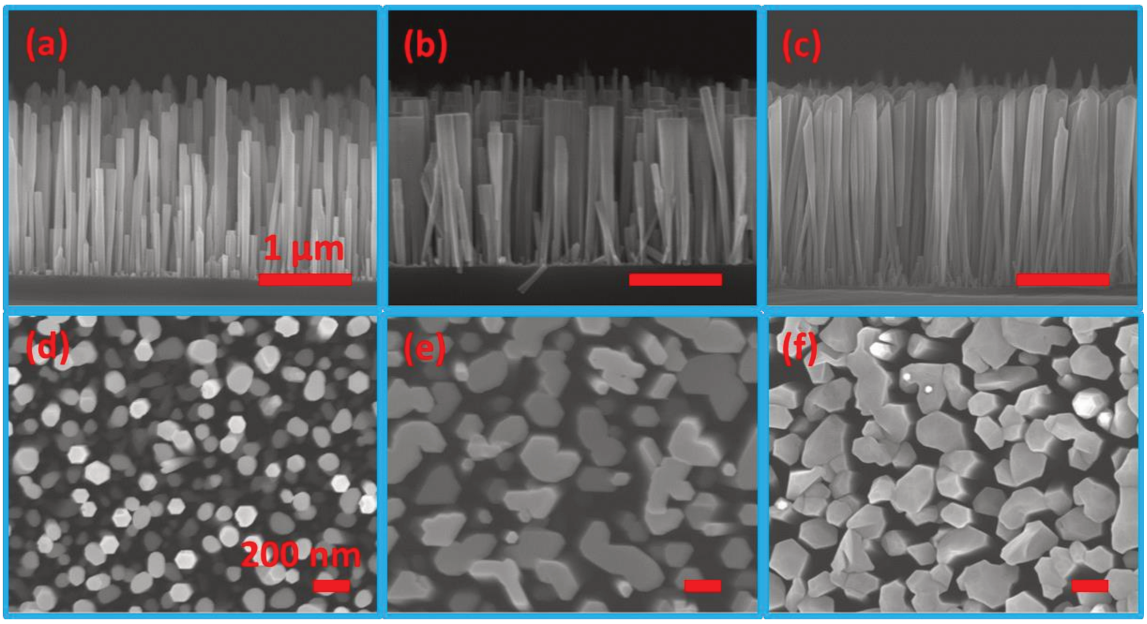

Figure 3.9 Side view (a, b, c) and top view (d, e, f) SEM images of GaN p-n junction NWs from sample N1913, N2490, and N2495, respectively. The scale bar is 1 µm for the first row images, and 200 nm for the second row images.

Low temperature PL measurements have also been performed on the as-grown GaN p-n junction samples. From Figure 3.10, the spectra of all the three samples contain a high intensity DAP emission, and a low intensity near band edge emission. The near band edge emission is dominated by donor bound exciton peak at 3.474 eV with a small shoulder at low energy side. For N2490, another peak at 3.466 eV is resolved in the spectrum, which is commonly attributed to Mg-related acceptor bound exciton [170]. DAP emission includes a peak around 3.25-3.27 eV and one LO phonon replica around 3.17-2.18 eV. N1913 manifests another broad peak around 2.7-2.8 eV, which was reported in the PL spectra of Mg-doped GaN epilayers before [69].

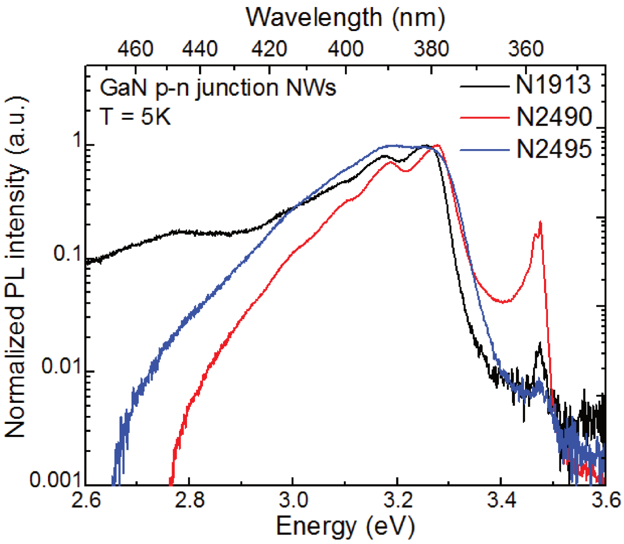

Figure 3.10 Normalized PL spectra of as-grown GaN p-n junction NW samples.

3.2 Electrical transport properties

As discussed at the beginning of this chapter, the electrical transport properties of Mg-doped or p-n junction GaN NWs are scarcely investigated in the literature. In this thesis, I probed the electrical transport properties of these nanostructures with the help of electron beam based methods, such as EBIC and VC on secondary electron images. Both methods require the fabrication of electrical contacts on the nanostructures, which brings us to the challenging situation on p-type GaN NW contact.

3.2.1 Ohmic contacts on p-type GaN NWs

Ohmic contacts on the n-type GaN and p-type GaN hold significant importance for GaN based devices, such as LEDs, lasers, and photodetectors. After decades of research efforts, ohmic contacts on n-type GaN using Ti / Al based metallization schemes can achieve contact resistivities as low as 10^{-6} Ω.cm^2, whereas the start of art p-type contact using Ni / Au can generally achieve a contact resistivity in the range of 10^{-1}-10^{-3} Ω.cm^2 [171].

The main difficulties for the formation of ohmic contacts on p-type GaN epilayer are:

- The unavailability of metals with large enough work function. Since GaN is a wide bandgap semiconductor with $E_g \approx 3.4$ eV, and the electron affinity in GaN is 4.1 eV, a metal with work function of 7.5 eV is needed for a good ohmic contact on p-type. However, most of the metal work functions are below 5.5 eV.
- The low doping concentrations achievable in p-type GaN. As seen from Table 3.1, the state of art hole concentration of the p-type GaN epilayer induced by Mg doping is limited to a value less than mid 10^{18} cm^{-3}.

Despite these challenges, ohmic contact on p-type GaN NW is even more complicated due to the nanoscale dimensions and wire geometry. Furthermore, in our case, it is even trickier since the hole concentrations in NWs are unknown. Therefore, it is a difficult and time-consuming task to fully investigate the contact mechanism for p-type NW ohmic contacts.

In this session, I will first briefly review the theoretical background of metal-semiconductor contact formation and the state of art literatures on ohmic contact on p-type GaN epilayer. Then, I will present our results on attempting to achieve ohmic contact on Mg doped GaN NWs, as well as GaN p-n junction NWs.

3.2.1.1 Theoretical background

Figure 3.11 illustrates the formation of a Schottky barrier when a metal and a p-type semiconductor are brought into contact. The metal work function is less than that of the p-type semiconductor, which is generally the case for p-type GaN. In (a), the metal and the semiconductor are both electrically neutral and isolated from each other. ϕ_{m}, χ_s, E_g represent the work function of the metal, the electron affinity of the isolated semiconductor, and the band gap of the semiconductor, respectively.[‡‡‡] When the metal and the semiconductor are connected, electrons flow from the metal into the empty states in the valence band of the semiconductor, which can be understood as holes transfer from the semiconductor to the metal. At equilibrium in (b), the Fermi levels are aligned at each side of the contact. There is a downward band bending related with a hole depleted region on the semiconductor side and an abrupt barrier in the metal side. At the contact, a potential barrier $V_{b,p}$ can hinder the holes diffusing towards the metal, and a Schottky barrier $\phi_{b,p}$ inhibits carrier injection from the metal to the semiconductor [172].

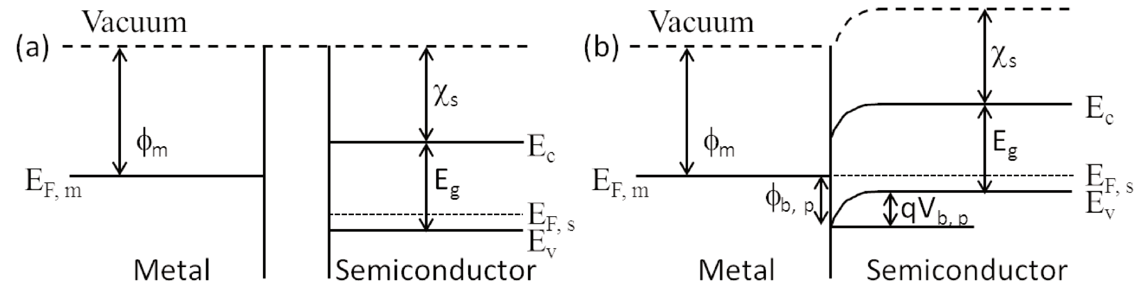

Figure 3.11 Energy diagram of a metal and a p-type semiconductor (such as p-type GaN). (a) Before contact, the metal and the p-type semiconductor are isolated. (b) After contact, with charge equilibrium, a Schottky barrier $\phi_{b,p}$ is formed.

This Schottky barrier can be calculated using the following equation:

$$\phi_{b,p} = (\chi_s + E_g) - \phi_m \qquad \textbf{(3.1)}$$

Under zero bias and for lowly doped semiconductor, $V_{b,p}$ can be approximated as $qV_{b,p} \approx \phi_{b,p} - E_a$, where E_a is the acceptor ionization energy. Moreover, $V_{b,p}$ can be either decreased or increased under forward or reverse bias.

In experiment, it is mainly found that the Schottky barrier is less sensitive to the work function of the metal due to Fermi level pinning at the semiconductor surface. Bardeen proposed surface states (dangling bonds, surface defects, etc.) at the junction could be

---

[‡‡‡] Electron affinity χ_s is defined as the energy obtained by moving an electron from the vacuum just outside the semiconductor to the bottom of the conduction band just inside the semiconductor; the work function ϕ_m is the minimum energy needed to remove an electron from a solid to a point in the vacuum immediately outside the solid surface.

the origin of this pinning. These surface states commonly have a narrow distribution of energies within the bandgap of the semiconductor surface, and they are characterized by a "neutral level" ϕ_0. In this case, the Schottky barrier between a metal and a p-type semiconductor can be expressed by equation (3.2), where γ is a function of the density of the surface states [172].

$$\phi_{b,p} = \gamma\left(\chi_s + E_g - \phi_m\right) + (1-\gamma)\phi_0 \tag{3.2}$$

When there are no surface states, $\gamma = 1$, equation (3.2) becomes the ideal Schottky contact situation in equation (3.1). On the other hand, when the density of the surface states are very high, γ is close to 0, the surface states become the main determinant of the Schottky barrier, instead of the metal work function.

Ohmic contact is generally feathered by a linear I-V relationship through the contact with low contact resistance (about 10^{-6} Ω.cm^2). In the particular case of p-type GaN, studies have shown that the Fermi level at GaN surfaces may not be fully pinned [173], [174], thus the Schottky barrier height is weakly dependent on the metal work function. Metals with a large work function (such as Ni, Au, Pd and Pt) are preferred for creating low barrier contacts on p-GaN. Moreover, different approaches can be applied to improve current injection through the Schottky barrier, creating ohmic contacts in the broad sense. These approaches include annealing the junction in order to damage the semiconductor near the contact region, which could create gap states for conduction, or increasing the doping level near the semiconductor surface as high as possible so that the depletion layer is sufficiently narrow, allowing an enhancement of tunneling assisted transport.

3.2.1.2 State of art literature

In the past two decades, many efforts have been made in achieving p-type ohmic contact with specific contact resistance less than 10^{-4} Ω.cm^2. Different metal schemes, surface preparation methods as well as annealing conditions have been employed to reduce the specific contact resistance of the p-type contact [175]. The characteristics of some of the state of the art p-type ohmic contacts are listed in Table 3.4. The hole concentration of the epilayer (p) is at the level of 10^{17} cm^{-3} in these references.

The Ni/Au metallization is one of the most thoroughly studied p-type contacts. It is generally proposed that the formation of NiO when annealing Ni/Au contact in air or oxygen, is crucial for reducing the contact resistance. Ho et al. reported that contact resistance as low as 10^{-6} Ω.cm^2 can be achieved by annealing Ni (5 nm)/Au (5 nm) contact in air at 500 °C [176]. Upon annealing, Ni can diffuse out through the Au layer and reacts with oxygen in the atmosphere. Thus, the Ni/Au films become a mixture of crystalline NiO, Au particles, and amorphous Ni-Ga-O phases (see Figure 3.12). NiO is a p-type semiconductor, and its direct contact with p-type GaN is probably responsible for the ohmic behavior. Another group has found that ohmic Ni/Au contact can be achieved by first the preoxidation of the GaN surface, inducing more Ga vacancies, and then the removal of the oxides using $(NH4)_2S_x$ solution [177].

Other types of metal combinations have been explored to create ohmic contact on p-type GaN. Both Pd/Ni and Pd/Ni/Au contacts have been reported to form Pd gallides, Ga_2Pd_5 and Ga_5Pd phases upon annealing. This reaction can generate more Ga vacancies below the contact, which help to reduce the contact resistance [178], [179]. Another high work function metal Pt (5.12-5.93 eV) has also been used to obtain ohmic contact. A two-step surface treatment has been reported to achieve ohmic Pt contact with specific contact resistance of 2×10^{-5} Ω.cm^2 [180].

Moreover, due to the strain-induced piezoelectric field and the large valence band discontinuity between GaN and InGaN, InGaN/GaN superlattices could achieve hole concentration as high as 1×10^{19} cm^{-3} [181]. Therefore, a highly Mg-doped InGaN layer can be used as a contact layer for creating ohmic contact on p-type GaN. A 2 nm thick $In_{0.19}Ga_{0.81}N$ layer between Pt/Au contact and p-type GaN has been reported to obtain a specific contact resistance of 10^{-6} Ω.cm^2 [182].

Table 3.4 Characteristics of ohmic contacts with different metal schemes on p-type GaN epilayer

Contact metals and thickness (nm)	**p (cm^{-3})**	**Surface treatment**	**Annealing condition**	**ρ_c (Ω.cm^2)**	**Reference**
Ni/Au (5/5)	2×10^{17}	HCl solution for 1 min	500°C 1 min in air	4×10^{-6}	[183]
Ni/Au (20/100)	3.4×10^{17}	First preoxidation at 750°C for 30 min in air, then treated with $(NH_4)_2S_x$ solution at 60 °C for 30 min	500°C 10 min in air	4.5×10^{-6}	[177]
Pd/Ni (3/7)	3.3×10^{17}	Dip into boiling aqua regia solution (HCl: HNO_3 = 3:1)	500°C 1 min in air	5.7×10^{-5}	[178]
Pd/Ni/Au (10/20/30)	2×10^{17}	Dip in buffered hydrofluoric acid	500°C 1 min in N_2	2.4×10^{-5}	[179]
Pt (25)	1.8×10^{17}	First boiled BOE for 10 min and $(NH_4)_2S_x$ solution for 10 min, then BOE for 30 s.	No	2×10^{-5}	[180]
$In_{0.19}Ga_{0.81}N$/Pd/Au (2/20/130)	4×10^{17}	Dip in HCl solution	No	1.1×10^{-6}	[182]

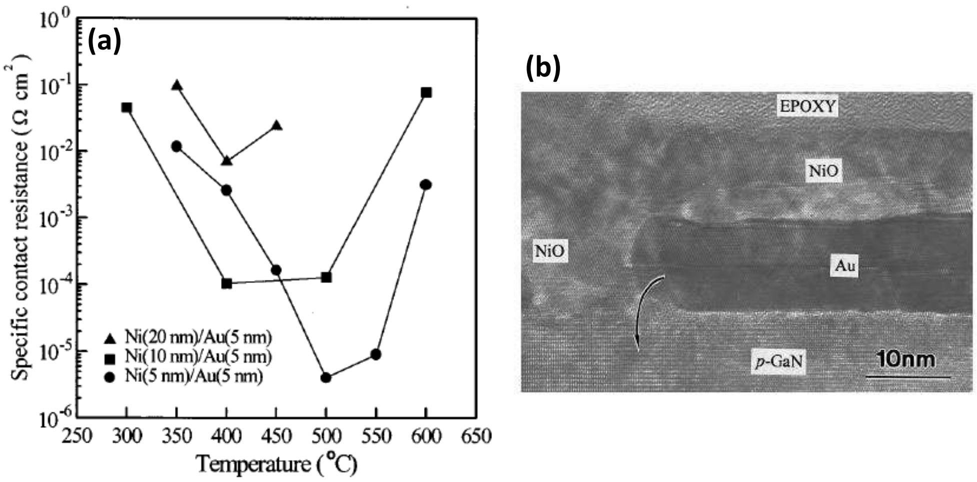

Figure 3.12 (a) Specific contact resistance of Ni/Au contacts to p-GaN as a function of annealing temperature for different metal thickness. (b) TEM image showing the cross-section microstructure of the Ni / Au contact after annealing at 500 °C in air for 1 min [183].

Although these results are promising, the reaction at the p-GaN / contact interface seems to be crucial to reduce the contact resistance; however, the mechanism of the ohmic contact formation is far from being understood. In reality, this ohmic contact formation strongly depends on many factors, such as the doping level and the surface properties of the p-type GaN [175], the contact scheme [183], and the annealing conditions (temperature, ambient, etc.) [184]. Therefore, it is difficult to establish a reproducible p-type ohmic contact recipe.

Besides these metals, indium tin oxide (ITO) is an interesting alternative contact material. In fact, ITO is one of the most widely used transparent contact materials in devices, such as solar cell, liquid crystal displays and photodetectors. A direct contact of ITO on p-type GaN is non-ohmic [185], nevertheless, the combinations of ITO with other materials, such as Ni [186], Zn-Ni [187], and p-InGaN [188], have shown ohmic contact behaviors. In fact, the as-deposited ITO films behave as an insulator, and become conducting upon annealing with a wide direct optical band gap of 3.6 eV [189]. The electrical and optical properties of the ITO film are a strong function of many parameters, including deposition conditions and annealing conditions [190]. In addition, Musolino et al. have reported an improved p-type GaN top contact in GaN NW based LEDs with 120 nm-thick ITO compared to the common Ni (5 nm)/Au (5 nm) contact scheme [191].

3.2.1.3 Contacts on Mg doped GaN NWs

Ni/Au metallization As one of the most commonly used p-type ohmic contacts, Ni/Au metallization scheme was firstly explored on Mg doped GaN NWs.

Ideally, GaN NWs with the highest doping level should be used to investigate the ohmic contact conditions. Unfortunately, in the case of Mg doped GaN NWs, both the hole concentration and the Mg doping level are difficult to access. SEM-EDX measurements have been performed on several Mg doped GaN NW samples with a length of 3 μm. Sample N2092 has shown a Mg concentration of $(3.35\pm0.37)\times10^{19}$ cm^{-3}, while the Mg level in the other samples is below the detection limit of the SEM-EDX, which is around 10^{19} cm^{-3}. The hole concentration in N2092 is therefore estimated to be 1×10^{18} cm^{-3}, assuming similar acceptor ionization energy (245 meV) compared to Mg doped GaN epilayers grown by MBE [159].

The growth conditions of N2092 are briefly described in the following for further reference. Sample N2092 has been grown at a substrate temperature around 830 °C (Ga desorption of 5.6 s), with a 3 nm thick AlN buffer. The growth was started by GaN NW nucleation for 20 minutes and followed by Mg doped part for 20 hours. The nominal Ga/N flux was 1/3 and the same for both the nucleation and the Mg doped part. The Mg cell temperature was kept at 210 °C during the growth.

Numerous NWs taken from N2092 have been dispersed on Si substrates covered with 500 nm thick insulating thermal oxide and eventually contacted by conventional EBL or laser lithography for testing different surface treatments and contacting schemes. As stated before, the metal deposition is realized by an electron beam evaporator (Plassys company). For contact deposition on Mg doped NWs, the base pressure in the chamber is lower than 3×10^{-6} Torr, in order to eliminate contamination as much as possible. The total thickness of the metal contact is on the same level as the diameter of the Mg doped NW (around 80 nm for sample N2092), with the purpose of getting a continuous metal film covering the NW.

As listed in Table 3.5, for N2092_01, Ni/Au contact (30 nm and 50 nm, respectively) was deposited without any surface treatments. The devices were annealed up to 500 °C in air, and no electrical activities were observed from −1 V to +1 V using a Keithley sourcemeter (detection limit down to 1 nA), suggesting the presence of a very high resistance (more than 1 GΩ). These Ni/Au contacts seem to be quite rough and do not have a smooth interface with the NW from SEM observation, such as Figure 3.13 (a).

Surface condition plays an important role in p-type contact formation. A thin layer of surface oxides is possibly creating an insulating layer at the metal/NW interface, preventing the current flow. The same contact process was repeated with an extra dip in HCl solution (37%) for 30 s (N2092_02) and 1 min (N2092_03) before the metal deposition, aiming at removing possible oxides at the NW surface. Both N2092_02 and N2092_03 have shown improved I-V characteristics upon annealing until 500 °C in air. A non-linear, asymmetric I-V relation with around 10 nA under 1V has been observed for a few devices in both samples. However, it was not possible to use FET measurement on these devices in order to evaluate the doping level due to the large contact resistance (no current modulation observed).

Another recipe adopted from MOCVD microwires [192] has also been tested (N2092_04). A bilayer of Ni/Au (5 nm/5 nm) were deposited in the first lithography, following 1 min immersion in HCl to remove the native oxides. Then, the devices were annealed at 500 °C in air for 5 min in order to promote the formation of NiO. Afterwards, a second lithography was realized with the deposition of another bilayer Ni/Au (10 nm/200 nm). This recipe was reported to form a low resistance contact on GaN microwires [192]. However, for N2092_04, no improvement of electrical performance was observed compared to N2092_02 and N2092_03.

Table 3.5 Different contact conditions investigated on sample N2092

Sample Name	**Metalization scheme**	**Surface treatments**	**Annealing conditions**
N2092_01	Ni/Au (30 nm/50 nm)	None	500 °C in air for 5 min
N2092_02	Ni/Au (30 nm/50 nm)	HCl 30 s	500 °C in air for 5 min
N2092_03	Ni/Au (30 nm/50 nm)	HCl 1 min	500 °C in air for 5 min
N2092_04	Ni/Au (5 nm/5 nm) + annealing + Ni/Au (10 nm/200 nm)	HCl 1 min (1st litho) + RIE O_2 5 s (2rd litho)	500 °C in air for 5 min

Despite these unsuccessful attempts, another observation worth noticing is the morphology variation of the metal contact after annealing. As shown in Figure 3.13 (b), some dark areas start to appear when annealing Ni/Au contact at 300 °C for 5 min. More obviously, many dark spots are present on Ni/Au surface after annealing at 500 °C for 5 min in N2092_04 (Figure 3.13 c&d).

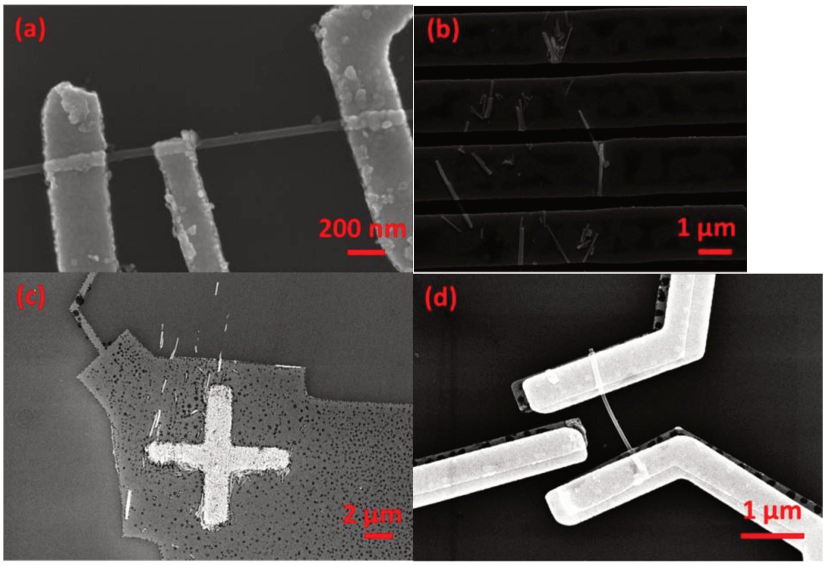

Figure 3.13 SEM images of Ni/Au contact on Mg doped GaN NWs. (a) One contacted NW from N2092_01 before annealing. (b) Ni/Au contact after annealing at 300 °C for 5 min. (c) Ni/Au contact on the SiO_2 substrate from N2092_04. (d) Ni/Au contact on the NW from N2092_04.

This phenomenon has also been observed by other researchers [193]. As cited in Figure 3.14, the Ni/Au contacting film is rather smooth and conformal before annealing, and it becomes rough and contains micro-cracks after annealing. A possible explanation is illustrated in Figure 3.14 (c). Upon annealing, Ni atoms diffuse through the Au layer to the surface, and react with O_2, forming NiO. The contact layer thus contains a Au-rich underlying layer with large voided areas and a NiO layer on top. These void areas (the dark feathers in the SEM images) are present at both the metal/SiO_2 and the metal/NW interfaces. They can cause severe cracking or delamination of the Ni/Au film from the SiO_2 substrate, as observed in the SEM images. Moreover, the size of the void regions is on the same order of magnitude to that of the NWs. The reduced contact areas due to these void regions are much more significant in the case of NWs compared to microwires or epilayers. Therefore, a very high contact resistance, with a non-ohmic behavior, has been observed on annealed Ni/Au contact to Mg-doped GaN NWs.

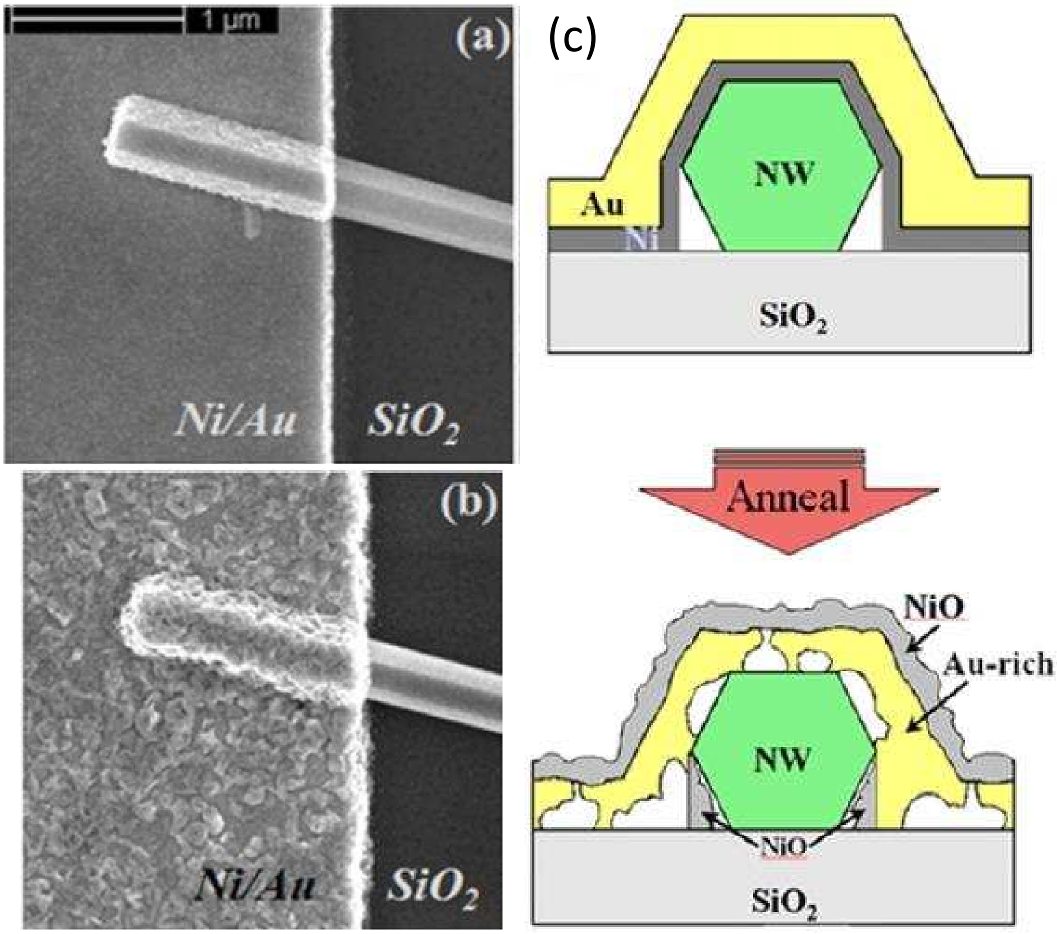

Figure 3.14 Microstructure evolution of Ni/Au contacts on GaN NWs upon annealing [193]. (a) As-deposited Ni/Au contact for a NW device on a SiO_2 substrate. (b) the same NW device after N_2/O_2 annealing. (c) Illustration of Ni/Au contact structure on a NW dispersed on SiO_2 before and after annealing in N_2/O_2 ambient.

Other metallization schemes: ITO As stated before, ITO is an interesting alternative contact material. There are many techniques to deposit ITO films, and the sputtering method is known for producing high quality and conformal ITO films. In this thesis, ITO films were deposited by striking the ITO target using argon plasma at room temperature, in a sputtering machine (DP850 "Alliance concept "company).

GaN p-n junction NWs from sample N1913 have been employed to experiment the ITO contact, since the presence of p-n junction in this sample has been witnessed by KPFM previously [139]. For the growth details of sample N1913, please refer to Table 3.3. The diameter of the NWs is around 70 nm at the bottom, and it increases gradually reaching up to 120 nm on the top because of Mg incorporation. Therefore, the thickness of the ITO films has been chosen to be 100 nm.

GaN p-n junction NWs have been dispersed on Si substrates covered with 500 nm thick insulating thermal oxide and patterned with two-probe contact by conventional EBL. O_2 plasma RIE process has been carried out for 5 s and a dip in HCl solution (37%) has been realized for 1 min precedent of the ITO sputtering.

The as-patterned devices did not show any electrical activities since the as-deposited ITO film is an insulator. Annealing was proceeded by putting the sample at different temperatures (250 °C, 300 °C, 350 °C, 400 °C, 450 °C, 500 °C, 550 °C gradually) in air for 10 min, and electrical measurements (I-V and EBIC) were conducted after annealing at each temperature. As expected, the ITO becomes more conductive with increasing annealing temperature, and interesting EBIC results have been obtained on two axial p-n junction NWs after annealing the devices at 550 °C. The details and comprehension of the EBIC characterization results will be discussed in the following sections.

Before switching to EBIC measurements, I would like to mention a side study on ITO electrical and morphological evolution under different annealing temperatures. ITO films were sputtered on $Si+SiO_2$ substrates. SEM observations and I-V measurements were carried out after annealing the films under different temperatures in air for 10 min. The as-deposited ITO films are smooth, and the morphology of the film does not vary much with increasing annealing temperature until 600 °C. As shown in Figure 3.15 (b), some micro-cracks start to appear after annealing the films at 600 °C. On the other hand, the resistivity of the ITO film gradually decreases when increasing annealing temperature until 600 °C. At 600 °C, the film seems to be more resistive and electrically unstable. Therefore, 550 °C is a favorable temperature for annealing ITO films.

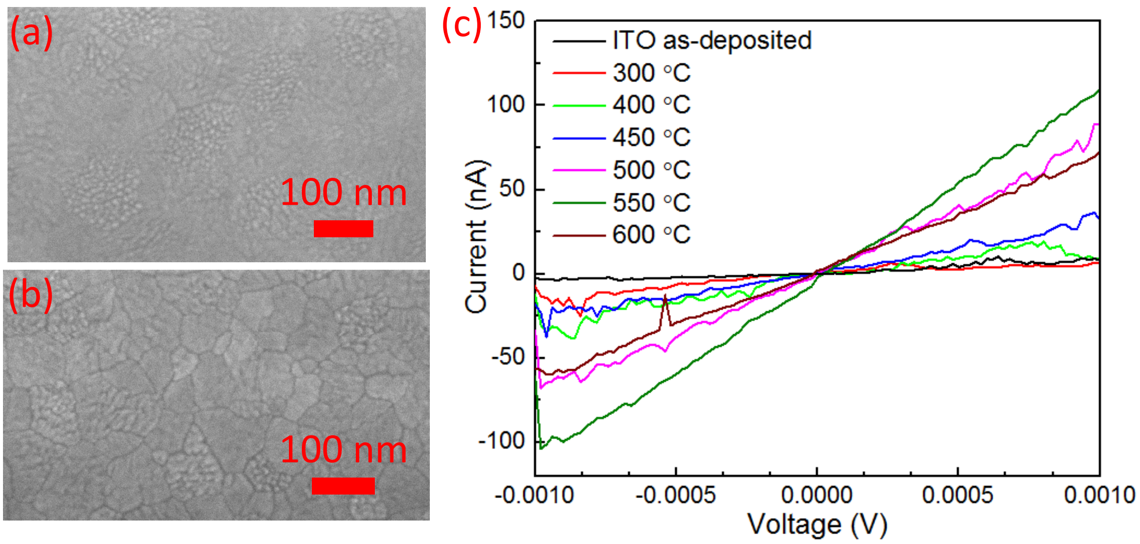

Figure 3.15 The electrical and morphological evolution of ITO films under different annealing temperatures. SEM images of ITO films as-deposited (a) and after annealing at 600 °C (b). (c) The I-V characteristics of ITO films under different annealing temperatures.

3.2.2 The localization of p-n junction on the axial GaN NWs

3.2.2.1 The principle of EBIC

In EBIC measurements, the charge carriers generated by the electron beam of the microscope are collected by an electric field within the material and sensed as a current in an external circuit. This technique reveals inhomogeneities in the electrical properties of the material, and was originally developed for mapping electrically active defects in Si based integrated circuit technology. Along with the improvements in SEM instrumentation, EBIC technique has a high spatial resolution due to the small beam size (around a few nanometers), and it has been employed to determine important physical parameters nowadays, such as carrier lifetime, diffusion length, defect energy levels, and surface recombination velocities [194].

As illustrated in Figure 2.17 in Chapter 2, the interaction between the incident electrons and the sample can give rise to phonons, plasmons, Auger electrons, X-rays, photons, secondary electrons, and charge carriers (electron-hole pairs). Some of them, such as Auger electrons, X-rays, photons, secondary electrons, tend to leave the sample, whereas the others, such as heat, electrons, and charge carriers, will stay in the sample. In the absence of an internal electric field, these charge carriers will either recombine or diffuse to recombination sites, thus no current is produced. If there is an electric field localized within the sample such as at a p-n junction or near a Schottky contact, the electrons and holes drift in opposite directions, creating a low current. With the help of an amplifier, this current can be measured in an external circuit and used as the video input signal of the SEM, forming an EBIC image.

There are two types of EBIC imaging geometries on p-n junction: plan-view and cross-section (as illustrated in Figure 3.16). In plan-view EBIC imaging, the electron beam scans perpendicular to the p-n junction, and defects serving as recombination sites will appear darker in the EBIC image due to lower current from those regions. On the other hand, in cross-sectional EBIC imaging, the electron beam scans parallel to the p-n junction. This configuration is usually used for the location and characterization of the junction, as well as the determination of the diffusion lengths [194].

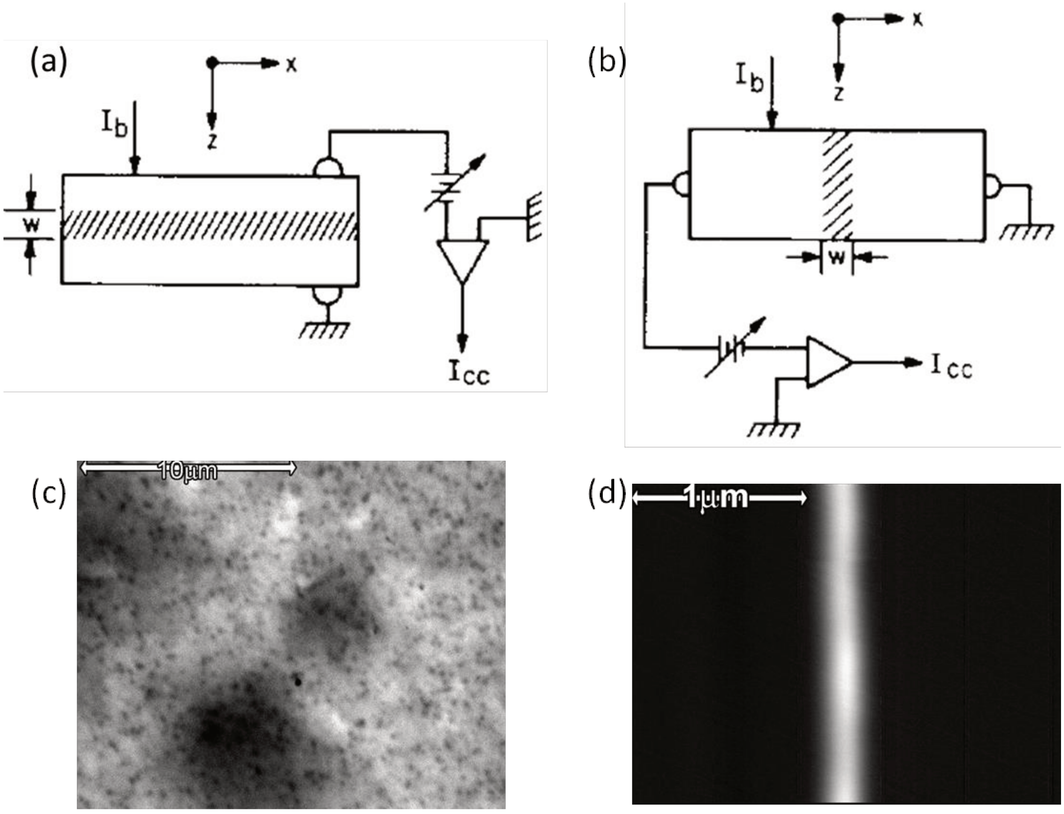

Figure 3.16 Schematic illustrations of two types of EBIC imaging geometries of p-n junction. The electron beam scans (a) perpendicular and (b) parallel to the p-n junction. The depletion region is denoted with cross hatching, taken from [194]. (c) Plan-view EBIC image showing defects in a diode. (d) Cross-sectional EBIC signal of a p-n junction, taken from [195].

3.2.2.2 Theoretical background on abrupt p-n junction

Before the investigation of GaN p-n junction NWs by electron beam based techniques, I would like to briefly review some electrical characteristics of an abrupt p-n junction.

Let us consider an ideal p-n junction with non-degenerate and constant doping level at each side (N_A in the p-type side and N_D in the n-type side). When the n-type side and the p-type side are brought in contact, there is diffusion of electrons from the n-type side to the p-type side, as well as diffusion of holes in the opposite direction, due to concentration gradient. These diffusion processes will lead to a net positive charge on the n-side, and a net negative charge on the p-side. Consequently, an electrical field is formed between the n-side and the p-side. This electrical field can induce a drift current, which moves electrons back to the n-side, and holes back to the p-side. At equilibrium, the diffusion current is completely balanced by the drift current, and the Fermi levels are aligned between n-side and p-side, accompanied with a band bending at the junction.

As shown in Figure 3.17, the n-type semiconductor is neutral from x = −∞ to x = X_L, and it is charged with the ionized donors in the region $X_L \leq x \leq 0$, whereas for the p-type semiconductor, it is neutral from x = X_R to x = +∞ and it is charged with the uncompensated acceptor ions in the region $0 < x \leq X_R$. Assuming there are no free carriers in the depletion region (from x = X_L to x = X_R), we have the charge neutrality equation:

$$\boldsymbol{N_D\,|X_L| = N_A|X_R|} \qquad \textbf{(3.3)}$$

where $|X_L|$,$|X_R|$ are the depletion region on n-side and p-side, respectively. Thus, the total depletion width $W = |X_L| + |X_R|$.

Assuming an abrupt transition between neutral material and the space charge region (the Shockley approximation), one can calculate the behavior of the potential ϕ by solving the Poisson equation in the one-dimensional case.

$$\boldsymbol{\frac{\partial^2\phi}{\partial x} = -\frac{\rho}{\varepsilon_{GaN}}} \qquad \textbf{(3.4)}$$

Parameter ε_{GaN} is the permittivity of GaN, given by $\varepsilon_{GaN} = 9.7 \times \varepsilon_0$ at 300 K, where ε_0 is the vacuum permittivity (8.854 x 10^{-12} $F.m^{-1}$). And ρ is the volume charge density. From equation (3.4), we can eventually deduce that the total depletion width W:

$$\boldsymbol{W = \sqrt{2\varepsilon_{GaN}\left(V_{bi} - V_{pn}\right)/qN_{eff}}} \qquad \textbf{(3.5)}$$

In this equation, $N_{eff} = \frac{N_A N_D}{N_A+N_D}$ is the effective doping level, V_{pn} is the applied voltage on p-region of the p-n junction and V_{bi} is called the "built-in voltage", which is the electrostatic potential drop at the junction without external bias. We have $V_{bi} = \frac{kT}{q}\ln\left(\frac{N_A N_D}{n_i^2}\right)$, where k is the Boltzmann constant, T is the temperature in Kelvin, and n_i is the intrinsic carrier concentration in GaN (n_i = 1.9 x 10^{-10} cm^{-3} at room temperature). The thermal voltage $V_t = \frac{kT}{q}$ is 0.026 V at 300 K, if N_D is on the level of 10^{18} cm^{-3}, V_{bi} ranges between 3.3 V and 3.2 V for N_A varying from 10^{17} to 10^{15} cm^{-3}, respectively.

When increasing forward bias ($V_{pn} > 0$), the depletion width reduces, and an increasing current will flow through the p-n junction; on the other hand, under reverse bias ($V_{pn} < 0$), the depletion region expends, the p-n junction acts like an insulator with only a very small leakage current. The I-V characteristic of a p-n junction can be described by Shockley diode equation:

$$\boldsymbol{I_{pn} = I_s(e^{\frac{V_{pn}}{nV_t}} - 1)} \quad \textbf{(3.6)}$$

Where I_{pn} is the current passing through the p-n junction, I_s is the saturation current, and n is the ideality factor. Under positive bias, I_{pn} increases exponentially as a function of V_{pn}. Under negative bias, I_{pn} rapidly reaches a small saturation value (J_s). n is generally ranging between 1 and 2.

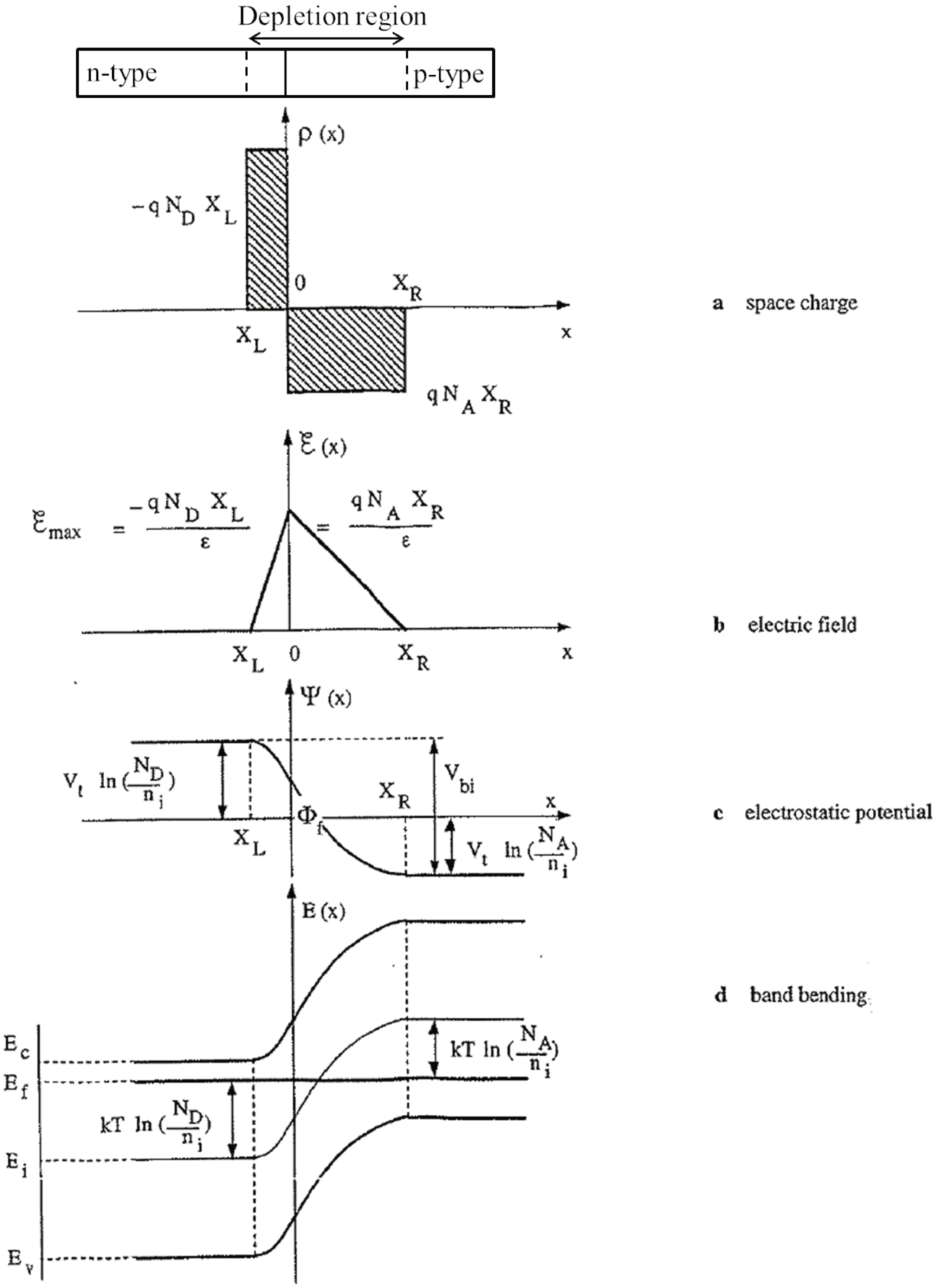

Figure 3.17 Schematic distribution of space charge (a), electric field (b), electrostatic potential (c), band bending (d) in a p-n junction diode in equilibrium under 0 V bias.[§§§]

[§§§] Figure 3.17 is extracted from G. Groeseneken, Master course November-December 2011, K.U. Leuven, Belgium.

3.2.2.3 GaN NWs p-n junction witnessed by EBIC

A few axial GaN p-n junction NWs from sample N1913 have been patterned with two-probe ITO contact. After contact annealing at 550 °C, two NW devices have been successfully characterized by EBIC technique. Figure 3.18 shows the SEM images of these two devices NW #1 (a) and NW #2 (b). Notice that both NW #1 and NW #2 manifest a radial widening from one end (n-type side) to the other end (p-type side), and the ITO contacts are well located at the two ends of the NW. The diameters of the NW at each end and the length between two contacts were measured using high resolution SEM images and summarized in Table 3.6. We can see the diameters of the two NWs are quite similar, with a difference of 5% or less.

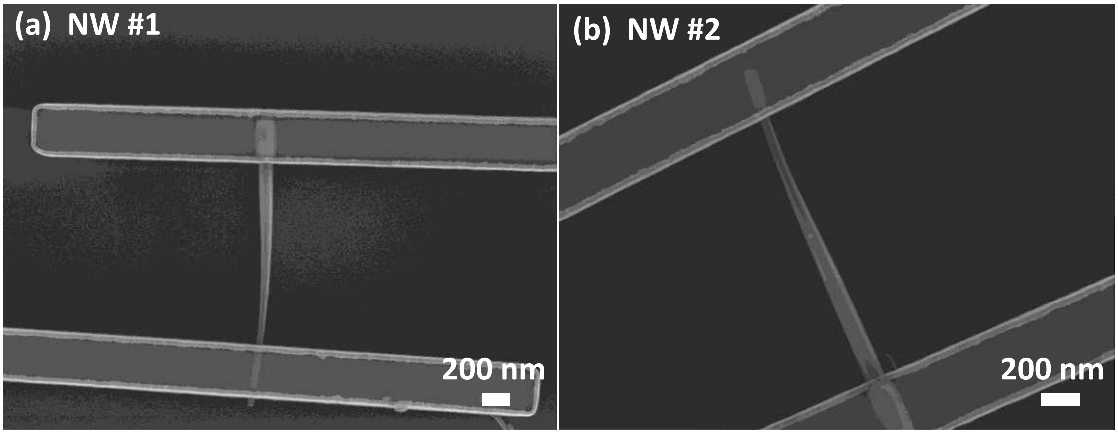

Figure 3.18 SEM images of two contacted axial GaN p-n junction NWs

Table 3.6 Summary of NW dimensions in the two devices

NW	n-type diameter at the contact	p-type diameter at the contact	Length btw two contacts
#1	68 nm	115 nm	1295 nm
#2	67 nm	121 nm	1500 nm

The I-V curves of NW #1 and NW #2 are presented in Figure 3.19 (a). Although these two NWs are taken from the same sample, different electrical behaviors have been observed. For NW #1, a nonlinear, nonexponential I-V behavior can be discerned when applying voltage from −3 V to +3 V. The current passing in the device is 40 nA under +3 V and 10 nA under -3V, corresponding to a high current density of 600 A/cm^2 and 150 A/cm^2, respectively, when taking the average diameter of 100 nm. On the other hand, for NW #2, the current is below detection limit (1 nA) when changing the voltage from −3 V to +3 V.

From the I-V curve in log-log scale of NW #1, two transport regimes are exhibited with different α values in $I \sim V^{\alpha}$. An ohmic behavior ($I \sim V$) with a very high resistance of

368 MΩ is observed from −3 V to +0.8 V bias, while a space-charge-limited current (SCLC) with relation of $I{\sim}V^{2.3}$ is obtained from +0.8 V to +3 V bias. The exponential I-V relationship of the p-n junction seems to be masked by these two transport regimes. The ohmic behavior indicates the presence of a highly resistive part in the device. The p-GaN is very likely to contribute for the resistive part, since n-GaN is considered to be highly conductive according to Chapter 2. Assuming that the 368 MΩ is due to the p-GaN part in NW #1, we can deduce the resistivity of the p-GaN to be 395 Ω.cm. Taking the state of the art p-GaN epilayer mobility value 10 $cm^2.V^{-1}.s^{-1}$, the hole concentration of the p-GaN is calculated to be 1.6×10^{15} cm^{-3}, which is in the agreement with the Mg doping level estimated from the EBIC measurements later. Moreover, the p-GaN part is probably partially insulating due to surface states, inducing radial near surface depletion [196].

In terms of SCLC, it has already been reported in III-nitride NWs [197], [198], and it occurs generally when the injected charge density is higher than the free carrier concentrations in the sample. In our case, the observation of SCLC in NW #1 is probably related with the axial p-n junction. Under positive bias, the holes are injected from the ohmic contact into the p-type region. For bias voltage higher than 0.8 V, the injected carrier density is higher than thermal equilibrium carrier density, because of low the p-n barrier at this bias. Whereas for negative bias voltage, the p-n barrier limits the carrier injection from the pn junction and thus the SCLC is not observed.

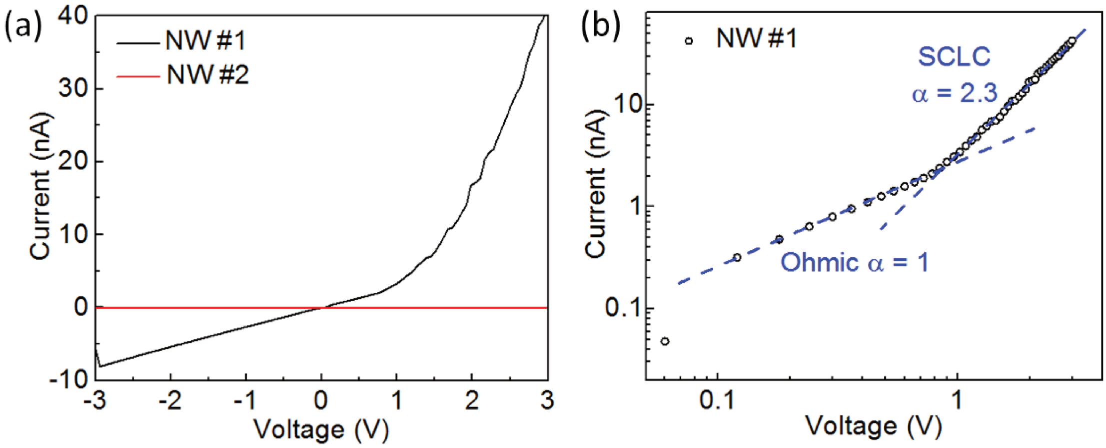

Figure 3.19 I-V characteristics of NW #1 and #2 from −3 V to +3V. (a) I-V curves of NW #1 and #2 in linear scale. (b) I-V plot of NW #1 in log-log scale. The blue dashed line is the linear fitting, revealing two regions correlated with ohmic and SCLC transport at low and high biases, respectively.

With the aim of revealing the physical nature of these NW devices, EBIC measurements has been performed. As illustrated in Figure 3.20 (a), a focused electron beam scans the NW device to create charged carriers. These carriers can be separated by any electric field localized within the device such as at a p-n junction, and so forming an induced current. An amplifier is connected to the n-GaN side to detect this EBIC current, while a voltmeter is used to apply a bias on the p-GaN side for bias dependence measurements.

An typical EBIC image of an axial GaAs p-n junction NW is shown in Figure 3.20 (b) [140], where the bright EBIC signal within the NW is a result of the strong electric field at the p-n junction, and it is proportional to the EBIC current. The profile of the EBIC signal (in logarithmic scale) along the NW is schematically shown in Figure 3.20 (c), assuming that the depletion region is free of carriers and the surface recombination is negligible. The plateau of the EBIC signal maps the electric field in the depletion region, whereas the reduction of the EBIC current at each neutral side is exponentially correlated with minority carrier diffusion lengths under low injection conditions. Thus, the analysis of the EBIC signal allows to extract important information, such as depletion region width, electron diffusion length in p-type GaN ($L_{e,p}$), as well as hole diffusion length in n-type GaN ($L_{h,n}$) [134], [142].

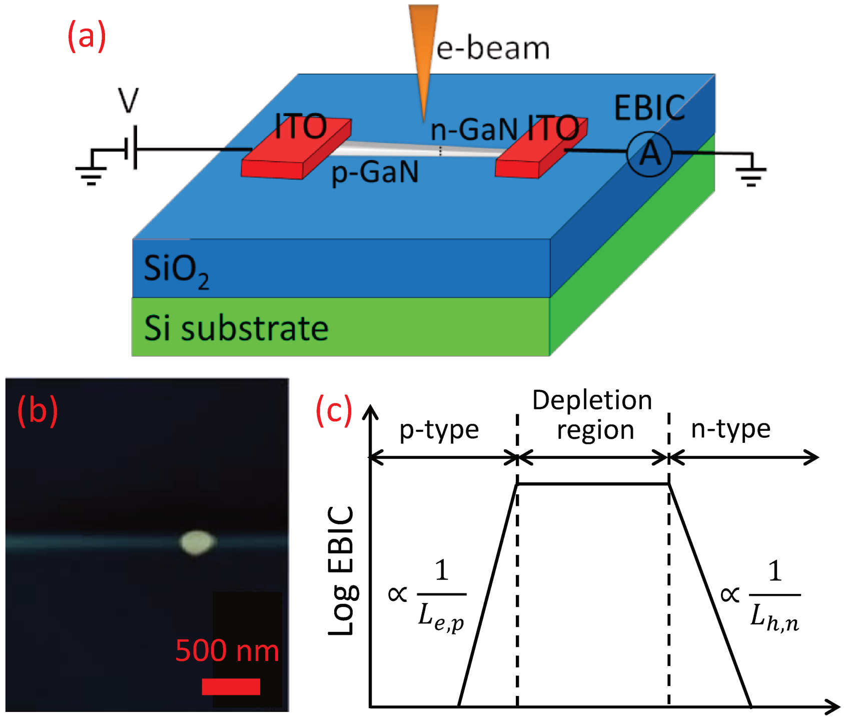

Figure 3.20 (a) Scheme of the EBIC measurement on single GaN axial p-n junction NW. (b) EBIC image of an axial GaAs p-n junction NW, taken from [142]. (c) EBIC current profile (in logarithmic scale) as a function of NW position in the ideal case.

The electron beam energy is kept at 5 keV for NW #1 and 4 keV for NW #2 with a current of 4.6 pA, in order to have less beam damage possible while maintaining the spatial resolution. The SEM scan was perpendicular to the NWs axis for a higher EBIC resolution in the axial direction of NWs. Indeed, the low EBIC current needs large amplification, which limits the signal bandwidth, to match the video format of the SEM external input. A consequence of this is that the EBIC signal could appear larger than the physical diameter of the NWs.

Figure 3.21 presents the EBIC images as well as the corresponding SEM images for NW #1 (a) and NW #2 (b) devices under 0V bias. For NW #1, although the SEM image is not very clear due to repetitive high-magnification electron beam scanning contaminations, the EBIC signal (darker area on the EBIC image) can directly localize the position of the p-n junction within the NW. The situation is even more obvious for NW #2. In the SEM image, a voltage contrast can be observed from the left side (bright, p-GaN) to the right side (dark, n-GaN), while the location of the p-n junction is manifested by the respective EBIC signal. No EBIC signal has been observed at both n-contact and p-contact for the two NW devices, a signature of ohmic or quasiohmic contact behavior.

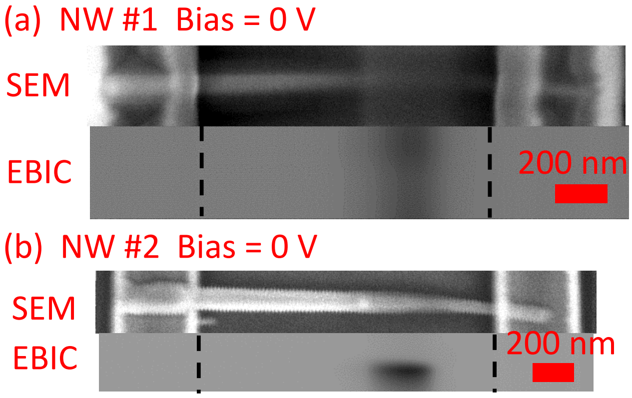

Figure 3.21 SEM and EBIC images of the measured NW #1 (a) and NW #2 (b) devices under 0 V bias. The dashed black line delineates the edges of the contacts.

The EBIC and corresponding SEM profiles along the NW are plotted in Figure 3.22. For NW #1, no voltage contrast can be observed on the SEM images due to the contaminations, while the EBIC profile consists of the contributions of the depletion region and the carrier diffusions from each neutral side. Notice that the EBIC signal is asymmetrical, indicating different physical behaviors of the neutral n and p parts. On the other hand, for NW #2, the position of the EBIC signal coincides with the location of the contrast change in SEM profile, and furthermore it corresponds to the enlargement of the NW diameter, confirming the presence of the axial p-n junction. In addition, the SEM profile is influenced by a few factors, such as topography of the sample and the existence of the p-n junction. The small peak on p-GaN in the SEM profile is correlated to the “dust” of unknown origin seen on the p-side of NW #2 (see Figure 3.21 (b)).

A comparison of the EBIC signal between NW #1 and NW #2 is shown in Figure 3.23. The EBIC signal is normalized and aligned with respect to the maximum value, presented in linear scale. The EBIC signal from the depletion region is similar for the two NWs, whereas a discrepancy can be observed from the diffusion part. Both NWs are placed as p-GaN on the left side and n-GaN on the right side. The EBIC current decreases faster for NW #2 on both p-GaN and n-GaN side, suggesting shorter carrier diffusion lengths ($L_{e,p}$ and $L_{h,n}$) in NW #2. A detailed investigation on the carrier diffusion lengths is presented later.

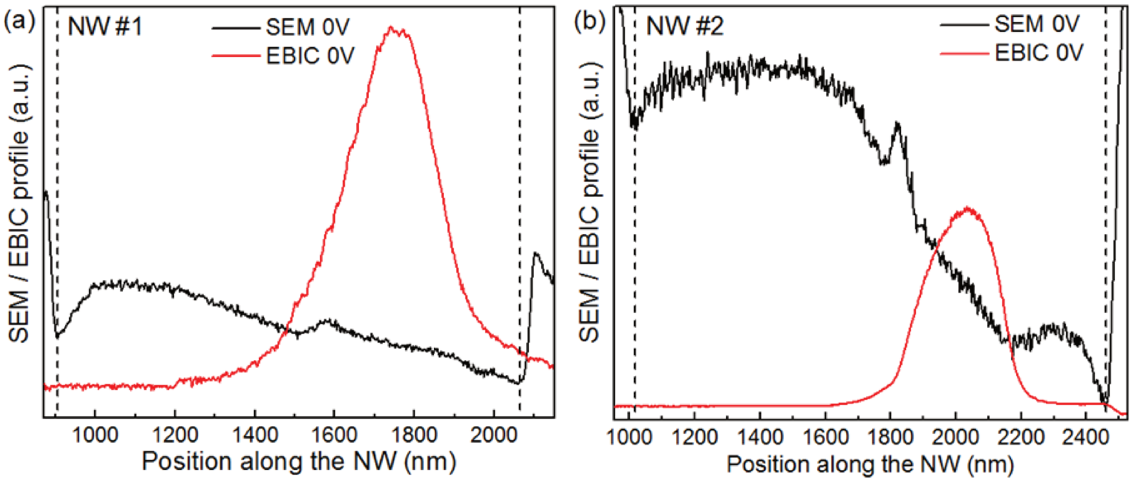

Figure 3.22 SEM / EBIC profiles as a function of the position along the NW for NW #1 (a) and NW #2 (b), respectively. The relative positions of the SEM voltage contrast and the EBIC signal are schematically shown, and no absolute value is accounted on the y-axis. The dashed black line delineates the edges of the contacts.

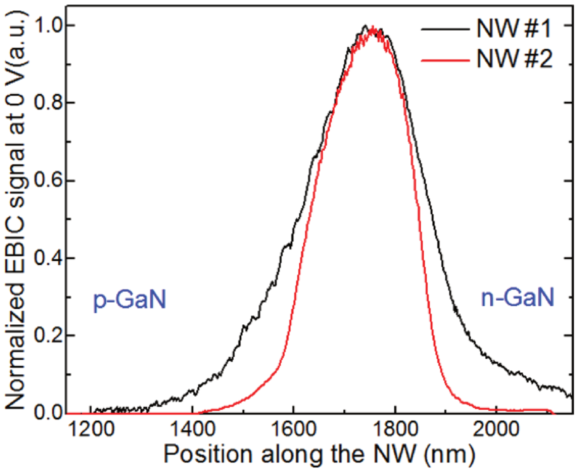

Figure 3.23 Normalized EBIC signal at 0V for NW #1 & #2 in linear scale.

3.2.3 The determination of depletion width and diffusion length on the axial p-n junction GaN NWs

3.2.3.1 Bias dependent EBIC measurements

In order to disclose more the physical nature of these two NW devices, bias dependent EBIC experiments have been performed.

Figure 3.24 shows the EBIC images and the corresponding SEM images under varying voltages for NW #1. The SEM images are not very clear due to the beam scanning pollutions and only serve as contact position references for the alignment of the different EBIC images. Under positive bias, the dark EBIC signal at the p-n junction gradually decreases until disappearance due to the shrinkage of the depletion region as expected. At the same time, another EBIC signal is observed near the p-contact. This EBIC current follows in the opposite direction (white contrast) and increases when raising the positive bias. On the other hand, under negative bias, the p-n junction EBIC signal remains around the same position, and its intensity increases with higher negative voltages, indicating higher electric field at the junction.

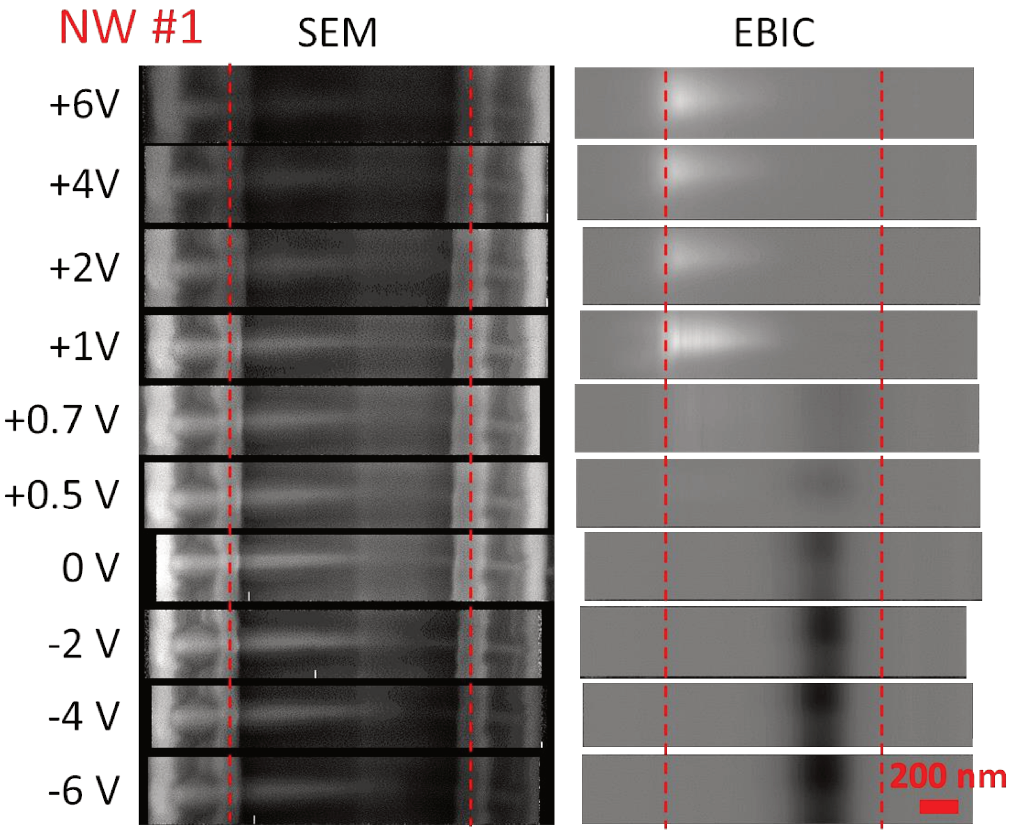

Figure 3.24 SEM and EBIC images measured under varying applied voltages for NW #1. All the images under negative voltages are taken in the same amplifier conditions, whereas the offset and gain of the amplifier are changed for positive biases in order to avoid saturating the grayscale image. The dashed red line is the eye guidance for the edges of the contacts. The contrasts of the SEM images are adjusted to show the contour of the NW.

Figure 3.25 illustrates the EBIC signal intensities along NW #1 under different biases. The evolution of the EBIC current has been readily observed. Under 0V bias, only a small EBIC current in the vicinity of the p-n junction is present. Interestingly, the position of the p-n junction visualized by EBIC corresponds to the part of the NW with distinguishable morphology change. When applying positive voltage, the EBIC current near the p-n junction gradually decreases, while another EBIC current flowing in the opposite direction presents itself near the p-contact up to the neutral p-GaN NW. The p-n junction EBIC current disappears at +1 V, whereas the other EBIC current continues to increase with a peak at the edge of the ITO p-contact. The appearance of this current suggests the presence of a strong electric field on p-GaN, which facilitates carrier collections near p-contact. In fact, both the electric field on p-GaN and the p-n junction electric field can be recognized from the EBIC signal under +0.7 V. Since these two fields are close to each other, both diffusion and drift contribute to the EBIC current on possibly partially depleted p-GaN. On the other hand, the p-n junction EBIC current rises with increasing negative bias. As the focus of this study, the analysis and understanding of this EBIC current is presented later in-depth.

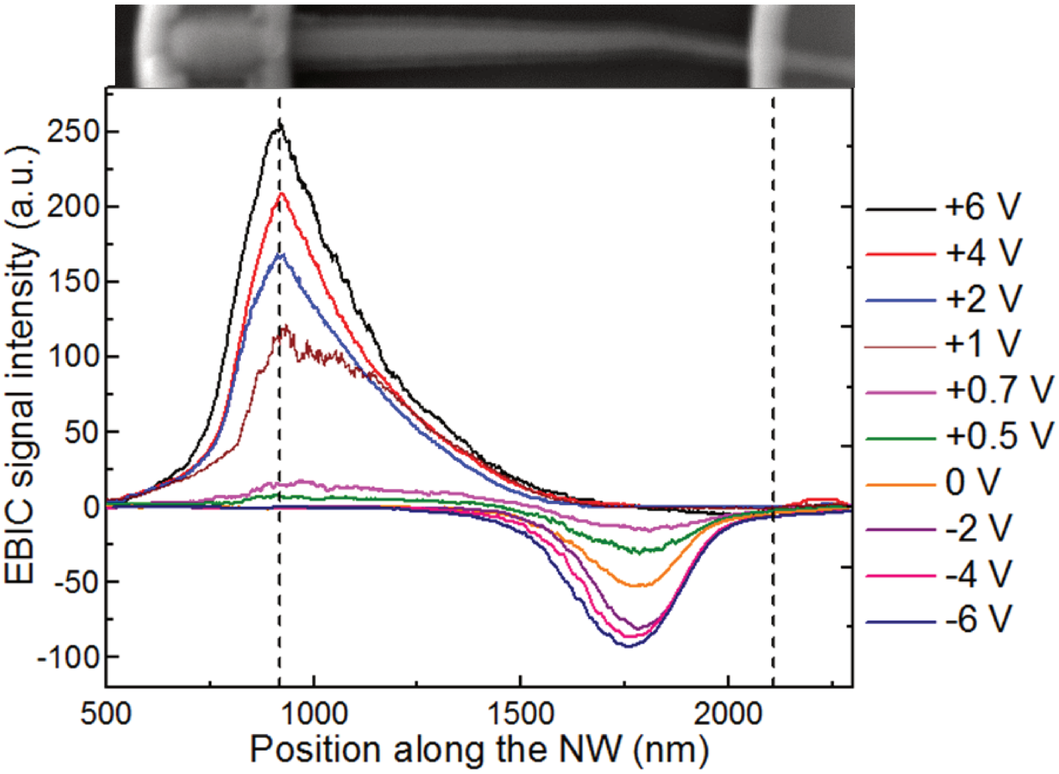

Figure 3.25 EBIC signal intensities along NW #1 from -6 V to +6V. The EBIC signals are extracted from the EBIC images by removing the background level and correcting the offset and gain of the amplifier. A SEM image is placed on top of the plot for relating the EBIC signal position with the actual NW. The dashed black line is the eye guidance for the edges of the contacts.

The same experiments have been conducted on NW #2. Figure 3.26 presents the EBIC images and the corresponding SEM images from +8 V to −10 V bias for NW #2. A clear SEM voltage contrast can be observed from p-GaN (bright) to n-GaN (dark). Moreover, this contrast enhances with increasing negative bias and reduces with increasing positive bias, as expected for the surface voltage contrast of p-n junction. A careful investigation of the SEM voltage contrast is delivered in 3.2.4. In terms of the EBIC images, similar observations compared to NW #1 have been obtained with the appearance of an EBIC signal near the p-contact under positive bias, and enhancement of the p-n junction EBIC signal with increasing negative bias.

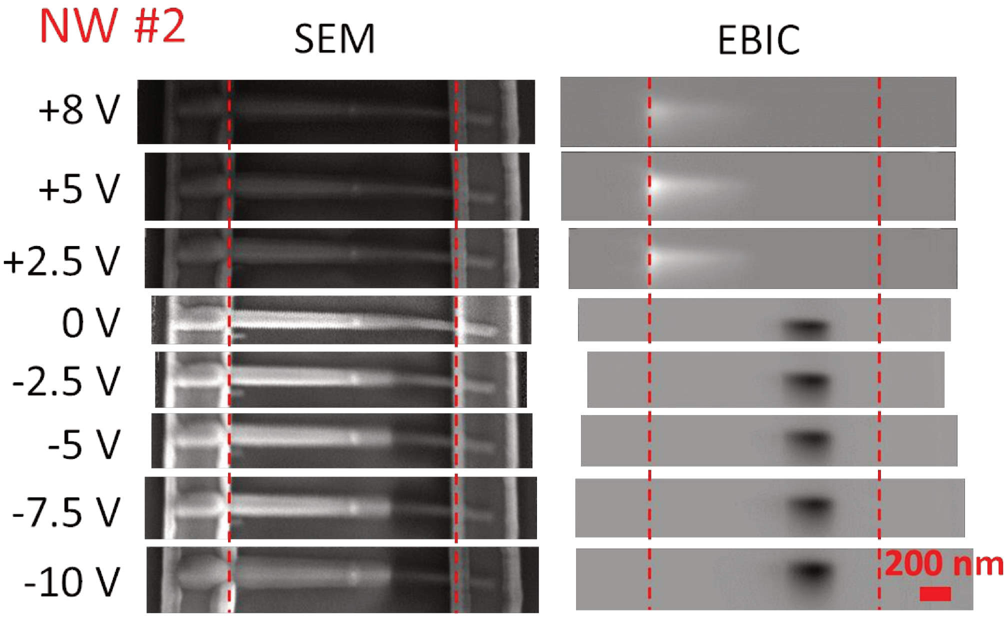

Figure 3.26 SEM and EBIC images measured under varying applied voltages for NW #2. All the images are taken in the same amplifying conditions except the EBIC image at +8 V. The gain (from 500 pA/V to 1 nA/V) is adjusted for this image to avoid signal saturation. The dashed red line is the eye guidance for the edges of the contacts.

Figure 3.27 shows the profile of the EBIC signals along NW #2 under varying voltages. Similar to NW #1, besides the diffusion current of the minority carriers, the strong electric field on possibly partially depleted p-GaN NW can drift the carriers to reach ITO contact, contributing to the high EBIC current near the p-contact under positive bias. This field seems to influence the electrostatic environment of the p-n junction, signified by the peculiar behavior of EBIC current on the left under negative bias. In addition, the “dust” on this NW appears to be a carrier recombination center, causing the inflection point on the EBIC current profile.

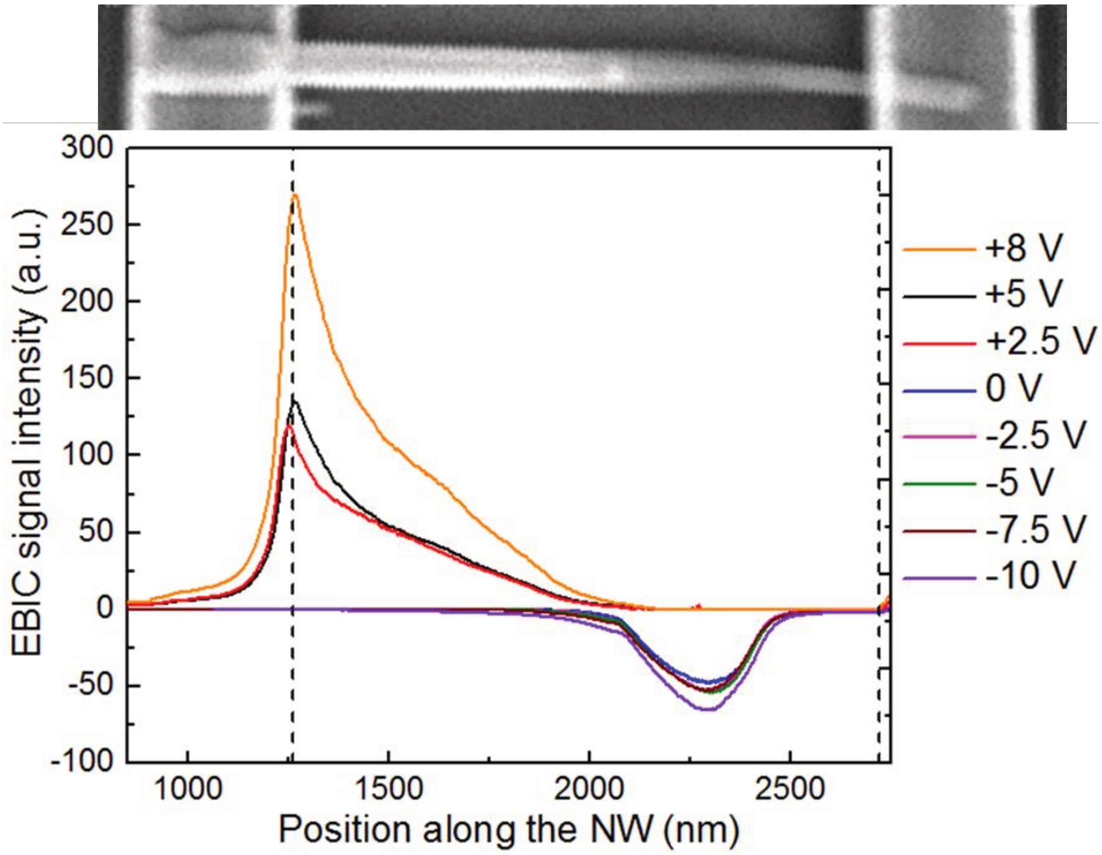

Figure 3.27 EBIC image profiles under different biases for NW #2. The EBIC signals are extracted from the EBIC images by removing the background level and correcting the offset and gain of the amplifier. A SEM image is placed on top of the plot for relating the EBIC signal position with the actual NW. The dashed black line is the eye guidance for the edges of the contacts.

Summarizing the discussions above, a schematic band diagram has been proposed in Figure 3.28. Under forward regime, no potential barrier is present at the p-n junction to prevent carrier transport. There is a strong electric field on p-GaN NW since it is very resistive. Due to this field, addition to the diffusion current, electrons in p-type can be also drifted and collected at p-type contact, while holes in p-type can easily transport to n-type, and then recombine with the electrons. Alternatively, under reverse regime, the electrons in p-type need to travel through the p-n junction to be collected, where they possibly recombine before reaching the n-type contact.

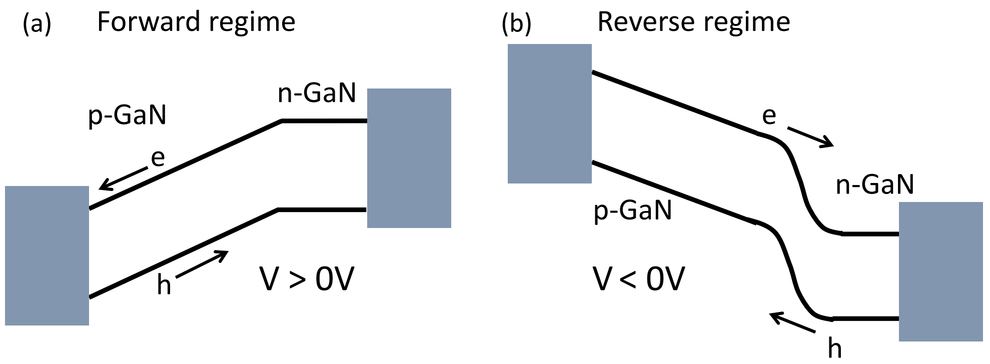

Figure 3.28 Schematic band diagram of the NW p-n junction devices under (a) forward and (b) reverse regimes.

Now let us focus on the EBIC signal of the axial GaN p-n junction. Normally an extension of the depletion width for the p-n junction is expected when applying negative voltages. Figure 3.29 illustrates the normalized EBIC signals from p-n junction in NW #1 and #2 under different negative biases. For NW #1, at first sight, it seems the EBIC signals at different voltages are very close to each other, and a small deviation is observed near the right end of the EBIC signal. If we compared the SEM image with the EBIC signal, we can see that this variation occurs near the ITO contact on n-type GaN NW. Nevertheless, the EBIC signals at 0 V and −6 V are almost overlapped on the n-side, whereas a small deviation is noticed on the p-side. It is difficult to say whether this deviation is a signature of the p-n junction depletion width extension under negative bias, therefore modeling is needed for more quantitative studies. For NW #2, the situation is more complicated. The presence of “dust” on p-side of NW has led to an inflection point on the EBIC signal. Moreover, the EBIC behaviors of p-GaN on the two sides of the “dust” are different. On the right, the EBIC current does not vary with different voltages, whereas on the left, it gradually increases with the rise of the voltage, suggesting the existence of an electric field on this part of the NW. Therefore, it is necessary to perform modeling of the EBIC signal to disclose the underlying physics of these two NW devices.

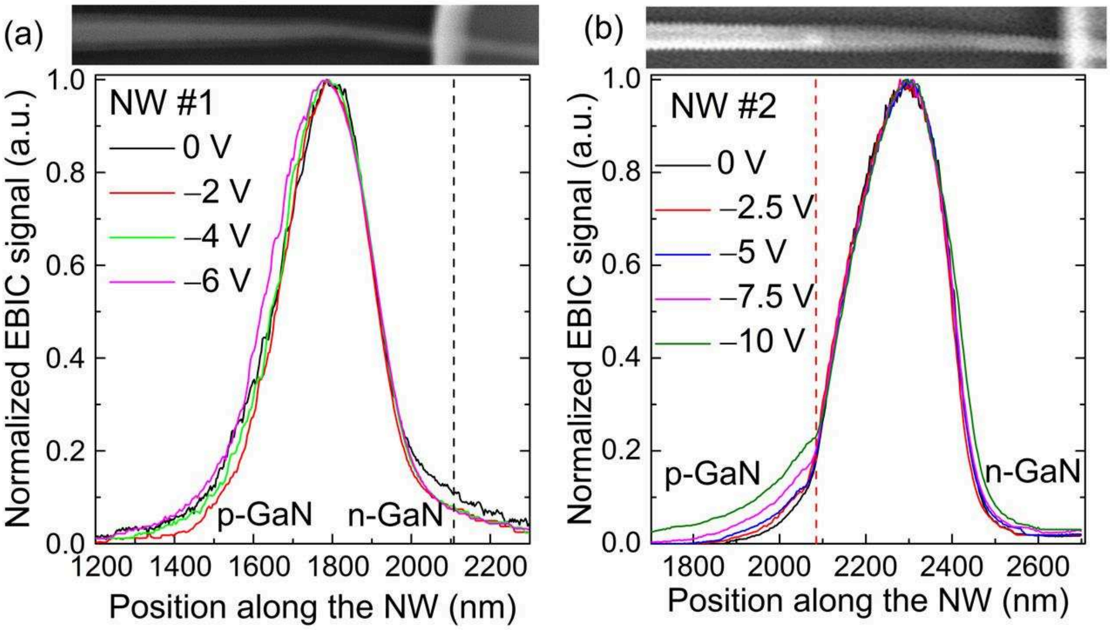

Figure 3.29 Normalized EBIC signals from p-n junction in NW #1 (a) and #2 (b) under different negative voltages. Corresponding SEM images are placed on top of the plots. The black dashed line in (a) delineates the edge of ITO contact on n-GaN, whereas the red dashed line in (b) locates the position of the "dust" seen on the p-side of NW #2.

3.2.3.2 The EBIC signal simulations of the p-n junction

The EBIC signal of a p-n junction in core-shell GaN microwires has been modelled by a previous colleague [134], and the same method has been employed in this thesis. Only a brief description of the modelingprocess is presented here, for more information please refer to the thesis of P. Tchoulfian [113].

Injection conditions The EBIC signal is closely related with the excess carriers created by the interaction between incident electron beam and the sample. When the amount of excess carriers is smaller than that of the majority carriers in the sample, only the diffusion current of the minority carriers is measured in EBIC. In this case, the device is under low injection conditions and the analysis of the EBIC signal provides us the diffusion length of the minority carriers. On the contrary, if the concentration of excess carriers is higher than the majority carriers concentration, the diffusions of both minority and majority carriers contribute to the EBIC current, giving rise to a more complicated system [199]. Therefore, the concentration of excess carriers Δn, p has been firstly estimated by equation (3.7), assuming the average electron-hole pair energy is $3E_g$:

$$\boldsymbol{\Delta n, p = \frac{E_0(1-a)}{V} \times \frac{1}{3E_g} \times \frac{i_B \times \tau}{e}} \tag{3.7}$$

where E_0 is the e-beam energy, a = 0.176 is the backscattering coefficient, V is the electron sample interaction volume, $E_g = 3.4$ V is the GaN bandgap energy, i_B is the beam current, τ is the excess carrier lifetime, and e is the elementary charge.

The interaction volume can be then approximated by a sphere with diameter $D_{K\text{-}O}$ [200] given by:

$$D_{K-O} = \frac{27.6 \times A \times E_0^{1.67}}{Z^{0.89} \times d} \tag{3.8}$$

where $\langle A \rangle = 42$ g/mol is the average atomic mass of GaN, $\langle Z \rangle = 19$ is the average atomic number of GaN, d = 6.15 g/cm^2 is the density of GaN.

Based on these two equations, Δn, p is plotted as a function of i_B under different e-beam energy assuming $\tau = 100$ ps in Figure 3.30 [113]. As mentioned before, i_B equals 4.6 pA, while the electron beam energy is kept at 5 keV and 4 keV, for NW #1 and #2 respectively. As indicated by the red arrows, the densities of the excited excess carriers are around 4×10^{14} cm^{-3} for NW #1 and 1×10^{15} cm^{-3} for NW #2. These values have been compared with the majority carrier concentrations extracted from EBIC analysis in both n and p type NWs later, in order to determine whether the low injection conditions are fulfilled.

A more accurate evaluation of the interaction volume can be achieved by using a Monte Carlo simulation program named CASINO. This software is able to simulate the electron trajectory in solid upon the interaction with low energy e-beam (0.1 to 30 keV). Figure 3.31 illustrates the simulation results of absorbed energy distribution in GaN when struck by an e-beam with 4 keV energy (the e-beam condition for NW #2) [113]. The value of each line in (a) and (b) corresponds to the percentage of the energy outside of each equivalent region. 95% of the incident electron energy is concentrated within 60 nm from the impact point at vertical (depth) and lateral distance. Therefore, for a NW with a diameter of 70 nm on the n-side, and 120 nm on the p-side, most of the incident e-beam energy is focused within the NW. Moreover, the cumulated absorbed energy can be plotted as a function of interaction depth (c) and lateral position (d) for e-beam with different energies [113]. We can conclude that both the interaction depth and lateral position are less than 100 nm for e-beam energies of 4 keV and 5 keV. Accordingly, the interaction volume V simulated by CASINO remains completely inside the NW, and thus has been employed to model the EBIC signal.

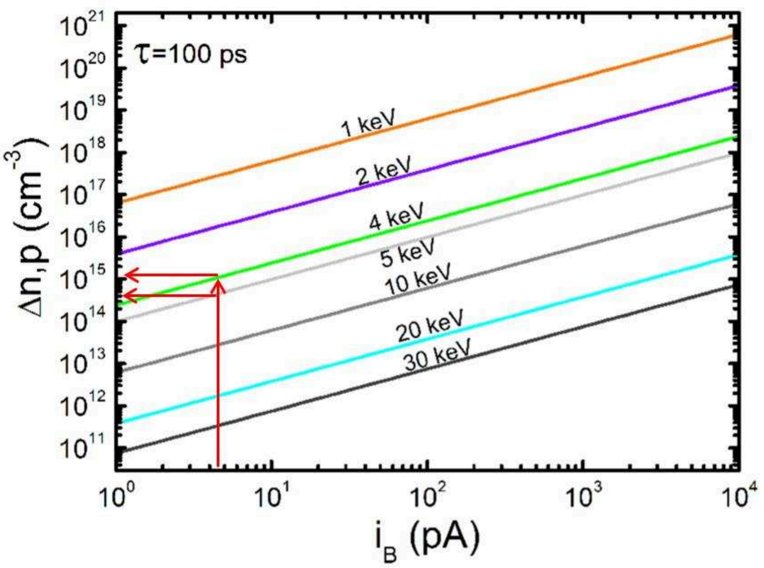

Figure 3.30 The volume density of the excess carriers Δn, p as a function of the beam current i_B with different e-beam energy, taken from [113]. The red arrows indicate the e-beam conditions in this thesis.

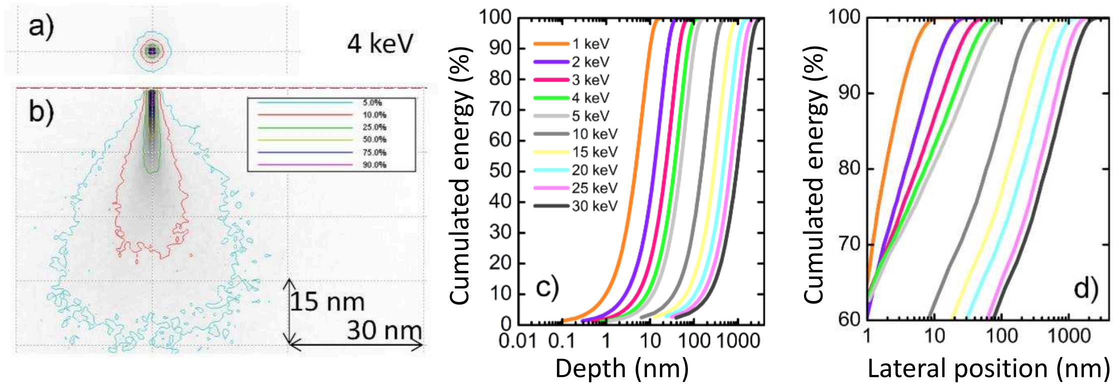

Figure 3.31 CASINO simulations of the electron beam-sample interaction [113]. (a) Top view and (b) side view absorbed energy distribution in GaN struck by an e-beam with 4 keV energy. The values in the legend represent the percentage of the energy outside of the corresponding lines. The cumulated absorbed energy is plotted as a function of depth (c), lateral position (d) for e-beam with different energies.

The modeling of EBIC current in the vicinity of a p-n junction Once created, the excess minority carriers will diffuse in the materials, and the nonequilibrium minority carrier density Δp (x,y,z), taking the n-side as an example, fulfills the continuity equation (3.9):

$$D\,\nabla^2 \Delta p\,(x,y,z) - \frac{1}{\tau}\Delta\, p\,(x,y,z) + g\,(x,y,z) = 0 \tag{3.9}$$

Here, D represents the diffusivity and is related with the diffusion length L and carrier lifetime τ by $D = L^2/\tau$. Function g(x,y,z) describes the generation of minority carriers. Hence, the first part of this equation signifies the diffusion of created carriers, the second part indicates the radiative and non-radiative recombination of these carriers, and the last part stands for the generation of the carriers upon e-beam bombardment.

With the EBIC measurements configuration shown in Figure 3.32, equation (3.9) can be solved using a method developed by Bonard and Ganière [201]. The p-n junction is located between –dj and 0 along the x-axis with a depletion width of W, and the e-beam scans parallel to the p-n junction (the same to the case in this thesis). If the system is translational invariant along the y-axis, the generation function g(x,y,z) can be summed across y to yield h(x,z). For e-beam bombardment on the surface at x = 0, the generation of electron-hole pairs in the small volume dxdz is estimated by equation (3.10):

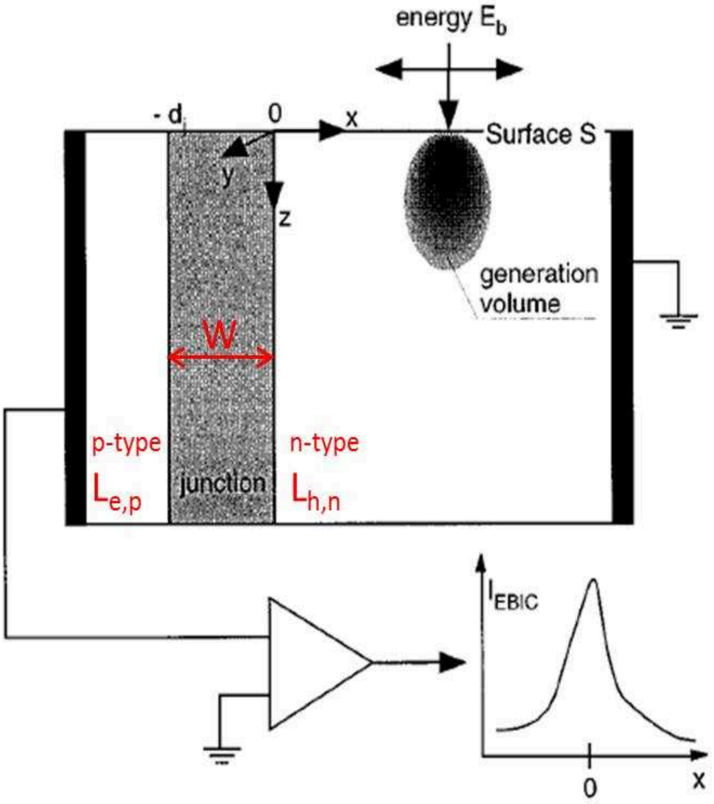

Figure 3.32 The configuration of the EBIC measurement model from Bonard and Ganiere [201].

$$h(x,z) = \frac{1}{2\sqrt{\pi}\sigma_x\sigma_z^3} exp\left(-\frac{x^2}{\sigma_x^2}\right) z^2 exp\left(-\frac{z}{\sigma_z}\right) dxdz \tag{3.10}$$

where σ_x and σ_z describe the lateral e-beam extension and its penetration depth, respectively. The values of σ_x and σ_z depend on the sample as well as the e-beam parameters. Parish et al. has proposed a method to determine the values of σ_x and σ_z with the help of Monte Carlo simulation [202]. If we separate the x, z variables, equation (3.10) writes:

$$h(x,z) = k(x)\, j(z), \qquad where\ k(x) = A\, exp\left(-\frac{x^2}{\sigma_x^2}\right), j(z) = Bz^2 exp\left(-\frac{z}{\sigma_z}\right) \tag{3.11}$$

where A and B are constants. After the linearization of the functions k(x) and j(z), the values of σ_x and σ_z are related to the slopes of the corresponding curves as shown in Figure 3.33 [113]. By plotting the Monte Carlo data k(x) and j(z) is the linearized fashion, we can have access to the values of σ_x and σ_z under specific e-beam conditions. Following this process, the values of σ_x and σ_z in our case are estimated to be 38 nm and 11 nm for NW #2 (4 keV), and 55 nm and 17 nm for NW #1 (5 keV).

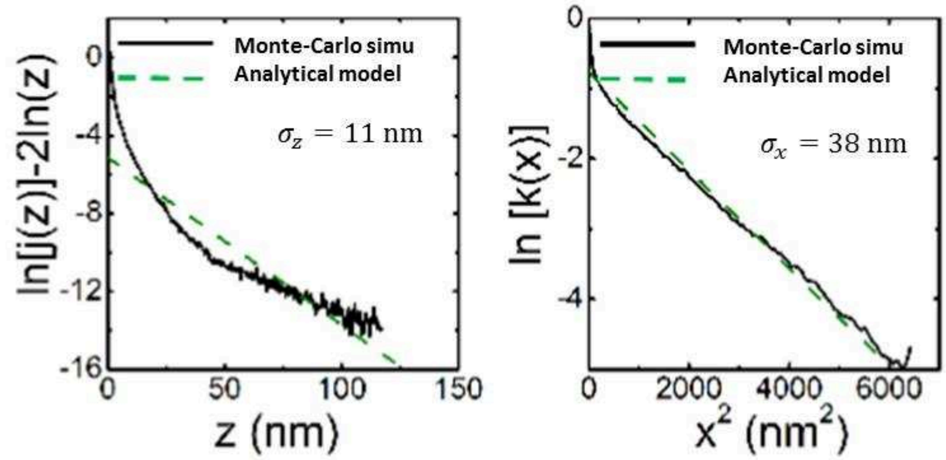

Figure 3.33 Linearization process on (a) x-axis, (b) z-axis to determine the values of σ_x and σ_z under e-beam energy of 4 keV, taken from [113].

The analytical solution of the equation (3.9) can be obtained by the use of Green functions and Fourier transforms. Alternatively, Bonard and Ganière [201] has come out with an expression to numerically simulate the EBIC current by adapting the collection efficiency proposed by Donolato [203].

The EBIC current along x-axis can be expressed by the minority collection efficiency of the junction at a distance:

$$\boldsymbol{I_{EBIC}(x) = \int_{-\infty}^{+\infty} d\tilde{x} \int_{0}^{\infty} h(\tilde{x} - x, \tilde{z}) \varphi(\tilde{x}, \tilde{z}) d\tilde{z}} \tag{3.12}$$

where h(x, z) is defined by (3.10), and $\varphi(x, z)$ is the carrier collection efficiency.

Different boundary conditions in different regions can lead to the expression of $\varphi(x, z)$ in each part of the p-n junction. If there is no carrier recombination in the depletion region, then $\varphi(x, z) = 1, -d_j \leq x \leq 0$. Whereas for the minority carriers created on the neutral n and p side, $\varphi(x, z)$ is a function of the minority carrier diffusion length, diffusivity, and surface recombination velocity if surface recombination effect is not neglected. The detailed expressions of $\varphi(x, z)$ can be found in reference [201], therefore will not be listed here.

It is worth mentioning that the EBIC current in the neutral region far from the contact fulfils the exponential decay relationship with the diffusion length when we neglect the surface recombination.

$$I_{EBIC} \propto e^{(-x/L)}, L = \sqrt{D\tau} \qquad \textbf{(3.13)}$$

3.2.3.3 Quantitative analysis of the depletion width and carrier diffusion length in the axial GaN p-n junction NWs

With no external bias As we discussed in the previous section, the EBIC signal is closely related with the depletion width, carrier diffusion length and surface recombination velocity. In order to quantitatively evaluate these values in the axial GaN p-n junction NW, the Bonard and Ganière model [201] has been used. This method has been successfully applied on the EBIC signal of p-n junction in core-shell GaN microwires [134]. The spatial distribution of the excited excess carriers is taken into account by using equation (3.10), in which the values of σ_x and σ_z are calculated from the previous section. Therefore, all the excess carriers generated in the depletion region, and the neutral n- and p-regions are considered.

The reported surface recombination velocity values are in the range of 1.1×10^4-7×10^4 cm/s for the GaN epilayers [204], and 9×10^3 cm/s for GaN NWs [205] in the literature. Another EBIC study of GaN epilayer devices has found that the surface recombination is negligible, probably arising from the surface passivation by the polymerization of the hydrocarbon layer deposited by e-beam. Hence, the surface recombination is considered negligible in the EBIC signal modeling.

Figure 3.34 has displayed the modeling of EBIC signals under 0 V. For NW #1 (a), the modeling curve fits well the experiment data in the vicinity of the p-n junction, while a discrepancy is observed at the right foot of EBIC signal near the n-contact. The presence of the ITO contact has an influence on the carrier collection, and this feather is not taking into account in the model. This modeling gives a depletion region width W of 116 nm, carrier diffusion length in p-GaN $L_{e,p}$ of 122 nm and carrier diffusion length in n-GaN $L_{h,n}$ of 77 nm. From equation (3.5), we have the effective doping level N_{eff1} = 2.5×10^{17} cm^{-3}, taking V_{pn} = 0V and W = 116 nm. From the growth condition of sample N1913 (see Table 3.3), the donor N_{d1} doping level is estimated to be 2-3$\times10^{18}$ cm^{-3}, therefore the acceptor N_{a1} doping level is calculated to be 2.8−2.9$\times10^{17}$ cm^{-3} using $N_{eff} = N_AN_D/(N_A+N_D)$. For NW #2, the modeling curve coincides with the experimental data in the region of the p-n junction except near the “dust” on the p-GaN. As discussed before, the “dust” on this NW is possibly acting as a carrier recombination center, influencing the carrier dynamics in the NW. The modeling parameters for this NW are: W = 125 nm, $L_{e,p}$ = 170 nm, $L_{h,n}$ = 40 nm. If we perform the same calculations for NW #2, N_{eff2} is found to be 2.2×10^{17} cm^{-3}. Assuming N_{d2} is also about 2-3$\times10^{18}$ cm^{-3}, we can estimate N_{a2} = 2.4-2.5$\times10^{17}$ cm^{-3}. The estimated doping levels and carrier diffusion lengths of NW #1 & #2 are summarized and compared with literature values in Table 3.7.

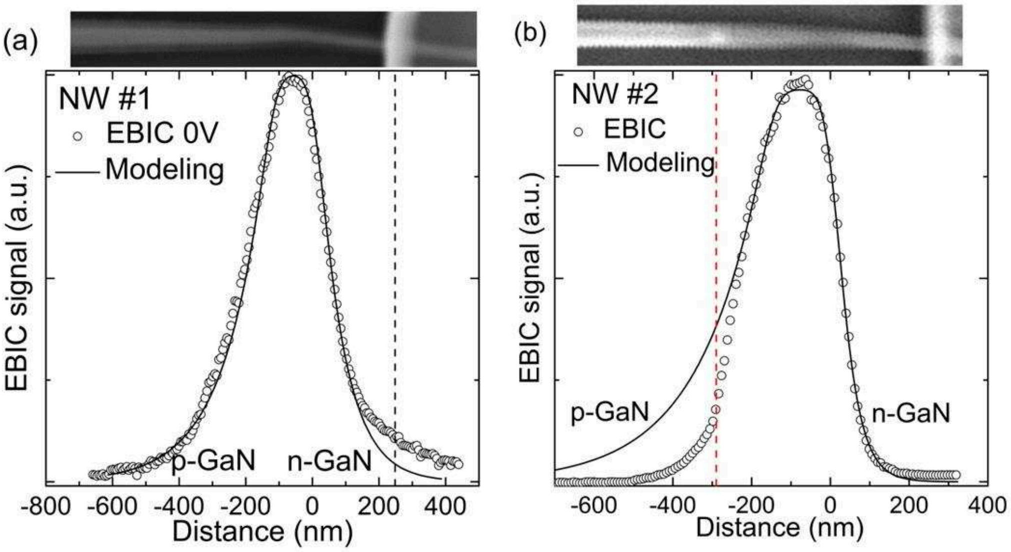

Figure 3.34 The modeling of the EBIC signal from the p-n junction under 0 V for NW #1 (a) and #2 (b). (a) The modeling parameters for NW #1 are: W = 116 nm, $L_{e,p}$ = 122 nm, $L_{h,n}$ = 77 nm, the black dashed line delineates the edge of the ITO contact on n-GaN. (b) The modeling parameters for NW #2 are: W = 125 nm, $L_{e,p}$ = 170 nm, $L_{h,n}$ = 40 nm, and the red dashed line locates the position of the “dust” on the p-GaN in NW #2. The x-axes are shifted according to the modeling so that the junction is at 0 nm.

For both NW #1 & #2, the n-GaN part is metallic at a Si donor doping concentration of 2-3×10^{18} cm^{-3}, thus the electron concentration in this part n = N_d = 2-3×10^{18} cm^{-3}. And this value is much higher than the densities of the excited excess carriers created by the e-beam (4×10^{14} cm^{-3} for NW #1 and 1×10^{15} cm^{-3} for NW #2). Therefore, the low injection condition is satisfied on the n-GaN part, and $L_{h,n}$ represents the minority carrier (hole) diffusion length. On the other hand, the situation for the p-GaN part is complicated. With acceptor doping level of (2.4-2.9)×10^{17} cm^{-3}, the hole concentration is in the range of 1×10^{15} cm^{-3}, considering an acceptor ionization energy of 245 meV [159]. Moreover, as discussed before, the p-GaN part is possibly partially depleted due to surface states, which gives a free hole concentration lower than the densities of the excess carriers during EBIC measurements. Therefore, the low injection condition is probably not fulfilled on the p-GaN part, and the extracted value of $L_{e,p}$ is actually a result of both minority and majority carriers diffusion. The values of $L_{e,p}$ are listed in Table 3.7 as the modeling parameters of the EBIC signal, and thus will not be compared with the other $L_{e,p}$ values in the literature. In addition, the hole concentration level of 1×10^{15} cm^{-3} on p-GaN is consistent with the I-V measurements.

As revealed in 2.4.4, the NID NWs manifests a high inhomogenous non-intentional n-type doping ranging from 4×10^{17} to 6×10^{18} at/cm^{-3} from one NW to another. The discrepancy between NW #1 and NW #2 is probably originated from a different level of non-intentional doping. In particular, the non-intentional n-type doping is possibly lower in NW #1 than NW #2, signified by a higher $L_{h,n}$ value in NW #1. Moreover, this non-intentional doping could act as compensating donors in p-GaN part. Thus, although both NW #1 and NW #2 are from the same sample N1913, a higher acceptor doping level N_a is observed in NW #1 due to less compensation. In addition, this dissimilarity in non-intentional doping is also in agreement with the different I-V electrical behaviors between the two NWs.

Table 3.7 also lists the doping levels and carrier diffusion lengths on n-GaN and p-GaN in core-shell microwires [134] and bulk device [195]. The values of $L_{h,n}$ in these two NWs are on the order of the 50 nm and comparable to the reported values in GaN microwires and bulk device, suggesting that the surface recombination indeed does not play a role in our case.

Table 3.7 The doping levels and carrier diffusion lengths in NW #1&#2, microwires and bulk GaN extracted from EBIC measurements.

Parameters	**NW #1**	**NW #2**	**Microwire** [134]	**Bulk** [195]
N_d (cm^{-3})	2-3×10^{18}	2-3×10^{18}	3.5×10^{18}	Not mentioned
$L_{h,n}$ (nm)	77	40	15	70
N_a (cm^{-3})	(2.8-2.9)×10^{17}	(2.4-2.5)×10^{17}	3×10^{18}	Not mentioned
$L_{e,p}$ (nm)	122	170	57	80

The influence of external voltages The same modeling procedures has been performed on the EBIC negative bias dependence signals for NW #1 in Figure 3.35. The same as in Figure 3.34, the discrepancy between the modeling and the experimental data at the right foot of EBIC signals is a result of the n-contact. Concerning NW #2, the EBIC negative bias dependence signals are completely overlapped in the vicinity of the p-n junction. Therefore, the three parameters W, $L_{e,p}$, $L_{h,n}$ are considered the same at different negative biases.

Table 3.8 lists the modeling parameters for each EBIC signal of NW #1 and #2 at different biases. The error bars represent the range of the parameter values where the modeling curve and the experimental data seems overlapped by naked eyes. As discussed before, both minority and majority carriers diffusion contribute to the EBIC current in the p-GaN part since the low injection condition is not satisfied. The value of $L_{e,p}$ is listed here only for further reference. In terms of $L_{h,n}$ in the n-GaN part, the extracted values from the modeling do not seem to vary much with changing voltages, keeping at 75 nm for NW #1 and 40 nm for NW #2 in average.

According to equation (3.5), a linear characteristic is expected between the square of the depletion width (W^2) and the applied voltage (V_{pn}). Thus, W^2 is plotted as a function of the applied voltage V in Figure 3.36. Contrary to the dashed theoretical lines, the W^2

value increases maybe a little with the rising negative voltage for NW #1, and it was considered at the same value for NW #2. This disagreement can be explained by the presence of the highly resistive and possibly partial depleted p-GaN part. The p-GaN part and the p-n junction are connected in series, and the most of the applied voltage will drop on the p-GaN part which is more resistive. The voltage at the boundary of the p-n junction equals to the bias voltage minus the voltage at the boundary of the p-region. In this case, no or limited depletion width extension of the p-n junction is observed under increasing negative biases. Since the acceptor doping level is lower in NW #2 (more resistive), the W^2 does not change for NW #2, while it increases only a little with the rising negative voltage for NW #1.

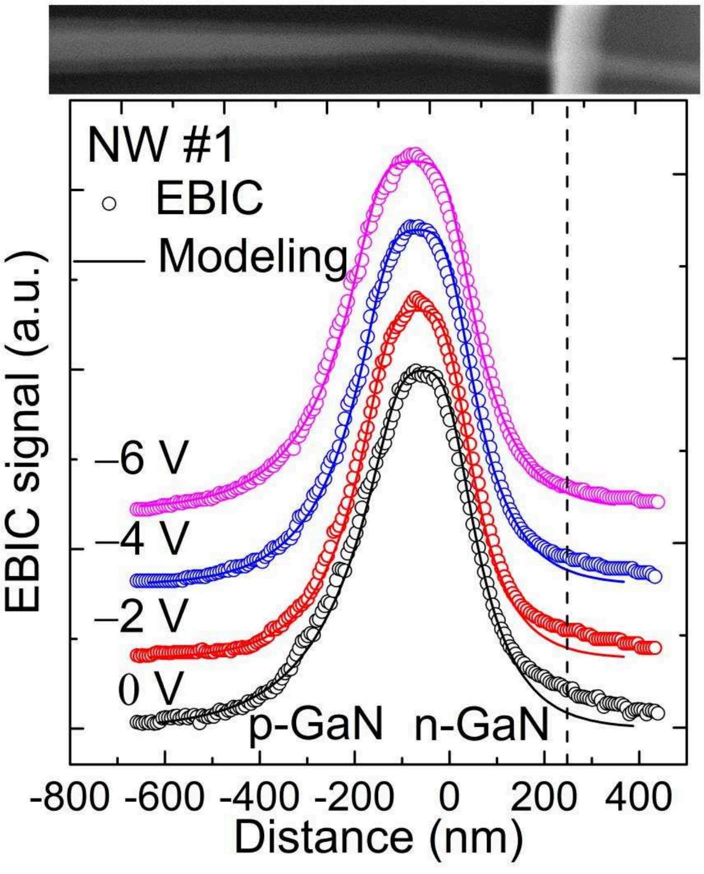

Figure 3.35 The modeling of the EBIC signals from the p-n junction under different negative voltages for NW #1. The EBIC signals under different negative voltages are shifted vertically for clarity, the values of the y-axis have no physical meaning. The black dashed line delineates the edge of the ITO contact on n-GaN. The modeling parameters are listed in Table 3.8.

Table 3.8 Modeling parameters bias dependent EBIC signals of NW #1 & #2.

	Applied Voltage V_{pn} (V)	**W (nm)**	**$L_{e, p}$ (nm)**	**$L_{h, n}$ (nm)**
NW #1	0	116 ± 20	122 ± 15	77 ± 15
	−2	135 ± 20	90 ± 15	69 ± 15
	−4	136 ± 20	100 ± 15	76 ± 15
	−6	153 ± 20	108 ± 15	80 ± 15
NW #2	0; −2.5; −5; −7.5; −10	125 ± 20	170 ± 15	40 ± 15

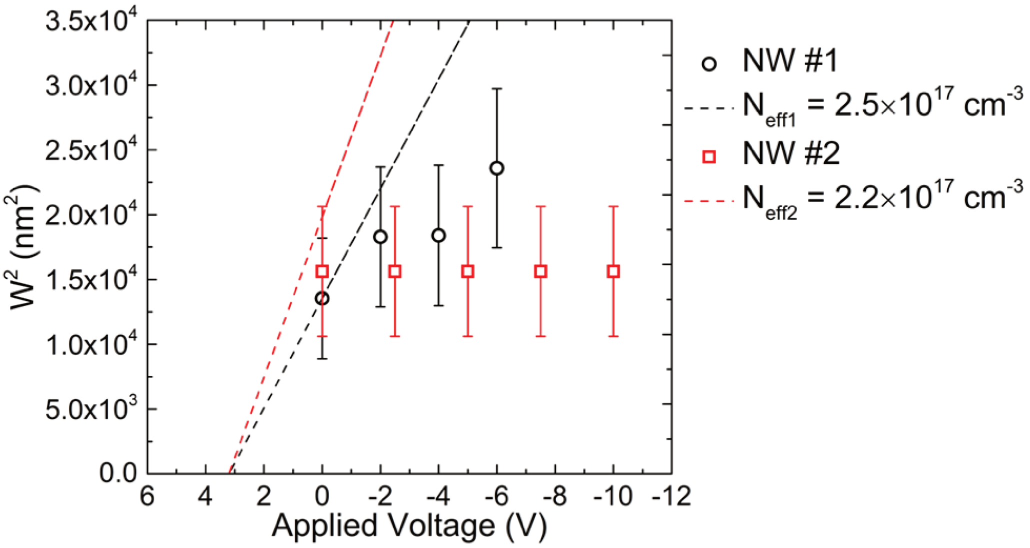

Figure 3.36 The square of the depletion width as a function of the applied voltages for NW #1 & #2. The black (NW #1) and red (NW #2) dashed lines demonstrate a theoretical relationship between W^2 and V_{pn} from equation (3.5), taking V_{bi} = 3.2 V and the depletion width values at 0 V bias for each NW.

3.2.4 Secondary electron voltage contrast (VC) of the p-n junction

As mentioned in the beginning of this chapter, SEM VC has been employed to delineate the electrostatic potentials across a p-n junction, and deduce doping levels in core-shell [134] and axial p-n junction wires [141]. It has been often reported that the p-doped region appears brighter than n-doped regions due to a difference of secondary electron escape depth from the surface [206]. However, the SEM VC across a p-n junction is a complex phenomenon influenced not only by physical factors, such as the n and p doping level and the topography of the sample, but also by many experimental factors, such as magnification, electron dose, e-beam energy, working distance, extractor voltage and surface treatment as reported in the literature [207]–[210].

In this study, the SEM images are taken before the EBIC images under each bias, serving not only as the references for lateral alignment of EBIC images, but also as the observation for VC. The experimental factors are the following: an Everhart-Thornley detector with 258 grid bias, 14 mm typical working distance, magnification of 80000, ~1 μm^2 image dimension, e-beam energy of 4-5 keV, and e-beam current of 4.6 pA.

As shown in Figure 3.24 and Figure 3.26, the SEM images for NW #1 are not very clear due to the beam scanning pollutions, whereas a clear SEM VC is observed in the neighborhood of the p-n junction for NW #2. Therefore, the following discussion only concerns NW #2.

As witnessed in Figure 3.26, the p-GaN part appears to be whiter than the n-GaN, and this contrast enhances with increasing negative bias and reduces with increasing positive bias. For more quantitative analysis, the SEM profiles of NW #2 under different biases are plotted in Figure 3.37. Indeed, a bias dependent SEM contrast is observed in the neighborhood of the p-n junction (the red dashed rectangle). Meanwhile, the "dust" on the p-GaN has appeared as a small peak in the SEM profile. In addition, the morphological shape of the NW could also influence the SEM signal.

The SEM contrast in the vicinity of the p-n junction (around 600 nm length) under negative bias has been fitted according to the parabolic potential equation in ideal abrupt p-n junction in Figure 3.38. Surprisingly, the depletion width of the p-n junction extracted from the fitting reduces with increasing negative voltages. From the previous EBIC analysis, we know that the depletion width does not change much with respect to the applied voltages. One possible reason of this disparity is the e-beam contamination during SEM and EBIC observations. As shown in Figure 3.39, the e-beam contamination is obvious when we compare the SEM image of NW #2 before (a) and after (b) EBIC measurements. The e-beam seems to deposit a hydrocarbon layer around the surface of the NW, which enlarges the NW diameter and reduces the emission of the secondary electrons. Therefore, in our case, SEM VC is very limited for determining the doping levels on each side of the p-n junction.

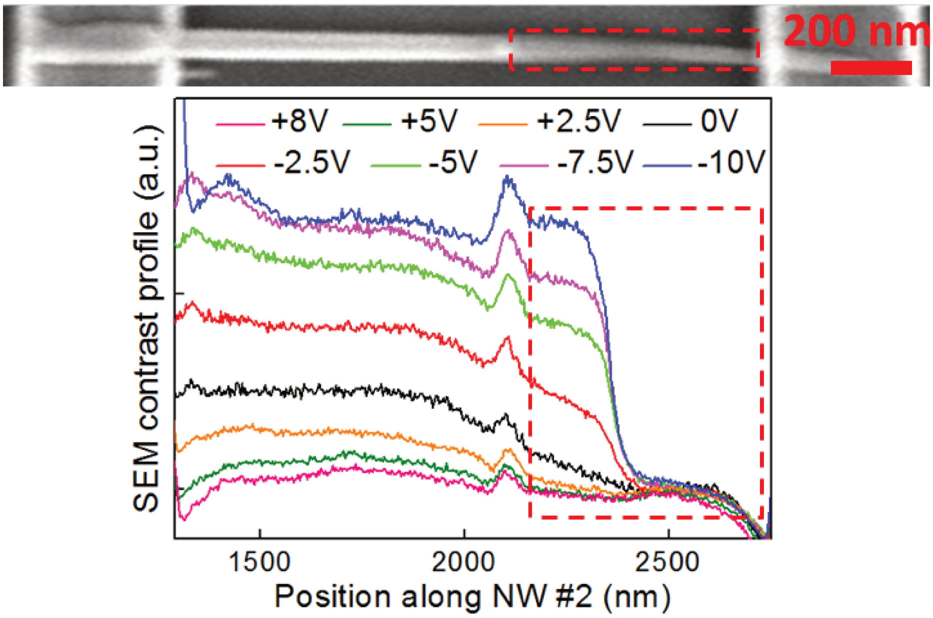

Figure 3.37 SEM contrast profile along the NW #2 under different biases from −10 V to +5V. A SEM image is placed on the top to show the relative position on the NW. The red dashed rectangle delineates the area of interest containing the p-n junction, which will be fitted in Figure 3.38.

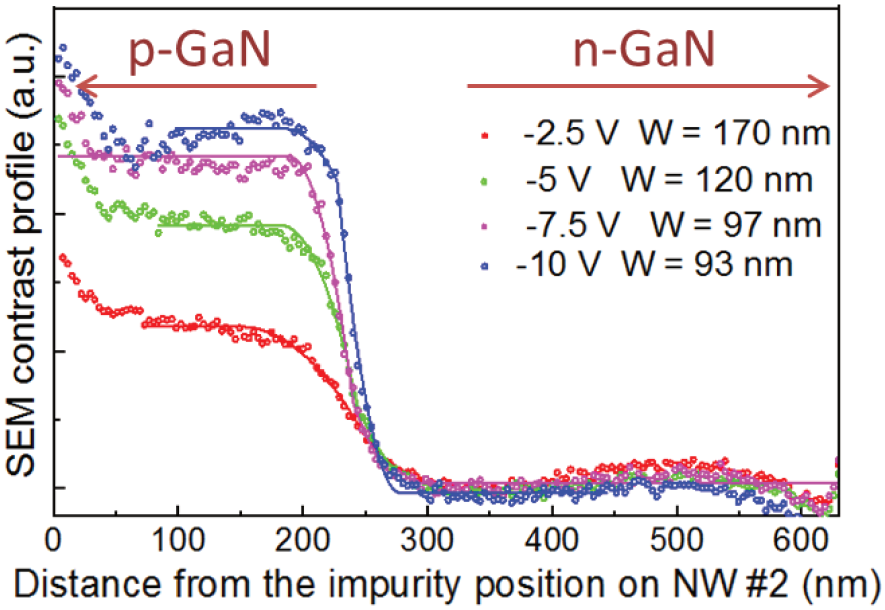

Figure 3.38 The fitting of the SEM voltage contrast profile from the impurity position on p-GaN to the n-contact.

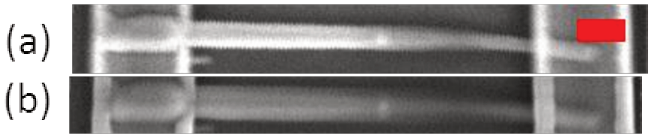

Figure 3.39 Two SEM images of NW #2 (a) before and (b) after the EBIC measurements under 0 V. The scale bar is 200 nm.

3.3 Conclusions of the chapter

In this chapter, the MBE growth conditions of Mg-doped and axial GaN p-n junction NWs have been explored in order to achieve significant Mg incorporation, and the electrical properties of the axial GaN p-n junction NWs have been investigated using EBIC technique.

In particular, Mg cell temperature and growth substrate temperature have been found to play an important role in Mg incorporation in the PA-MBE system. A two-step growth method has been proposed for improving Mg incorporation and employed for the growth of axial GaN p-n junction NWs.

EBIC technique imaged the presence of the p-n junction in two single NWs and clearly demonstrated its operation under reverse and forward polarization. The acceptor doping level was determined to be around 2-3×10^{17} cm^{-3}, taking the donor doping level at 2-3×10^{18} cm^{-3} estimated from the results of Chapter 2. The hole diffusion length in n-GaN was measured to be 75 nm for NW #1 and 43 nm for NW #2. Under positive bias, EBIC reveals the high resistive nature of the p-GaN, which is consistent with reduced p-n junction depletion width extension under negative bias. In addition, SEM VC technique has been found to be limited in our case due to e-beam contaminations. Last but not the least, ITO contact has been shown to form an ohmic or quasiohmic contact on n and p-type GaN NWs.

CONCLUSIONS AND PROSPECTS

The aim of this PhD work was to investigate the n and p-type doping of GaN NWs. To do so, two extensive studies have been dedicated to Si-doped GaN NWs and axial GaN p-n junction NWs. The NWs were grown by plasma-assisted molecular beam epitaxy and a combination of optical, structural, and electrical characterization techniques was employed. In particular, it has to be stressed that there were almost no direct electrical measurements on GaN NWs at the beginning of this PhD. The current work advances the field by demonstrating the experimental evidence of a p-n junction in GaN NW.

Si-doped GaN NWs

Regarding n-type doping, I have presented a systematic investigation on a series of Si-doped GaN NWs grown at the same conditions except Si cell temperatures.

The incorporation of Si induces a morphological variation of the NWs at Si cell temperature above 938 °C. A widening of the NW was observed and the top facets of the NW switched from 6-fold symmetry to 12-fold symmetry when Si cell temperature reached 950 °C. A broadening of the near-band edge emission peak and a rising of the donor-acceptor pair emission in photoluminescence spectra have been recognized upon Si doping. Several Si related defect modes have been observed on Raman spectra, and a tensile strain related with E_{2h} mode frequency variation, increases with Si cell temperature until 950 °C, where the relaxation occurs. The Si content mapping at the nanoscale by energy-dispersive X-ray spectroscopy helps to elucidate the above observations. NWs grown with Si cell temperature of 950 °C were shown to have a core with an average Si concentration of 2.5×10^{20} at/cm^3 and an outer part with Si concentration of 6.5×10^{20} at/cm^3, whereas the NWs with Si cell temperature of 938 °C contains a homogenous Si distribution of 1×10^{20} at/cm^3. More Si can be incorporated in GaN NWs compared to 2D layer counterparts.

A NW contacting process based on electron beam lithography has been developed to perform electrical measurements on single NWs. Direct transport measurements on single Si-doped NWs have shown a controlled doping with resistivity from 10^2 to 10^{-3} Ω.cm, and a carrier concentration from 10^{17} to 10^{20} cm^{-3}. FET measurements combined with 2D finite element simulation have shown a high mobility in these NWs, comparable to the state of the art mobility value of GaN epilayer.

GaN p-n junction NWs

Regarding the second part of the manuscript, the MBE growth conditions of Mg-doped and axial GaN p-n junction NWs have been explored in order to achieve significant Mg incorporation, and the electrical properties of the axial GaN p-n junction NWs have been investigated using EBIC technique.

In particular, Mg cell temperature and growth substrate temperature have been found to play an important role in Mg incorporation in the PA-MBE system. A two-step growth method has been proposed for improving Mg incorporation and employed for the growth of axial GaN p-n junction NWs.

EBIC technique has visualized the presence of the p-n junction in two single NWs and clearly demonstrated its operation under reverse and forward polarization. The acceptor doping level was determined to be around $2\text{-}3\times10^{17}$ cm^{-3}, taking the donor doping level at $2\text{-}3\times10^{18}$ cm^{-3} estimated from the results of Si-doped GaN NWs. The hole diffusion length in n-GaN was measured to be 75 nm for NW #1 and 43 nm for NW #2. Under positive bias, EBIC reveals the high resistive nature of the p-GaN, which is consistent with reduced p-n junction depletion width extension under negative bias. In addition, SEM VC technique has been found to be limited in our case due to e-beam contaminations. Last but not the least, ITO contact has been shown to form an ohmic or quasiohmic contact on n and p-type GaN NWs.

Prospects

As estimated by the EBIC measurements in Chapter 3, the Mg doping level achieved on axial GaN p-n junction NWs is around $2\text{-}3\times10^{17}$ cm^{-3}, which still has some distance compared to the Mg concentration in the state of art Mg-doped GaN epilayers listed in Table 3.1. Therefore, it would be interesting to improve the Mg content in GaN p-n junction NWs and perform EBIC measurements on them. With a less resistive p-GaN, more voltages will drop on the boundary of the p-n junction, thus typical behaviors such as depletion width extension under increasing negative bias could be observed.

Moreover, ITO was found to achieve quasiohimic contact on p-GaN NWs, and the detailed contact formation mechanism is beyond the scope of the thesis. The investigation on the ITO contact formation would be beneficial for GaN NWs, even III-nitrides NWs based devices.

The following of this work

The work presented in this manuscript not only provides guidelines for the fabrication of the GaN NW based devices, but also demonstrates a good protocol for studying the doping of other III-nitride NWs. Indeed, a new ANR project called EMOUVAN (emission de lumière UV avec des nanofils) has been launched recently. Under the frame of this project, Madalina Siladie has started her thesis on the MBE growth and electrical transport properties of AlGaN NWs since October 2016. I hope that the knowledge and technological process developed in the current work will help to progress the study on these NWs.

REFERENCES

[1] H. Amano, N. Sawaki, I. Akasaki, and Y. Yoyoda, “Metalorganic vapor phase epitaxial growth of a high quality GaN film using an AlN buffer layer,” Appl. Phys. Lett., vol. 48, pp. 353–355, 1986.

[2] S. Nakamura, T. Mukai, and M. Senoh, “Thermal annealing effects on p-type Mg-doped GaN films,” Jpn. J. Appl. Phys, vol. 31, pp. L139–L142, 1992.

[3] H. Amano, M. Kito, K. Hiramatsu, and I. Akasaki, “p-type conduction in Mg-doped GaN treated with low-energy electron beam irradiation (LEEBI),” Jpn. J. Appl. Phys., vol. 28, pp. L2112–L2114, 1989.

[4] S. Nakamura, T. Mukai, and M. Senoh, “Candela-class high-brightness InGaN/AlGaN double-heterostructure blue-light-emitting diodes,” Appl. Phys. Lett., vol. 64, pp. 1687–1689, 1994.

[5] S. Nakamura, M. Senoh, S. ichi Nagahama, N. Iwasa, T. Yamada, T. Matsushita, H. Kiyoku, and Y. Sugimoto, “InGaN-based multi-quantum-well-structure laser diodes,” Jpn. J. Appl. Phys., vol. 35, pp. L74–L76, 1996.

[6] K. Yoshizawa, M. Kikuchi, A. Mori, M. Fujita, N. Kishino, “Growth of self-organized GaN nanostructures on Al2O3 (0001) by RF-radical source molecular beam epitaxy,” Jpn. J. Appl. Phys., vol. 36, pp. L459–L462, 1997.

[7] M. A. Sanchez-Garcia, E. Calleja, E. Monroy, F. J. Sanchez, F. Calle, E. Munoz, and R. Beresford, “The effect of the III/V ratio and substrate temperature on the morphology and properties of GaN- and AlN-layers grown by molecular beam epitaxy on Si(1 1 1),” J. Cryst. Growth, vol. 183, pp. 23–30, 1998.

[8] S. Zhao, H. P. T. Nguyen, M. G. Kibria, and Z. Mi, “III-nitride nanowire optoelectronics,” Prog. Quantum Electron., vol. 44, pp. 14–68, 2015.

[9] H. Morkoç, Handbook of Nitride Semiconductors and Devices, Materials Properties, Physics and Growth. Wiley, 2009.

[10] J. Wu, “When group-III nitrides go infrared: new properties and perspectives,” J. Appl. Phys., vol. 106, p. 11101, 2009.

[11] T. Zhu and R. A. Oliver, “Unintentional doping in GaN,” Phys. Chem. Chem.

Phys., vol. 14, pp. 9558–9573, 2012.

[12] S. Keller, H. Li, M. Laurent, Y. Hu, N. Pfaff, J. Lu, D. F. Brown, N. a Fichtenbaum, J. S. Speck, S. P. Denbaars, and U. K. Mishra, "Recent progress in metal-organic chemical vapor deposition of (000-1) N-polar group-III nitrides," Semicond. Sci. Technol., vol. 29, p. 113001, 2014.

[13] S. W. Kaun, "Growth optimization of metal-polar III-nitride high-electron-mobility transistor structures by molecular beam epitaxy," University of California Santa Barbara, 2014.

[14] M. Suzuki, T. Uenoyama, and A. Yanase, "First-principles calculations of effective-mass parameters of AlN and GaN," Phys. Rev. B, vol. 52, pp. 8132–8139, 1995.

[15] F. Bernardini, V. Fiorentini, and D. Vanderbilt, "Spontaneous polarization and piezoelectric constants of III-V nitrides," Phys. Rev. B, vol. 56, pp. R10024-10027, 1997.

[16] R. Dwiliński, R. Doradziński, J. Garczyński, L. P. Sierzputowski, A. Puchalski, Y. Kanbara, K. Yagi, H. Minakuchi, and H. Hayashi, "Excellent crystallinity of truly bulk ammonothermal GaN," J. Cryst. Growth, vol. 310, pp. 3911–3916, 2008.

[17] Y. Mori, M. Imade, K. Murakami, H. Takazawa, H. Imabayashi, Y. Todoroki, K. Kitamoto, M. Maruyama, M. Yoshimura, Y. Kitaoka, and T. Sasaki, "Growth of bulk GaN crystal by Na flux method under various conditions," J. Cryst. Growth, vol. 350, pp. 72–74, 2012.

[18] I. Grzegory, "High pressure growth of bulk GaN from solutions in gallium," J. Phys. Condens. Matter, vol. 13, pp. 6875–6892, 2001.

[19] K. Motoki, "Development of gallium nitride substrates," SEI Tech. Rev., vol. 70, pp. 28–35, 2010.

[20] L. Liu and J. H. Edgar, "Substrates for gallium nitride epitaxy," Mater. Sci. Eng. R Reports, vol. 37, pp. 61–127, 2002.

[21] W. P. McCray, "MBE deserves a place in the history books," Nat. Nanotechnol., vol. 2, pp. 259–261, 2007.

[22] A. Y. Cho, "How molecular beam epitaxy (MBE) began and its projections into the future," J. Cryst. Growth, vol. 201/202, pp. 1–7, 1999.

[23] B. A. Joyce and T. B. Joyce, "Basic studies of molecular beam epitaxy - past, present and some future directions," J. Cryst. Growth, vol. 264, pp. 605–619, 2004.

[24] G. Biasiol and L. Sorba, "Molecular beam epitaxy: principles and applications," Cryst. growth Mater. energy Prod. energy-saving Appl., pp. 66–83, 2001.

[25] H. P. Maruska and J. J. Tietjen, "The preparation and properties of vapor-deposited single-crystal-line GaN," Appl. Phys. Lett., vol. 15, pp. 327–329, 1969.

[26] H. M. Manasevit, F. M. Erdmann, and W. I. Simpson, "The use of metalorganics in the preparation of semiconductor materials," J. Electrochem. Soc. solid state Sci., vol. 118, pp. 1864–1867, 1971.

[27] P. Bogusławski and J. Bernholc, "Doping properties of C, Si, and Ge impurities in GaN and AlN," Phys. Rev. B, vol. 56, pp. 9496–9505, 1997.

[28] J. Neugebauer and C. G. Van De Walle, “Native defects and impurities in GaN,” Adv. Solid State Phys., vol. 35, p. 25, 1996.

[29] P. Prystawko, M. Leszczynski, B. Beaumont, P. Gibart, E. Frayssinet, W. Knap, P. Wisniewski, M. Bockowski, T. Suski, and S. Porowski, “Doping of Homoepitaxial GaN Layers,” Phys. Status Solidi, vol. 210, pp. 437–443, 1998.

[30] M. Leroux, B. Beaumont, N. Grandjean, P. Lorenzini, S. Haffouz, P. Venne, J. Massies, and P. Gibart, “Luminescence and reflectivity studies of undoped , n- and p-doped GaN on (0001) sapphire,” Mater. Sci. Eng. B, vol. 50, pp. 97–104, 1997.

[31] P. R. Hageman, W. J. Schaff, J. Janinski, and Z. Liliental-weber, “n-type doping of wurtzite GaN with germanium grown with plasma-assisted molecular beam epitaxy,” J. Cryst. Growth, vol. 267, pp. 123–128, 2004.

[32] R. Niebuhr, K. H. Bachem, U. Kaufmann, M. Maier, C. Merz, B. Santic, and P. Schlotter, “Electrical and optical properties of oxygen doped GaN grown by MOCVD using N_2O,” J. Electron. Mater., vol. 26, pp. 1127–1130, 1997.

[33] I. Lee, I. Choi, C. Lee, E. Shin, D. Kim, S. K. Noh, S. Son, K. Yong, H. J. Lee, I. Lee, I. Choi, S. Son, K. Y. Lim, and H. J. Lee, “Stress relaxation in Si-doped GaN studied by Raman spectroscopy,” J. Appl. Phys., vol. 83, p. 5787, 1998.

[34] J. Sánchez-Páramo, J. M. Calleja, M. A. Sánchez-García, and E. Calleja, “Optical investigation of strain in Si-doped GaN films,” Appl. Phys. Lett., vol. 78, pp. 4124–4126, 2001.

[35] Z. Chine, A. Rebey, H. Touati, E. Goovaerts, M. Oueslati, B. El Jani, and S. Laugt, “Stress and density of defects in Si-doped GaN,” Phys. Status Solidi, vol. 203, pp. 1954–1961, 2006.

[36] S. Zhao, A. T. Connie, M. H. T. Dastjerdi, X. H. Kong, Q. Wang, M. Djavid, S. Sadaf, X. D. Liu, I. Shih, H. Guo, and Z. Mi, “Aluminum nitride nanowire light emitting diodes: breaking the fundamental bottleneck of deep ultraviolet light sources,” Sci. Rep., vol. 5, p. 8332, 2015.

[37] Y. Huang, X. Duan, Y. Cui, and C. M. Lieber, “Gallium nitride nanowire nanodevices,” Nano Lett., vol. 2, pp. 101–104, Feb. 2002.

[38] K. Kishino, A. Kikuchi, H. Sekiguchi, and S. Ishizawa, “InGaN/GaN nanocolumn LEDs emitting from blue to red,” Proc. SPIE, vol. 6473, p. 64730T–1–64730T–12, 2007.

[39] J. C. Johnson, H.-J. Choi, K. P. Knutsen, R. D. Schaller, P. Yang, and R. J. Saykally, “Single gallium nitride nanowire lasers,” Nat. Mater., vol. 1, pp. 106–110, 2002.

[40] A. L. Bavencove, G. Tourbot, E. Pougeoise, J. Garcia, P. Gilet, F. Levy, B. André, G. Feuillet, B. Gayral, B. Daudin, and L. S. Dang, “GaN-based nanowires: from nanometric-scale characterization to light emitting diodes,” Phys. Status Solidi, vol. 207, pp. 1425–1427, 2010.

[41] F. Furtmayr, M. Vielemeyer, M. Stutzmann, J. Arbiol, S. Estradé, F. Peirò, J. R. Morante, and M. Eickhoff, “Nucleation and growth of GaN nanorods on Si (111) surfaces by plasma-assisted molecular beam epitaxy - The influence of Si- and Mg-doping,” J. Appl. Phys., vol. 104, no. 3, p. 34309, 2008.

[42] T. Stoica and R. Calarco, “Doping of III-nitride nanowires grown by molecular

beam epitaxy," IEEE J. Sel. Top. Quantum Electron., vol. 17, pp. 859–868, 2011.

[43] T. Richter, H. Lu, R. Meijers, R. Calarco, and M. Marso, "Doping concentration of GaN nanowires determined by opto-electrical measurements," Nano Lett., vol. 8, pp. 3056–3059, 2008.

[44] R. Calarco, M. Marso, T. Richter, A. I. Aykanat, R. Meijers, A. v. d. Hart, T. Stoica, and H. Luth, "Size-dependent photoconductivity in MBE-grown GaN - Nanowires," Nano Lett., vol. 5, pp. 981–984, 2005.

[45] L. M. Mansfield, K. A. Bertness, P. T. Blanchard, T. E. Harvey, A. W. Sanders, and N. A. Sanford, "GaN nanowire carrier concentration calculated from light and dark resistance measurements," J. Electron. Mater., vol. 38, pp. 495–504, 2009.

[46] N. A. Sanford, L. H. Robins, P. T. Blanchard, K. Soria, B. Klein, B. S. Eller, K. A. Bertness, J. B. Schlager, and A. W. Sanders, "Studies of photoconductivity and field effect transistor behavior in examining drift mobility, surface depletion, and transient effects in Si-doped GaN nanowires in vacuum and air," J. Appl. Phys., vol. 113, p. 174306, 2013.

[47] P. Parkinson, C. Dodson, H. J. Joyce, K. A. Bertness, N. A. Sanford, L. M. Herz, and M. B. Johnston, "Noncontact measurement of charge carrier lifetime and mobility in GaN nanowires," Nano Lett., vol. 12, pp. 4600–4604, 2012.

[48] K. Hestroffer, "Croissance et caractérisation de nanofils de GaN et d'hétérostructures filaires de GaN / AlN," Université Grenoble Alpes, 2012.

[49] A. L. Rosa, J. Neugebauer, J. E. Northrup, C. D. Lee, and R. M. Feenstra, "Adsorption and incorporation of silicon at GaN(0001) surfaces," Appl. Phys. Lett., vol. 80, pp. 2008–2010, 2002.

[50] J. A. GOLOVCHENKO, "The tunneling microscope: a new look at the atomic world," Science, vol. 232, pp. 48–53, 1986.

[51] R. Mata, K. Hestroffer, J. Budagosky, A. Cros, C. Bougerol, H. Renevier, and B. Daudin, "Nucleation of GaN nanowires grown by plasma-assisted molecular beam epitaxy: The effect of temperature," J. Cryst. Growth, vol. 334, pp. 177–180, 2011.

[52] O. Landré, R. Songmuang, J. Renard, E. Bellet-Amalric, H. Renevier, and B. Daudin, "Plasma-assisted molecular beam epitaxy growth of GaN nanowires using indium-enhanced diffusion," Appl. Phys. Lett., vol. 93, p. 183109, 2008.

[53] T. Auzelle, "Nanofils de GaN / AlN nucleation, polarité et hétérostructures quantiques," Université Grenoble Alpes, 2015.

[54] R. Langer, "The strains and their effects in semiconducting heterostructures of element III nitrides," Université de Grenoble 1, 2000.

[55] R. Songmuang, T. Ben, B. Daudin, D. González, and E. Monroy, "Identification of III-N nanowire growth kinetics via a marker technique," Nanotechnology, vol. 21, p. 295605, 2010.

[56] S. Fernández-Garrido, J. Grandal, E. Calleja, M. A. Sánchez-García, and D. López-Romero, "A growth diagram for plasma-assisted molecular beam epitaxy of GaN nanocolumns on Si(111)," J. Appl. Phys., vol. 106, p. 126102, 2009.

[57] S. Fernandez-Garrido, V. M. Kaganer, K. K. Sabelfeld, T. Gotschke, J. Grandal,

E. Calleja, L. Geelhaar, and O. Brandt, "Self-regulated radius of spontaneously formed GaN nanowires in molecular beam epitaxy," Nano Lett., vol. 13, pp. 3274–3280, 2013.

[58] V. Consonni, "Self-induced growth of GaN nanowires by molecular beam epitaxy: a critical review of the formation mechanisms," Phys. status solidi, vol. 7, pp. 699–712, 2013.

[59] R. Songmuang, O. Landré, and B. Daudin, "From nucleation to growth of catalyst-free GaN nanowires on thin AlN buffer layer," Appl. Phys. Lett., vol. 91, p. 251902, 2007.

[60] Z. Yang, L. K. Li, and W. I. Wang, "GaN grown by molecular beam epitaxy at high growth rates using ammonia as the nitrogen source," Appl. Phys. Lett., vol. 67, pp. 1686–1688, 1995.

[61] Y. Cordier, B. Damilano, P. Aing, C. Chaix, F. Linez, F. Tuomisto, P. Vennegues, E. Frayssinet, D. Lefebvre, M. Portail, and M. Nemoz, "GaN films and GaN/AlGaN quantum wells grown by plasma assisted molecular beam epitaxy using a high density radical source," J. Cryst. Growth, vol. 433, pp. 165–171, 2016.

[62] Y. Kawai, S. Chen, Y. Honda, M. Yamaguchi, H. Amano, H. Kondo, M. Hiramatsu, H. Kano, K. Yamakawa, S. Den, and M. Hori, "Achieving high-growth-rate in GaN homoepitaxy using high-density nitrogen radical source," Phys. Status Solidi, vol. 8, pp. 2089–2091, 2011.

[63] B. M. McSkimming, C. Chaix, and J. S. Speck, "High active nitrogen flux growth of GaN by plasma assisted molecular beam epitaxy," J. Vac. Sci. Technol. A, vol. 33, p. 05E128-1-05E128-9, 2015.

[64] B. M. McSkimming, F. Wu, T. Huault, C. Chaix, and J. S. Speck, "Plasma assisted molecular beam epitaxy of GaN with growth rates > 2.6µm/h," J. Cryst. Growth, vol. 386, pp. 168–174, 2014.

[65] L. Rigutti, G. Jacopin, A. D. L. Bugallo, M. Tchernycheva, E. Warde, F. H. Julien, R. Songmuang, E. Galopin, L. Largeau, and J.-C. Harmand, "Investigation of the electronic transport in GaN nanowires containing GaN/AlN quantum discs," Nanotechnology, vol. 21, p. 425206, 2010.

[66] B. Monemar, P. P. Pasko, T. Pasko, J. P. Bergman, G. Pozina, W. M. Chen, P. N. Hai, I. A. Buyano, H. Amano, and I. Akasaki, "Optical characterization of III-nitrides," Mater. Sci. Eng. B, vol. 93, pp. 112–122, 2002.

[67] T. Auzelle, B. Haas, M. Den Hertog, J.-L. Rouvière, B. Daudin, and B. Gayral, "Attribution of the 3.45 eV GaN nanowires luminescence to inversion domain boundaries," Appl. Phys. Lett., vol. 107, p. 51904, 2015.

[68] E. Calleja, M. A. Sánchez-Garciá, F. J. Sánchez, F. Calle, F. B. Naranjo, E. Muñoz, U. Jahn, and K. Ploog, "Luminescence properties and defects in GaN nanocolumns grown by molecular beam epitaxy," Phys. Rev. B, vol. 62, pp. 16826–16834, 2000.

[69] M. A. Reshchikov and H. Morkoç, "Luminescence properties of defects in GaN," J. Appl. Phys., vol. 97, pp. 1–95, 2005.

[70] K. Kornitzer, T. Ebner, K. Thonke, R. Sauer, C. Kirchner, V. Schwegler, M. Kamp, M. Leszczynski, I. Grzegory, and S. Porowski, "Photoluminescence and

reflectance spectroscopy of excitonic transitions in high-quality homoepitaxial GaN films," Phys. Rev. B, vol. 60, pp. 1471–1473, 1999.

[71] M. Yoshikawa, M. Kunzer, J. Wagner, H. Obloh, P. Schlotter, R. Schmidt, N. Herres, and U. Kaufmann, "Band-gap renormalization and band filling in Si-doped GaN films studied by photoluminescence spectroscopy," J. Appl. Phys., vol. 86, pp. 4400–4402, 1999.

[72] M. Feneberg, S. Osterburg, K. Lange, C. Lidig, B. Garke, and R. Goldhahn, "Band gap renormalization and Burstein-Moss effect in silicon- and germanium-doped wurtzite GaN up to 10^{20} cm^{-3}," Phys. Rev. B, vol. 90, p. 75203, 2014.

[73] A. Wolos, Z. Wilamowski, M. Piersa, W. Strupinski, B. Lucznik, I. Grzegory, and S. Porowski, "Properties of metal-insulator transition and electron spin relaxation in GaN:Si," Phys. Rev. B, vol. 83, p. 165206, 2011.

[74] E. F. Schubert, I. D. Goepfert, W. Grieshaber, and J. M. Redwing, "Optical properties of Si-doped GaN," Appl. Phys. Lett., vol. 71, pp. 921–924, 2001.

[75] E. Iliopoulos, D. Doppalapudi, H. M. Ng, and T. D. Moustakas, "Broadening of near-band-gap photoluminescence in n-GaN films," Appl. Phys. Lett., vol. 73, pp. 375–377, 1998.

[76] F. Furtmayr, M. Vielemeyer, M. Stutzmann, A. Laufer, B. K. Meyer, and M. Eickhoff, "Optical properties of Si- and Mg-doped gallium nitride nanowires grown by plasma-assisted molecular beam epitaxy," J. Appl. Phys., vol. 104, p. 74309, 2008.

[77] J. Desheng, Y. Makita, K. Ploog, and H. J. Queisser, "Electrical properties and photoluminescence of Te-doped GaAs grown by molecular beam epitaxy," J. Appl. Phys., vol. 53, p. 999, 2001.

[78] H. Tang and J. B. Webb, "Growth of high mobility GaN by ammonia-molecular beam epitaxy," Appl. Phys. Lett., vol. 74, pp. 2373–2374, 1999.

[79] D. Sam-Giao, "Optical study of GaN nanowires and GaN / AlN microcavities," Université Grenoble Alpes, 2012.

[80] C. V. Raman, "A Change of Wave-length in Light Scattering," Nature, vol. 121. pp. 619–619, 1928.

[81] U. Haboeck, H. Siegle, A. Hoffmann, and C. Thomsen, "Lattice dynamics in GaN and AlN probed with first- and second-order Raman spectroscopy," Phys. Status Solidi, vol. 0, pp. 1710–1731, 2003.

[82] P. Perlin, J. Camassel, W. Knap, T. Taliercio, J. C. Chervin, T. Suski, I. Grzegory, and S. Porowski, "Investigation of longitudinal-optical phonon-plasmon coupled modes in highly conducting bulk GaN," Appl. Phys. Lett., vol. 67, pp. 2524–2526, 1995.

[83] T. Kozawa, T. Kachi, H. Kano, Y. Taga, M. Hashimoto, N. Koide, and K. Manabe, "Raman scattering from LO phonon-plasmon coupled modes in gallium nitride," J. Appl. Phys., vol. 75, pp. 1098–1101, 1994.

[84] R. Mata, A. Cros, K. Hestroffer, and B. Daudin, "Surface optical phonon modes in GaN nanowire arrays: dependence on nanowire density and diameter," Phys. Rev. B, vol. 85, p. 35322, 2012.

[85] K. Jeganathan, R. K. Debnath, R. Meijers, T. Stoica, R. Calarco, D. Grützmacher,

and H. Lüth, "Raman scattering of phonon-plasmon coupled modes in self-assembled GaN nanowires," J. Appl. Phys., vol. 105, p. 123707, 2009.

[86] D. Wang, C. C. Tin, J. R. Williams, M. Park, Y. S. Park, C. M. Park, T. W. Kang, and W. C. Yang, "Raman characterization of electronic properties of self-assembled GaN nanorods grown by plasma-assisted molecular-beam epitaxy," Appl. Phys. Lett., vol. 87, p. 242105, 2005.

[87] P. Tchoulfian, F. Donatini, F. Levy, B. Amstatt, A. Dussaigne, P. Ferret, E. Bustarret, and J. Pernot, "Thermoelectric and micro-Raman measurements of carrier density and mobility in heavily Si-doped GaN wires," Appl. Phys. Lett., vol. 103, p. 202101, 2013.

[88] P. Perlin, C. Jauberthie-carillon, J. P. Itic, A. S. Miguel, and A. Polian, "Raman scattering and x-ray absorption spectroscopy in GaN under high pressure," Phys. Rev. B, vol. 45, pp. 83–89, 1992.

[89] R. Cuscó, L. Artús, D. Pastor, F. B. Naranjo, and E. Calleja, "Local vibrational modes of H complexes in Mg-doped GaN grown by molecular beam epitaxy," Appl. Phys. Lett., vol. 84, pp. 897–899, 2004.

[90] S. Fritze, A. Dadgar, H. Witte, M. Bügler, A. Rohrbeck, J. Bläsing, A. Hoffmann, and A. Krost, "High Si and Ge n-type doping of GaN doping - Limits and impact on stress," Appl. Phys. Lett., vol. 100, p. 122104, 2012.

[91] V. Y. Davydov, N. S. Averkiev, I. N. Goncharuk, D. K. Nelson, I. P. Nikitina, A. S. Polkovnikov, A. N. Smirnov, M. A. Jacobson, and O. K. Semchinova, "Raman and photoluminescence studies of biaxial strain in GaN epitaxial layers grown on 6H-SiC," J. Appl. Phys., vol. 82, pp. 5097–5102, 1997.

[92] M. Watanabe and D. B. Williams, "The quantitative analysis of thin specimens: A review of progress from the Cliff-Lorimer to the new ζ-factor methods," J. Microsc., vol. 221, pp. 89–109, 2006.

[93] J.-L. Pouchou and F. Pichoir, "Quantitative Analysis of Homogeneous or Stratified Microvolumes Applying the Model 'PAP,'" in Electron Probe Quantitation, K. F. J. Heinrich and D. E. Newbury, Eds. Boston, MA: Springer US, 1991, pp. 31–75.

[94] J. Neugebauer, "Surfactants and antisurfactants on group-III-nitride surfaces," Phys. Status Solidi, vol. 0, pp. 1651–1667, 2003.

[95] F. Schuster, A. Winnerl, S. Weiszer, M. Hetzl, J. A. Garrido, and M. Stutzmann, "Doped GaN nanowires on diamond: Structural properties and charge carrier distribution," J. Appl. Phys., vol. 117, p. 44307, 2015.

[96] L. Largeau, D. L. Dheeraj, M. Tchernycheva, G. E. Cirlin, and J. C. Harmand, "Facet and in-plane crystallographic orientations of GaN nanowires grown on Si(111)," Nanotechnology, vol. 19, p. 155704, 2008.

[97] J. Northrup and J. Neugebauer, "Theory of GaN(10-10) and (11-20) surfaces," Phys. Rev. B, vol. 53, pp. R10477–R10480, 1996.

[98] A. D. L. Bugallo, M. Tchernycheva, G. Jacopin, L. Rigutti, F. H. Julien, S.-T. Chou, Y.-T. Lin, P.-H. Tseng, and L.-W. Tu, "Visible-blind photodetector based on p-i-n junction GaN nanowire ensembles," Nanotechnology, vol. 21, p. 315201, 2010.

[99] K. Storm, F. Halvardsson, M. Heurlin, D. Lindgren, A. Gustafsson, P. M. Wu, B.

Monemar, and L. Samuelson, “Spatially resolved Hall effect measurement in a single semiconductor nanowire,” Nat. Nanotechnol., vol. 7, pp. 718–722, 2012.

[100] O. Hultin, G. Otnes, M. T. Borgström, M. Björk, L. Samuelson, and K. Storm, “Comparing hall effect and field effect measurements on the same single nanowire,” Nano Lett., vol. 16, pp. 205–211, 2016.

[101] J. P. Degrave, D. Liang, and S. Jin, “A general method to measure the hall effect in nanowires: examples of FeS_2 and MnSi,” Nano Lett., vol. 13, pp. 2704–2709, 2013.

[102] J. Tang, G. Yu, C.-Y. Wang, L.-T. Chang, W. Jiang, C. He, and K. L. Wang, “Versatile fabrication of self-aligned nanoscale hall devices using nanowire masks,” Nano Lett., vol. 16, p. 3109−3115, 2016.

[103] C. Blömers, T. Grap, M. I. Lepsa, J. Moers, S. Trellenkamp, D. Grützmacher, H. Lüth, and T. Schäpers, “Hall effect measurements on InAs nanowires,” Appl. Phys. Lett., vol. 101, no. 15, 2012.

[104] R. M. Langford, T.-X. Wang, M. Thornton, A. Heidelberg, J. G. Sheridan, W. Blau, and R. Leahy, “Comparison of different methods to contact to nanowires,” J. Vac. Sci. Technol. B, vol. 24, pp. 2306–2311, 2006.

[105] A. M. Lord, T. G. Maffeis, A. S. Walton, D. M. Kepaptsoglou, Q. M. Ramasse, M. B. Ward, J. Köble, and S. P. Wilks, “Factors that determine and limit the resistivity of high-quality individual ZnO nanowires,” Nanotechnology, vol. 24, p. 435706, 2013.

[106] F. Hernández-Ramírez, J. Rodríguez, O. Casals, E. Russinyol, A. Vilà, A. Romano-Rodríguez, and M. Abid, “Characterization of metal-oxide nanosensors fabricated with focused ion beam (FIB),” Sensors Actuators B Chem., vol. 118, pp. 198–203, 2006.

[107] T. Richter, H. Luth, R. Meijers, R. Calarco, and M. Marso, “Doping concentration of GaN nanowires determined by opto-electrical measurements,” Nano Lett., vol. 8, pp. 3056–3059, 2008.

[108] F. Donatini and L. S. Dang, “A single-step electron beam lithography of buried nanostructures using cathodoluminescence imaging and low temperature,” Nanotechnology, vol. 21, p. 375303, 2010.

[109] P. Tchoulfian, F. Donatini, F. Levy, B. Amstatt, P. Ferret, and J. Pernot, “High conductivity in Si-doped GaN wires,” Appl. Phys. Lett., vol. 102, p. 122116, 2013.

[110] J.-S. Hwang, F. Donatini, J. Pernot, R. Thierry, P. Ferret, and L. S. Dang, “Carrier depletion and exciton diffusion in a single ZnO nanowire,” Nanotechnology, vol. 22, p. 475704, 2011.

[111] F. Donatini, A. de Luna Bugallo, P. Tchoulfian, G. Chicot, C. Sartel, V. Sallet, and J. Pernot, “Comparison of three e-beam techniques for electric field imaging and carrier diffusion length measurement on the same nanowires,” Nano Lett., vol. 16, pp. 2938–2944, 2016.

[112] M. A. Mohammad, M. Muhammad, S. K. Dew, and M. Stepanova, “Fundamentals of Electron Beam Exposure and Development,” in Nanofabrication: Techniques and Principles, M. Stepanova and S. Dew, Eds. Vienna: Springer Vienna, 2012, pp. 11–41.

[113] P. Tchoulfian, “Propriétés électriques, optiques et électro-optiques de microfils GaN pour la réalisation de LEDs,” Université Grenoble Alpes, 2015.

[114] S. E. Mohney, Y. Wang, M. A. Cabassi, K. K. Lew, S. Dey, J. M. Redwing, and T. S. Mayer, “Measuring the specific contact resistance of contacts to semiconductor nanowires,” Solid. State. Electron., vol. 49, pp. 227–232, 2005.

[115] M. E. Lin, Z. Ma, F. Y. Huang, Z. F. Fan, L. H. Allen, and H. Morkoç, “Low resistance ohmic contacts on wide band-gap GaN,” Appl. Phys. Lett., vol. 64, pp. 1003–1005, 1994.

[116] J. Pernot, F. Donatini, and P. Tchoulfian, “Doping and Transport,” in Wide Band Gap Semiconductor Nanowires 1, John Wiley & Sons, Inc., 2014, pp. 99–123.

[117] R. Gurwitz and I. Shalish, “Method for electrical characterization of nanowires,” Nanotechnology, vol. 22, p. 435705, 2011.

[118] S. Chevtchenko, X. Ni, Q. Fan, A. A. Baski, and H. Morkoç, “Surface band bending of a-plane GaN studied by scanning Kelvin probe microscopy,” Appl. Phys. Lett., vol. 88, p. 122104, 2006.

[119] M. Kocan, A. Rizzi, H. Lüth, S. Keller, and U. K. Mishra, “Surface potential at as-grown GaN (0001) MBE layers,” Phys. Status Solidi, vol. 234, pp. 773–777, 2002.

[120] O. Wunnicke, “Gate capacitance of back-gated nanowire field-effect transistors,” Appl. Phys. Lett., vol. 89, pp. 1–4, 2006.

[121] D. R. Khanal and J. Wu, “Gate coupling and charge distribution in nanowire field effect transistors,” Nano Lett., vol. 7, pp. 2778–2783, 2007.

[122] C. G. Van de Walle, C. Stampfl, and J. Neugebauer, “Theory of doping and defects in III–V nitrides,” J. Cryst. Growth, vol. 189–190, pp. 505–510, 1998.

[123] M. Schäfer, M. Günther, C. Länger, J. Müßener, M. Feneberg, P. Uredat, M. T. Elm, P. Hille, J. Schörmann, J. Teubert, T. Henning, P. J. Klar, and M. Eickhoff, “Electrical transport properties of Ge-doped GaN nanowires,” Nanotechnology, vol. 26, p. 135704, 2015.

[124] M. Asif Khan, J. N. Kuznia, J. M. Van Hove, D. T. Olson, S. Krishnankutty, and R. M. Kolbas, “Growth of high optical and electrical quality GaN layers using low-pressure metalorganic chemical vapor deposition,” Appl. Phys. Lett., vol. 58, pp. 526–527, 1991.

[125] H. Strite, S., Morkoç, “GaN, AlN, and InN: a review,” J. Vac. Sci. Technol. B, vol. 10, pp. 1237–1266, 1992.

[126] H. M. Ng, D. Doppalapudi, T. D. Moustakas, N. G. Weimann, and L. F. Eastman, “The role of dislocation scattering in n-type GaN films,” Appl. Phys. Lett., vol. 73, pp. 821–823, 1998.

[127] X. Liu, L. Wang, D.-C. Lu, D. Wang, X. Wang, and L. Lin, “The influence of thickness on properties of GaN buffer layer and heavily Si-doped GaN grown by metalorganic vapor-phase epitaxy,” J. Cryst. Growth, vol. 189–190, pp. 287–290, 1998.

[128] I. Halidou, Z. Benzarti, Z. Chine, T. Boufaden, and B. El Jani, “Heavily silicon-doped GaN by MOVPE,” Microelectronics J., vol. 32, pp. 137–142, 2001.

[129] A. Motayed, A. V. Davydov, S. N. Mohammad, and J. Melngailis, “Experimental

investigation of electron transport properties of gallium nitride nanowires," J. Appl. Phys., vol. 104, p. 24302, 2008.

[130] S. Zhao, B. H. Le, D. P. Liu, X. D. Liu, M. G. Kibria, T. Szkopek, H. Guo, and Z. Mi, "p-type InN nanowires," Nano Lett., vol. 13, pp. 5509–5513, 2013.

[131] A. T. Connie, S. Zhao, S. M. Sadaf, I. Shih, Z. Mi, X. Du, J. Lin, and H. Jiang, "Optical and electrical properties of Mg-doped AlN nanowires grown by molecular beam epitaxy," Appl. Phys. Lett., vol. 106, p. 213105, 2015.

[132] T. J. Kempa, S. K. Kim, R. W. Day, H. G. Park, D. G. Nocera, and C. M. Lieber, "Facet-selective growth on nanowires yields multi-component nanostructures and photonic devices," J. Am. Chem. Soc., vol. 135, pp. 18354–18357, 2013.

[133] Y. H. Ra, R. Navamathavan, H. Il Yoo, and C. R. Lee, "Single nanowire light-emitting diodes using uniaxial and coaxial InGaN/GaN multiple quantum wells synthesized by metalorganic chemical vapor deposition," Nano Lett., vol. 14, pp. 1537–1545, 2014.

[134] P. Tchoulfian, F. Donatini, F. Levy, A. Dussaigne, P. Ferret, and J. Pernot, "Direct imaging of p-n junction in core-shell GaN wires," Nano Lett., vol. 14, pp. 3491–3498, 2014.

[135] M. Tchernycheva, V. Neplokh, H. Zhang, P. Lavenus, L. Rigutti, F. Bayle, F. H. Julien, A. Babichev, G. Jacopin, L. Largeau, R. Ciechonski, G. Vescovi, and O. Kryliouk, "Core–shell InGaN/GaN nanowire light emitting diodes analyzed by electron beam induced current microscopy and cathodoluminescence mapping," Nanoscale, vol. 7, pp. 11692–11701, 2015.

[136] F. Limbach, E. Schäfer-Nolte, R. Caterino, T. Gotschke, T. Stoica, E. Sutter, and R. Calarco, "Morphology and optical properties of Mg doped GaN nanowires in dependence of growth temperature," J. Optoelectron. Adv. Mater., vol. 12, pp. 1433–1441, 2010.

[137] Y. S. Park, C. M. Park, C. J. Park, H. Y. Cho, S. J. Lee, T. W. Kang, S. H. Lee, J. E. Oh, K. H. Yoo, and M. S. Son, "Electron trap level in a GaN nanorod p-n junction grown by molecular-beam epitaxy," Appl. Phys. Lett., vol. 88, p. 192104, 2006.

[138] A. Imtiaz, T. M. Wallis, J. C. Weber, K. J. Coakley, M. D. Brubaker, P. T. Blanchard, K. A. Bertness, N. A. Sanford, and P. Kabos, "Imaging the p-n junction in a gallium nitride nanowire with a scanning microwave microscope," Appl. Phys. Lett., vol. 104, p. 263107, 2014.

[139] A. Minj, A. Cros, T. Auzelle, J. Pernot, and B. Daudin, "Direct assessment of p–n junctions in single GaN nanowires by Kelvin probe force microscopy," Nanotechnology, vol. 27, p. 385202, 2016.

[140] M. D. Brubaker, P. T. Blanchard, J. B. Schlager, A. W. Sanders, A. M. Herrero, A. Roshko, S. M. Duff, T. E. Harvey, V. M. Bright, N. A. Sanford, and K. A. Bertness, "Toward discrete axial p-n junction nanowire light-emitting diodes grown by plasma-assisted molecular beam epitaxy," J. Electron. Mater., vol. 42, pp. 868–874, 2013.

[141] Y. Lu, M. Lu, Y. Yang, H. Chen, L. Chen, and S. Gwo, "Dynamic visualization of axial p-n junctions in single GaN nanorods under electrical bias," ACS Nano, vol. 7, pp. 7640–7647, 2013.

[142] C. Gutsche, R. Niepelt, M. Gnauck, A. Lysov, W. Prost, C. Ronning, and F. J. Tegude, “Direct determination of minority carrier diffusion lengths at axial GaAs nanowire p-n junctions,” Nano Lett., vol. 12, pp. 1453–1458, 2012.

[143] J. Neugebauer and C. G. Van de Walle, “Chemical trends for acceptor impurities in GaN,” J. Appl. Phys., vol. 85, pp. 3003–3005, 1999.

[144] S. Nakamura, M. Senoh, and T. Mukai, “Highly p-typed Mg-doped GaN films grown with GaN buffer layers,” Jpn. J. Appl. Phys., vol. 30, pp. L1708–L1711, 1991.

[145] I. P. Smorchkova, E. Haus, B. Heying, P. Kozodoy, P. Fini, J. P. Ibbetson, S. Keller, S. P. DenBaars, J. S. Speck, and U. K. Mishra, “Mg doping of GaN layers grown by plasma-assisted molecular-beam epitaxy,” Appl. Phys. Lett., vol. 76, p. 718, 2000.

[146] H. Alves, M. Böhm, A. Hofstaetter, H. Amano, S. Einfeldt, D. Hommel, D. M. Hofmann, and B. K. Meyer, “Compensation mechanism in MOCVD and MBE grown GaN: Mg,” Phys. B, vol. 308–310, pp. 38–41, 2001.

[147] A. Dussaigne, B. Damilano, J. Brault, J. Massies, E. Feltin, and N. Grandjean, “High doping level in Mg-doped GaN layers grown at low temperature,” J. Appl. Phys., vol. 103, p. 13110, 2008.

[148] C. A. Hurni, J. R. Lang, P. G. Burke, and J. S. Speck, “Effects of growth temperature on Mg-doped GaN grown by ammonia molecular beam epitaxy,” Appl. Phys. Lett., vol. 101, p. 102106, 2012.

[149] M. Malinverni, J. M. Lamy, D. Martin, E. Feltin, J. Dorsaz, A. Castiglia, M. Rossetti, M. Duelk, C. Velez, and N. Grandjean, “Low temperature p-type doping of (Al)GaN layers using ammonia molecular beam epitaxy for InGaN laser diodes,” Appl. Phys. Lett., vol. 105, p. 241103, 2014.

[150] S. D. Burnham, G. Namkoong, D. C. Look, B. Clafin, and W. A. Doolittle, “Reproducible increased Mg incorporation and large hole concentration in GaN using metal modulated epitaxy,” J. Appl. Phys., vol. 104, p. 24902, 2008.

[151] G. Namkoong, E. Trybus, K. K. Lee, M. Moseley, W. A. Doolittle, and D. C. Look, “Metal modulation epitaxy growth for extremely high hole concentrations above 10^{19} cm^{-3} in GaN,” Appl. Phys. Lett., vol. 93, p. 172112, 2008.

[152] B. Gunning, J. Lowder, M. Moseley, and W. Alan Doolittle, “Negligible carrier freeze-out facilitated by impurity band conduction in highly p-type GaN,” Appl. Phys. Lett., vol. 101, p. 82106, 2012.

[153] B. P. Gunning, C. A. M. Fabien, J. J. Merola, E. A. Clinton, W. A. Doolittle, S. Wang, A. M. Fischer, and F. A. Ponce, “Comprehensive study of the electronic and optical behavior of highly degenerate p-type Mg-doped GaN and AlGaN,” J. Appl. Phys., vol. 117, p. 45710, 2015.

[154] M. Zhong, J. Roberts, W. Kong, A. S. Brown, and A. J. Steckl, “p-type GaN grown by phase shift epitaxy,” Appl. Phys. Lett., vol. 104, p. 12108, 2014.

[155] S. Guha, N. A. Bojarczuk, and F. Cardone, “Mg in GaN: incorporation of a volatile species at high temperatures during molecular beam epitaxy,” Appl. Phys. Lett., vol. 71, p. 1685, 1997.

[156] V. Ramachandran, R. M. Feenstra, W. L. Sarney, L. Salamanca-Riba, J. E. Northrup, L. T. Romano, and D. W. Greve, “Inversion of wurtzite GaN(0001) by

exposure to magnesium," Appl. Phys. Lett., vol. 75, p. 808, 1999.

[157] A. J. Ptak, T. H. Myers, L. T. Romano, C. G. Van De Walle, and J. E. Northrup, "Magnesium incorporation in GaN grown by molecular-beam epitaxy," Appl. Phys. Lett., vol. 78, pp. 285–287, 2001.

[158] T. S. Cheng, S. V. Novikov, C. T. Foxon, and J. W. Orton, "Mechanisms of magnesium incorporation into GaN layers grown by molecular beam epitaxy," Solid State Commun., vol. 109, pp. 439–443, 1999.

[159] S. Brochen, J. Brault, S. Chenot, A. Dussaigne, M. Leroux, and B. Damilano, "Dependence of the Mg-related acceptor ionization energy with the acceptor concentration in p-type GaN layers grown by molecular beam epitaxy," Appl. Phys. Lett., vol. 103, p. 32102, 2013.

[160] Z. Zhong, F. Qian, D. Wang, and C. M. Lieber, "Synthesis of p-type gallium nitride nanowires for electronic and photonic nanodevices," Nano Lett., vol. 3, pp. 343–346, 2003.

[161] Y. S. Park, J. H. Na, R. A. Taylor, C. M. Park, K. H. Lee, and T. W. Kang, "The recombination mechanism of Mg-doped GaN nanorods grown by plasma-assisted molecular-beam epitaxy," Nanotechnology, vol. 17, pp. 913–916, 2006.

[162] J. Arbiol, S. Estradé, J. D. Prades, A. Cirera, F. Furtmayr, C. Stark, A. Laufer, M. Stutzmann, M. Eickhoff, M. H. Gass, A. L. Bleloch, F. Peiró, and J. R. Morante, "Triple-twin domains in Mg doped GaN wurtzite nanowires: structural and electronic properties of this zinc-blende-like stacking," Nanotechnology, vol. 20, p. 145704, 2009.

[163] F. Limbach, R. Caterino, T. Gotschke, T. Stoica, R. Calarco, L. Geelhaar, and H. Riechert, "The influence of Mg doping on the nucleation of self-induced GaN nanowires," AIP Adv., vol. 2, no. 1, pp. 0–6, 2012.

[164] Q. Wang, X. Liu, M. G. Kibria, S. Zhao, H. P. Nguyen, K. H. Li, Z. Mi, T. Gonzalez, and M. P. Andrews, "p-type dopant incorporation and surface charge properties of catalyst-free GaN nanowires revealed by micro-Raman scattering and X-ray photoelectron spectroscopy," Nanoscale, vol. 6, pp. 9970–9976, 2014.

[165] M. G. Kibria, S. Zhao, F. a. Chowdhury, Q. Wang, H. P. T. Nguyen, M. L. Trudeau, H. Guo, and Z. Mi, "Tuning the surface Fermi level on p-type gallium nitride nanowires for efficient overall water splitting," Nat. Commun., vol. 5, p. 3825, 2014.

[166] M. G. Kibria, F. A. Chowdhury, S. Zhao, M. L. Trudeau, H. Guo, and Z. Mi, "Defect-engineered GaN: Mg nanowire arrays for overall water splitting under violet light," Appl. Phys. Lett., vol. 106, p. 113105, 2015.

[167] B. Monemar, P. Paskov, G. Pozina, C. Hemmingsson, P. Bergman, D. Lindgren, L. Samuelson, X. Ni, H. Morkoç, T. Paskova, Z. Bi, and J. Ohlsson, "Photoluminescence of Mg-doped m-plane GaN grown by MOCVD on bulk GaN substrates," Phys. Status Solidi, vol. 208, pp. 1532–1534, 2011.

[168] J. K. Zettler, C. Hauswald, P. Corfdir, M. Musolino, L. Geelhaar, H. Riechert, O. Brandt, and S. Fernández-Garrido, "High-temperature growth of GaN nanowires by molecular beam epitaxy: toward the material quality of bulk GaN," Cryst. Growth Des., vol. 15, pp. 4104–4109, 2015.

[169] R. Sarkar, R. Fandan, K. R. Khiangte, S. Chouksey, A. M. Josheph, S. Das, S.

Ganguly, D. Saha, and A. Laha, “Comprehensive investigation on the correlation of growth, structural and optical properties of GaN nanowires grown on Si(111) substrates by plasma assisted molecular beam epitaxy technique,” arXiv Prepr. arXiv 1603.08603, Mar. 2016.

[170] B. Monemar, P. P. Paskov, G. Pozina, C. Hemmingsson, J. P. Bergman, T. Kawashima, H. Amano, I. Akasaki, T. Paskova, S. Figge, D. Hommel, and A. Usui, “Evidence for two Mg related acceptors in GaN,” Phys. Rev. Lett., vol. 102, p. 235501, 2009.

[171] S. J. Pearton, J. C. Zolper, R. J. Shul, and F. Ren, “GaN: Processing, defects, and devices,” J. Appl. Phys., vol. 86, pp. 1–78, 1999.

[172] E. H. Rhoderick, “The physics of schottky barriers?,” Rev. Phys. Technol., vol. 1, pp. 81–95, 1970.

[173] T. Mori, T. Kozawa, T. Ohwaki, Y. Taga, S. Nagai, S. Yamasaki, S. Asami, N. Shibata, and M. Koike, “Schottky barriers and contact resistances on p-type GaN,” Appl. Phys. Lett., vol. 69, p. 3537, 1996.

[174] H. Ishikawa, S. Kobayashi, Y. Koide, S. Yamasaki, S. Nagai, J. Umezaki, M. Koike, and M. Murakami, “Effects of surface treatments and metal work functions on electrical properties at p-GaN/metal interfaces,” J. Appl. Phys., vol. 81, pp. 1315–1322, 1997.

[175] J. Chen and W. D. Brewer, “Ohmic contacts on p-GaN,” Adv. Electron. Mater., vol. 1, p. 1500113, 2015.

[176] J.-K. Ho, C.-S. Jong, C. C. Chiu, C.-N. Huang, C.-Y. Chen, and K.-K. Shih, “Low-resistance ohmic contacts to p-type GaN,” Appl. Phys. Lett., vol. 74, p. 4491, 1999.

[177] C. Sen Lee, Y. J. Lin, and C. T. Lee, “Investigation of oxidation mechanism for ohmic formation in Ni/Au contacts to p-type GaN layers,” Appl. Phys. Lett., vol. 79, pp. 3815–3817, 2001.

[178] H. W. Jang, K. H. Kim, J. K. Kim, S. W. Hwang, J. J. Yang, K. J. Lee, S. J. Son, and J. L. Lee, “Low-resistance and thermally stable ohmic contact on p-type GaN using Pd/Ni metallization,” Appl. Phys. Lett., vol. 79, pp. 1822–1824, 2001.

[179] H. K. Cho, T. Hossain, J. W. Bae, and I. Adesida, “Characterization of Pd/Ni/Au ohmic contacts on p-GaN,” Solid. State. Electron., vol. 49, pp. 774–778, 2005.

[180] J.-S. Jang, S.-J. Park, and T.-Y. Seong, “Formation of low resistance Pt ohmic contacts to p-type GaN using two-step surface treatment,” J. Vac. Sci. Technol. B, vol. 17, pp. 2667–2670, 1999.

[181] I. Ingan, A.-G. Furthermore, M. Algan, M. Ingan, G. Sls, and E. Gan, “Efficient hole generation above 10^{19} cm^{-3} in Mg-doped InGaN / GaN superlattices at room temperature,” Jpn. J. Appl. Phys, vol. 39, pp. L95–L96, 2000.

[182] K. Kumakura, T. Makimoto, and N. Kobayashi, “Low resistance non-alloy ohmic contact to p-type GaN using Mg-doped InGaN contact layer,” Phys. Status Solidi, vol. 188, pp. 363–366, 2001.

[183] J.-K. Ho, C.-S. Jong, C. C. Chiu, C.-N. Huang, K.-K. Shih, L.-C. Chen, F.-R. Chen, and J.-J. Kai, “Low-resistance ohmic contacts to p-type GaN achieved by the oxidation of Ni/Au films,” J. Appl. Phys., vol. 86, p. 4491, 1999.

[184] Z. Z. Chen, Z. X. Qin, Y. Z. Tong, X. D. Hu, T. J. Yu, Z. J. Yang, X. M. Ding, Z. H. Li, and G. Y. Zhang, “Thermal annealing effects on Ni/Au contacts to p type GaN in different ambient,” Mater. Sci. Eng. B, vol. 100, pp. 199–203, 2003.

[185] Y. C. Lin, S. J. Chang, C. W. Kuo, and S. C. Chen, “InGaN / GaN light emitting diodes with Ni / Au , Ni / ITO and ITO p-type contacts,” Solid. State. Electron., vol. 47, pp. 849–853, 2003.

[186] R. H. Horng, D. S. Wuu, Y. C. Lien, and W. H. Lan, “Low-resistance and high-transparency Ni / ITO ohmic contacts to p-type GaN,” Appl. Phys. Lett., vol. 79, pp. 2925–2927, 2001.

[187] S. W. Chae, K. C. Kim, D. H. Kim, T. G. Kim, S. K. Yoon, B. W. Oh, D. S. Kim, H. K. Kim, and Y. M. Sung, “Highly transparent and low-resistant ZnNi /ITO Ohmic contact on p-type GaN,” Appl. Phys. Lett., vol. 90, p. 181101, 2007.

[188] J.-S. Jang and T.-Y. Seong, “Low-resistance and thermally stable indium tin oxide ohmic contacts on strained p-$In_{0.15}Ga_{0.85}N$ ⁄ p-GaN layer,” J. Appl. Phys., vol. 101, p. 13711, 2007.

[189] A. Antony, M. Nisha, R. Manoj, and M. K. Jayaraj, “Influence of target to substrate spacing on the properties of ITO thin films,” Appl. Surf. Sci., vol. 225, pp. 294–301, 2004.

[190] M. Gulen, G. Yildirim, S. Bal, A. Varilci, I. Belenli, and M. Oz, “Role of annealing temperature on microstructural and electro-optical properties of ITO films produced by sputtering,” J. Mater. Sci. Mater. Electron., vol. 24, pp. 467–474, 2013.

[191] M. Musolino, A. Tahraoui, F. Limbach, J. Lahnemann, U. Jahn, O. Brandt, L. Geelhaar, and H. Riechert, “Understanding peculiarities in the optoelectronic characteristics of light emitting diodes based on (In,Ga)N / GaN nanowires,” Appl. Phys. Lett., vol. 105, p. 83505, 2014.

[192] A. Messanvi, “Composants photoniques à base de fils de nitrures d ’ élément s III : du fil unique aux assemblées,” Universite Grenoble Alpes, 2015.

[193] A. M. Herrero, P. T. Blanchard, A. Sanders, M. D. Brubaker, N. A. Sanford, A. Roshko, and K. A. Bertness, “Microstructure evolution and development of annealed Ni/Au contacts to GaN nanowires,” Nanotechnology, vol. 23, p. 365203, 2012.

[194] H. J. Leamy, “Charge collection scanning electron microscopy,” J. Appl. Phys., vol. 53, pp. R51–R80, 1982.

[195] J. C. Gonzalez, K. L. Bunker, and P. E. Russell, “Minority-carrier diffusion length in a GaN-based light-emitting diode,” Appl. Phys. Lett., vol. 79, pp. 1567–1569, 2001.

[196] S. Barbet, R. Aubry, M. A. Di Forte-Poisson, J. C. Jacquet, D. Deresmes, T. Ḿlin, and D. Thŕon, “Surface potential of n- and p-type GaN measured by Kelvin force microscopy,” Appl. Phys. Lett., vol. 93, p. 212107, 2008.

[197] B. S. Simpkins, M. A. Mastro, C. R. Eddy, J. K. Hite, and P. E. Pehrsson, “Space-charge-limited currents and trap characterization in coaxial AlGaN/GaN nanowires,” J. Appl. Phys., vol. 110, p. 44303, 2011.

[198] A. A. Talin, F. Léonard, B. S. Swartzentruber, X. Wang, and S. D. Hersee, “Unusually strong space-charge-limited current in thin wires,” Phys. Rev. Lett.,

vol. 101, p. 76802, 2008.

[199] D. Cavalcoli and A. Cavallini, “Evaluation of diffusion length at different excess carrier concentrations,” Mater. Sci. Eng. B, vol. 24, pp. 98–100, 1994.

[200] K. Kanaya and S. Okayama, “Penetration and energy-loss theory of electrons in solid targets,” J. Phys. D. Appl. Phys., vol. 5, pp. 43–58, 2002.

[201] J. Bonard and J. Ganière, “Quantitative analysis of electron-beam-induced current profiles across p–n junctions in GaAs/$Al_{0.4}Ga_{0.6}As$ heterostructures,” J. Appl. Phys., vol. 79, pp. 6987–6994, 1996.

[202] C. M. Parish and P. E. Russell, “On the use of Monte Carlo modeling in the mathematical analysis of scanning electron microscopy-electron beam induced current data,” Appl. Phys. Lett., vol. 89, p. 192108, 2006.

[203] C. Donolato, “Reciprocity theorem for charge collection by a surface with finite collection velocity: application to grain boundaries,” J. Appl. Phys., vol. 76, pp. 959–966, 1994.

[204] T. Onuma, N. Sakai, T. Igaki, T. Yamaguchi, A. A. Yamaguchi, and T. Honda, “Comparative study of surface recombination in hexagonal GaN and ZnO surfaces,” J. Appl. Phys., vol. 112, p. 63509, 2012.

[205] J. B. Schlager, K. A. Bertness, P. T. Blanchard, L. H. Robins, A. Roshko, and N. A. Sanford, “Steady-state and time-resolved photoluminescence from relaxed and strained GaN nanowires grown by catalyst-free molecular-beam epitaxy,” J. Appl. Phys., vol. 103, p. 124309, 2008.

[206] I. Volotsenko, M. Molotskii, Z. Barkay, J. Marczewski, P. Grabiec, B. Jaroszewicz, G. Meshulam, E. Grunbaum, and Y. Rosenwaks, “Secondary electron doping contrast: theory based on scanning electron microscope and Kelvin probe force microscopy measurements,” J. Appl. Phys., vol. 107, p. 14510, 2010.

[207] C. Schönjahn, R. F. Broom, C. J. Humphreys, A. Howie, and S. A. M. Mentink, “Optimizing and quantifying dopant mapping using a scanning electron microscope with a through-the-lens detector,” Appl. Phys. Lett., vol. 83, pp. 293–295, 2003.

[208] M. El-Gomati, F. Zaggout, H. Jayacody, S. Tear, and K. Wilson, “Why is it possible to detect doped regions of semiconductors in low voltage SEM: a review and update,” Surf. Interface Anal., vol. 37, pp. 901–911, 2005.

[209] F. Mika and L. Frank, “Two-dimensional dopant profiling with low-energy SEM,” J. Microsc., vol. 230, pp. 76–83, 2008.

[210] P. Kazemian, C. Rodenburg, and C. J. Humphreys, “Effect of experimental parameters on doping contrast of Si p-n junctions in a FEG-SEM,” Microelectron. Eng., vol. 73–74, pp. 948–953, 2004.

APPENDICES

APPENDIX A PUBLICATIONS, CONFERENCES & WORKSHOPS

This PhD work has led to the following publications and presentations:

Publications

- Fang Z., Donatini F., Pernot J., Daudin B., Visualization and quantitative analysis of axial p-n junction on single GaN nanowire by electron beam based techniques. (to be submitted)
- Auzelle T., Biquard X., Roussel H., Bellet-Amalric E., Fang Z., Cros A., Daudin B., Unraveling the strain state of GaN down to single nanowires. Journal of Applied Physics (2016) 120, 225701
- Rozas-Jimenez E., Cros A., Murcia-Mascaros S., Fang Z., Daudin B., Phonon-plasmon coupling in Si doped GaN nanowires. Materials Science in Semiconductor Processing (2016) 55, 63-66
- Fang Z., Robin E., Rozas-Jimenez E., Cros A., Donatini F., Mollard N., Pernot J., Daudin B., Si donor incorporation in GaN nanowires. Nano letters (2015) 15(10), 6794 – 6801

Conferences and workshops

- Visulization and quantitative analysis of axial p-n junction on single GaN nanowire by electron beam based techniques

  Fang Z., Donatini F., Robin E., Pernot J., Daudin B., MRS fall meeting, Boston, USA, 2016 (Oral presentation)
- Visulization and quantitative analysis of axial p-n junction on single GaN nanowire by three electron beam based techniques

  Fang Z., Donatini F., Robin E., Pernot J., Daudin B., International Workshop on Nitride Semiconductors (IWN), Orlando, USA, 2016 (Oral presentation)
- Structural and transport properties of Si doped GaN nanowires

  Fang Z., Robin E., Rozas-Jimenez E., Cros A., Donatini F., Mollard N., Pernot J., Daudin B, Conpound Semiconductor Week (CSW), Toyama, Japan, 2016 (Oral presentation)
- High Si incorporation in MBE-grown GaN nanowires

  Fang Z., Robin E., Rozas-Jimenez E., Cros A., Donatini F., Mollard N., Pernot J., Daudin B., Nanowire growth workshop, Barcelone, Spain, 2015 (poster)
- Structural and transport properties of Si doped GaN nanowires

Fang Z., Robin E., Rozas-Jimenez E., Cros A., Donatini F., Mollard N., Pernot J., Daudin B., 11th International Conference on Nitride Semiconductor (ICNS), Beijing, China, 2015 (poster) Best poster award

- The growth of GaN nanowires

  Fang Z., Pernot J.,Daudin B., Journées Nationales du Réseau Doctoral en Micro-nanoélectronique (JNRDM), Bordeaux, France, 2015 (poster)

Summer schools

- Pulse school epitaxy updates and promises, Porquerolles, France, 2015
- Ganex school on the physics and applications of nitrides, Nice, France, 2015